Grand Canyon Monitoring
and Research Center

JUN 15 1997

Received
Flagstaff, AZ

Physics of flow, sediment transport, hydraulic geometry, and channel geomorphic adjustment during flash floods in an ephemeral river, the Paria River, Utah and Arizona

by

David Joseph Topping

A dissertation submitted in partial fulfillment
of the requirements for the degree of

Doctor of Philosophy

University of Washington

1997

Approved by _____
Chairperson of Supervisory Committee

Program Authorized
to Offer Degree Department of Geological Sciences

Date May 30, 1997

VOLUME 2

© Copyright 1997

David Joseph Topping

Chapter 3: DEVELOPMENT AND TESTING OF A GEOMORPHICALLY COUPLED FLOW AND SEDIMENT-TRANSPORT MODEL

Section 3.1: INTRODUCTION

The major goal of work presented in this chapter is the development and testing of a physically based, reach-averaged, flow and sediment-transport model for the Lees Ferry, AZ reach of the Paria River that is coupled to the channel geomorphologic evolution during floods through mass conservation of each sediment size class between the bed and the flow. As illustrated in Chapter 2, the bankfull channel cross-section geometry in the Paria River is determined, to a large degree, by mass conservation of gravel-sized sediment on a reach scale. Furthermore, the reach-scale enlargement of the channel cross-section that occurs during a flood, as finer sediment sizes go into suspension, must also be set, to some degree, by reach-scale conservation of mass of the finer sediment sizes, i.e., sand, silt, and, clay. Therefore, prior to the development of the flow and sediment-transport model in this chapter, statistical analyses were first conducted on suspended-sediment data from the Paria River to determine: (1) the size range of sediment for which mass is largely conserved on the reach scale during a flood, and, therefore controls the geomorphic change of the channel during a flood; and (2) the size range of sediment that is largely advected through a reach during a flood and, therefore, has no impact on the geomorphology of the channel in that reach.

Following these analyses, the chapter is organized into 6 major sections, in which: the physical framework of and the working hypotheses and physical assumptions that drive the flow and sediment-transport model are discussed; a general overview of the model is presented to illustrate the 2-way physical coupling between the flow and sediment-transport components of the model; a quantitative description of the bed to conserve the reach-scale mass of sediment between the bed and the flow is formulated; the flow component of the model is derived; the suspended-sediment transport component of the model is derived; and finally, the model predictions of flow and sediment-transport are tested against the flume data of Kennedy (1961) and Guy and others (1966) and the Rio Puerco data of Nordin (1963), i.e., the highest suspended-sediment concentration data from a river for which velocity and sediment concentration profiles were measured. Also presented, in the section describing the flow component of the model, is a subsection focused on the nature of roughness and drag associated with suspended-sediment transport over antidune and upper-plane bed configurations; this section is included in this chapter because antidunes are a common type of bedform in the Paria River (as mentioned in Chapter 2).

Section 3.2: SUSPENDED SEDIMENT IN THE PARIA RIVER

3.2a: Introduction and presentation of the data

The Paria River has one of the longest term suspended-sediment records in the world for a river of its type and size. From October 1, 1947 through September 30, 1976, quasi-daily samples of suspended sediment were collected in the Lees Ferry, AZ reach and analyzed for concentration; and, from July 7, 1954 through September 26, 1976, 145 of these samples were also analyzed for the distribution of sediment grain sizes. Furthermore, in 1983, 81 additional samples were collected and analyzed for both concentration and grain-size distribution (Figures 3.1 and 3.2).

From October 1, 1947 through September 30, 1976, depth-integrated suspended-sediment samples were collected and analyzed for concentration on a daily basis during times of steady flow, and more frequently during floods. At the lowest flows, though, when suspended sediment concentrations were especially low, samples would be composited for several days prior to analysis for concentration. The measured depth-integrated suspended-sediment concentration as a function of instantaneous fluid discharge for the non-composited measurements is shown in Figure 3.1a (these measurements were checked for errors and typed into an ascii computer file from the original USGS field notes). Note that the variation in suspended-sediment concentration can be as great as five orders of magnitude for the same discharge.

The cross-section of the Paria River is relatively poorly mixed in the cross-stream direction and large cross-stream gradients are present in sediment concentration (Figure 3.1b). Of the 7756 measurements in Figure 3.1a, the concentrations of 3158 samples collected at individual measurement verticals were analyzed prior to cross-sectional compositing. Thus, for these samples, the cross-stream difference in measured suspended-sediment concentration, which illustrates the degree to which the cross-section of the river is mixed, could be evaluated (Figure 3.1b). Note that, as with the measurements of suspended-sediment concentration in Figure 3.1a, the cross-stream difference in suspended-sediment concentration can be as great five orders of magnitude for the same discharge.

Not only is the Paria River noted for its abundant suspended-sediment data, but it is also renowned for measured "hyperconcentrations" of suspended sediment; indeed, the Lees Ferry, AZ reach of the Paria River is the "birthplace" of the term "hyperconcentrated flow" (Beverage and Culbertson, 1964). The Paria River is the site of both the second and fourth highest depth-integrated suspended-sediment concentrations ever measured on any river in the world (44% by volume on September 18, 1983 and 41% by volume on

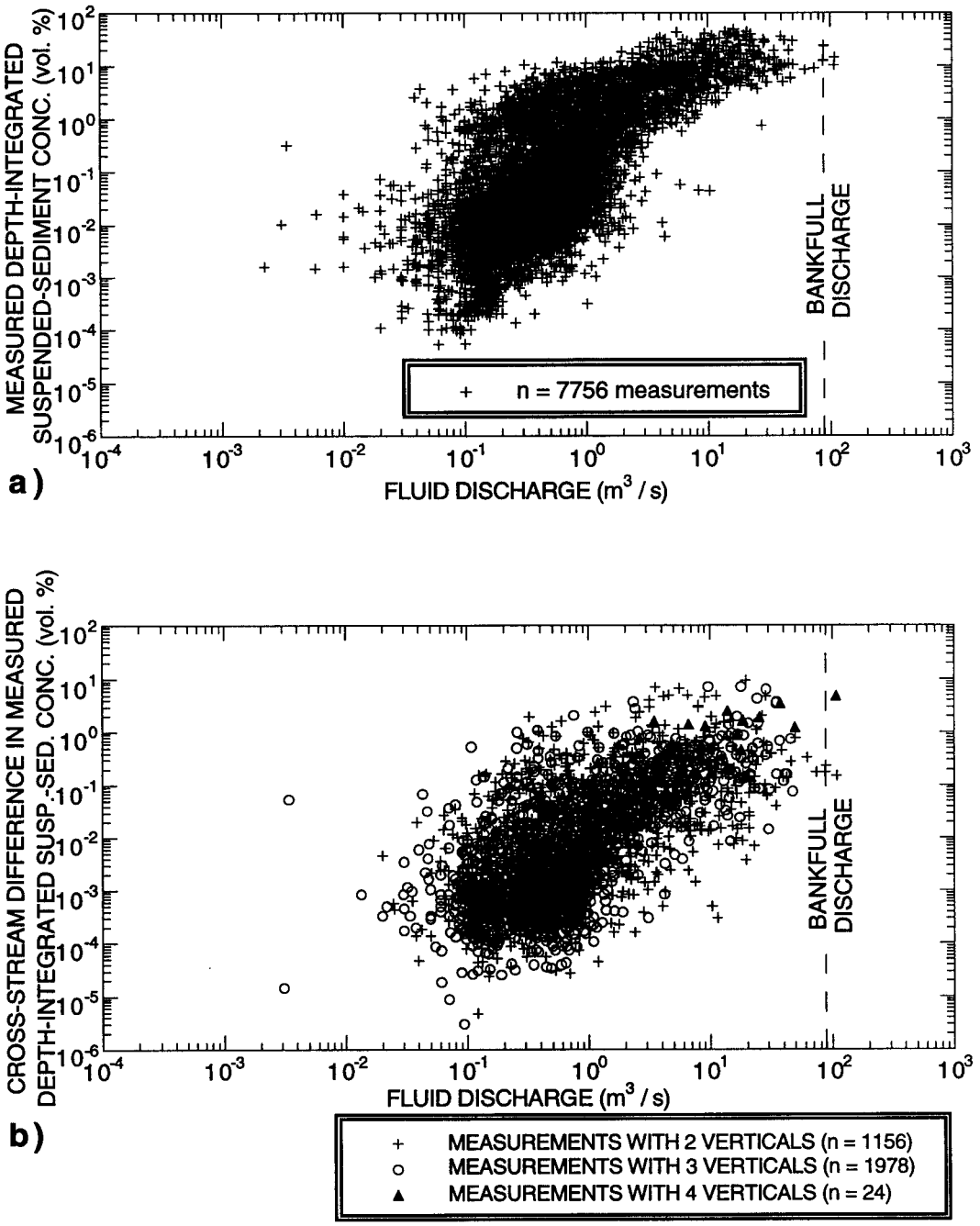

Figure 3.1: **(a)** Measured cross-sectionally integrated depth-integrated suspended-sediment concentration in the Paria River at Lees Ferry from October 1, 1947 through September 30, 1975. The instantaneous discharge associated with each suspended-sediment measurement was determined from the instantaneous discharge time series presented in Section 2.4d. Because instantaneous discharges could not be computed, measurements made from October 1, 1975 through September 30, 1976 could not be included in this figure. **(b)** Measured maximum difference in cross-stream depth-integrated suspended-sediment concentration in the Paria River at Lees Ferry, AZ from October 1, 1947 through September 30, 1975.

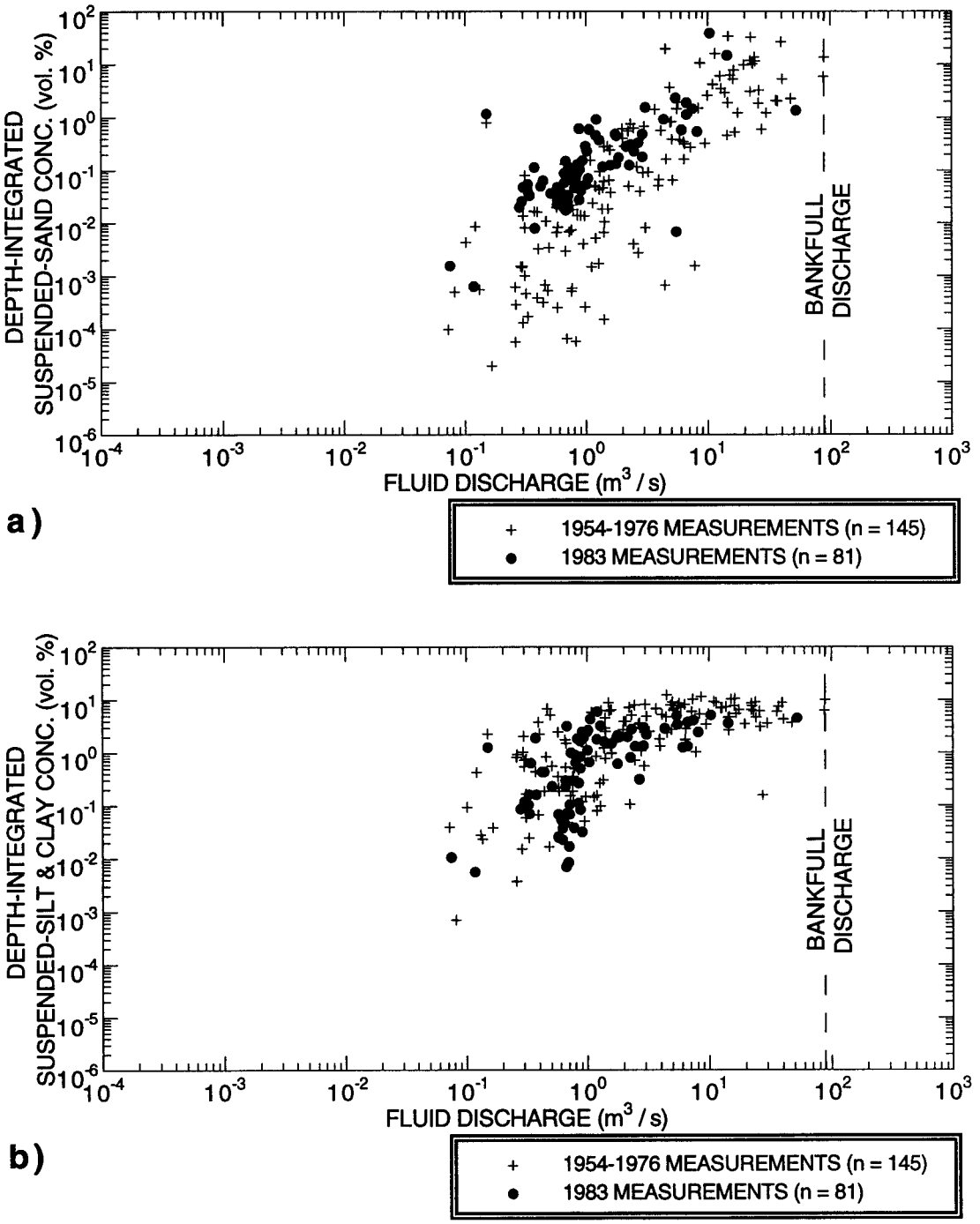

Figure 3.2: **(a)** Measured cross-sectionally integrated depth-integrated suspended-sand concentration in the Paria River at Lees Ferry, AZ from July 7, 1954 through September 26, 1976 and July 1, 1983 through December 3, 1983. **(b)** Measured cross-sectionally integrated depth-integrated suspended-silt and clay concentration in the Paria River at Lees Ferry, AZ from July 1, 1954 through September 26, 1976 and July 1, 1983 through December 3, 1983.

August 27, 1952). The highest depth-integrated suspended-sediment concentration measured in a river (45% by volume) was measured on the Rio Puerco in New Mexico (Bondurant, 1950, 1951), and the third highest (43% by volume on March 20, 1982) was measured on the Toutle River in Washington following an eruption of Mt. St. Helens (Pierson and Scott, 1985). The Paria River samples are the highest and second highest concentrations measured with standard USGS depth-integrating samplers with isokinetic nozzles; both the Rio Puerco and Toutle River samples were open-bottle dip samples of lesser reliability. Since "hyperconcentrations" of suspended sediment are common in the Paria River (e.g., Figure 3.1a), the flow and sediment-transport model developed in this chapter has been designed to include the relevant physical effects of concentrations of suspended-sediment in the hyperconcentrated range.

3.2b: Methods of USGS sample collection and laboratory analysis

Because predictions from the flow and sediment-transport model developed in this chapter are to be tested, in Chapter 4, against Paria River suspended-sediment data, it is important to review how these data were collected and analyzed by the USGS.

Sample collection in the field

From October 1, 1947 through September 30, 1964, the suspended-sediment samples were collected in the vicinity of the post-1925 gage; and, from October 1, 1964 through September 30, 1976, the majority of samples were collected near the new post-1963 highway bridge (Figure 2.4). At low flows, the 1947-1976 samples were collected by use of a DH-48 depth-integrating suspended sediment sampler (Figure 3.3a) either near the gage prior to October 1, 1964 or near the highway bridge starting October 1, 1964. At higher flows, the samples were collected with a D-43 depth-integrating suspended sediment sampler (Figure 3.3b) at Cableway 2. Samples were normally collected at up to three stations, i.e., verticals, across the channel located at 25%, 50%, and 75% of the bankfull channel width, with a clean bottle used for each station; only 24 out of 7756 measurements were made at four verticals. Since one or more of the stations were usually dry during sampling, one or two bottles were collected at only one or two verticals across the channel for the majority of the 7756 quasi-daily measurements. Of the 145 grain-size analyzed samples collected from 1954-1976 (Figure 3.2), 32 are single-bottle samples collected at one vertical, 84 are two-bottle samples collected at two verticals, 24 are three-bottle samples collected at all three verticals, and only five are samples of greater than three

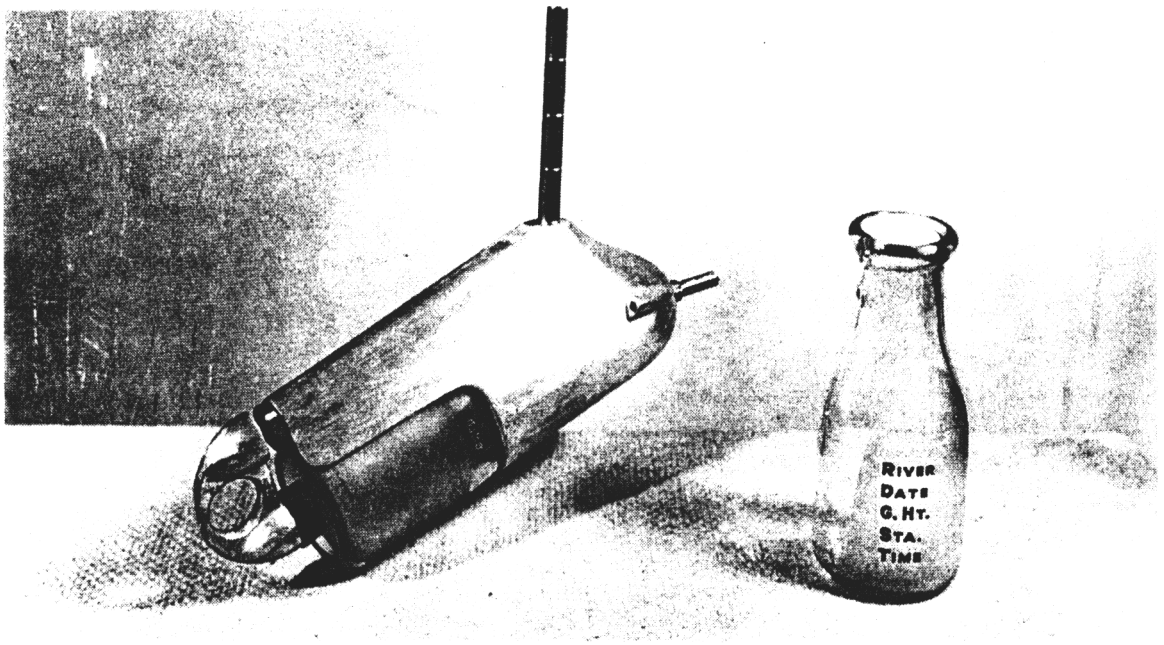

a)

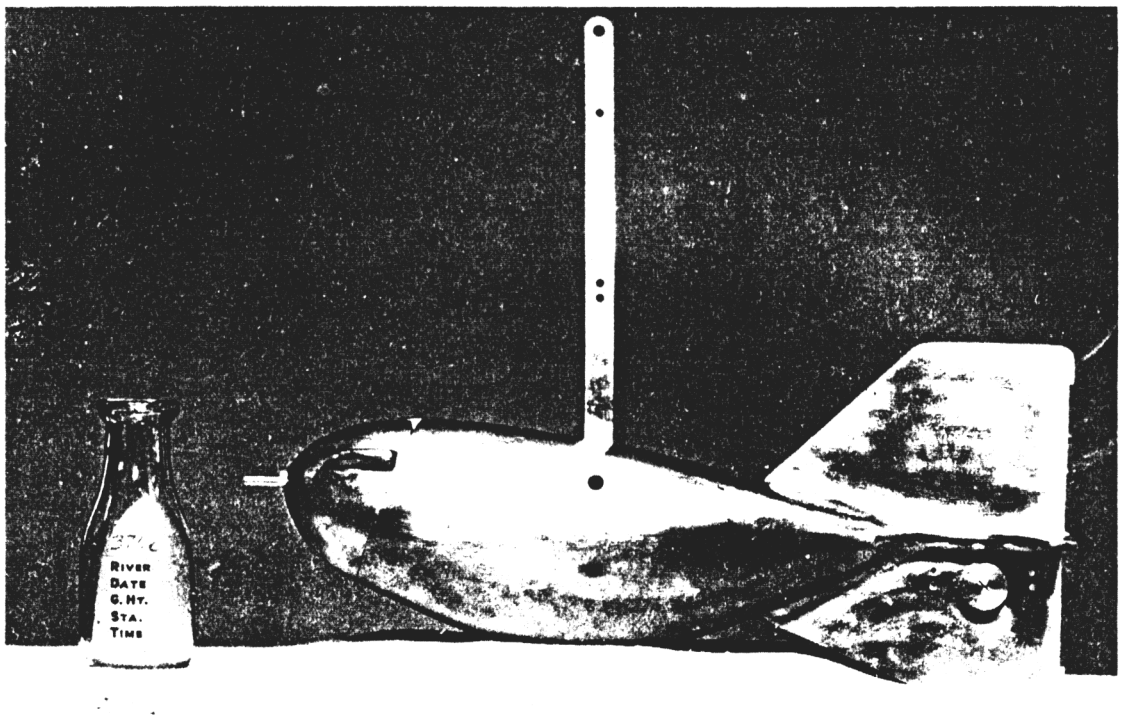

b)

Figure 3.3: **(a)** DH-48 depth-integrating suspended-sediment sampler; this sampler design was used to collect the majority of the 1947-1976 samples. **(b)** D-43 depth-integrating suspended-sediment sampler; this sampler design was used to collect the higher discharge 1947-1976 samples from Cableways 1 and 2. Photographs from Subcommittee on Sedimentation, Federal Inter-agency River Basin Committee (1952).

bottles. The 1983 data were collected by the equal-width increment method, later described in Edwards and Glysson (1988), in the incised reach in the vicinity of the gaging station.

For both the DH-43 and D-43 samplers, the sampling technique was to begin at the surface and lower the sampler at a constant transit velocity until the sampler struck the bed and then raise the sampler at the same transit velocity. The sampler transit velocity was chosen such that the pint bottle inside was almost full when the sampler broke the surface. Both samplers are designed to sample at the local flow velocity, therefore, the collected sample is a discharge-weighted sample; and, given the quasi-logarithmic shape of a velocity profile in a river, more of the sample is collected from the upper part of the flow than the lower part. Each sampler leaves an unsampled zone near the bed; the DH-48 can sample to 9 cm above the bed and the D-43 can sample to 12 cm above the bed (Subcommittee on Sedimentation, Federal Inter-agency River Basin Committee, 1952). Therefore, depth-integrated samplers provide poor estimates of average sediment-concentration for any grain-size with a high concentration gradient near the bed and work the best for grain-sizes with no concentration gradient, i.e. wash load. In addition to this common trait of all depth-integrated samplers, the D-43 sampler had two design flaws that would make its use in the Paria River problematic, resulting in increased measurement error. Guy and Norman (1970) state that: (1) "With an increase in depth, velocity, or turbulence, the stability of the instrument decreased;" and, (2) "The tail-vane extension acted as a pivot point when it touched the streambed and the suspension cable became slack. The head of the sampler would swing sideways before the return trip to the surface." The second condition would always be satisfied in any river in which the D-43 was used; and, since mean velocities of 2-3 m/s are common in the Paria River, the first condition would usually apply when the D-43 was used in the Paria River.

Grain-size analysis

Of the more than 8000 quasi-daily suspended-sediment samples collected from October 1, 1954 through September 30, 1976 in the Lees Ferry reach of the Paria River, 145 samples were analyzed for grain-size distribution. Grain-size distribution of the silt and clay fraction of this data set was analyzed in deionized water by a standard USGS pipet analysis [method described by Guy (1969)]. Of the 145 samples, only eight samples were split in half, with one half analyzed in a flocculated state in native Paria River water and the other half in a deflocculated state in deionized water containing a dispersant; Figure 3.4 illustrates the difference in the results of the two analyses. Grain-size distribution of the sand fraction of the 1954-1976 data set was analyzed by the USGS by use of a visual

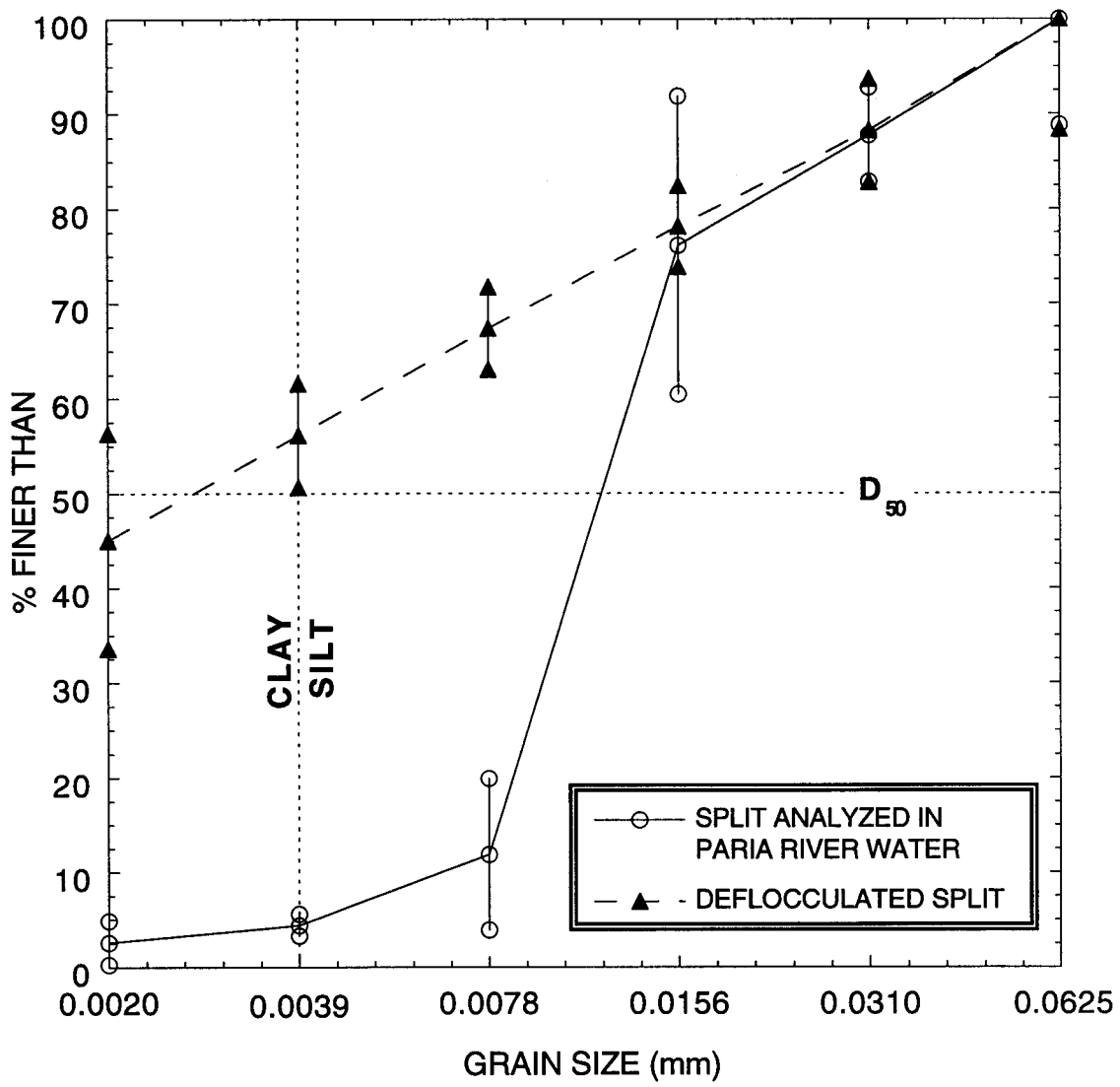

Figure 3.4: Cumulative grain-size distributions of the flocculated and deflocculated suspended-silt and clay in the Paria River at Lees Ferry, AZ for the 8 samples analyzed both in native Paria River water and in deionized water containing a dispersant; error bars are plus and minus 1 standard deviation.

accumulation tube in 1 ϕ intervals for 88 of the samples, and by use of wet sieves in 1 ϕ intervals for 55 of the samples [methods described by Guy (1969)]. Grain-size distribution of the sand fraction of the 1983 data set was analyzed by the Bureau of Reclamation by the use of wet sieves in 1 ϕ intervals; grain-size distribution of the silt and clay fraction of the 1983 data was not analyzed. For use in this study, the original field and laboratory notes for the 1954-1976 grain-size analyzed suspended-sediment samples were obtained from Julia B. Graf of the Arizona District of the USGS-WRD. All values in these notes were checked for errors prior to use. Resolution of grain size was improved in the 88 grain-size analyses processed with a visual accumulation tube by reanalyzing the graphs from the tubes at 1/2 ϕ instead of the standard 1 ϕ interval; and, in order to have a consistent data set, the 136 grain-size analyses processed with wet sieves were graphically interpolated to 1/2 ϕ intervals.

3.2c: Statistical analysis of the Paria River grain-size analyzed suspended-sediment data

With a methodology similar to that used to analyze Paria River cross-section geometry in Section 2.5b-4b, statistical analyses were conducted on the 226 grain-size analyzed suspended-sediment samples to address three questions. First, does the number of sampling verticals greatly affect the data? Second, do the antecedent conditions in the channel (e.g., time since the last flood, size of the last flood, time between the last two floods) have any large impact on the concentration of any size range of the suspended sediment; and, for which sizes of the suspended sediment is the concentration in equilibrium with the reach-averaged hydraulics and supply on the bed? Third, for which sizes of suspended sediment is the concentration not related to the local hydraulics or supply, but rather advected into the Lees Ferry reach during each flood and therefore related largely to upstream hillslope processes?

For these analyses, the independent variable was defined as the log-transformed instantaneous fluid discharge at the time of the suspended-sediment measurement; the dependent variable was defined as the log-transformed concentration of the suspended sediment in the grain-size range of interest. Because the variance in concentration is large in depth-integrated suspended-sediment data (i.e., greater than one order of magnitude at all discharges) and the number of data is relatively small (i.e. 226 compared to 2490 for the discharge measurements used in Section 2.5b-4b), a level of significance of 0.0001 rather than 0.05 was chosen so that the F-tests would discriminate between only the largest differences in the data. Also, because the binning of this data was partially subjective,

various bin sizes, numbers, and bin combinations were used in each step to attempt to remove the potential binning-scheme dependence of the analysis.

The first step in this analysis was to divide the suspended sediment data into two bins, one of total sand and one of combined silt and clay; then, the following analyses were conducted on each bin. Five potential controls on sediment concentration were investigated in a five-step progressive manner; that is, if a difference at the 0.0001 level of significance were found at a certain step, the data would be subdivided into new bins before proceeding to the next step. One other potential control, the number of verticals in the suspended-sediment measurement, was also investigated. Potential controls on sediment concentration were thus investigated in the following six tests expressed as questions. **(TEST 1)** At a given instantaneous fluid discharge, does the concentration depend on the year of the suspended-sediment measurement? **(TEST 2)** At a given instantaneous fluid discharge, does the concentration depend on season? **(TEST 3)** At a given instantaneous fluid discharge, does the concentration depend on the time since the "last flood peak"? In these analyses, a base flow of 8.5 m^3/s was chosen for defining a flood peak because it is the discharge at which the entire bottom of the channel in the Lees Ferry study area is covered by water, thus, it is the probable lowest discharge that can potentially advect substantial quantities of sediment into the Lees Ferry reach. Furthermore, a flood peak was considered to be distinct from a previous flood peak only when the discharge between the two peaks decreased below a base discharge of 3.79 m^3/s (this base discharge was chosen, in Chapter 2, to define a flood because it is one standard deviation above the mean instantaneous discharge of 0.77 m^3/s). **(TEST 4)** At a given instantaneous fluid discharge, does the concentration depend on the time between the last two flood peaks? **(TEST 5)** At a given instantaneous fluid discharge, does the concentration depend on the size of the last flood peak? **(TEST 6)** At a given instantaneous fluid discharge, does the measured concentration depend on the number of measurement verticals? Detailed binning schemes and statistics for these analyses appear in Appendix 2.

Table 3.1 shows whether the variance in concentration as a function of discharge is greater or smaller when the data are broken into bins. At each step in Table 3.1, if the null hypothesis could be rejected at the 0.0001 level of significance, the answer shown in the box is "yes" and the level of significance, p, at which the data in the subdivided bins are different is shown in parentheses. Likewise, if the null hypothesis could not be rejected, the answer shown in the box is "no" and the level of significance at which the data would be different (for the various binning schemes shown in Appendix 2) appears in parentheses.

Table 3.1: Results of the statistical analysis of the grain-size analyzed suspended-sediment data; summary of the rejection of the null hypothesis for a common regression line at the 0.0001 level of significance, *p*.

	SAND VOLUME CONCENTRATION AS A FUNCTION OF FLUID DISCHARGE		SILT & CLAY VOLUME CONCENTRATION AS A FUNCTION OF FLUID DISCHARGE		
TEST 1: YEAR	**YES** ***(p = 3.9e-13)*** (see Appendix 2, Table 1) **1954-1976**: NO *(p = 0.16)* **1983**		NO *(p ≥ 6.7e-3)* (see Appendix 2, Table 11)		
TEST 2: SEASON	NO *(p = 0.073)* (see Appendix 2, Table 2)	NO *(p = 1.0)* (see Appendix 2, Table 3)	**YES** ***(p = 4.8e-7)*** (see Appendix 2, Table 12) **MONSOON SEASON (July 1 - October 31)**		**"NON-MONSOON" SEASON (November 1 - June 30)**
TEST 3: TIME SINCE LAST FLOOD PEAK	NO *(p ≥ 0.079)* (see Appendix 2, Table 4)	NO *(p ≥ 0.14)* (see Appendix 2, Table 5)	**YES** ***(p = 2.4e-6)*** (see Appendix 2, Table 13) **≤100 HOURS SINCE LAST FLOOD PEAK**: NO *(p = 1.0)*	**>100 HOURS SINCE LAST FLOOD PEAK**: NO *(p = 1.0)*	NO *(p =1.0)* (see Appendix 2, Table 14)
TEST 4: TIME BETWEEN LAST 2 FLOOD PEAKS	NO *(p ≥ 0.041)* (see Appendix 2, Table 6)	NO *(p = 1.0)* (see Appendix 2, Table 7)	NO *(p = 1.0)* (see Appendix 2, Table 15)	NO *(p ≥ 0.057)* (see Appendix 2 Table 16)	NO *(p = 1.0)* (see Appendix 2, Table 17)
TEST 5: DISCHARGE OF LAST FLOOD PEAK	**YES** ***(p = 8.6e-6)*** (see Appendix 2, Table 8) **PEAK OF LAST FLOOD ≤28.3 m^3/s** **PEAK OF LAST FLOOD >28.3 m^3/s**: NO *(p = 0.18)*	NO *(p = 0.048)* (see Appendix 2, Table 9)	NO *(p ≥ 0.011)* (see Appendix 2, Table 18)	NO *(p = 1.0)* (see Appendix 2, Table 19)	NO *(p = 1.0)* (see Appendix 2, Table 20)
TEST 6: NUMBER OF VERTICALS IN THE MEASUREMENT	NO *(p ≥ 0.071)* (see Appendix 2, Table 10)	NO INFO. ON NUMBER OF VERTICALS AVAILABLE	NO *(p = 0.14)* (see Appendix 2, Table 21)		

Because of the large variance inherent in depth-integrated suspended-sediment data, problems arose during certain analyses. In some cases, regression lines could not be fit to data within the chosen bins at the 0.0001 level of significance, and the variance in the system was increased for the binned over the unbinned data. For example, in the case of investigating the dependence of silt and clay concentration during the "non-monsoon" season on the discharge of the last flood peak, none of the binning schemes resulted in viable regression lines at the 0.0001 level of significance. Thus, the total mean squares was used instead of the residual mean squares to characterize the variance in the data in each bin, resulting in increased variation in the system for the binned relative to variation in the system for the unbinned "non-monsoon" season data. Since variation was increased in the system by binning the data, a negative F statistic was calculated and the null hypothesis of a common regression line could only be rejected at the 1.0 level of significance.

Only four significant differences exist in the grain-size analyzed suspended-sediment data at the 0.0001 level of significance (Table 3.1, Figure 3.5). (1) The suspended-sand data collected from 1954 to 1976 are different from the suspended-sand data collected in 1983. This is interpreted below to be mainly due to the difference in cross-section geometry of the channels in which the 1954-1976 and 1983 data sets were collected. (2) At the same discharge and independent of the time after a flood peak, the suspended-sand concentration after a smaller flood peak, i.e., peaks less than about 28.3 m^3/s or roughly 30% of the bankfull discharge of 90 m^3/s, is higher than the suspended-sand concentration after a larger discharge flood peak. (3) The suspended-silt and clay concentration during the monsoon season (July 1 through October 31) is enhanced relative to the suspended-silt and clay concentration during the "non-monsoon" season (November 1 through June 30). (4) Finally, the suspended-silt and clay concentration decays with time after a flood in the monsoon season. At the same discharge, the concentration of silt and clay within 100 hours of a flood is enhanced relative to the concentration of silt and clay in excess of 100 hours after a flood.

Discussion

Results of the statistical analysis of the grain-size analyzed suspended-sediment data discussed below suggest strongly that: sand is largely in equilibrium with the local hydraulics (determined by the channel geometry) and supply on the bed, while the silt and clay are largely advected into the Lees Ferry reach from upstream. Thus, the sand is more strongly coupled to the local channel morphology than the silt and clay. Both the sand and the silt and clay are affected by the antecedent conditions in the channel, but in opposing

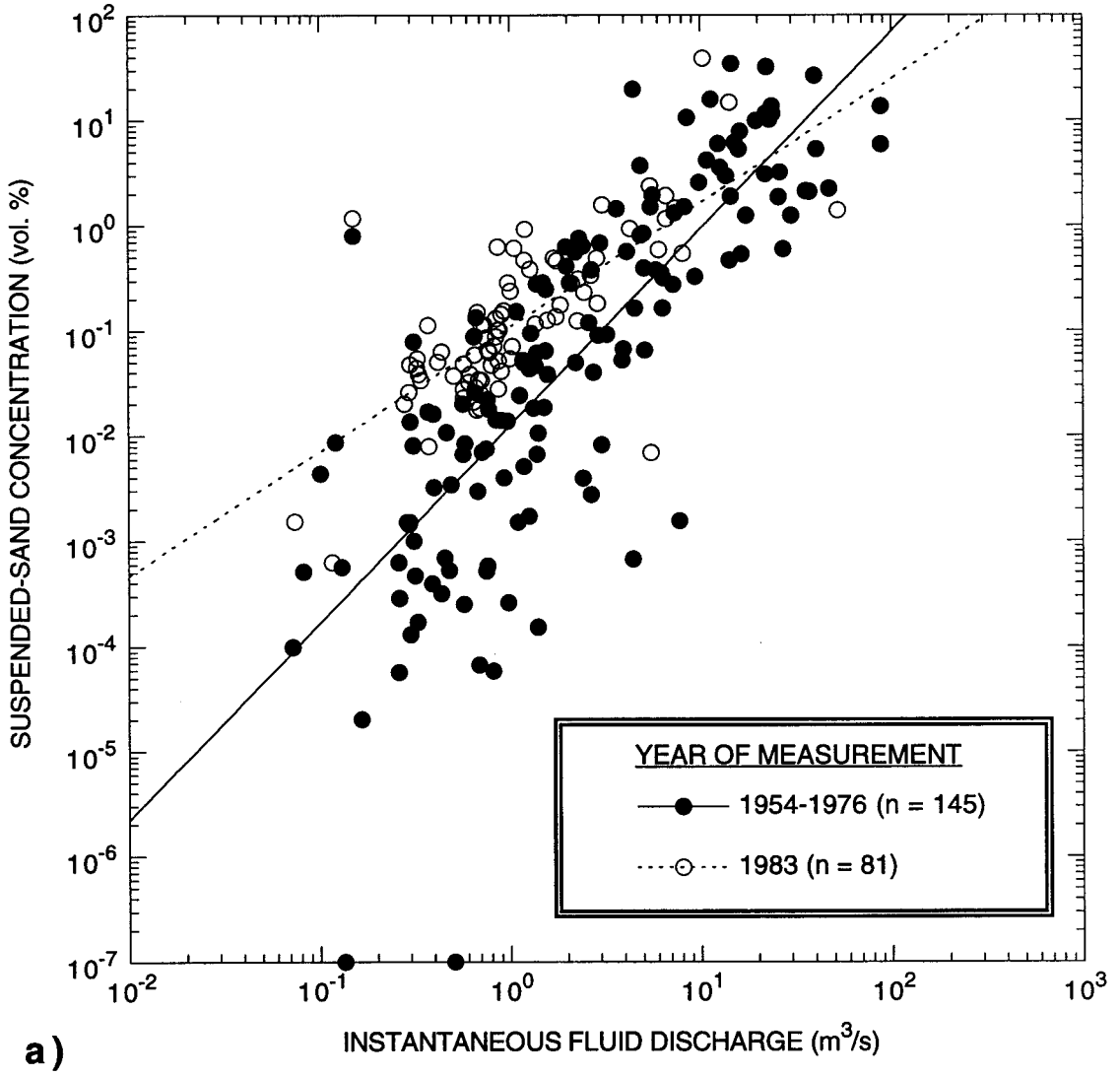

Figure 3.5: **(a)** 1954-1976 and 1983 suspended-sand concentration as a function of instantaneous fluid discharge; these data bins are different at the 3.9×10^{-13} level of significance. The lines are the log-linear regressions fit to the data in these bins. Points plotted on the x-axis are measurements of zero sand concentration.

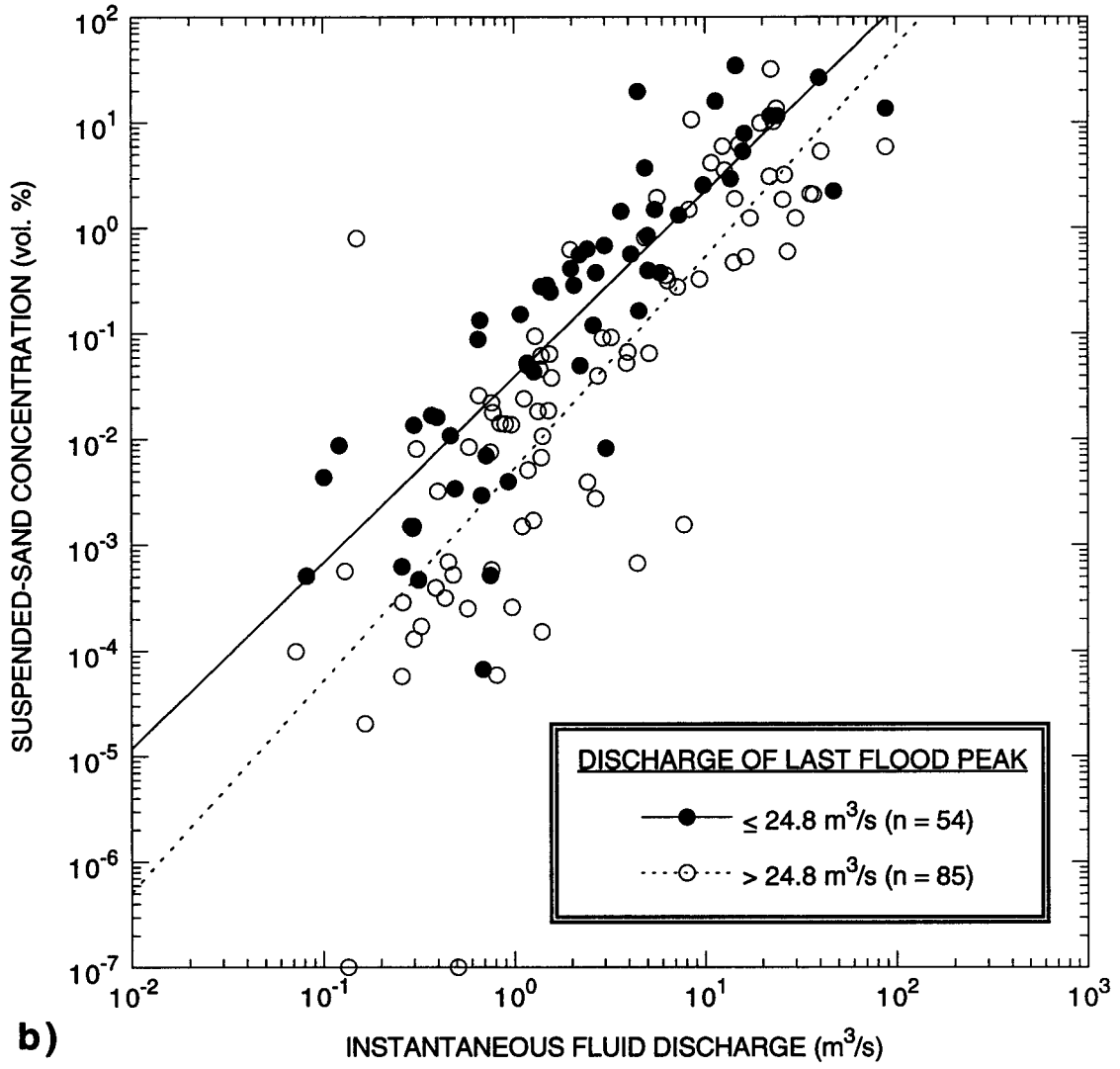

Figure 3.5 (continued): **(b)** 1954-1976 suspended-sand concentration as a function of instantaneous fluid discharge following flood peaks ≤ 24.8 m^3/s and flood peaks > 24.8 m^3/s; these data bins are different at the 8.6×10^{-6} level of significance. The lines are the log-linear regressions fit to the data in these bins. Points plotted on the x-axis are measurements of zero sand concentration.

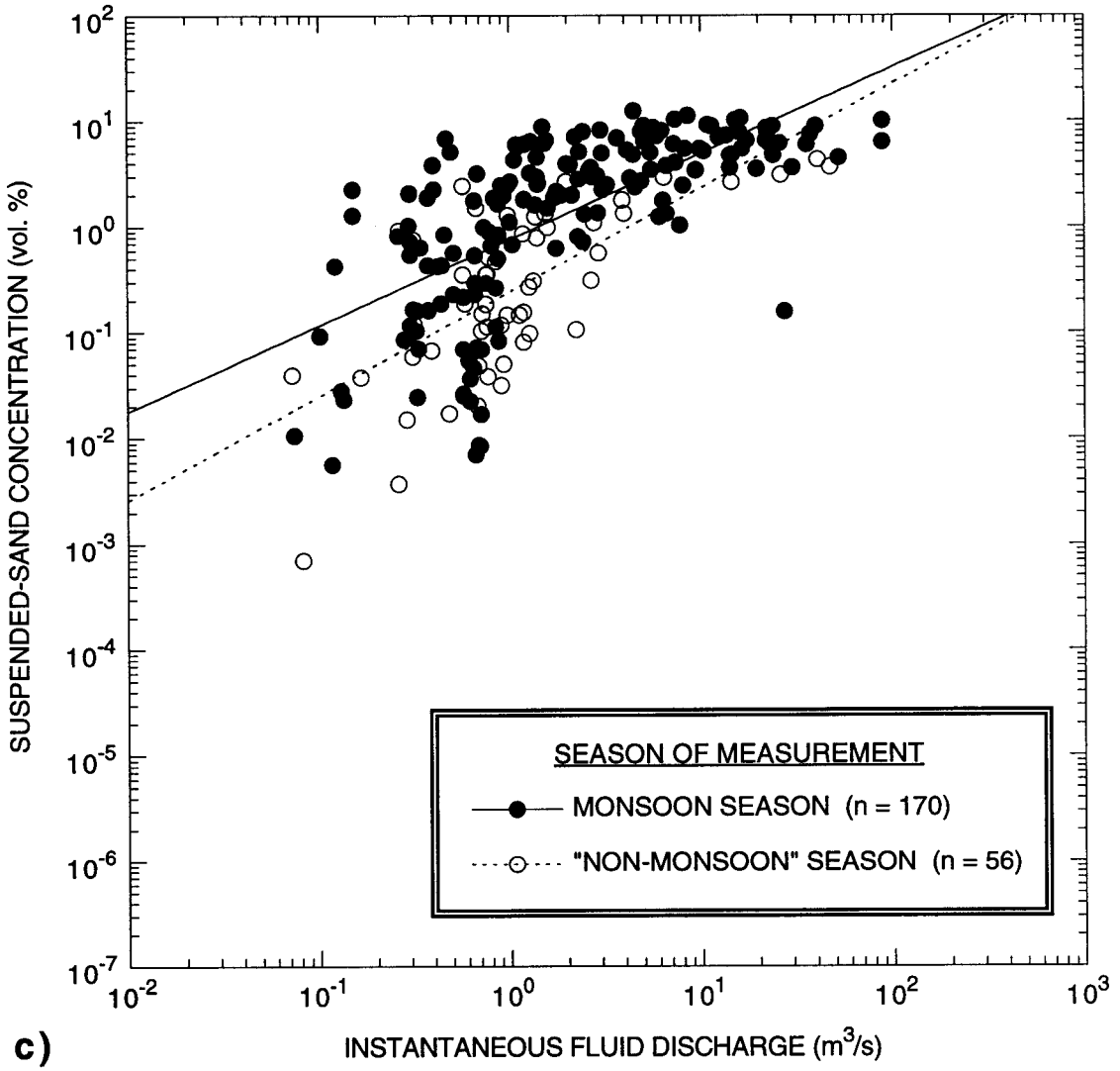

Figure 3.5 (continued): (c) Monsoon and "non-monsoon" season suspended-silt and clay concentration as a function of instantaneous fluid discharge; these data bins are different at the 4.8×10^{-7} level of significance. The lines are the log-linear regressions fit to the data in these bins.

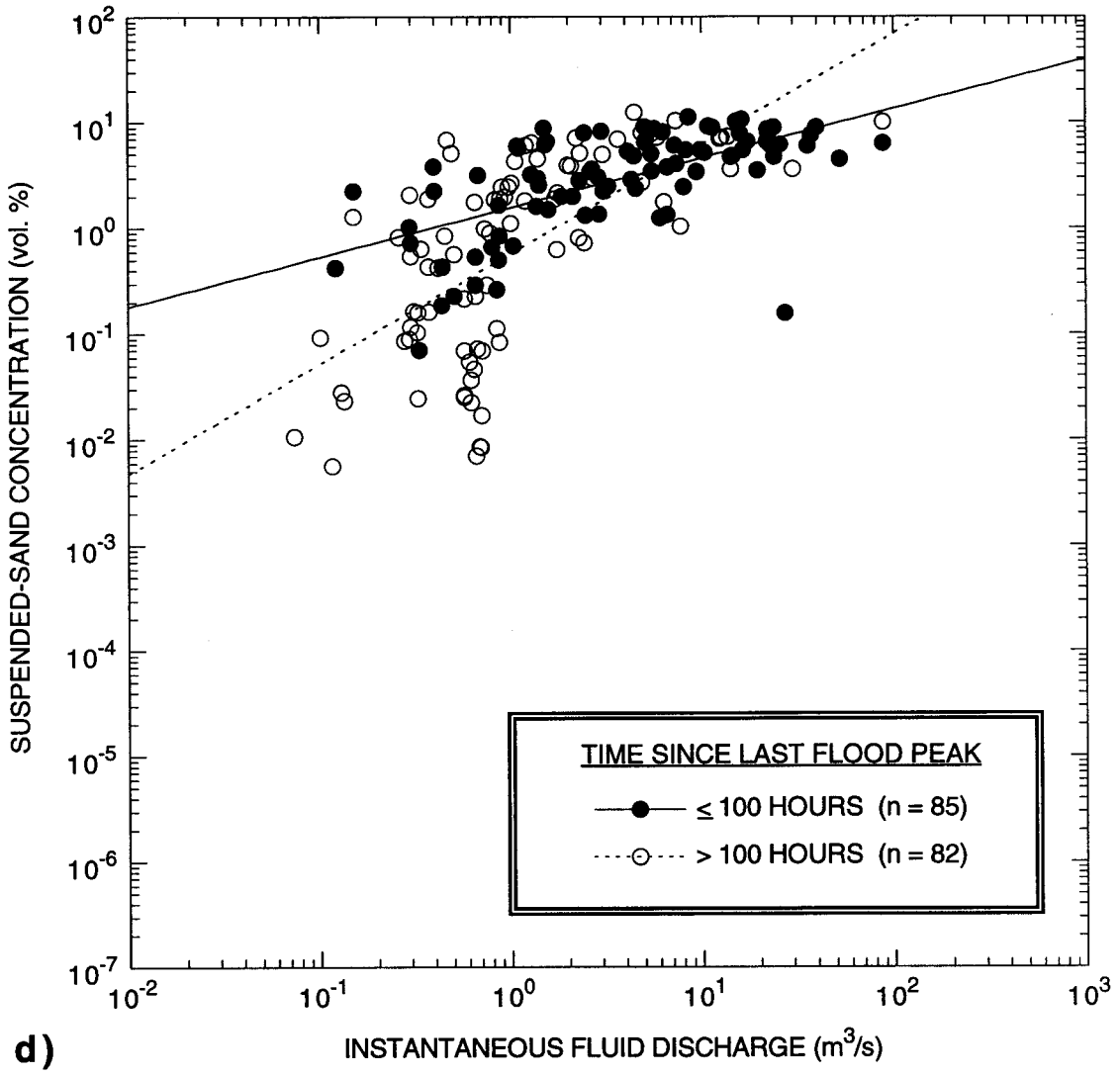

Figure 3.5 (continued): **(d)** Monsoon season suspended-silt and clay concentration as a function of instantaneous fluid discharge within 100 hours and greater than 100 hours after a flood peak; these data bins are different at the 2.4×10^{-6} level of significance. The lines are the log-linear regressions fit to the data in these bins.

ways. Silt and clay concentration is the most sensitive to the antecedent conditions and is enhanced after floods during the monsoon season. In contrast, sand concentration is decreased after large floods independent of season.

For the suspended-sand portion of the data set, the only major differences exist between: (1) the 1954-1976 and the 1983 data; and (2) data collected after small (i.e., <30% of the bankfull discharge) and larger floods. All other differences in the data are at least two orders of magnitude less significant. The difference between the 1954-1976 and the 1983 data is interpreted to be largely due to the difference in cross-section geometry of the channel in which the two data sets were collected (e.g., Figure 2.17). Because the depth of flow for a certain discharge would be greater in the incised reach than in the equilibrium reach, the boundary shear stress would be higher in the incised reach. Thus, if the concentration of suspended sand is largely in equilibrium with the reach-scale hydraulics, the concentration of suspended-sand should be higher in the actively degrading, incised reach for all flows where the supply of sand on the bed is not exhausted. Since this is, in fact, the case, it is hypothesized that the concentration of suspended sand is largely in equilibrium with the reach-averaged hydraulics and sand supply on the bed.

A secondary control of the amount of sand in suspension, is the peak discharge of the last flood. As shown in Figure 3.5b, at the same discharge, the concentration of suspended sand may be higher by about a factor of five following a small flood (i.e., a flood less than about 30% of the bankfull discharge) relative to the concentration of suspended sand after a larger flood. This difference in concentration is interpreted to be a result of larger floods causing a net depletion of the supply of sand on the bed with smaller floods causing a net replenishment of this supply in the Lees Ferry reach and not the result of evolution of the grain-size distribution on the bed during larger floods. This interpretation is supported by: analyses of the suspended-sand grain-size distributions that show that, though the amount of sand in suspension may decrease after the passage of a larger flood, the sand in the system does not coarsen; and evidence presented in Figure 2.42 that shows that the sand grain-size distributions in the Paria River have been constant with respect to time. A depleted state of the sand supply is not typical for the majority of time, however, since 84% of all Paria River floods over the period of record have been smaller than the 28.3 m^3/s discharge used as the upper bound for small floods in the statistical tests.

A change in sand supply between the depleted and replenished states may not have a large topographic signature. For example, the mean thickness of the sand, silt, and clay overlying the gravel in the equilibrium channel portion of the Lees Ferry in March-April

1993 was 15 cm (see Section 2.5a); this thickness probably represents the replenished sand-supply state of the channel since it was measured following a series of small floods. To produce the lower concentrations of suspended sand after larger floods, the mean thickness of the sand, silt, and clay overlying the gravel on the bed would only have to be decreased from about 15 to 3 cm (see Section 2.5a) during the flood; thus, the required change in channel geometry would be subtle, as indicated in Section 2.5b-4a. Reach-averaged cross-section geometry following overbank floods in 1925, 1939-1940, and 1963 is indistinguishable, at one standard deviation, from that measured in 1993 (see Figure 2.35). However, the 1925, 1939-1940, and 1963 cross-sections are all slightly larger than the 1993 cross-section, with this difference possibly due to the temporarily depleted sand supply in the reach following the large floods in 1925, 1939, 1940, and 1963.

For the suspended silt and clay portion of the data set, the only major controls on concentration are the season and, within the monsoon season, the time since the last flood peak. The suspended-silt and clay concentration field does not react as strongly as the suspended-sand concentration field to changes in the reach-averaged channel geometry and is largely advected into the reach during floods, especially during the monsoon season. Also, the suspended-silt and clay concentration is enhanced the most by advection within 100 hours of a flood peak during the monsoon season. Finally, since the "non-monsoon" season suspended-silt and clay concentration, like the concentration of suspended sand, depends mainly on the instantaneous discharge, it may also be in equilibrium with the reach-averaged hydraulics and supply on the bed.

Difference in the behavior of the suspended-silt and clay concentrations during the monsoon and "non-monsoon" seasons is interpreted to reflect the different processes that produce floods during the two seasons. During the monsoon season, floods are produced by runoff generated by intense precipitation during convective thunderstorms in the upper part of the drainage basin. This runoff erodes silt and clay from the hillslopes, which is then advected down the channel; this elevated amount of silt and clay can be advected through the length of the entire river system until it is exhausted, i.e., apparently after about 100 hours after the initial passage of the flood peak by Lees Ferry. In contrast, during the "non-monsoon" season, floods in the Paria River basin are mainly generated either by direct snowmelt or by rain-on-snow events at the higher elevations. These types of events do not erode material from the hillslopes as effectively as the intense rainfall during thunderstorms; and, therefore, the "non-monsoon" season concentration of silt and clay should be closer to being in equilibrium with the reach-averaged hydraulics and supply on the bed.

The statistically determined differences between the sand and the silt-and-clay portions of the suspended-sediment data can be tied directly to differences in downstream advection length of each grain size during a hypothetical flood. The downstream advection length, L_A, of a given grain size can be defined as:

$$L_A = \frac{L_S U_A}{w_s}, \tag{3.1}$$

where L_S is the settling length scale, U_A is the velocity scale, and w_s is the settling velocity of the given grain size. In other words, the downstream advection length is the approximate distance a particle will travel in suspension before encountering the bed. To illustrate the relative differences in the advection lengths of the sand and the silt and clay during a flood, a scale analysis has been conducted on equation 3.1 to determine the order of magnitude of the advection lengths of three grain sizes, 0.2 cm (sand-gravel break), 0.0625 cm (sand-silt break), and 0.00156 cm (median size of silt and clay in the Paria River) during a typical Paria River flood.

The appropriate settling length scale is the center of mass of the suspended sediment concentration profile and is of order 10 cm during a typical Paria River flood. The velocity scale is taken as the mean fluid velocity and is of order 100 cm/s during a typical Paria River flood. Settling velocities calculated by the method of Dietrich (1982a) for quartz grains with a Corey shape factor of 0.7 and a Powers index of 3.5 in 20°C water for the 0.2 cm, 0.00625 cm, and 0.00156 cm diameter grains are 19 cm/s, 0.29 cm/s, and 0.019 cm/s, respectively. Therefore, the coarsest sand will only travel approximately 100 cm in suspension before being in exchange with the bed, and the finest sand will travel approximately 100 m in suspension before being in exchange with the bed, while the silt and clay will travel about 1 km in suspension before encountering the bed. Since the average length of reaches between meanders in the lower Paria River is about 300-500 m, all material excepting the silt and clay should be in active exchange with the bed on a reach scale.

Finally, combination of the measurements presented in Section 2.5 that indicate that the cross-sectionally integrated volume of sand, silt, and, clay on the bed is constant from Cannonville to Lees Ferry with the statistical analysis that suggests that the concentrations of suspended sand and "non-monsoon" season silt and clay are largely in equilibrium with the local hydraulics and supply on the bed allows the construction of a key working hypothesis. This hypothesis (expanded in Section 3.3) states that the reach-averaged enlargement of the Paria River channel cross-section during a flood can calculated by

conserving the reach-averaged mass of every sediment grain size between the bed and flow.

Section 3.3: PHYSICAL FRAMEWORK FOR A GEOMORPHICALLY COUPLED FLOW AND SEDIMENT-TRANSPORT MODEL

The physical framework of this portion of the study relies on the conservation of both momentum and mass as applied to a reach of a river. Both are used to derive the equations for flow and sediment-transport components of the model. Conservation of mass also provides the coupling in the model between the flow and sediment-transport and the geomorphic evolution of the channel during floods.

In the development of a geomorphically coupled, flow and sediment-transport model, two working hypothesis are used. The first of these, reach averaging, provides the necessary simplification in the conservation of momentum equations to apply the second working hypothesis, reach-scale mass conservation of each sediment size class between the bed and the flow. This first of the two hypotheses states: "reach averaging removes from the problem all convective accelerations due to local irregularities in channel geometry and bed roughness and results in spatially averaged, steady, uniform flow in the reach-averaged cross-section." All natural rivers have irregular bed and bank topography; this geometric irregularity creates large local convective accelerations in the flow field, as well as large local gradients in the suspended-sediment concentration field. Also, the irregular distribution of sand and gravel on the bed of natural channels tends to enhance convective accelerations and spatial gradients in the suspended-sediment concentration field. Since the focus of this portion of the study is on reach-scale, rather than local, coupling of flow and sediment-transport to the geomorphology of the channel, reach averaging is employed to remove convective accelerations and to collapse the reach-scale flow and sediment-transport processes onto those acting on a single reach-averaged cross-section. The second working hypothesis states that: "in the reach-averaged cross-section, the mass of each sediment size class, including gravel, is conserved between the bed and the flow, thus providing direct coupling of the in-channel flow and sediment transport to the geomorphic response of the channel during floods."

Conservation of momentum and application of reach averaging

The conservation of momentum equations for an incompressible channel flow in a straight river for the streamwise direction (x-direction), cross-stream direction (y-direction), and vertical direction (z-direction) are:

(x-direction) $$\frac{\partial u}{\partial t}+u\frac{\partial u}{\partial x}+v\frac{\partial u}{\partial y}+w\frac{\partial u}{\partial z}=-\frac{1}{\rho}\frac{\partial P}{\partial x}+\frac{1}{\rho}\frac{\partial \tau_{xx}}{\partial x}+\frac{1}{\rho}\frac{\partial \tau_{yx}}{\partial y}+\frac{1}{\rho}\frac{\partial \tau_{zx}}{\partial z}, \quad (3.2)$$

(y-direction) $$\frac{\partial v}{\partial t}+u\frac{\partial v}{\partial x}+v\frac{\partial v}{\partial y}+w\frac{\partial v}{\partial z}=-\frac{1}{\rho}\frac{\partial P}{\partial y}+\frac{1}{\rho}\frac{\partial \tau_{xy}}{\partial x}+\frac{1}{\rho}\frac{\partial \tau_{yy}}{\partial y}+\frac{1}{\rho}\frac{\partial \tau_{zy}}{\partial z}, \quad (3.3)$$

(z-direction) $$\frac{\partial w}{\partial t}+u\frac{\partial w}{\partial x}+v\frac{\partial w}{\partial y}+w\frac{\partial w}{\partial z}=-\frac{1}{\rho}\frac{\partial P}{\partial z}+\frac{1}{\rho}\frac{\partial \tau_{xz}}{\partial x}+\frac{1}{\rho}\frac{\partial \tau_{yz}}{\partial y}+\frac{1}{\rho}\frac{\partial \tau_{zz}}{\partial z}-g, \quad (3.4)$$

where u, v, and w are respectively the x-direction, y-direction, and z-direction components of velocity, t is time, ρ is fluid density, P is pressure, g is the acceleration due to gravity, and τ_{xx} τ_{yx}, τ_{zx}, τ_{xy}, τ_{yy}, τ_{zy}, τ_{xz}, τ_{yz}, and τ_{zz} are the nine components of the stress tensor. The flow is approximated as steady since all temporal changes in velocity are small, except in the case of a flood bore (which will be dealt with below), so all partial derivatives with respect to time vanish. For the case of a straight reach, application of the reach-averaging working hypothesis results in uniform flow. So, all terms in the y-direction equation vanish, as do all convective accelerations and all partial derivatives with respect to x and z in the x-direction and z-direction equations. The x-direction equation then reduces to:

$$\frac{\partial P}{\partial x}=\frac{\partial \tau_{zx}}{\partial z}. \quad (3.5)$$

Moreover, the flow is assumed to be hydrostatic over the reach scale, so the z-direction equation reduces to:

$$\frac{\partial P}{\partial z}=-\rho g. \quad (3.6)$$

Integrating equation 3.6 with respect to z and ignoring the pressure at the surface, s, since the surface pressure is atmospheric, yields:

$$P=\rho g(s-z). \quad (3.7)$$

Differentiating equation 3.7 with respect to x yields:

$$\frac{\partial P}{\partial x}=\rho g\frac{\partial s}{\partial x}. \quad (3.8)$$

This can now be substituted into equation 3.5, which is then integrated with respect to z; and since τ_{zx} is zero at the surface, integration of equation 3.5 yields the familiar balance between total boundary shear stress, τ_b, and the depth-slope product:

$$\tau_b=-\rho g h\frac{\partial s}{\partial x}. \quad (3.9)$$

This balance is used to calculate the total boundary shear stress at all positions across the perimeter of the reach-averaged cross-section.

Physical justification of modeling the unsteady Paria River with a steady flow model

As shown in Chapter 2, the hydrograph of the Paria River is dominated by flash floods; therefore, the effects on sediment transport of unsteadiness and streamwise nonuniformity of flow associated with floods must be examined. These effects can be evaluated by conducting a scale analysis on the vertically averaged x-direction momentum equation for zero cross-stream flow:

$$\frac{\partial \langle u \rangle h}{\partial t} + \frac{\partial \langle u^2 \rangle h}{\partial x} = gh\frac{\partial s}{\partial x} + \frac{1}{\rho}\frac{\partial \langle \tau_{xx} \rangle h}{\partial x} - \frac{\tau_b}{\rho}, \tag{3.10}$$

where the quantities inside the $\langle\rangle$ are vertically averaged. For this analysis, a flood is assumed to be traveling down an effectively dry, idealized channel; this idealized channel is perfectly straight with parallel, smooth banks. As illustrated in Chapter 2, typical Paria River floods have durations of O(4) seconds at a single location, flood wavelengths of O(6) cm, vertically averaged velocities of O(2) cm/s, and flow depths of O(2) cm.[1] Fluid density, no matter how great the concentration of suspended sediment, is always O(0) g/cm^3. The wave shape of a flood is highly asymmetric; the rising limb is very steep, in many cases a bore, and the falling limb is very gradual (Figure 3.6). Using the convention described on pages 17-21 of Bejan (1984), each term in equation 3.10 will be expressed in an order of magnitude sense. In this convention, since the terms are not nondimensionalized as in other types of scale analyses, the most important terms will be of the largest order of magnitude. First, the order of magnitude of the unsteady term can be evaluated as:

$$\frac{\partial \langle u \rangle h}{\partial t} \sim \frac{\Delta U \Delta L_z}{t}, \tag{3.11}$$

where ΔU is the change in velocity scale over time scale t, and ΔL_z is the change in the z-direction length scale, i.e., the flow depth, over time scale t. Next, the order of magnitude of the x-direction convective-acceleration term due only to the shape of the flood wave can be evaluated as:

$$\frac{\partial \langle u^2 \rangle h}{\partial x} \sim \frac{\Delta\left(U^2\right)\Delta L_z}{L_x}, \tag{3.12}$$

where $\Delta(U^2)$ is the change in the square of the velocity scale over x-direction length scale L_x, and ΔL_z is the change in the z-direction length scale, i.e. flow depth, over x-direction length scale L_x. Finally, the order of magnitude of the pressure-gradient term can be

---

[1]The order of magnitude notation used herein is O(x) where x is the order of magnitude.

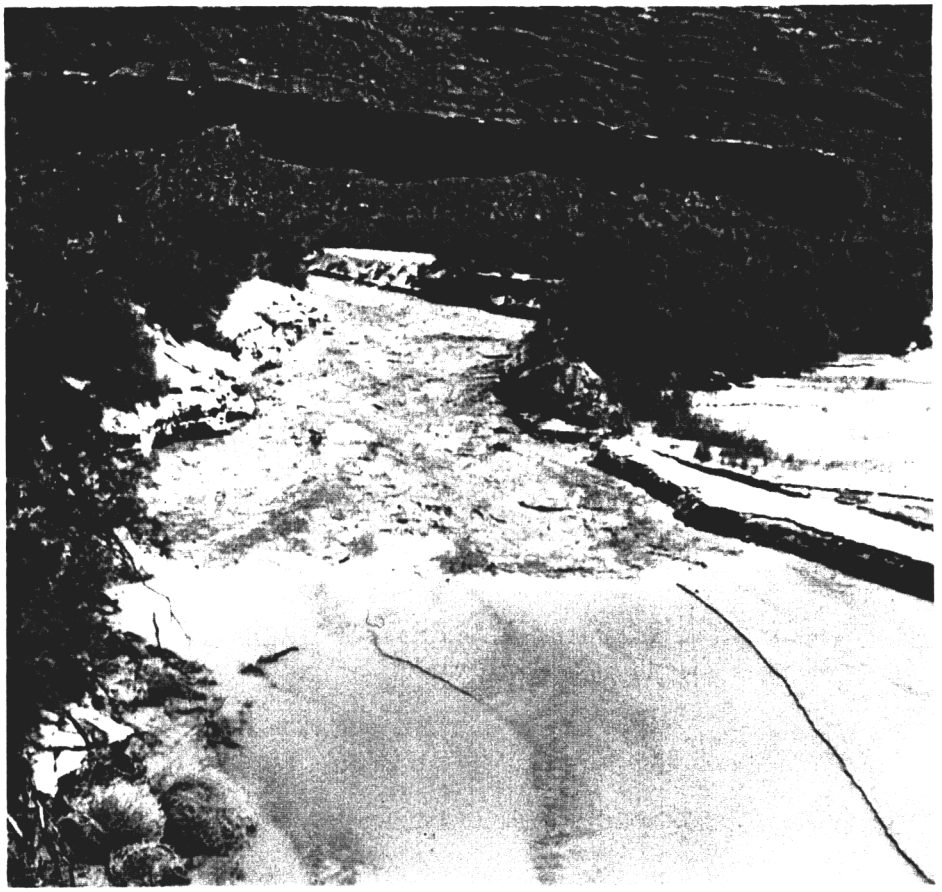

a)

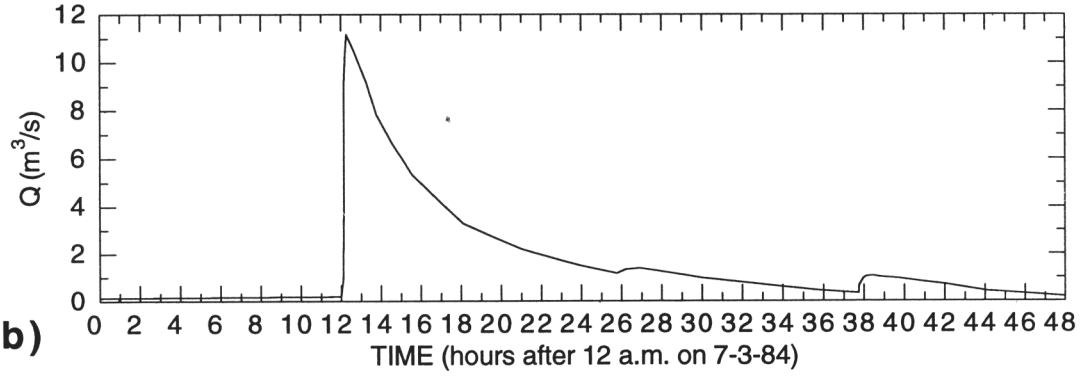

b)

Figure 3.6: **(a)** Upstream view of a flood bore traveling down the new river channel excavated by the National Park Service (old Paria River channel is partially visible in the right portion of the photograph). Photograph taken at 12:10 p.m. MST on July 3, 1984 from the post-1963 highway bridge. The circled number 3 in the upper left portion of the photograph has no significance; photograph from USGS files, Flagstaff, AZ.
(b) Hydrograph of the flood in Figure 3.6a at the Paria River gage.

evaluated as:

$$gh\frac{\partial s}{\partial x} \sim gL_z\frac{\Delta s}{L_x}, \tag{3.13}$$

where g is the gravitational acceleration and is O(3) cm/s^2, L_z is the z-direction length scale and is equal to the flow depth, and Δs is the change in water surface elevation over x-direction length scale L_x.

First, for the case of the falling limb of the flood, because of the wave-shape asymmetry, L_x is approximately the wavelength of the flood wave and is O(6) cm, and t is approximately the duration of the flood and is O(4) seconds. The water surface slope, $\Delta s/L_x$, cannot be significantly less than the reach-averaged channel slope and is O(-3). Thus, the order of magnitude of the unsteady term is:

$$\frac{\Delta U\Delta L_z}{t} = \frac{\mathrm{O}(2)\mathrm{O}(2)}{\mathrm{O}(4)} = \mathrm{O}(0), \tag{3.14}$$

the order of magnitude of the streamwise convective-acceleration term (due only to the shape of the flood wave) is:

$$\frac{\Delta U^2\Delta L_z}{L_x} = \frac{\mathrm{O}(4)\mathrm{O}(2)}{\mathrm{O}(6)} = \mathrm{O}(0), \tag{3.15}$$

and the order of magnitude of the streamwise pressure-gradient term is:

$$gL_z\frac{\Delta s}{L_x} = \mathrm{O}(3)\mathrm{O}(2)\mathrm{O}(-3) = \mathrm{O}(2). \tag{3.16}$$

$\langle\tau_{xx}\rangle$ is assumed to be very small compared to τ_b, and, therefore, τ_b must be of the largest order of magnitude in equation 3.16. Therefore, the order of magnitude of the total boundary shear stress, τ_b, for the case of the falling limb of the flood, must balance the streamwise pressure gradient term and be of O(2).

For the case of the flood bore, empirical observations suggest that the maximum possible water surface slope of the bore can be approximated as a breaking wave using the Michell (1893) wave-breaking criterion for deep water waves; therefore, $\Delta s/L_x$ is about 0.3 or O(-1). Because the channel in front of the bore is essentially dry, the x-direction length scale of the bore must be equal to the z-direction length scale, i.e., the depth of flow behind the bore, divided by the water surface slope and is O(3) cm; the time scale of passage of the bore, t, must be equal to the x-direction length scale of the bore divided by the velocity scale and is O(1) seconds. Thus, the order of magnitude of the unsteady term is:

$$\frac{\Delta U\Delta L_z}{t} = \frac{\mathrm{O}(2)\mathrm{O}(2)}{\mathrm{O}(1)} = \mathrm{O}(3), \tag{3.17}$$

the order of magnitude of the streamwise convective-acceleration term (due only to the shape of the flood wave) is:

$$\frac{\Delta U^2 \Delta L_z}{L_x} = \frac{O(4)O(2)}{O(3)} = O(3), \tag{3.18}$$

and the order of magnitude of the streamwise pressure-gradient term is:

$$gL_z \frac{\Delta s}{L_x} = O(3)O(2)O(-1) = O(4). \tag{3.19}$$

Again, $\langle \tau_{xx} \rangle$ is assumed to be very small compared to τ_b, and, therefore, τ_b must be of the largest order of magnitude in equation 3.19. τ_b, therefore, must be O(4), representing two orders of magnitude enhancement in the total boundary shear stress over that in a steady, uniform flow. However, since the time scale associated with the bore, O(1), is small compared to the time scale associated with the falling limb, O(4), the effect of the bore on the bulk sediment transport during the course of a flood can be ignored, and the steady, uniform flow approximation should be valid for 99.9% of the time in the Paria River.

Additional support for the steady, uniform flow approximation is provided by the highest USGS discharge measurement made on the Paria River between November 22, 1923 and August 14, 1972, for which flow velocities were determined by a Price current meter, and flow depths by sounding. This measurement was made on August 18, 1963 at a discharge of 38.2 m^3/s; velocities were measured at $0.8h$ (where the bed is at $0h$ and the surface at h) at six verticals across the channel. Given that the bed roughness is relatively uniform across the cross-section, the velocity at each vertical must scale with the square root of the depth at each vertical in a steady, uniform flow (e.g., as shown in Section 2.6a). As shown in Figure 3.7, the relationship between measured velocity at $0.8h$ and the square root of the flow depth yields an R^2 value of 0.933 and an F-statistic of 69.6 corresponding to a significance level of 0.000405. Therefore, if streamwise convective accelerations are present in the August 18, 1963 cross-section, they are identical at each vertical; and, because it is unlikely that the convective accelerations are identical at each vertical, further support is provided to the steady, uniform flow approximation.

Overview of the geomorphically coupled flow and sediment-transport model

In addition to the two working hypotheses stated above, five physical assumptions are used in the model development; the validity of each of these assumptions is tested in Chapter 4. These assumptions allow the reach-averaged cross-section to be divided into equally spaced computation verticals at which, for a given river stage, the velocity profile and suspended sediment concentration profile are solved iteratively by forcing the mass conservation of each sediment size class between the bed and the flow (Figure 3.8).

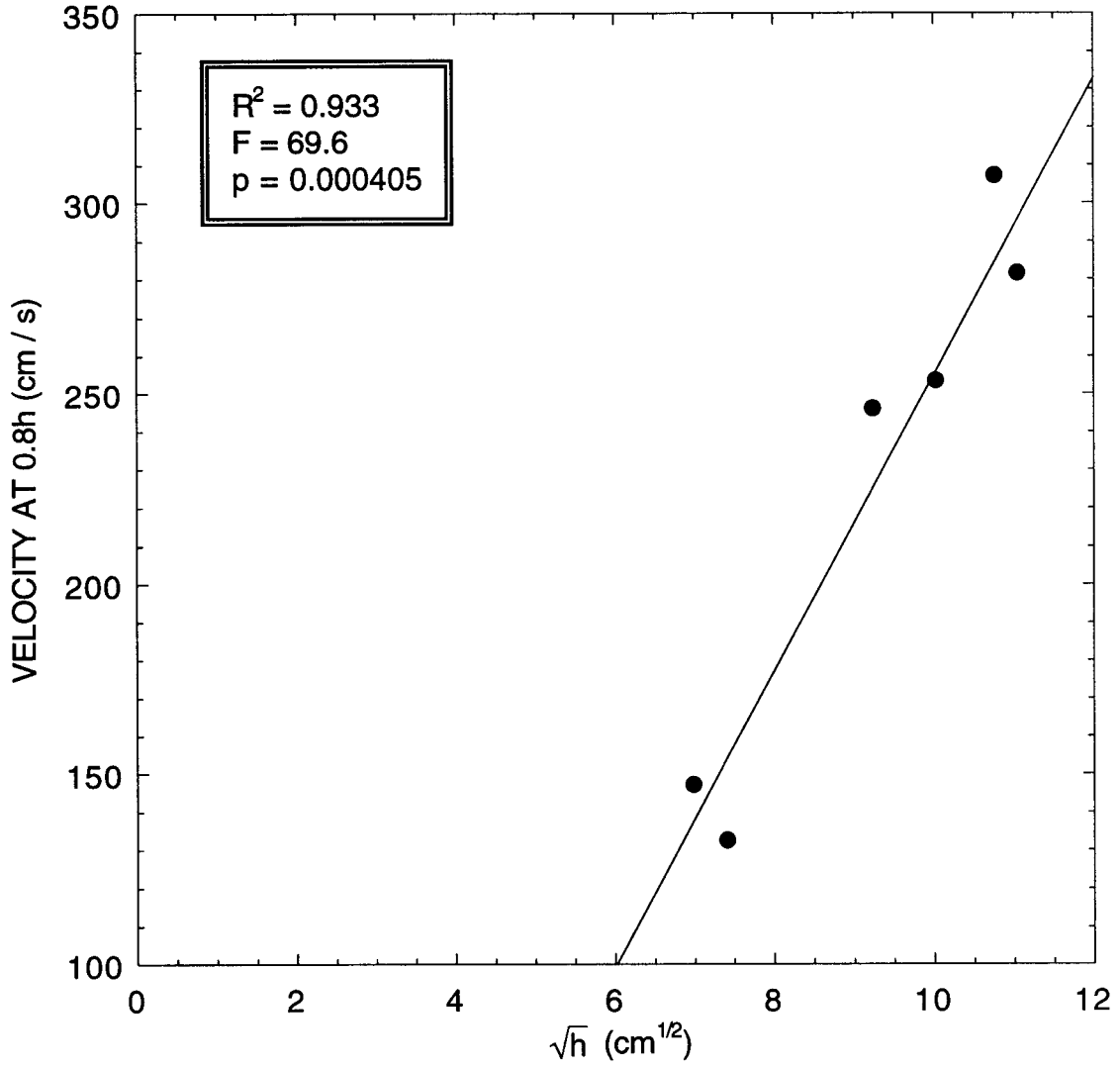

Figure 3.7: Velocity measurements at $0.8h$ as a function of $\sqrt{h}$ from the 38.2 m^3/s discharge measurement made between 10:55 a.m. and 11:10 a.m. on August 18, 1963 at Cableway 2. Line is the best-fit linear regression to the measurements.

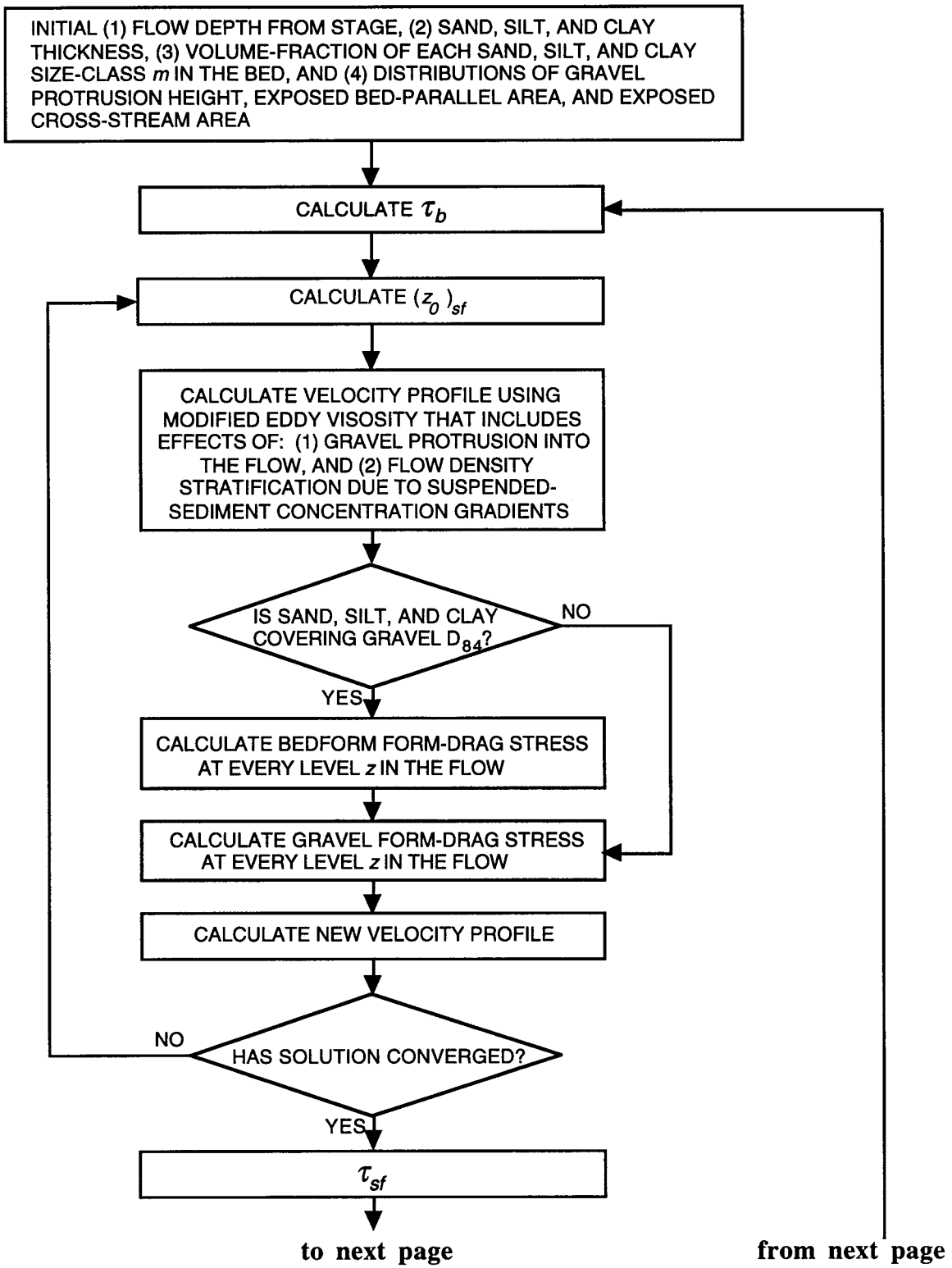

Figure 3.8 (part 1): Simplified flow chart showing the calculations performed at each computation vertical in the reach-averaged cross-section by the geomorphically coupled flow and sediment-transport model.

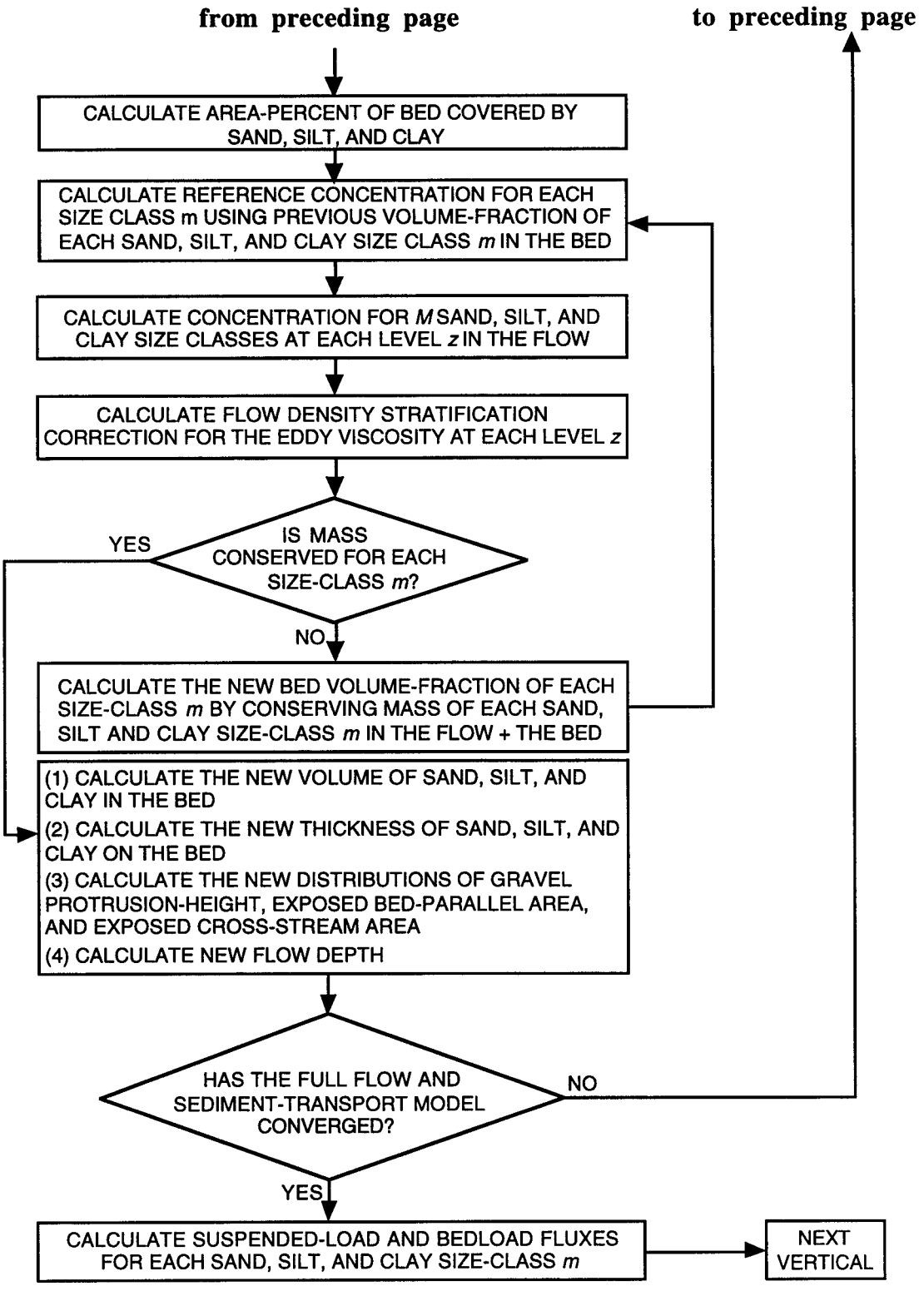

Figure 3.8 (part 2): Simplified flow chart showing the calculations performed at each computation vertical in the reach-averaged cross-section by the geomorphically coupled flow and sediment-transport model.

(1) Since the modeled reaches are straight, by reach-averaging, the cross-stream components of velocity are zero, therefore, the lateral advective transport of mass and momentum in the reach-averaged cross-section can be ignored. This assumption allows the velocity and sediment transport field to be solved independently at each cross-stream position in the reach-averaged cross-section and allows the mass of sediment to be conserved between the bed and the flow independently at each cross-stream position in the reach-averaged cross-section. Additional support for this assumption comes from the data in Figure 3.1b that show the poor degree to which the cross-section is mixed in the cross-stream direction. (2) Because, for most flows of interest, the skin-friction shear stress at each cross-stream position in the reach-averaged cross-section greatly exceeds the critical shear stress for every size of sand, silt, and clay on the bed, armoring of the sand, silt, and clay layer by coarser sand as finer sediment goes into suspension is relatively unimportant. Thus, the sand, silt, and clay layer is approximated as remaining uniformly mixed, with respect to grain size, as it thins as sediment goes into suspension from the bed. (3) Drag in the system is dominated by the spatially averaged bedform or gravel form drag at each cross-stream position in the reach-averaged cross-section. Form drag from channel scale features, e.g. bars and banks, is treated as negligible because the channel is straight with low amplitude bars, and the variance of bank topography in the streamwise direction is small (e.g., Figure 2.24). (4) The effect of vegetation form drag on the fluid discharge, sediment discharge, and channel geometric response during floods in the natural Paria River system is negligible (this was especially true prior to the invasion of non-native plants). (5) The vertical structure of the spatially averaged turbulence at each level can be modified to account for the physics from two effects: the area-weighted concentration of gravel sizes protruding into each level of the flow, and the vertical density gradients in the flow produced by the high suspended-sediment-concentration gradients.

Section 3.4: QUANTITATIVE DESCRIPTION OF THE BED FOR MASS CONSERVATION

Prior to formulating the equations for flow and sediment transport, the floor of the channel must be described in a manner that allows mass conservation of each size class of sand, silt, and clay between the bed and the flow. Since the surface of the underlying gravel delineates the base of the "suspendable" sand, silt, and clay layer, this exercise reduces to mathematically describing the detailed surface of the gravel layer as determined from the pebble counts in Section 2.5a, and then formulating a means to keep track of all size classes of sediment above this surface regardless of whether on the bed or in the flow.

The gravel grain-size distribution making up the bed is modeled by a log-normal grain-size distribution discretized in 0.025ϕ size increments. The unweighted, normalized number of particles in each gravel size class is defined by:

$$G_n = 0.025\frac{G_N}{\sigma(2\pi)^{1/2}}\exp\left[-\frac{1}{2}\left(\frac{D_n - D_{50}}{\sigma}\right)^2\right], \tag{3.20}$$

where G_n is the normalized number of particles of gravel in size-class n in the bed, G_N is set equal to 1.0 and is normalized number of gravel particles in the bed, D_n is the nominal spherical diameter of gravel of size-class n in ϕ units, D_{50} is the nominal spherical diameter of the geometric mean of the size-distribution in ϕ units, and σ is the standard deviation of the size-distribution in ϕ units.[2] The gravel particles in the Paria River are modeled as ellipsoidal (see Figure 2.18) with the c-axis (vertical axis) equal to $2D_n/3$, the a-axis (long-axis) equal to $4D_n/3$, and the b-axis (intermediate axis) equal to D_n. Based on field observations in the Paria River, the zero level of the flow, $z = 0$, is defined as the center of the particles with the a-axis parallel to the bed in the cross-stream direction, the b-axis parallel to the bed in the streamwise direction, and the c-axis parallel to the z-direction such that half of the c-axis, i.e., $D_n/3$, is protruding upward into the flow.

Derivation of the equation for the mass conservation of each size class of sand, silt, and clay and derivation of the equations for the influence of the gravel on both the drag and turbulence structure require redefining G_n in terms of an area-weighted concentration. Thus, the area-weighted concentration of each gravel size-class n, ϵ_{gn}, is defined as:

$$\epsilon_{gn} = \sum_{n=i}^{N}\left(\frac{\left(\left(A_{xy}\right)_n\right)_0 G_n}{\sum_{n=1}^{N}\left(\left(A_{xy}\right)_n\right)_0 G_n}\right), \tag{3.21}$$

where

$$\left(\left(A_{xy}\right)_n\right)_0 = \pi\frac{4}{3}\left(\frac{D_n}{2}\right)^2, \tag{3.22}$$

is the area of the ellipse defined by each gravel size-class n at the zero level. The difference between the unweighted, normalized number of particles in each gravel size-class determined by equation 3.20 and the area-weighted concentration of each gravel size class determined by equation 3.21 is illustrated in Figure 3.9.

After defining the nature of the surface of the gravel, the next step involves keeping track of both the thickness and aerial extent of sand, silt, and clay of each size-class m on

---

[2] ϕ units will not be used below; all calculations below will be performed in cgs units.

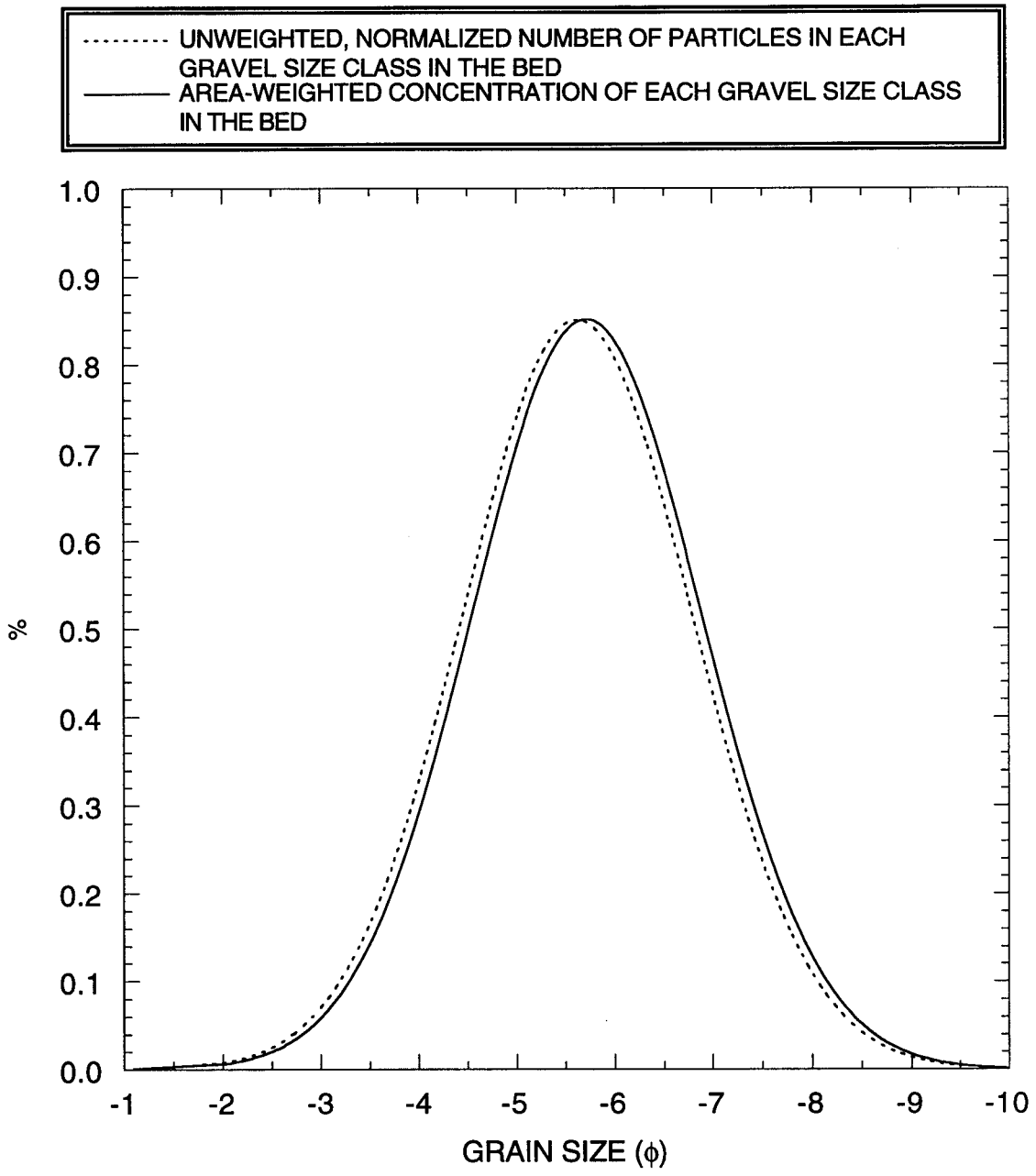

Figure 3.9: Comparison of the unweighted, normalized number of particles in each gravel size class from equation 3.20 with the area-weighted concentration of each gravel size class from equation 3.21; gravel grain-size distribution is that from the deepest part of the thalweg in the 1993 Lees Ferry reach-averaged cross-section and is discretized in 0.025ϕ increments.

the bed. The relationship used for mass conservation of each size class of sand, silt, and clay at each computation vertical is the widely used "erosion equation":

$$\frac{\partial V_b}{\partial t} + \frac{\partial V_s}{\partial t} + \nabla \cdot Q_s = 0, \tag{3.23}$$

which specifies that the temporal rate of change of the volume of sediment in the bed, V_b, plus the temporal rate of change of the volume of sediment in the flow, V_s, plus the spatial change in the sediment discharge, Q_s, equals zero. By virtue of reach averaging, the spatial term vanishes and we are left with:

$$\frac{\partial V_b}{\partial t} = -\frac{\partial V_s}{\partial t}. \tag{3.24}$$

For the purposes of modeling the Paria River, the sand, silt, and clay on the bed is divided into 1 size-class m to characterize the silt and clay and 10 equal-ϕ size-classes m ranging from 4 ϕ (sand-silt break) to -1 ϕ (sand-gravel break). At each vertical, the mass of each of the 11 size classes is conserved such that:

$$\frac{\partial V_m}{\partial t} = 0, \tag{3.25}$$

and,

$$V_m = f_{m_0} V_{b_0} = f_m V_b + \int_{T_s}^{z_a} \bar{c}_m dz + \int_{z_a}^{h} \bar{c}_m dz, \tag{3.26}$$

where V_m is the total volume of size-class m at each vertical in both the bed and the flow, f_{m0} is the volume fraction of m initially in the bed under dry conditions (for the Paria River, f_{m0} is set by the measured 1993 grain-size distributions for sediment types 1, 2, 3, and 4 in Table 2.3), V_{b0} is the total volume of sand, silt, and clay initially in the bed at each vertical under dry conditions, f_m is the volume fraction of size-class m in the bed during a particular flow event, V_b is the total volume of sand, silt, and clay remaining in the bed at each vertical during a particular flow event, $\bar{c}_m$ is the time-averaged volume concentration of size-class m at each level z in the flow, T_s is elevation of the top of the sand, silt, and clay layer, z_a is the top of the bedload saltation layer, and h is the local flow depth. Since V_b is defined as the total volume of sand, silt, and clay remaining in the bed at each vertical during a particular flow event, the derivation of equation 3.26 assumes uniform mixing of the sand, silt, and clay layer with no armoring of the surface as sediment goes into suspension. As will be shown in Chapter 4, this is a reasonable assumption for the Paria River, and exclusion of the effect of armoring by coarser sand should have little impact on the model-predicted amount of cross-section enlargement during a flood.

The total unit volume of sand, silt, and clay initially in the bed at each computation vertical under dry conditions can be defined as:

$$V_{b0} = \epsilon_b \int_0^{T_{s0}} \left(1 - A_g\right) dz, \tag{3.27}$$

where $\epsilon_b = 0.65$ is the volume concentration of sand, silt, and clay in the bed, A_g is the area-weighted concentration of gravel at each level z within the layer of sand, silt, and clay, and T_{s0} is the top of the layer of sand, silt, and clay under dry conditions (for the Paria River, T_{s0} is set by the values of the mean thickness of the sand, silt, and clay layer in Figure 2.24). Likewise, the total unit volume of sand, silt, and clay remaining in the bed during flow in the channel is:

$$V_b = \epsilon_b \int_0^{T_s} \left(1 - A_g\right) dz. \tag{3.28}$$

The area-weighted concentration of sand, silt, and clay for a given T_s is:

$$A_s = 1 - A_g, \tag{3.29}$$

and the area-weighted concentration of gravel at each level z is:

$$A_g = \sum_{n=i}^{N} \epsilon_{gn} \left(\left(A_{xy} \right)_n \right)_z, \tag{3.30}$$

where $\left(\left(A_{xy} \right)_n \right)_z$ is the area of the ellipse formed by a particle of gravel size-class n at level z,

$$\left(\left(A_{xy} \right)_n \right)_z = \pi \frac{\left((d_x)_n \right)_z \left(\left(d_y \right)_n \right)_z}{4}, \tag{3.31}$$

where $((d_x)_n)_z$ is the downstream (intermediate) axis of the ellipse and $((d_y)_n)_z$ is the cross-stream (major) axis of the ellipse. The summation in equation 3.31 is carried out for sizes i through N where i is the smallest gravel size-class n present at level z and N is the largest gravel particle on the bed. As can be seen in the two equations,

$$\left(\left(d_x \right)_n \right)_z = \mathrm{D}_n \sin\left(\cos^{-1}\left(\frac{z}{\mathrm{D}_n/3} \right) \right), \tag{3.32}$$

$$\left(\left(d_y \right)_n \right)_z = \frac{4}{3} \mathrm{D}_n \sin\left(\cos^{-1}\left(\frac{z}{\mathrm{D}_n/3} \right) \right), \tag{3.33}$$

$((d_x)_n)_z$ and $((d_y)_n)_z$ revert to the cross-stream diameter, $4\mathrm{D}_n/3$, and downstream diameter, D_n, of the particle when $z = 0$. The area of bed covered by sand, silt, and clay and the unit volume of sand, silt, and clay in the bed as a function of the thickness of the sand, silt, and clay layer is shown in Figure 3.10. For example, given a sand thickness of 1.7 cm, which corresponds to a sand, silt, and clay coverage of the bed of 66 area-% and a unit volume of sand, silt, and clay in the bed of 7.8 cm^3/cm^2, the D_{50} of the gravel is completely buried (Figure 3.10).

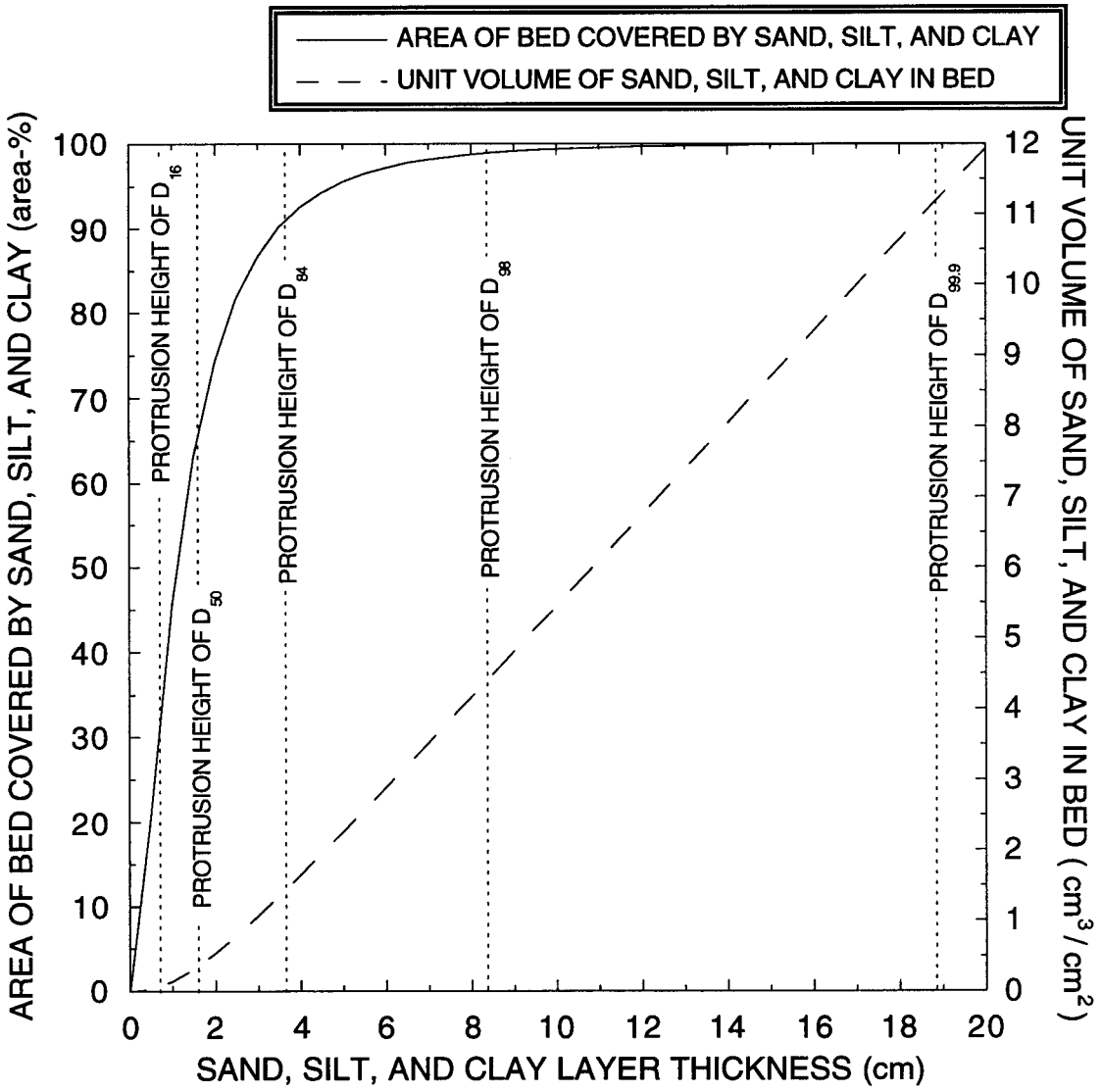

Figure 3.10: Area of the bed covered by sand, silt, and clay and the unit volume of sand, silt, and clay in the bed as functions of the thickness of the sand, silt, and clay layer in the deepest part of the thalweg in the 1993 Lees Ferry reach-averaged cross-section depicted in Figure 2.24. The amounts of sand, silt, and clay on the modeled bed required to bury D_{16}, D_{50}, D_{84}, D_{98}, and $D_{99.9}$ of the gravel are also shown.

Section 3.5: THE FLOW COMPONENT OF THE MODEL

As illustrated in Figure 3.8, the flow and sediment-transport components of the model are coupled, but for clarity, the flow component of the model will be described first in its entirety. In the following sections of this chapter, the phrase "spatially averaged" will be used to describe quantities that have been reach-averaged in the streamwise (x) dimension and the term "local" will be used to describe quantities that are evaluated at each level z in the flow. Since all convective accelerations have been removed from the problem, the pressure field becomes hydrostatic and the momentum equation reduces to the steady, uniform flow balance in equation 3.9. Moreover, since the reach-averaged flow is uniform, the vertical distribution of the total stress is linear (e.g., Tennekes and Lumley, 1972; Middleton and Southard, 1984) such that:

$$\tau_{zx}(z) = \tau_b\left(1-\frac{z}{h}\right), \tag{3.34}$$

where $\tau_{zx}(z)$ is the total shear stress at each level z in the vertical.

Stress partitioning

For the purposes of calculating the velocity and sediment transport at each level in the flow, the total shear stress must be partitioned into a fluid component, i.e., a component related to the velocity and sediment transport, and into form-drag components. Thus, the total stress is partitioned at each level z into a fluid stress, a form-drag stress due to the drag on gravel particles protruding through level z as in Wiberg and Smith (1987b, 1991) and Nelson and others (1991), and a form-drag stress due to the presence of dunes on the bed as in Smith and McLean (1977a). These three components of the total shear stress must be solved for in an iterative manner. The complete equation describing the partitioning of the local total stress is as follows:

$$\tau_{zx}(z) = \tau_f(z) + \tau_{gd}(z) + \tau_{dd}(z), \tag{3.35}$$

where $\tau_f(z)$ is the local fluid component of the stress at level z, $\tau_{gd}(z)$ is the gravel form-drag component of the stress at level z, and $\tau_{dd}(z)$ is the dune form-drag component of the stress at level z. As in Wiberg and Smith (1987b, 1991), the gravel form-drag stress term is further subdivided:

$$\tau_{gd}(z) = \tau_D(z) - (\tau_D)_s, \tag{3.36}$$

where $\tau_D(z)$ is the gravel form-drag stress resulting from gravel particles protruding through level z and $(\tau_D)_s$ is the gravel form-drag stress resulting from gravel particles protruding through the water surface.

Structure of the eddy viscosity

To solve for the streamwise velocity profile, the following constitutive equation for steady, horizontally uniform flow is used to relate the local fluid stress to the vertical gradient of the time-averaged velocity:

$$\tau_f(z) = \rho K(z) \frac{\partial \overline{u}}{\partial z}, \tag{3.37}$$

where ρ is the density of water, $K(z)$ is the eddy viscosity, and $\overline{u}$ is the time-averaged velocity. The eddy viscosity varies as a function of the flow and governs the exchange of momentum in the vertical due to turbulence. The presence of high concentrations of suspended sediment can have large effects on the vertical structure of the turbulence; thus $K(z)$ is a modification of the neutral clear-water eddy viscosity $(K(z))_N$:

$$K(z) = \left(K(z)\right)_N \phi_m{}^{-1}, \tag{3.38}$$

where the nondimensional shear, ϕ_m, is defined below in Section 3.6. The neutral eddy viscosity,

$$\left(K(z)\right)_N = u_{*f}(z) L(z), \tag{3.39}$$

is composed, as hypothesized by Wiberg and Smith (1987b), of a spatially averaged local velocity scale of the turbulence,

$$u_{*f}(z) = \left(\frac{\tau_f(z)}{\rho}\right)^{1/2}, \tag{3.40}$$

and a spatially averaged local length scale of the turbulence $L(z)$.

The most sensitive part of the flow model is the specification of $L(z)$. As in Wiberg and Smith (1991), $L(z)$ is approximated as a linear combination of a concentration-weighted normal-channel turbulence length scale and a length scale related to wakes produced by large roughness elements on the bed. The normal-channel turbulence length scale used is the 2-part form for channels with roughness elements very small compared to the flow depth (Rattray and Mitsuda, 1974). In the region $z \leq 0.2h$, the length scale of the turbulence is proportional with the distance away from the boundary, and:

$$L_f(z) = kz\left(1 - \frac{z}{h}\right), \tag{3.41}$$

and in the region $z > 0.2h$, the length scale of the turbulence is proportional to the flow depth:

$$L_f(z) = \frac{kh}{\beta}, \tag{3.42}$$

where k is von Karman's constant and is equal to 0.408 (Long and others, 1993), and β is a constant set equal to 6.25 by the matching height of $0.2h$.

The complete form of the spatially averaged local length scale of the turbulence at each level z, incorporating both the channel-scale and wake-scale components, is modified from Wiberg and Smith (1991):

$$L(z) = \left(1 - \sum_{n=i}^{N} e_{gn}\right) \frac{L_f(z)}{(1 - z/h)^{1/2}} + k \sum_{n=i}^{N} e_{gn} P_n, \tag{3.43}$$

where i represents the smallest gravel particle protruding through level z, N represents the largest gravel particle on the bed, e_{gn} is the area concentration of gravel of size n protruding through level z, and P_n is the vertical protrusion height of each size fraction n. The denominator $(1\text{-}z/h)^{1/2}$ in the term $L_f(z)/(1\text{-}z/h)^{1/2}$ arises because of the definition of the spatially averaged local velocity scale $u_{*f}(z)$ since:

$$u_{*T} = \left(\frac{\tau_b}{\rho}\right)^{1/2} = \left(\frac{\tau_{zx}(z)}{\rho(1 - z/h)}\right)^{1/2} = \frac{u_{*f}(z)}{(1 - z/h)^{1/2}}, \tag{3.44}$$

when $\tau_f(z)$ equals $\tau_{zx}(z)$ and the turbulence length scale must revert back to the 2-part form (for which the velocity scale is u_{*T}) when no gravel particles are protruding through the sand, silt, and clay layer on the bed. The protrusion height of each size n is defined as:

$$P_n = \frac{D_n}{2} - T_s \quad \text{when} \quad \frac{D_n}{2} > T_s, \tag{3.45a}$$

or,

$$P_n = 0 \quad \text{when} \quad \frac{D_n}{2} \le T_s, \tag{3.45b}$$

where T_s is the thickness of the sand, silt, and clay layer overlying the gravel.

Spatially averaged gravel form drag

To calculate the form-drag component of the stress contributed by each gravel particle protruding through the sand, silt, and clay layer, it is necessary to determine both the bed-parallel area of the particle at the top of the sand, silt, and clay layer and the area of the particle perpendicular to the flow above the sand, silt, and clay layer. The gravel form-drag component of the total stress at each level z is defined, as in Wiberg and Smith (1991), as:

$$\tau_D(z) = \sum_{n=i}^{N} \left(\frac{F_D}{A_{xy}}\right)_n, \tag{3.46}$$

where F_D is the total drag force integrated over gravel size-class n, and A_{xy} is the total bed-parallel area at T_s of gravel of size-class n. This summation is carried out for each level z for all grain-sizes of gravel protruding through that level. The total drag force integrated over each gravel size-class n is:

$$(F_D)_n = \frac{1}{2}\rho C_D \left\langle u^2 \right\rangle_n \left(\left(A_{yz} \right)_n \right)_{T_s} \epsilon_{gn}, \tag{3.47}$$

where C_D=0.5 is the drag coefficient for spheres over the appropriate Reynolds similarity range (Flammer and others, 1970; Schlichting, 1979), $\left\langle u^2 \right\rangle_n$ is the square of the velocity averaged over the cross-sectional area of the gravel of size-class n protruding into the flow above T_s, and $(A_{yz})_n$ is the cross-sectional area of the gravel of size-class n protruding into the flow above T_s. The quantity:

$$\left\langle u^2 \right\rangle_n = \frac{\int_{T_s+(z_0)_{sf}}^{D_n/3} u^2 dz}{P_n}, \tag{3.48}$$

is the vertically averaged square of the velocity acting over the protruding cross-sectional area of gravel of size-class n. The bed-parallel area of the gravel of size-class n at the top of the sand, silt, and clay layer is the area of a ellipse:

$$\left(\left(A_{xy} \right)_n \right)_{T_s} = \pi \frac{\left((d_x)_n \right)_{T_s} \left(\left(d_y \right)_n \right)_{T_s}}{4}, \tag{3.49}$$

where $((d_x)_n)_{T_s}$ is the downstream (minor) axis and $((d_y)_n)_{T_s}$ is the cross-stream (major) axis of the ellipse at the top of the sand layer. The cross-sectional area of gravel of size-class n protruding into the flow above the sand, silt, and clay layer is approximated as the area of a half-ellipse,

$$\left(A_{yz} \right)_n \approx \frac{1}{2}\pi P_n \frac{\left(\left(d_y \right)_n \right)_{T_s}}{2}. \tag{3.50}$$

Combining the above equations and simplifying yields the following relationship for the gravel form-drag stress at each level z:

$$\tau_D(z) = \frac{1}{2}\rho C_D \sum_{n=i}^{N} \left[\frac{\epsilon_{gn}}{\left((d_x)_n \right)_{T_s}} \int_{T_s+(z_0)_{sf}}^{D_n/3} u^2 dz \right]. \tag{3.51}$$

Figure 3.11 shows the conceptual initial and converged configuration of a portion of the bed. As sediment goes into suspension and the thickness, T_s, of the sand, silt, and clay layer decreases, more of the gravel contributes to the drag at each level z in the flow.

Spatially averaged dune form drag

The dune form-drag term is only present in equation 3.35 when dunes can exist on the bed. Observations in the Paria River suggest that dunes only occur when D_{84} of the gravel is buried by sand, silt, and clay (see Section 2.5a), so, in the model, dunes are only

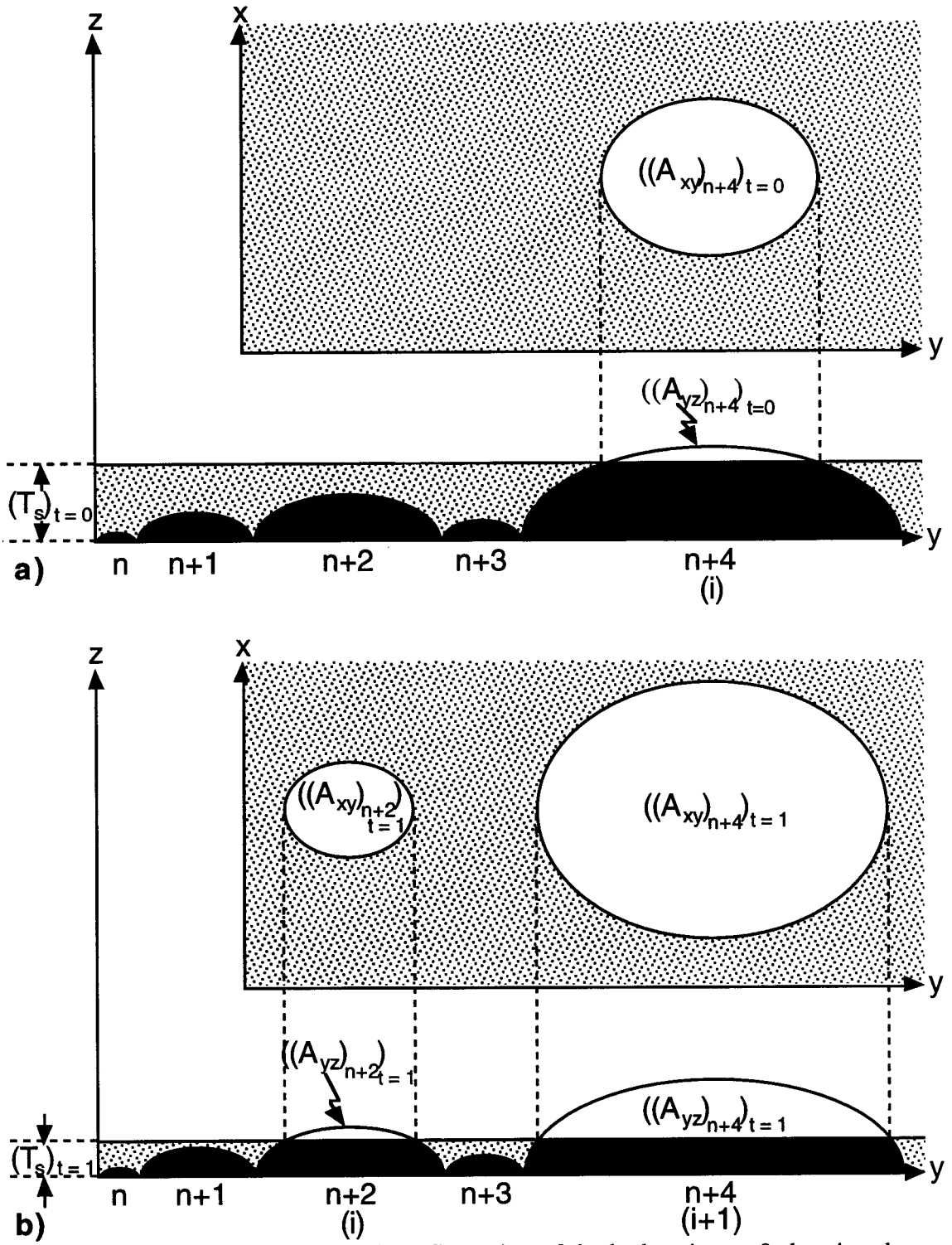

Figure 3.11: (**a**) Conceptual initial configuration of the bed at time t=0 showing the initial thickness of the sand, silt, and clay layer, initial cross-sectional area of gravel protruding through the sand, silt, and clay layer, and initial bed-parallel area of the exposed gravel. (**b**) Conceptual converged model-predicted configuration of the bed at time t=1. See text for definitions of the notation.

allowed to exist when this condition is satisfied. The dune form-drag component of the total stress is calculated by a modification of the method of Smith and McLean (1977a). First, the skin-friction component of the total boundary shear stress (equivalent to the fluid component of the total stress at the bed) is calculated:

$$\tau_{sf} = \left(\tau_b - \left(\tau_{gd}\right)_b\right) \Bigg/ \left\{1 + \frac{C_D}{2}\frac{H}{\lambda}\left[\frac{1}{k}\left(\ln\frac{H}{(z_0)_{sf}} - 1\right)\right]^2\right\}, \tag{3.52}$$

where τ_{sf} is the skin-friction component of the boundary shear stress, $(\tau_{gd})_b$ is the gravel form- drag component of the stress near the bed, $C_D = 0.21$ is the drag coefficient for separated flow over dunes (Smith and McLean, 1977a), H is the height of the dune, and λ is the wavelength of the dune.

To solve equation 3.52, it is necessary to specify values for the dune height and wavelength. Field measurements of dune heights in a sand bed river (Mohrig, 1994) indicate that a value of $H = 0.3h$ is a reasonable value for the maximum average dune height. For the locally starved bed case of the Paria River, the dune height is set equal to either the thickness of the sand layer over the gravel or $0.3h$, whichever is less. The dune wavelength is set empirically by a curve fitted to an analysis by D. Mohrig (written communication, 1991) of the data of Stein (1965):

$$\lambda = H\left\{19.10 + \frac{0.53}{(0.90 - X_s)^{2.03}}\right\}, \tag{3.53}$$

where X_s is the suspended fraction of the bed grain-size distribution, i.e., the fraction for which the skin-friction shear velocity is greater than the settling velocity (Figure 3.12). The approximate dune form-drag component of the total stress can be determined for each level z:

$$\tau_{dd} = \left\{\tau_b - \left[\left(\tau_{gd}\right)_b + \tau_{sf}\right]\right\}\left(1 - \frac{z}{h}\right) \qquad \text{when} \quad z \le H, \tag{3.54a}$$

or,

$$\tau_{dd} = 0 \qquad \text{when} \quad z > H. \tag{3.54b}$$

Furthermore, the vertical distribution of the spatially averaged form-drag component of the total stress in equation 3.54 is compatible with the spatially averaged vertical structure of the Reynolds stress measured by Nelson and others (1993) over 2-dimensional bedforms.

The flow-model equation

Finally, all of the "physical pieces" described above are combined into the

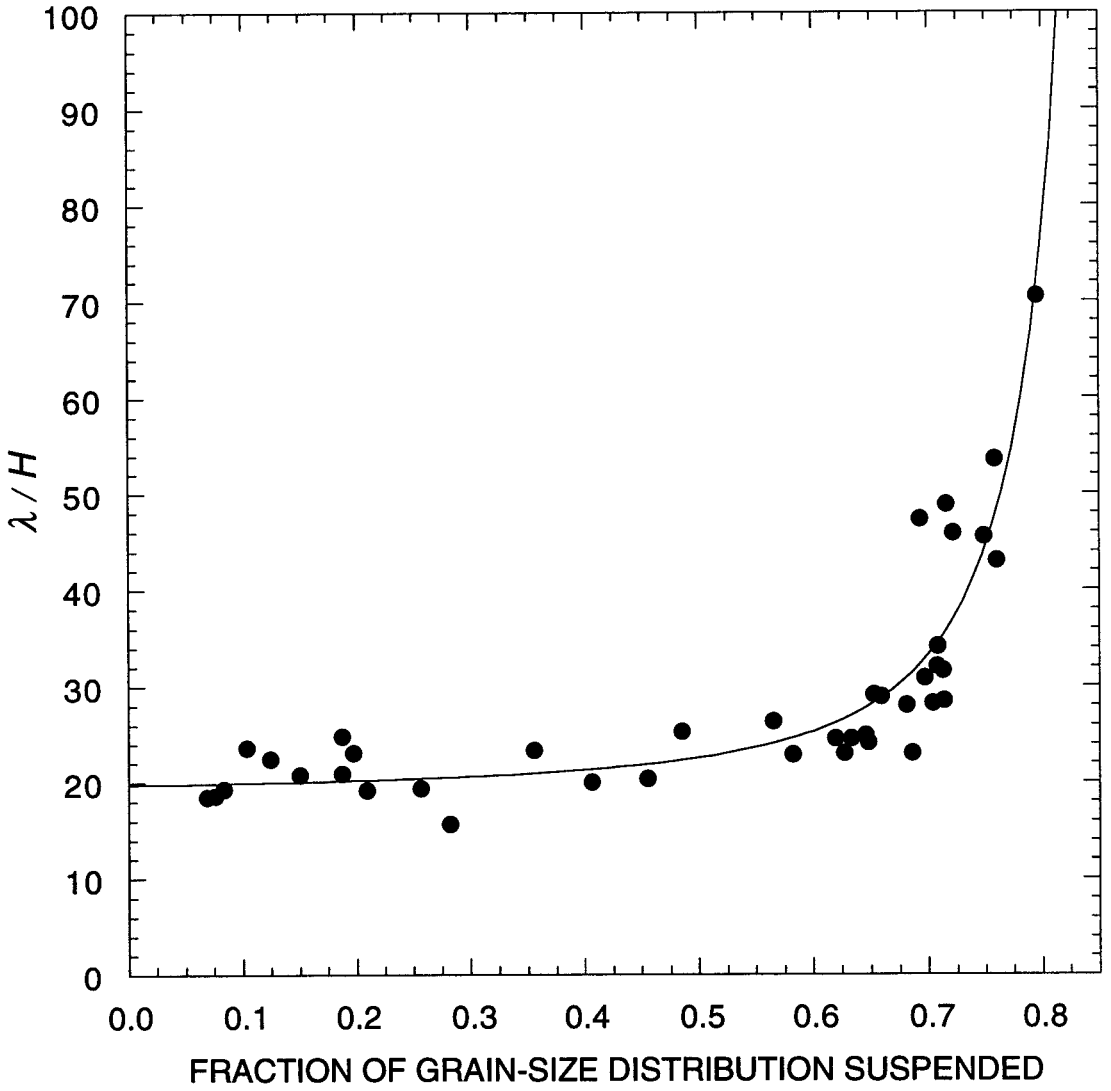

Figure 3.12: Dune wavelength nondimensionalized by dune height as a function of the fraction of the bed grain-size distribution that is suspended; 1991 analysis by D.C. Mohrig using the data of Stein (1965). Solid line is equation 3.53, i.e., the best-fit regression to the analysis of Mohrig.

deceptively simple equation for the downstream time-averaged velocity at each level z:

$$\overline{u}(z) = \int_{T_s+(z_0)_{sf}}^{z} \frac{u_{*f}(z)}{L(z)} dz. \tag{3.55}$$

Skin-friction roughness for cases of no sediment transport and bedload transport

The skin-friction roughness parameter, $(z_0)_{sf}$, sets the lower limit of integration in equations 3.48, 3.51, and 3.55 and is determined by three physically distinct processes, i.e., no sediment transport, bedload transport, and suspended-load transport. For the case of no sediment transport, the skin-friction roughness parameter is proportional to the height of the immobile roughness elements on the bed and is equal to the Nikuradse (1933) roughness parameter for hydraulically rough flow:

$$(z_0)_{sf} = \frac{k_s}{30}, \tag{3.56}$$

where k_s is the bed roughness length scale and is assumed to equal D_{50} of the sand, silt, and clay mixture on the bed. For the case where the dominant sediment-transport mode is bedload, i.e., the D_{50} Rouse number is greater than about 1, and thus momentum is being extracted from the flow primarily by saltating grains, the skin-friction roughness parameter is proportional to the thickness of the bedload layer. Thus, as determined by Wiberg and Rubin (1989), for the bedload-dominated case,

$$(z_0)_{sf} = 0.054\delta, \tag{3.57}$$

where δ is the thickness of the bedload saltation layer determined by the method of Wiberg and Rubin (1989).[3]

Nature of roughness and drag in suspended-sediment-transporting flows over either antidunes or upper-plane bed

Since both high suspended-sediment concentrations and antidunes are common in the Paria River, and because much confusion exists in the literature as to the nature of roughness and drag in flows with high suspended-sediment concentrations over antidunes, it was imperative to address this issue before modeling flow and sediment transport in the Paria River. As suggested by Gelfenbaum and Smith (1986), skin-friction roughness in flows with high suspended-sediment concentrations over a planar, immobile boundary, with no bedload saltation layer, increases exponentially with increasing concentration of near-bed suspended sediment:

---

[3]The D_{50} Rouse number is defined as $(w_s)_{D_{50}} / ku_{*T}$, where $(w_s)_{D_{50}}$ is the clear-water settling velocity of D_{50} of the bed material.

$$(z_0)_{sf} = \frac{k_s}{30}\exp\left[c_1(\rho_s/\rho_w)(\bar{\epsilon}_s)_{z_a}\right], \tag{3.58}$$

where ρ_s is the density of the sediment, ρ_w is the density of water, $(\bar{\epsilon}_s)_{z_a}$ is the time-averaged concentration of near-bed suspended sediment (calculated by equation 3.90 below), and c_1 is a constant. Furthermore, they determined that the value of c_1 was equal to 5.2 for the experiments of Einstein and Chien (1955). The structure of equation 3.58 is such that, at extremely low values of $(\bar{\epsilon}_s)_{z_a}$, the skin-friction roughness parameter reverts, as it must, to the value set by equation 3.56, where $(z_0)_{sf}$ is related to only the diameter of sand grains glued to the boundary in the Einstein and Chien (1955) experiments.

Equation 3.58 was derived for flow over a planar, immobile boundary whereas: natural rivers have a mobile boundary with some bedload transport of sediment; and, when the dominant sediment-transport mode is suspended load, the bed of the Paria River is not always planar, but may be composed of antidunes at higher Froude numbers. Therefore, equation 3.58 had to be modified so that, at extremely low values of $(\bar{\epsilon}_s)_{z_a}$, the skin-friction roughness parameter reverts, not to the Nikuradse roughness in equation 3.56, but to the bedload roughness in equation 3.57, such that:

$$(z_0)_{sf} = 0.054\delta\exp\left[c_1(\rho_s/\rho_w)(\bar{\epsilon}_s)_{z_a}\right]. \tag{3.59}$$

Values of c_1 in equation 3.59, for both suspended-load and bedload dominated cases, were determined by regression analysis of data from: the 34 upper-plane bed and antidune flume experiments of Kennedy (1961); the 57 upper-plane bed and antidune flume experiments of Guy and others (1966); and two velocity time-series measured over antidunes in Medano Creek on July 5, 1992 by Topping and J. Nelson (Figure 3.13). Also, the spatially averaged structure of velocity profiles measured over both upper-plane beds and antidunes in the laboratory was analyzed to determine if measurable form drag was associated with the presence of antidunes, or if equation 3.59 could describe the magnitude of the spatially averaged roughness associated with both upper-plane bed and antidunes.

Analysis of the flume data of Kennedy (1961) and Guy and others (1966) confirms that, when a significant amount of the bed material is in suspension, the skin-friction roughness parameter does increase exponentially with the near-bed concentration of suspended sediment (Figure 3.13). This enhancement of $(z_0)_{sf}$ occurs in all of their experiments where the D_{50} Rouse number was less than 1.15 and does not depend on whether the bed is planar or consists of antidunes. This analysis, presented in Figure 3.13, consisted of four steps. First, $(z_0)_{sf}$ was first determined for each experiment by fitting a quasi-logarithmic velocity profile [constructed from the 2-part eddy viscosity of Rattray

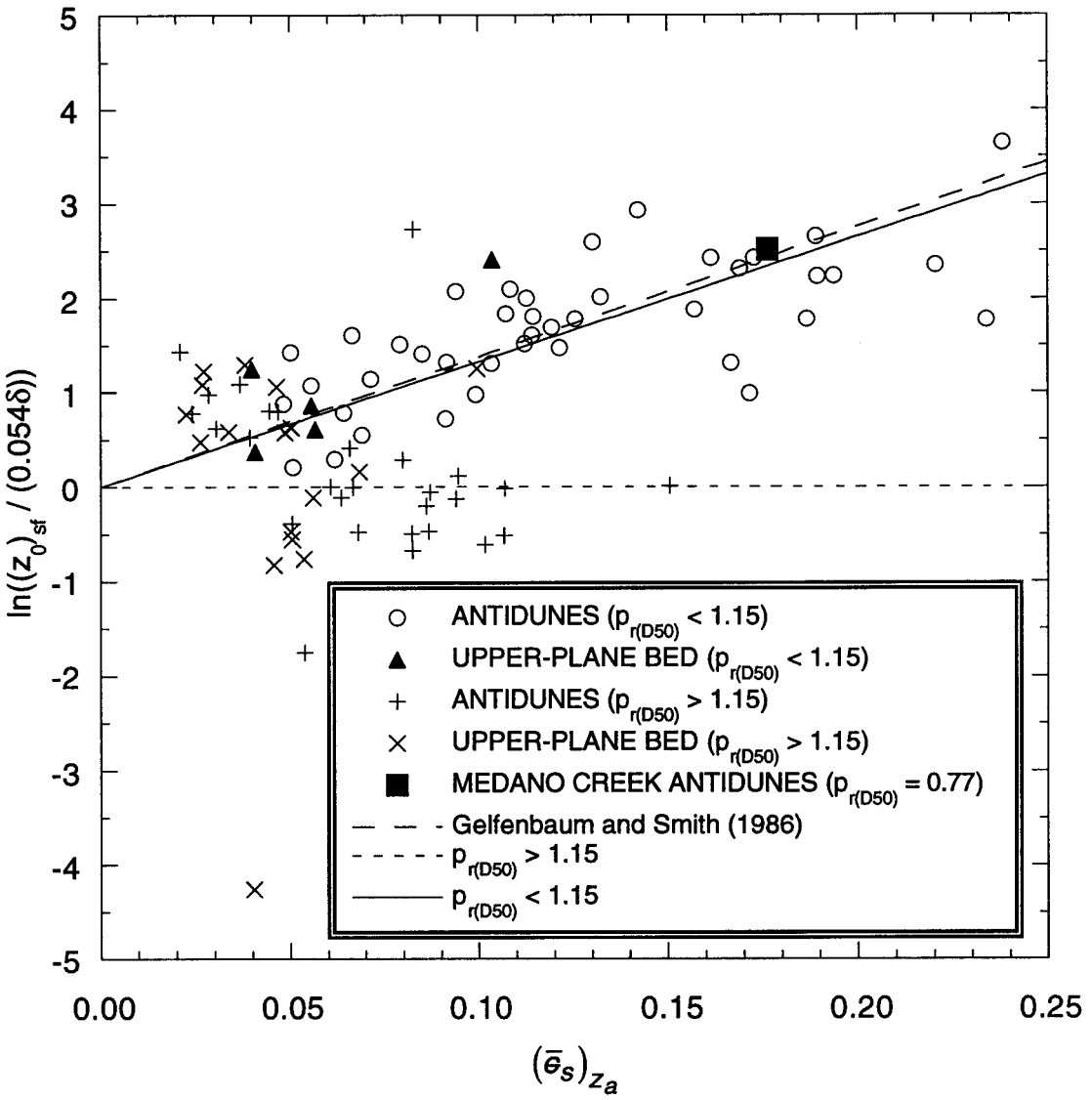

Figure 3.13: Natural logarithm of the "measured" skin-friction roughness parameter from each experiment nondimensionalized by the bedload skin-friction roughness parameter as a function of the predicted concentration of suspended-sediment at the top of the bedload layer. Lines associated with: c_1=0 when $p_{r(D_{50})}$, the D_{50} Rouse number, is greater than 1.15; c_1=5 when $p_{r(D_{50})}$ is less than 1.15; and c_1=5.2 from Gelfenbaum and Smith (1986) are shown.

and Mitsuda (1974)] to the measured mean velocity and the total shear velocity computed from the measured water surface slope and mean depth. Second, the dependent variable was set as $\ln((z_0)_{sf}/(0.054\delta))$, i.e., the natural logarithm of $(z_0)_{sf}$ divided by the bedload $(z_0)_{sf}$ of Wiberg and Rubin (1989), and the independent variable was set as $(\bar{c}_s)_{z_a}$, the concentration of suspended sediment at the top of the bedload layer predicted by equation 3.90 below. Third, the data were broken into two categories, with sediment transport primarily as suspended load or as bedload; a value of the D_{50} Rouse number equal to 1.15 (close to the theoretically determined value of 1 that separates bedload from suspended load) was empirically found to nicely break the data into the two categories. Fourth, regressions were fit to the data in each category; and, because $(z_0)_{sf}$ must revert to the bedload $(z_0)_{sf}$ of Wiberg and Rubin (1989) at low concentrations of near-bed suspended sediment, these regressions were forced through the origin. The slope of each regression in Figure 3.13, therefore, equals $c_1(\rho_s/\rho_w)$ for that category.

The value of c_1 was found to be 5 for the suspended-load dominated cases and 0 for the bedload dominated cases.[4] The least-squares regression fit to the suspended-load dominated cases yields a value of c_1=5 with a R^2 of only 0.482; however, the F-statistic of 42.81 indicates that the trend in $\ln(z_0/(0.054\delta))$ with respect to $(\bar{c}_s)_{z_a}$ is significant at the $4.42\text{x}10^{-8}$ level. The least-squares regression fit to the bedload dominated cases yields a value of c_1=0 and an R^2 value greater than 1 (due to the regression being forced through the origin). Not surprisingly, the F-statistic for this analysis is 0, thus indicating that no significant dependence of c_1 on $(\bar{c}_s)_{z_a}$ is justified for bedload-dominated cases. The behavior of the roughness appears not to be sensitive to whether the bed configuration consists of upper-plane bed or antidunes and seems to be sensitive only to the D_{50} Rouse number (Figure 3.13); this observation was investigated further by analyzing the spatially averaged structure of measured velocity profiles over both upper-plane beds and antidunes.

Analyses of the structure of velocity profiles measured by Guy and others (1966) indicate that, unlike in separated flow over dunes, no measurable spatially averaged form drag can be determined for flow over antidunes, thus finding support for the above treatment of the skin-friction roughness parameter (Table 3.2, Figure 3.14). For each of the upper-plane-bed and antidune flume runs with measured velocity profiles, the total shear velocity and roughness parameter were determined by the best-fit regression of a quasi-logarithmic velocity profile [constructed with the 2-part eddy viscosity of Rattray and

---

[4]The value of c_1=5 is similar to the value of c_1=5.2 from Gelfenbaum and Smith (1986).

Table 3.2: Comparison of the total shear velocity determined from spatially averaged measured velocity profiles to the total shear velocity determined from the depth-slope product, and comparison of the skin-friction roughness parameter determined from spatially averaged measured velocity profiles to the skin-friction roughness parameter determined by equations 3.57 or 3.59 (depending on the value D_{50} Rouse number) for the Guy and others (1966) upper-plane bed and antidune flume experiments.

D_{50} (mm)	RUN NO.	BEDFORM TYPE (*NOTE:* SW = standing wave in Guy and others' classification scheme)	MEAN FLOW DEPTH IN FLUME (cm)	MEAN FLOW DEPTH FROM VELOCITY PROFILES (cm)	NUMBER OF MEASURED VELOCITY PROFILES	$(u_*)_T$ FROM DEPTH-SLOPE PRODUCT (cm/s)	$(u_*)_T$ FROM FIT TO SPATIALLY AVERAGED VEL. PROF. (cm/s)	n (no. of points in regres-sion)	R^2 OF FIT TO VEL. PROF.	z_0 FROM FIT TO SPATIALLY AVERAGED VEL. PROF. (cm)	D_{50} ROUSE NO.	$(z_0)_{sf}$ FROM EQUATION 3.57 OR 3.59 (cm)
0.19	15	U-PLANE BED	24.1	23.5	3	5.14	6.41	24	0.925	0.00790	0.852	0.00317
0.19	10	U-PLANE BED	15.5	13.7	3	5.09	4.94	23	0.943	0.00164	0.858	0.00312
0.27	46	U-PLANE BED	22.6	21.2	3	6.08	6.39	29	0.895	0.00473	1.17	0.00310
0.28	22	U-PLANE BED	18.3	18.6	3	5.24	5.14	30	0.952	0.00543	1.31	0.00302
0.28	25	U-PLANE BED	21.9	20.7	3	6.54	6.15	29	0.949	0.00230	1.08	0.00693
0.28	28	U-PLANE BED	16.8	16.8	3	6.14	5.52	27	0.967	0.00133	1.16	0.00325
0.28	29	U-PLANE BED	15.8	15.4	3	6.57	5.87	31	0.937	0.00155	1.09	0.00703
0.28	26	ANTIDUNE	15.2	14.9	3	7.00	8.13	25	0.894	0.0135	1.02	0.00794
0.32	20	ANTIDUNE	16.8	16.4	3	9.65	9.48	30	0.945	0.00716	0.851	0.0202
0.32	19	U-PLANE BED	17.1	17.8	1	8.35	13.7	10	0.873	0.0932	1.20	0.00432
0.32	10	ANTIDUNE	18.0	16.3	3	11.2	8.96	26	0.917	0.00810	0.668	0.0310
0.32	9	ANTIDUNE	17.1	17.0	3	9.08	13.2	39	0.899	0.0542	1.05	0.0200
0.32	12	U-PLANE BED	20.4	19.5	3	9.56	7.88	30	0.939	0.00437	0.795	0.0179
0.32	11	ANTIDUNE	18.3	16.7	3	8.55	10.7	30	0.911	0.0157	1.11	0.0167
0.33	1	U-PLANE BED	15.5	15.9	1	6.65	5.39	11	0.991	0.000445	1.42	0.00419
0.45	39	ANTIDUNE-SW	16.8	17.8	3	7.75	10.1	24	0.879	0.0295	1.76	0.00668
0.45	26	U-PLANE BED	10.4	14.7	3	6.10	8.15	27	0.879	0.0189	2.19	0.00604
0.45	31	ANTIDUNE-SW	13.4	10.7	2	7.54	7.25	15	0.808	0.00408	1.78	0.00660
0.45	41	ANTIDUNE-SW	16.5	16.5	3	8.67	10.6	27	0.885	0.0236	1.57	0.00691
0.45	34	ANTIDUNE-SW	8.5	8.4	3	6.76	7.03	16	0.873	0.00514	1.99	0.00633
0.45	33	ANTIDUNE-SW	8.2	9.6	3	7.00	6.70	19	0.941	0.00299	1.89	0.00641
0.45	38	ANTIDUNE-SW	15.2	15.2	3	9.62	7.77	25	0.888	0.00133	1.42	0.00709
0.45	32	ANTIDUNE	11.3	11.1	2	8.52	7.60	15	0.806	0.00225	1.59	0.00687
0.45	45	ANTIDUNE	8.5	6.0	3	8.49	5.52	22	0.617	0.00129	1.61	0.00687
0.45	44	ANTIDUNE	8.5	8.7	3	8.67	6.71	21	0.761	0.000456	1.58	0.00691
0.45	42	ANTIDUNE	9.4	9.0	1	9.56	9.00	9	0.902	0.00378	1.45	0.00709
0.93	42	ANTIDUNE-SW	13.4	13.5	3	12.4	20.7	28	0.806	0.216	2.31	0.0197
0.93	40	ANTIDUNE-SW	11.6	10.2	3	11.8	18.8	21	0.862	0.209	2.42	0.0193
0.93	43	ANTIDUNE-SW	13.4	12.5	3	12.9	13.9	25	0.884	0.0239	2.23	0.0199
0.93	39	ANTIDUNE-SW	13.1	13.5	3	12.8	21.6	29	0.903	0.247	2.24	0.0199

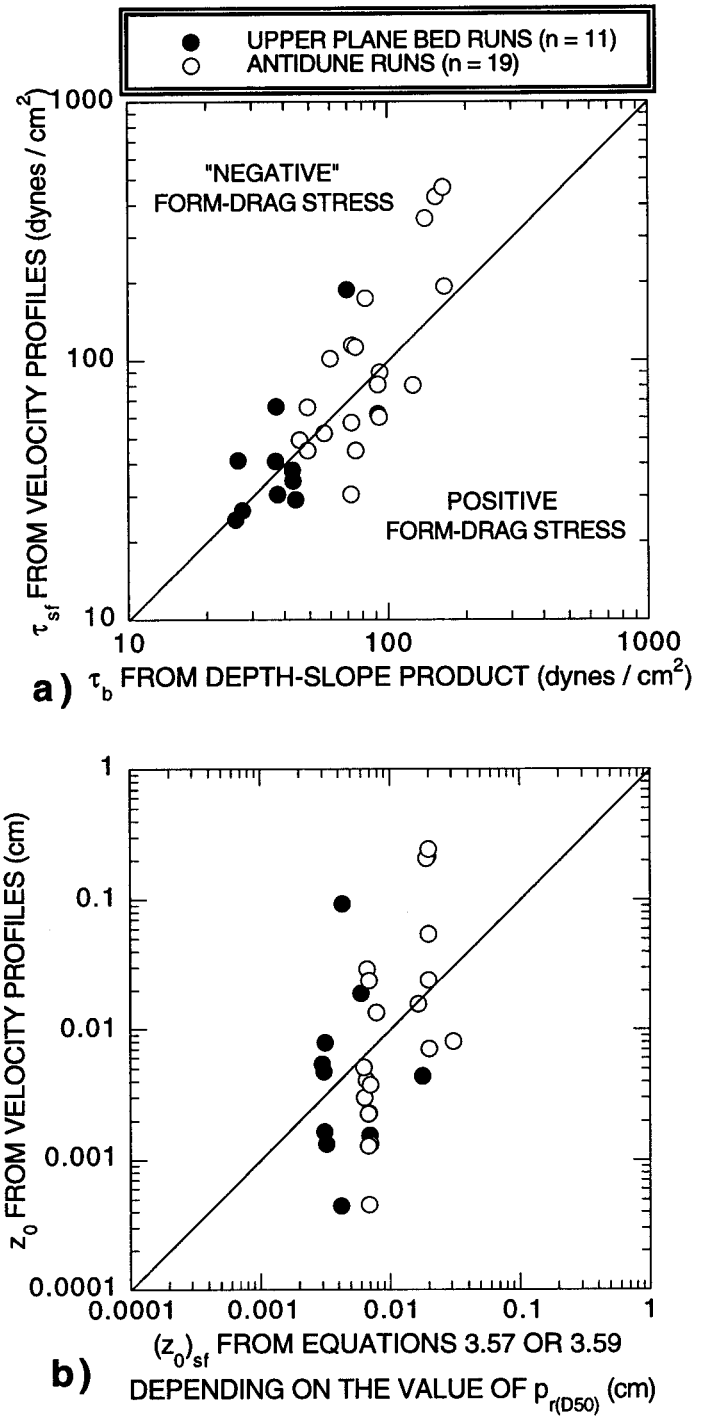

Figure 3.14: **(a)** $(\tau_b)_{vp}$ as a function of τ_b for the upper-plane bed and antidune flume runs of Guy and others (1966). Points plotting above the line of perfect agreement between $(\tau_b)_{vp}$ and τ_b have a physically impossible, "negative" form-drag component of the total stress and points plotting below the line of perfect agreement have a positive form-drag component of the total stress. **(b)** z_0 determined from the velocity profiles as a function of $(z_0)_{sf}$ determined by either equation 3.57 or 3.59 (depending on the value of the D_{50} Rouse number) for the same experiments.

Mitsuda (1974)] to the spatially averaged velocity measurements. Also, for each flume run, the total shear velocity was calculated from the depth-slope product, and the skin-friction roughness parameter was calculated from either equation 3.57 or 3.59, depending on the value of the D_{50} Rouse number. Results of these analyses are presented in Table 3.2; the graphs of the 30 regressed and measured velocity profiles appear in Appendix 3.

Comparison of the boundary shear stress determined from the spatially averaged velocity profiles, with the total boundary shear stress determined by the depth-slope product, indicates that these two quantities are equal within the error of the measurements for both the upper-plane bed and antidune flume runs. That is, no measurable spatially averaged form-drag stress in excess of that for flow over a planar bed is present in the case of antidunes (Figure 3.14a). Excellence of the average agreement between the boundary shear stresses determined by the two methods is shown by the ratio of the natural log-transformed velocity-profile-determined τ_b to the natural log-transformed depth-slope-product-determined τ_b; the mean plus-and-minus one standard deviation of this ratio is 1.02 ± 0.11 for the 11 upper-plane bed runs and 1.03 ± 0.12 for the 19 antidune runs.

Average agreement between z_0 determined from the spatially averaged velocity profiles and $(z_0)_{sf}$ predicted by either equations 3.57 or 3.59 (depending the value of the D_{50} Rouse number) is also good (Figure 3.14b), indicating that most of the roughness in the velocity profiles can be explained by roughness resulting from either bedload or suspended load. Scatter of the velocity profile-determined z_0 is centered about the line of perfect of agreement in Figure 3.14b, with the mean plus-and-minus one standard deviation of the ratio of the natural log-transformed velocity profile-determined z_0 to the natural log-transformed equation 3.58 or 3.59-determined $(z_0)_{sf}$ equal to 1.04 ± 0.29 for the 11 upper-plane bed runs and equal to 0.99 ± 0.35 for the 19 antidune runs illustrating no dependence of the skin-friction roughness parameter on bed state. Thus, the skin-friction roughness parameter is interpreted to equal to the bedload saltation skin-friction roughness parameter (determined by equation 3.57) for any case with a D_{50} Rouse number greater than about 1.15 and is interpreted to equal to the suspended-load skin-friction roughness parameter (determined by equation 3.59 with a value of c_1=5) for any case with a D_{50} Rouse number less than about 1.15.

Section 3.6: THE SUSPENDED-SEDIMENT COMPONENT OF THE MODEL

The suspended-sediment transport component of the model employs the conservation of mass relationships for a multicomponent fluid. First, following the

convention of Hunt (1969) and Smith (1977), the full conservation of mass equation for each sediment component is:

$$\frac{\partial \epsilon_m}{\partial t} + \nabla \cdot \left(\underline{U}_m \epsilon_m \right) = 0, \tag{3.60}$$

and for the water component is:

$$\frac{\partial \epsilon_w}{\partial t} + \nabla \cdot \left(\underline{U}_w \epsilon_w \right) = 0, \tag{3.61}$$

where ϵ_m is the volume concentration of sediment component m, ϵ_w is the volume concentration of the water component, $\underline{U}_m$ is the velocity tensor of sediment component m, and $\underline{U}_w$ is the velocity tensor of the water component.[5] The volume concentrations are defined as:

$$\sum_{m=1}^{M} \epsilon_m = \epsilon_s, \tag{3.62}$$

and,

$$\epsilon_s + \epsilon_w = 1. \tag{3.63}$$

The velocity tensor for the water component of the fluid, $\underline{U}_w$, is separated into a temporal mean portion, $\overline{\underline{U}}_w$, and a temporal fluctuating portion due to turbulence, $\underline{U}'_w$:

$$\underline{U}_w = \overline{\underline{U}}_w + \underline{U}'_w. \tag{3.64}$$

Likewise, the velocity tensor for each sediment component m, $\underline{U}_m$, is also separated into a temporal mean portion, $\overline{\underline{U}}_m$, and a temporal fluctuating portion due to turbulence, $\underline{U}'_m$:

$$\underline{U}_m = \overline{\underline{U}}_m + \underline{U}'_m. \tag{3.65}$$

The volume concentration of each sediment component, ϵ_m, is also separated into a temporal mean portion, $\bar{\epsilon}_m$, and a temporal fluctuating portion due to turbulence, ϵ'_m:

$$\epsilon_m = \bar{\epsilon}_m + \epsilon'_m, \tag{3.66}$$

and an analogous equation is developed for the concentration of water.

After time-averaging over a period long relative to the time-scale of the turbulent fluctuations and employing the above definitions, M equations of the form:

$$\frac{\partial \epsilon_m}{\partial t} + \nabla \cdot \left(\overline{\underline{U}}_m \bar{\epsilon}_m \right) + \nabla \cdot \left(\overline{\underline{U}'_m \epsilon'_m} \right) = 0 \tag{3.67}$$

result for each sediment component m. Likewise, the equation for the water component is:

$$\frac{\partial \epsilon_w}{\partial t} + \nabla \cdot \left(\overline{\underline{U}}_w \bar{\epsilon}_w \right) + \nabla \cdot \left(\overline{\underline{U}'_w \epsilon'_w} \right) = 0, \tag{3.68}$$

which by substituting equation 3.66 into equation 3.68, becomes:

---

[5]The symbolic convention used in this section is that underbars represent tensors and overbars represent time-averaged quantities.

$$\frac{\partial \epsilon_s}{\partial t} - \nabla \cdot \left(\underline{\overline{U}}_w \left(1 - \bar{\epsilon}_s \right) \right) + \nabla \cdot \left(\overline{\underline{U'}_w \epsilon'_s} \right) = 0 . \tag{3.69}$$

By approximating the turbulent mass fluxes by gradient-type diffusion as first done by O'Brian (1933), the sediment component equation becomes:

$$\frac{\partial \epsilon_m}{\partial t} + \nabla \cdot \left(\underline{\overline{U}}_m \bar{\epsilon}_m \right) - \nabla \cdot \left(K_\rho \nabla \bar{\epsilon}_m \right) = 0, \tag{3.70}$$

and the water component equation becomes:

$$\frac{\partial \epsilon_s}{\partial t} - \nabla \cdot \left(\underline{\overline{U}}_w \left(1 - \bar{\epsilon}_s \right) \right) - \nabla \cdot \left(K_\rho \nabla \bar{\epsilon}_s \right) = 0 . \tag{3.71}$$

Density stratification due to high suspended-sediment concentration gradients

For flows without the density stratification that results from high suspended-sediment concentration gradients, the neutral mass diffusion, $(K_\rho(z))_N$, is equal to the clear-water momentum diffusion, $(K(z))_N$, i.e. the neutral eddy viscosity from equation 3.38. In the Paria River, this assumption cannot be made because of the high suspended-sand-concentration gradients that accompany the typically high concentrations of suspended sediment. Turbulence-damping effects of high concentrations of suspended sediment were first investigated by Vanoni (1944), subsequently documented in flume experiments by Einstein and Chien (1955) and Vanoni and Brooks (1957), and first theoretically treated in terms of the gradient Richardson number by Monin and Yaglom (1965). Furthermore, the turbulence-damping effects of high concentrations of suspended sediment have been documented in rivers similar to the Paria River by Nordin (1963, 1964) and Nordin and Dempster (1963). Nordin (1964) showed empirically that turbulence damping did not occur when high concentrations of silt and clay, i.e., wash load, were present, but rather only occurred when high concentrations of sand were present in the lower part of the flow. Thus, Nordin (1964) provided the first evidence from a river that the structure of the turbulence is not affected by overall sediment concentration and is only affected by high concentration gradients. To account for the turbulence-damping effects of the high density gradients produced by the high concentration gradients accompanying the high suspended-sand concentrations in the Paria River, the density stratification correction developed by Smith and McLean (1977a, 1977b) and further refined and tested by McLean (1991a, 1991b, 1992) is used below to modify the local length scale of the turbulence within the eddy viscosity.

As a flow becomes progressively more density stratified with increasing suspended-sediment-concentration gradients, the spatially averaged local length scale of the turbulence (defined in equations 3.41 and 3.42) gets progressively shorter. To reflect this,

as in Smith and McLean (1977a, 1977b) the neutral form of the momentum diffusion (eddy viscosity) at each level z, $(K(z))_N$, is modified by the inverse of the nondimensional shear, ϕ_m :

$$K(z) = \left(K(z)\right)_N \phi_m{}^{-1} = (K(z))_N \left(1 - \alpha(\gamma_m)_0 \frac{\tau_f(z)}{\tau_f(0)} \mathbf{Ri}_g\right), \tag{3.72}$$

where the constant $(\gamma_m)_0$= 5.4, since the gradient Richardson number, $\mathbf{Ri}_g$, is critical at 0.25. Likewise, as in Smith and McLean (1977a, 1977b), the neutral form of the mass diffusion at each level z, $(K_\rho(z))_N$, is modified by the inverse of the nondimensional shear for mass:

$$K_\rho(z) = \left(K_\rho(z)\right)_N \phi_\rho{}^{-1} = (K_\rho(z))_N \left(1 - \alpha(\gamma_\rho)_0 \frac{\tau_f(z)}{\tau_f(0)} \mathbf{Ri}_g\right), \tag{3.73}$$

where ϕ_ρ is the nondimensional shear for mass and is analogous to ϕ_m, and $(\gamma_\rho)_0$=7.3 since when $\mathbf{Ri}_g$ is critical, α (defined below) is 0.74. The values of $(\gamma_m)_0$=5.4 and $(\gamma_\rho)_0$=7.3 have been shown to work well in tests by McLean (1991b) of the density stratification correction theory against available suspended-sediment data measured in flumes.

The quantity,

$$\alpha = \frac{K_\rho(z)}{K(z)} = \frac{\left(K_\rho(z)\right)_N \phi_\rho{}^{-1}}{\left(K(z)\right)_N \phi_m{}^{-1}}, \tag{3.74}$$

is the ratio of the mass diffusion to the momentum diffusion. α is equal to 1 in neutral (clear-water) conditions and, as indicated by measurements in the atmospheric boundary layer (Businger and others, 1971; Wieringa, 1980), α is equal to 0.74 in stably stratified conditions.

The gradient Richardson number:

$$\mathbf{Ri}_g = \frac{-g \dfrac{\partial \rho_f}{\partial z}}{\rho_f \left(\dfrac{\partial u}{\partial z}\right)^2}, \tag{3.75}$$

is the local balance of the fluid density gradient resulting from the suspended-sediment-concentration gradient and the fluid shear; ρ_f in equation 3.75 is the bulk fluid density calculated by equation 3.86 (described below). Turbulence is fully damped and the flow becomes laminar when $\mathbf{Ri}_g$=0.25 (e.g., Businger and others, 1971; Smith and McLean, 1977a, 1977b; Rohr and others, 1988; Mason and Derbyshire, 1990; McLean, 1991b, 1992); thus, at $\mathbf{Ri}_g$=0.25, the mechanism for suspending sediment, i.e., turbulence, is "shut off". Density stratification, therefore, is the physical effect that places an upper limit on how much sediment can be "suspended" in a given flow.

Sediment velocity and the nonzero vertical velocity of water in the presence of suspended sediment

By virtue of conservation of mass in a multicomponent system, an upward flux of water is driven by the settling sediment and unlike in steady, uniform clear-water flows, the vertical velocity component of the water does not equal zero. In suspended-sediment calculations, it is generally assumed that the sediment velocity is equal to the water velocity minus the settling velocity of the sediment; therefore, the sediment velocity for each component m is equal to the velocity of the water component minus the settling velocity of the sediment component m, w_m:

$$\underline{U}_m = \underline{U}_w - w_m. \tag{3.76}$$

For steady, horizontally uniform flow and after making the above substitution for the sediment velocity, the sediment component m equation simplifies to:

$$\bar{\epsilon}_m(\bar{w}_w - w_m) - \alpha K(z)\frac{\partial \bar{\epsilon}_m}{\partial z} = 0, \tag{3.77}$$

and the water component equation simplifies to:

$$-\bar{w}_w(1-\bar{\epsilon}_s) - \alpha K(z)\frac{\partial \bar{\epsilon}_s}{\partial z} = 0. \tag{3.78}$$

Summing equation 3.77 over all sediment components m and combining it with equation 3.78 yields the following equation for the upward flux of water driven by the settling sediment:

$$\bar{w}_w = \sum_{m=1}^{M} \bar{\epsilon}_m w_m. \tag{3.79}$$

Concentration profiles for the m components of suspended sediment

Several final steps are required to derive the concentration profile for each sediment component m. By multiplying equation 3.77 by a factor of $(1-\bar{\epsilon}_s)$ and equation 3.78 by a factor of $\bar{\epsilon}_m$, and combining to form a single equation for the conservation of mass of each sediment component m and the water component yields:

$$\alpha K(z)\left[(1-\bar{\epsilon}_s)\frac{\partial \bar{\epsilon}_m}{\partial z} + \bar{\epsilon}_m \frac{\partial \bar{\epsilon}_s}{\partial z}\right] + \bar{\epsilon}_m w_m(1-\bar{\epsilon}_s) = 0. \tag{3.80}$$

Equation 3.80 is then divided by a factor of $(1-\bar{\epsilon}_s)^2$ to result in the convenient form:

$$\alpha K(z)\left[\frac{(1-\bar{\epsilon}_s)\partial \bar{\epsilon}_m/\partial z + \bar{\epsilon}_m\, \partial \bar{\epsilon}_s/\partial z}{(1-\bar{\epsilon}_s)^2}\right] + \frac{\bar{\epsilon}_m w_m}{(1-\bar{\epsilon}_s)} = 0. \tag{3.81}$$

Since

$$\frac{\partial}{\partial z}\left(\frac{\bar{e}_m}{1-\bar{e}_s}\right)=\left[\frac{(1-\bar{e}_s)\partial\bar{e}_m/\partial z+\bar{e}_m\,\partial\bar{e}_s/\partial z}{(1-\bar{e}_s)^2}\right], \tag{3.82}$$

by differentiation by parts, and

$$d\left[\ln\left(\frac{\bar{e}_m}{1-\bar{e}_s}\right)\right]=\frac{\frac{\partial}{\partial z}\left(\frac{\bar{e}_m}{1-\bar{e}_s}\right)}{\left(\frac{\bar{e}_m}{1-\bar{e}_s}\right)}, \tag{3.83}$$

it follows that:

$$\left[\ln\left(\frac{\bar{e}_m}{1-\bar{e}_s}\right)\right]_z=\left[\ln\left(\frac{\bar{e}_m}{1-\bar{e}_s}\right)\right]_{T_s+z_a}\int_{T_s+z_a}^{z}-\frac{w_m}{\alpha K(z)}dz, \tag{3.84}$$

where T_s+z_a is the lower limit of integration and is equal to the position of the top of the bedload layer. Simplifying yields the final equation for the time-averaged volume concentration of each sediment component m at each level z in the flow:

$$\left(\frac{\bar{e}_m}{1-\bar{e}_s}\right)_z=\left(\frac{\bar{e}_m}{1-\bar{e}_s}\right)_{T_s+z_a}\exp\left[-\int_{T_s+z_a}^{z}\frac{w_m}{\alpha K(z)}dz\right]. \tag{3.85}$$

Settling velocity of suspended sediment and the "hindered settling" effect

Because of the presence of suspended sediment in the flow, the clear-water density and viscosity cannot be used to calculate w_m in equation 3.85. Therefore, for the Paria River, the settling velocity for each sediment component (i.e., size class) m was calculated by the method of Dietrich (1982a) using a bulk fluid density and viscosity rather than a clear-water density and viscosity. To account for increased buoyancy forces resulting from the presence of suspended sediment, the bulk fluid density at each level z, $\rho_f(z)$, can be determined exactly such that:

$$\rho_f(z)=\rho_w+(\rho_s-\rho_w)(\bar{e}_s)_z, \tag{3.86}$$

where ρ_w is the density of clear water at a given temperature. And, the bulk fluid dynamic viscosity at each level z, $\mu_f(z)$, is calculated by the relationship of Batchelor and Green (1972),

$$\mu_f(z)=\mu_w\left(1+2.5(\bar{e}_s)_z+7.6(\bar{e}_s)_z^{\,2}\right), \tag{3.87}$$

where μ_w is the dynamic viscosity of clear water at a given temperature; Batchelor and Green (1972) added the second order term to the relationship originally developed by Einstein (1906). This type of modification of the density and viscosity of the flow due to the presence of suspended sediment was first proposed by Gelfenbaum and Smith (1986).

Combination of the upward flow driven by the settling grains, which manifests itself in the $(1-\bar{e}_s)$ terms in the denominators of equation 3.85, with the increased fluid density and viscosity due to suspended sediment comprises the two-part process termed "hindered settling" by Graf (1971); this process was first documented in experiments by Nordin (1963, 1964). The "hindered settling" effect acts against the effect of density stratification by increasing sediment concentrations and decreasing the sediment concentration gradient. In the first part of this process, settling coarser grains drive the upward flow of water (see equation 3.79), which reduces the effective settling velocity of the finer grains, thus increasing the concentration of finer sediment at each level z. In the second part of this process, the increased buoyancy forces resulting from the increased density and viscosity reduce the actual settling velocity, w_m, further increasing the concentration of sediment at each level z.

The lower boundary condition

The last and perhaps most important part of the suspended-sediment model is the treatment of the lower boundary condition at z_a. The level of z_a is set equal to the top of the bedload layer, δ, as determined by the Wiberg and Rubin (1989) modification to the formulation of Dietrich (1982b):

$$\frac{\delta}{D_{50}} = \frac{a_1 T_*}{1 + a_2 T_*}, \tag{3.88}$$

where $T_*=\tau_f(0)/\tau_{cr}$ is defined as the transport stage, a_1=0.68 is a constant, and:

$$a_2 = 0.02035(\ln D_{50})^2 + 0.02203(\ln D_{50}) + 0.07090. \tag{3.89}$$

The time-averaged concentration of each sediment size-class m at level z_a, $(\bar{e}_m)_{za}$, is set by a linear version of the functional form developed by Smith and McLean (1977a):

$$(\bar{e}_m)_{z_a} = A_s f_m \epsilon_b \gamma S_*, \tag{3.90}$$

where A_s is the area concentration of sand, silt, and clay on the bed as determined by equation 3.29, f_m is the volume fraction of sediment size-class m in the bed as determined by equation 3.26, ϵ_b is the concentration of sand, silt, and clay in the bed and is equal to 0.65, and γ is a constant and is set equal to 0.0045 (Wiberg, pers. comm.). S_* is the excess shear stress defined by Smith and McLean (1977a):

$$S_* = \frac{\tau_f(0) - \tau_{cr}}{\tau_{cr}}, \tag{3.91}$$

where τ_{cr} is the critical shear stress for D_{50} of the sand, silt, and clay mixture in the bed determined by the method of Wiberg and Smith (1987b) using a d/k_s value of 1. The total sand, silt, and clay concentration at z_a is:

$$\left(\bar{\epsilon}_s\right)_{z_a} = \sum_{m=1}^{M} \left(\bar{\epsilon}_m\right)_{z_a}. \tag{3.92}$$

An upper limit of $\left(\bar{\epsilon}_s\right)_{z_a}$ =0.50A_s is imposed to preclude overly high concentrations at z_a. When this condition is reached, the time-averaged concentration of each sediment size-class m at level z_a is calculated as:

$$\left(\bar{\epsilon}_m\right)_{z_a} = 0.5 A_s f_m. \tag{3.93}$$

Is lateral diffusion of suspended sediment important?

As shown in Section 3.3, since the modeled reaches of the Paria River are essentially straight, reach-averaging sets all lateral advective transport of sediment equal to zero, so diffusion is the only mechanism by which sediment can move laterally in the reach-averaged cross-section. So far, this effect has been neglected in the model, and the suspended-sediment model developed above has included the advective and diffusive processes operating in the vertical dimension only. Furthermore, since the lateral diffusion of suspended-sediment has been used as an important process by various workers to model the geomorphology of river channels (e.g. Parker, 1978b; Ikeda and Izumi, 1991), the importance of this process in the Paria River must be evaluated.

The measurements of Fischer (1973) indicate that the lateral mass diffusion coefficient is approximately a factor of two greater than the mass diffusion coefficient in the z-direction; hence the lateral mass diffusion coefficient will be approximately twice the value of the local eddy viscosity. To evaluate the relative importance of advective and diffusive transport of suspended sediment in each direction in the reach-averaged cross-section, scale analysis can be conducted on a simplified version of the coupled suspended-sediment advection-diffusion equation,

$$\frac{\partial \bar{\epsilon}_s}{\partial t} + \frac{\partial\left(\bar{u}\bar{\epsilon}_s\right)}{\partial x} + \frac{\partial\left(\bar{v}\bar{\epsilon}_s\right)}{\partial y} - \frac{\partial\left(w_s\bar{\epsilon}_s\left(1-\bar{\epsilon}_s\right)\right)}{\partial z} = \frac{\partial}{\partial x}\left(2K\frac{\partial \bar{\epsilon}_s}{\partial x}\right) + \frac{\partial}{\partial y}\left(2K\frac{\partial \bar{\epsilon}_s}{\partial y}\right) + \frac{\partial}{\partial z}\left(K\frac{\partial \bar{\epsilon}_s}{\partial z}\right). \tag{3.94}$$

Since reach-averaging removes all streamwise gradients in velocity and sediment concentration, all terms in equation 3.94 with gradients in the x-direction vanish. Also, since reach-averaging removes all cross-stream velocities, the y-direction advective term in equation 3.94 also vanishes. Thus, for the steady-state solution in the reach-averaged cross-section, we are left with the following balance between the vertical advective

transport of suspended sediment and the lateral and vertical diffusive transport of suspended sediment:

$$-w_s \frac{\partial\left(\bar{e}_s\left(1-\bar{e}_s\right)\right)}{\partial z} = \frac{\partial}{\partial y}\left(2K\frac{\partial \bar{e}_s}{\partial y}\right) + \frac{\partial}{\partial z}\left(K\frac{\partial \bar{e}_s}{\partial z}\right). \tag{3.95}$$

First, using the convention from in Section 3.3 to scale the vertically averaged x-direction momentum equation, the order of magnitude of the z-direction advective term can be evaluated as:

$$w_s \frac{\partial\left(\bar{e}_s\left(1-\bar{e}_s\right)\right)}{\partial z} \sim w_s \frac{\Delta\bar{e}_s\left(1-\Delta\bar{e}_s\right)}{L_z}. \tag{3.96}$$

For a typical Paria River flood: the appropriate vertical length scale, L_z, is the flow depth and is O(2) cm; the settling velocity of D_{50} of the suspended sediment, w_s, is O(0) cm/s; the change in volumetric sediment concentration over the flow depth, $\Delta\bar{e}_s$, is O(-1); and the change in volumetric water concentration over the flow depth, $\left(1-\Delta\bar{e}_s\right)$, is O(0). Therefore,

$$w_s \frac{\Delta\bar{e}_s\left(1-\Delta\bar{e}_s\right)}{L_z} = \mathrm{O}(0)\frac{\mathrm{O}(-1)\mathrm{O}(0)}{\mathrm{O}(2)} = \mathrm{O}(-3). \tag{3.97}$$

Since the lateral mass diffusion coefficient, $2K$, does not depend on y, the order of magnitude of the y-direction diffusive term can be evaluated as:

$$\frac{\partial}{\partial \mathrm{y}}\left(2K\frac{\partial \bar{e}_s}{\partial \mathrm{y}}\right) \sim \frac{2K}{L_y}\left(\frac{\Delta\bar{e}_s}{L_y}\right). \tag{3.98}$$

For a typical Paria River flood: the appropriate horizontal length scale, L_y, is one-half of the channel width and is O(3) cm; the lateral mass diffusion coefficient, $2K$, is O(0)O(2) cm^2/s; and the maximum change in volumetric sediment concentration over half of the channel width, $\Delta\bar{e}_s$, is O(-1). Therefore,

$$\frac{2K}{L_y}\left(\frac{\Delta\bar{e}_s}{L_y}\right) = \frac{\mathrm{O}(0)\mathrm{O}(2)}{\mathrm{O}(3)}\left(\frac{\mathrm{O}(-1)}{\mathrm{O}(3)}\right) = \mathrm{O}(-5). \tag{3.99}$$

The order of magnitude of the z-direction diffusive term can be evaluated as:

$$\frac{\partial}{\partial \mathrm{z}}\left(K\frac{\partial \bar{e}_s}{\partial \mathrm{z}}\right) \sim \frac{\Delta K\Delta\bar{e}_s}{{L_z}^2}. \tag{3.100}$$

For a typical Paria River flood: again, the appropriate vertical length scale, L_z, is the flow depth and is O(2) cm; the change in the eddy viscosity, K, over the flow depth is O(2) cm^2/s; and the maximum change in volumetric sediment concentration over the flow depth, $\Delta\bar{e}_s$, is O(-1). Therefore,

$$\frac{\Delta K\Delta\bar{e}_s}{{L_z}^2} = \frac{\mathrm{O}(2)\mathrm{O}(-1)}{\mathrm{O}(4)} = \mathrm{O}(-3). \tag{3.101}$$

Since the term governing the lateral diffusive transport of suspended sediment is two orders of magnitude smaller than the terms governing the vertical advective and diffusive transport of suspended sediment in the reach-averaged cross-section, the exclusion of the effect of lateral diffusion from the model is justified. Because it is two orders of magnitude less important, the lateral diffusive transport of suspended sediment should significantly affect neither the bulk sediment transport through the reach-averaged cross-section nor the geomorphic adjustment of the reach-averaged cross-section during a flood.

Section 3.7: CALCULATION OF FLUID AND SEDIMENT DISCHARGE THROUGH THE MODEL-PREDICTED CROSS-SECTION

After the flow and sediment transport portions of the model have converged, and the equilibrium cross-section geometry for a given flow has been calculated, the unit fluid and sediment discharges at each computation vertical in the cross-section may be calculated. The unit fluid discharge, q, is simply:

$$q = \int_{(z_0)_{sf}}^{h} \overline{u} dz, \tag{3.102}$$

and the unit suspended-load flux for each sediment size-class m is:

$$(q_s)_m = \int_{z_a}^{h} (\overline{u}\overline{e}_m) dz. \tag{3.103}$$

Since the total load of sand, silt, and clay through the modeled cross-section consists of bedload in addition to suspended load, and it is desirable to know the relative quantity of each size class of sediment that is transported as either bedload or suspended load, the bedload transport of sediment in each size-class m is modeled as described below. First, the nondimensional unit bedload transport rate, ϕ_b, is calculated by a modified form of the Meyer-Peter and Müller (1948) bedload equation proposed by Wiberg and Smith (1989):

$$\phi_b = c_0 \left(\tau_* - (\tau_*)_{cr} \right)^{3/2}, \tag{3.104}$$

where τ_* is the nondimensional skin-friction shear stress for the model-predicted D_{50} of the sand, silt, and clay mixture remaining on the bed:

$$\tau_* = \frac{\tau_f(0)}{\left[(\rho_s - \rho) g D_{50} \right]}, \tag{3.105}$$

and $(\tau_*)_{cr}$ is the Shields number for the model-predicted D_{50} of the sand, silt, and clay mixture remaining on the bed:

$$(\tau_*)_{cr} = \frac{\tau_{cr}}{\left[(\rho_s - \rho) g D_{50} \right]}. \tag{3.106}$$

The quantity c_0 varies with shear stress; for low transport rates, that is, for $(\tau_* - (\tau_*)_{cr}) \leq 0.08$, $c_0 = 5.7$ (Fernandez Luque and van Beek, 1976); for higher transport rates, $0.08 < (\tau_* - (\tau_*)_{cr}) \leq 0.3$, $c_0 = 8$ (Meyer-Peter and Müller, 1948); and for very high transport rates, $(\tau_* - (\tau_*)_{cr}) > 0.3$, $c_0 = 12$ (Wilson, 1966).

The unit bedload sediment flux, q_b, is then calculated from the definition of the nondimensional unit bedload transport rate:

$$\phi_b = \frac{q_b}{\left[\left(\frac{\rho_s - \rho}{\rho}\right) g D_{50}\right]}. \tag{3.107}$$

Results of Wilcock and McArdell (1993) indicate that relating the fractional bedload transport rate for each sediment size-class m to the volume fraction of sediment size-class m in the bed is a reasonable approximation for the range of sand sizes in the Paria River. Therefore, the fractional unit bedload flux of each sediment size-class m for all sediment sizes with a settling velocity greater than the skin-friction shear velocity is modeled as:

$$(q_b)_m = f_m q_b. \tag{3.108}$$

The unit total-load flux, q_T,, is the sum of the fractional bedload and suspended load fluxes:

$$q_T = \sum_{m=1}^{M} (q_b)_m + \sum_{m=1}^{M} (q_s)_m. \tag{3.109}$$

Finally, the total fluid discharge, Q, through the modeled cross-section is then:

$$Q = \int_0^W q dy, \tag{3.110}$$

where W is the flow topwidth, and the total sediment (sand, silt, and clay) discharge, Q_T, through the modeled cross-section is:

$$Q_T = \int_0^W q_T dy. \tag{3.111}$$

Section 3.8: SENSITIVITY OF MODEL PREDICTIONS TO VARYING THE THICKNESS OF THE SAND , SILT, AND CLAY LAYER

The effects of varying the thickness of the sand, silt, and clay layer on the model-predicted, spatially averaged profiles of: fluid stress, turbulence length scale, gradient Richardson number, suspended-sediment concentration, and velocity are illustrated in Figure 3.15. For the example depicted in this figure, the flow depth is held constant at 50 cm, and the water surface slope is held constant at 0.004; hence the total boundary shear stress is held constant 196 dynes/cm^2. The gravel grain-size distribution used is that of the deepest part of the thalweg in the 1993 reach-averaged cross-section (Figure 2.23).

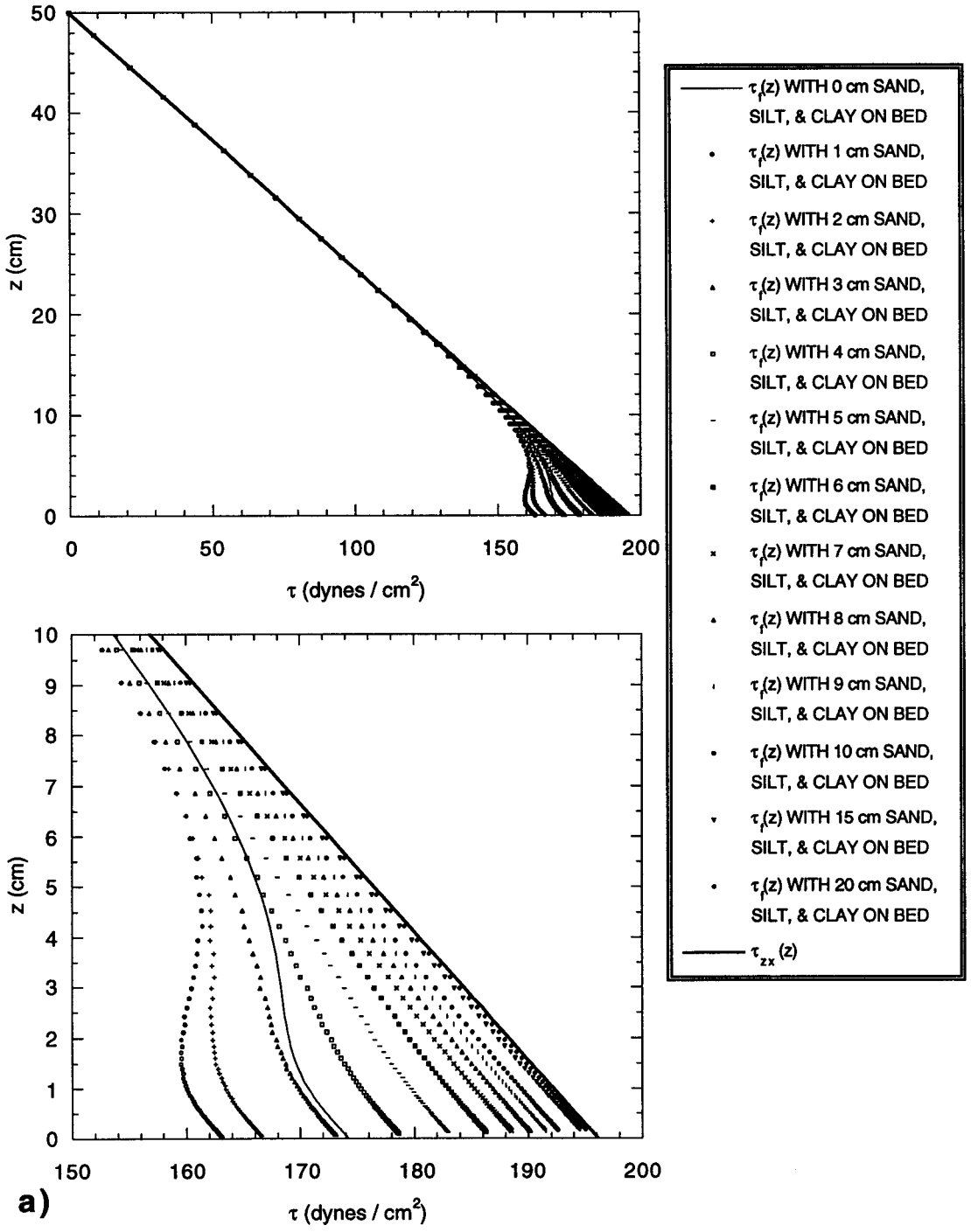

Figure 3.15: **(a)** Modeled profiles of $\tau_f(z)$ for various thicknesses of the sand, silt, and clay layer and the modeled profile of $\tau_{zx}(z)$. The upper graph shows the profiles for the full 50 cm depth of the flow and the lower graph is an expanded view of the profiles in the lower 10 cm of the flow.

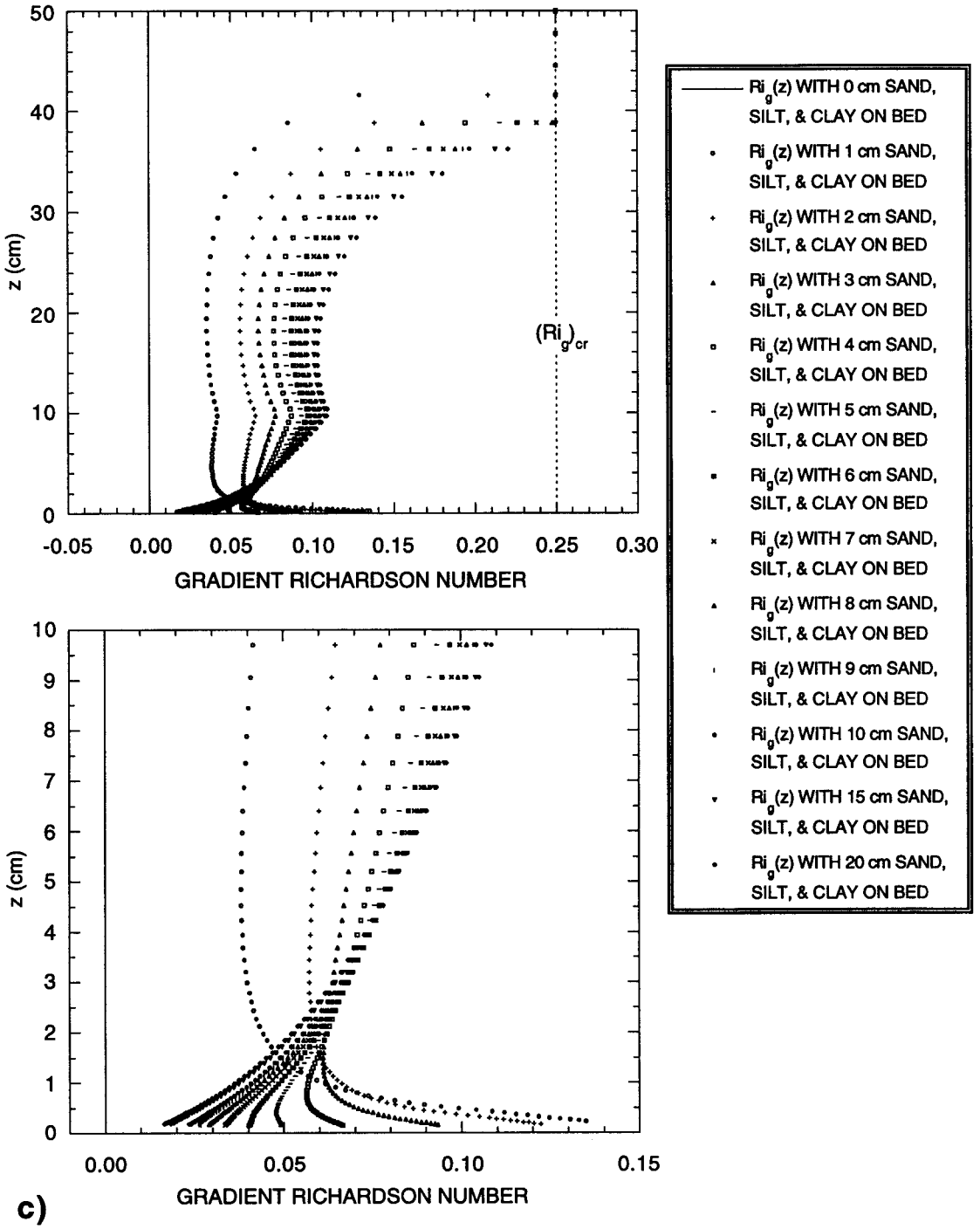

c)

Figure 3.15 (continued): (c) Modeled profiles of $\mathbf{Ri}_g(z)$ for various thicknesses of the sand, silt, and clay layer; the break in slope at z=10 cm is due to the $0.2h$ matching height in $L_f(z)$. The upper graph shows the profiles for the full 50 cm depth of the flow and the lower graph is an expanded view of the profiles in the lower 10 cm of the flow. Also shown is the value of the critical gradient Richardson number, 0.25, at which the turbulence is fully damped. Note how $\mathbf{Ri}_g(z)$=0 when the thickness of the sand, silt, and clay layer is equal to zero and no sediment is in suspension.

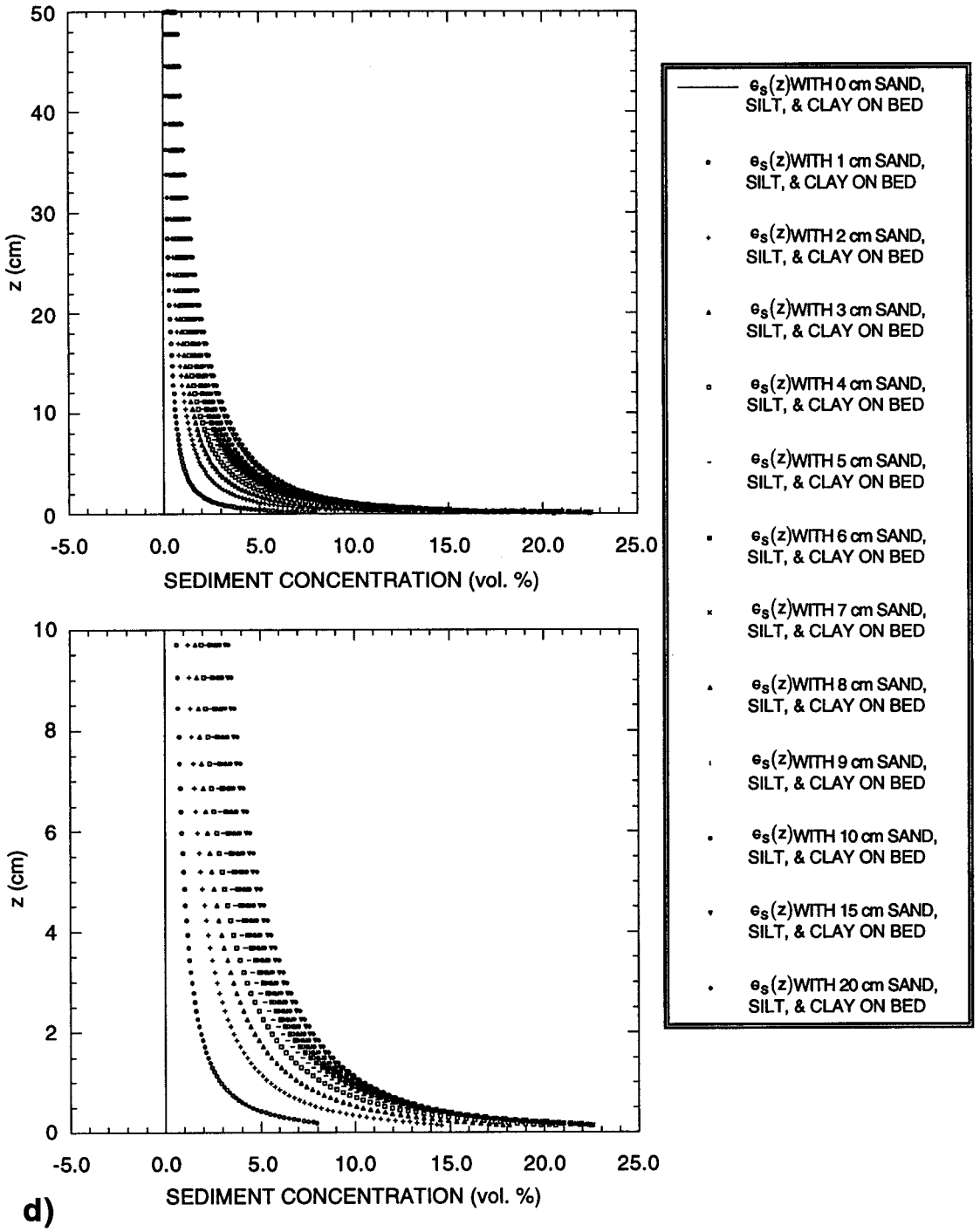

Figure 3.15 (continued): **(d)** Modeled profiles of $e_s(z)$ for various thicknesses of the sand, silt, and clay layer. The upper graph shows the profiles for the full 50 cm depth of the flow and the lower graph is an expanded view of the profiles in the lower 10 cm of the flow.

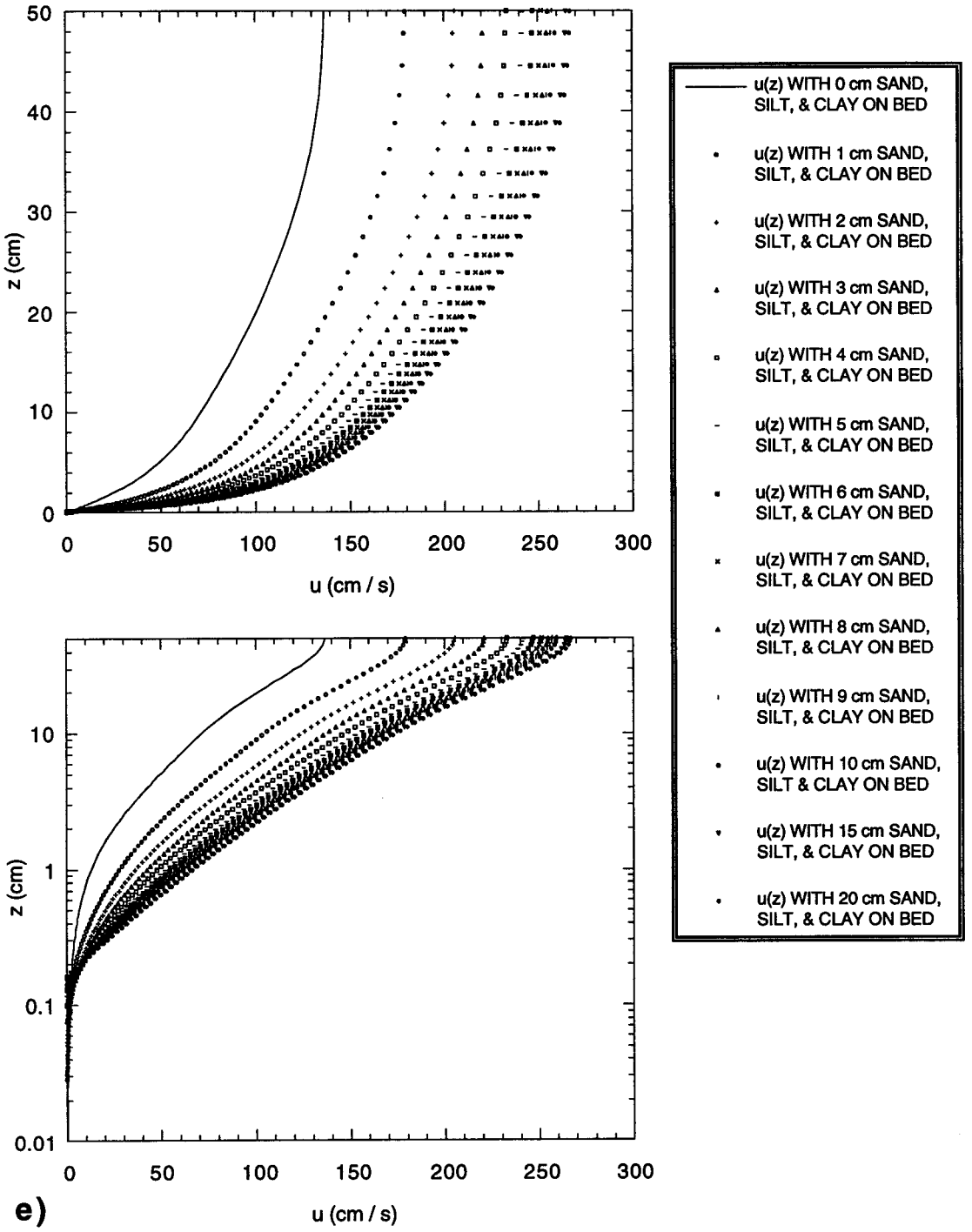

Figure 3.15 (continued): **(e)** Modeled profiles of $u(z)$ for various thicknesses of the sand, silt, and clay layer. Both graphs show the profiles for the full 50 cm depth of the flow; the upper graph is in linear space and the lower graph is in semi-log space. Note how the value of $(z_0)_{sf}$ increases as the sand, silt, and clay layer thickens and $(\epsilon_s)_{z_a}$ increases in Figure 3.15d .

The largest reduction in the skin-friction shear stress available to transport sediment is not predicted by the model to occur over a completely gravel bed, but over a gravel bed partially buried by finer sediment (Figure 3.15a). Since increasing the thickness of the sand, silt, and clay layer from 0 to 1 cm increases the area of the bed covered by sand, silt, and clay from 0% to about 50% (e.g., Figure 3.10), the greatest near-bed velocity, and, therefore, the greatest near-bed value of the gravel form-drag stress occurs when about 1 cm of sand, silt, and clay is partially burying the gravel.

Because of density stratification, the model predicts that, with increasing thickness of the sand, silt, and clay layer, the length scale of the turbulence in the interior of the flow will decrease to values much less than would be expected in a clear-water flow over a flat bed (Figure 3.15b). As the thickness of the sand, silt, and clay layer increases and more sediment is available to go into suspension, the density stratification builds in the interior of the flow, partially damping the turbulence. The degree to which the density stratification develops can be evaluated in Figure 3.15c. As the thickness of the sand, silt, and clay layer increases, the aerial coverage of sand, silt, and clay increases and the near-bed concentration of suspended sediment predicted by equation 3.90 increases. Thus, in response increasing amounts of sediment going into suspension, the gradient Richardson numbers near the bed decrease rapidly as the shear near the bed increases while the gradient Richardson numbers in the interior of the flow increase as the shear in the upper part of the flow decreases. The combined effects of the increased near-bed fluid stress, decreased turbulence length scale, and increasing density stratification with increasing thickness of the sand, silt, and clay layer on the suspended-sediment-concentration and velocity profiles are shown in Figures 3.15d and 3.15e.

Section 3.9: TESTS OF THE FLOW AND SEDIMENT-TRANSPORT MODEL AGAINST LABORATORY DATA

The experiments of Kennedy (1961) and Guy and others (1966) are ideal for testing the flow and sediment transport model since they cover an extremely wide range of flow and sediment-transport conditions. Therefore, all of the laboratory flume runs of Kennedy (1961) and the flume runs of Guy and others (1966) where D_{50} of the bed material equaled 0.019, 0.027, 0.028, 0.032, 0.033, 0.045, and 0.093 cm were used to test the model.[6] Flow conditions in these experiments ranged from subcritical flow over lower-plane bed, ripples, dunes, and upper-plane bed to supercritical flow over antidunes; sediment transport

[6]The graded-bed runs and the runs with added clay of Guy and others (1966) were not used in the comparison.

conditions ranged from dominantly bedload transport over lower-plane bed, ripples, and dunes, to dominantly suspended-load transport over upper-plane bed and antidunes.

For each flume run, nine size classes of sediment were chosen to model the bed, and the initial bed grain-size distribution was taken as the reported measured grain-size distribution. As in the case of the Paria River, the grain-size distribution of the bed for each modeled experimental run was allowed to evolve by forcing the local conservation of mass of each size-class m using equation 3.26 and an initial sediment thickness, T_{s0}, on the floor of the flume of 20 cm; this approximate thickness of the sediment layer was determined from published photographs of the flume experiments. For each flume run, the initial flow depth was chosen such that the water depth for the converged solution with sediment in suspension would match the reported mean flow depth.

Model predictions were compared to measurements of: total load (i.e., suspended-load plus bedload) concentration; D_{50} of the total load; the sorting of the total load; the depth-integrated suspended load concentration; D_{50} of the suspended load; the mean velocity (Figures 3.16 and 3.17). The modeled depth-integrated suspended-load concentration, $\langle \bar{e}_s \rangle$, is defined as:

$$\langle \bar{e}_s \rangle = \frac{1}{h} \int_{z_a}^{h} \bar{e}_s dz, \tag{3.112}$$

and the modeled total-load concentration is defined as the total sediment discharge from equation 3.111 divided by the fluid discharge from equation 3.110. Sorting of the total load, σ_S, is defined as:

$$\sigma_s = \frac{1}{2}\left(\frac{D_{50}}{D_{16}} + \frac{D_{84}}{D_{50}}\right). \tag{3.113}$$

The model does best in predicting total load (Figure 3.16a). The model also does reasonably well for predicting the grain-size distribution of the total load (Figure 3.16b and Figure 3.16c). Most of the disagreement between the model predictions and measurements of the total-load D_{50} and sorting is the result of the Guy and others (1966) experiments that used the coarsest two (i.e., the D_{50} = 0.45 and 0.93 mm) sediment-size distributions in the 8-foot-wide flume. The model-predicted sorting of the total load is still quite good, if these two sets of experiments are excluded from the comparison. Data from these two sets of experiments are much more internally inconsistent than data from the other experiments (Figures 3.17h and 3.17i); thus, exclusion of these two sets of experiments from the comparison can be justified.

In addition to measuring the total load leaving the flume, Guy and others (1966) measured the depth-integrated suspended load concentration at various stations in the flume

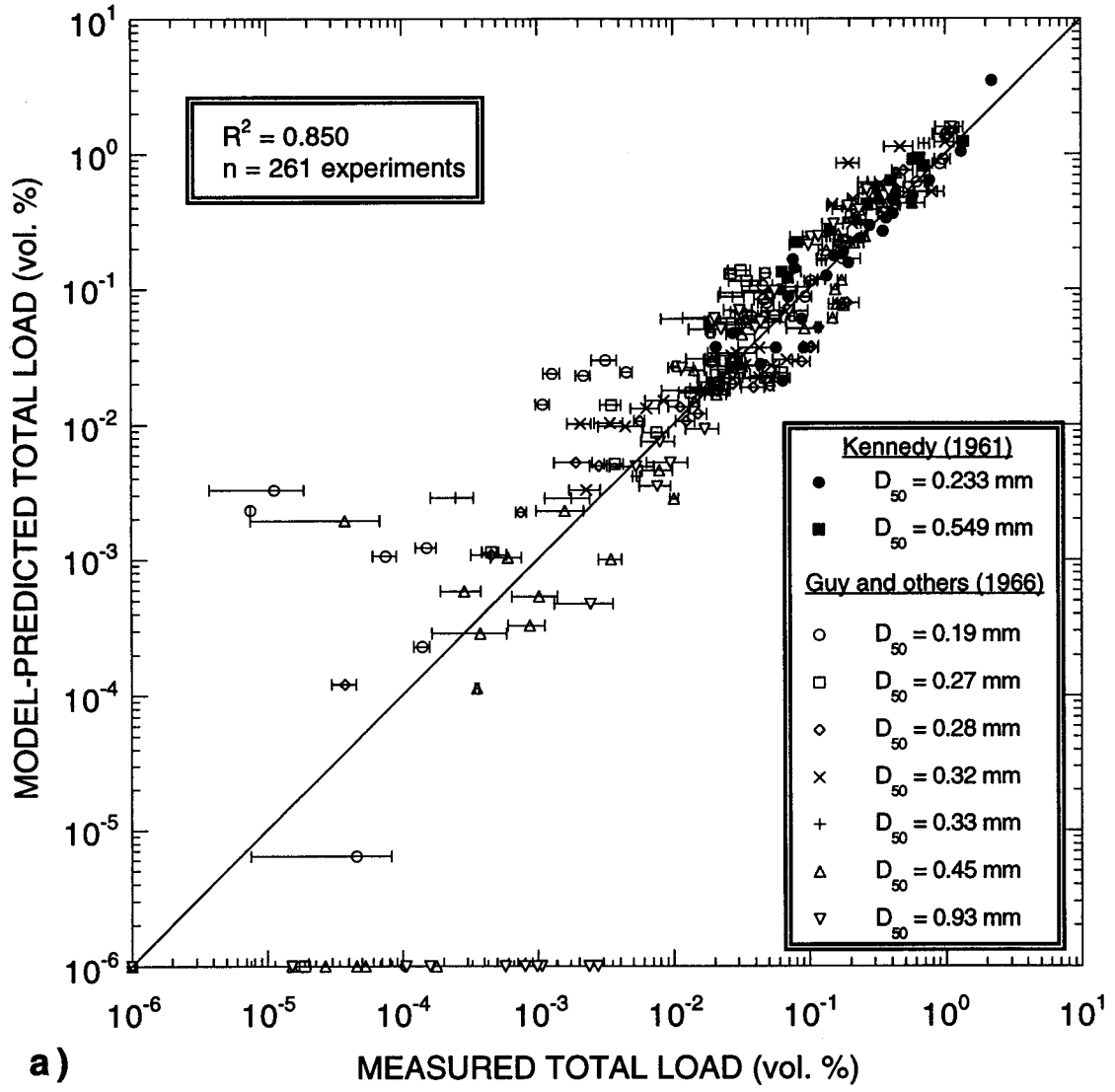

Figure 3.16: **(a)** Model-predicted vs. measured total-load concentration for the Kennedy (1961) and Guy and others (1966) experiments; values appearing on either the x- or y-axis are zero values. Error bars for plus and minus one standard deviation of the measurements of Guy and others (1966) appear in this figure; no error bars are associated with the measurements of Kennedy (1961) since he did not report measurement error. R^2 value is that calculated for the line of perfect agreement between the model predictions and the measurements.

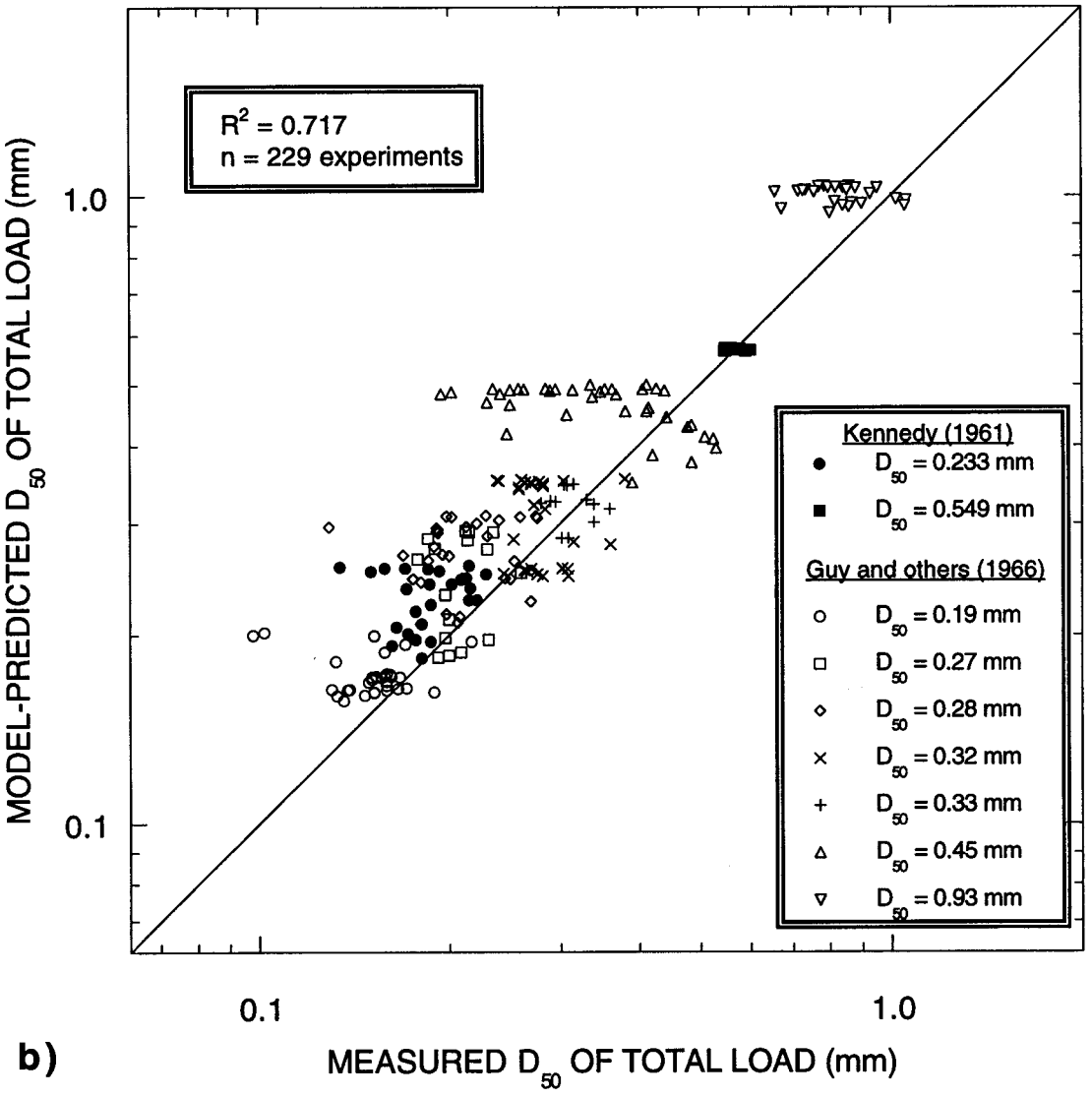

b)

Figure 3.16 (continued): (b) Model-predicted vs. measured D_{50} of the total load for the Kennedy (1961) and Guy and others (1966) experiments. R^2 value is that calculated for the line of perfect agreement between the model predictions and the measurements.

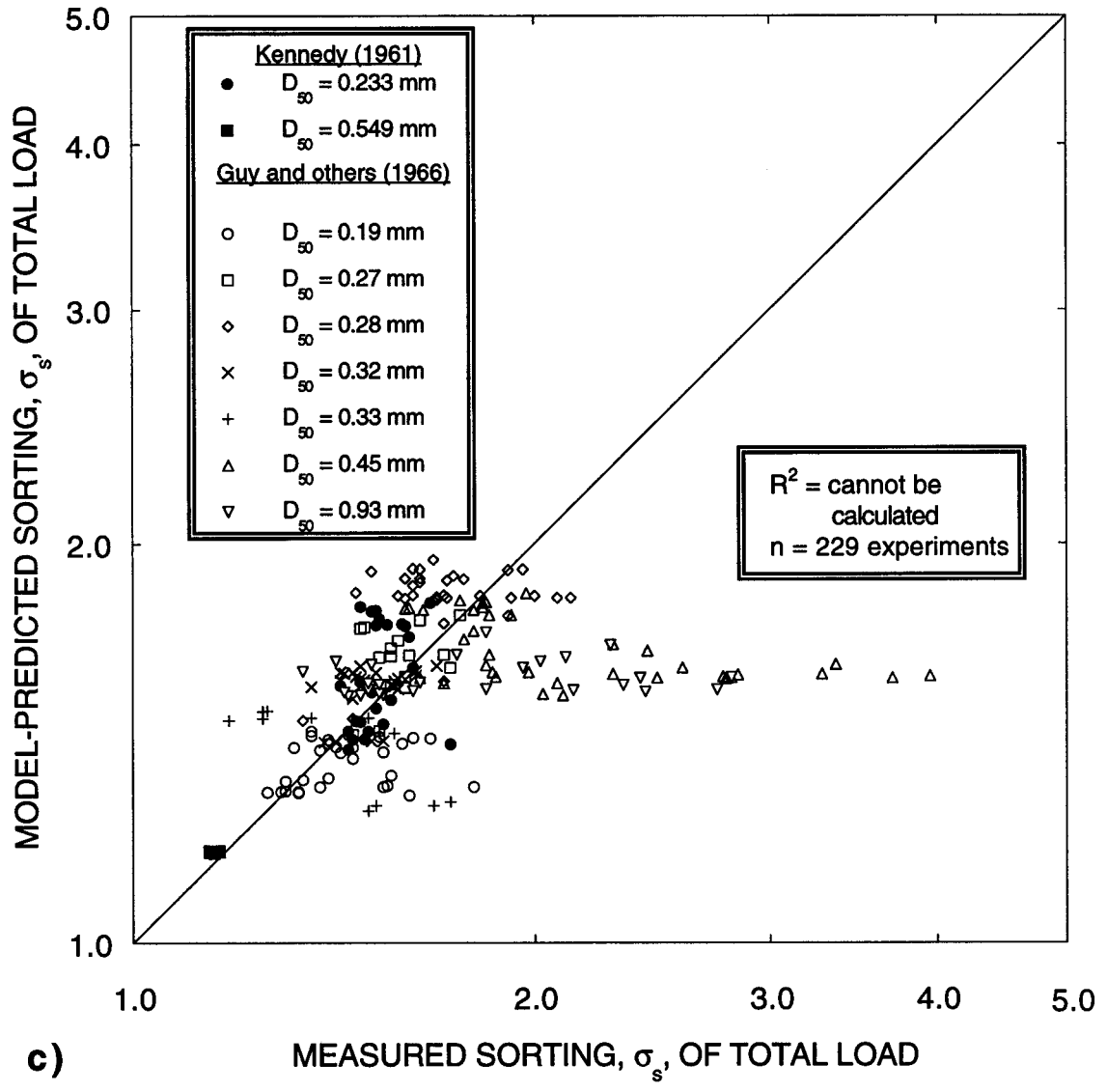

Figure 3.16 (continued): (c) Model-predicted vs. measured sorting of the total load for the Kennedy (1961) and Guy and others (1966) experiments. Because the residual sum of squares was larger than the total sum of squares, the R^2 value for the line of perfect agreement between the model predictions and the measurements could not be calculated.

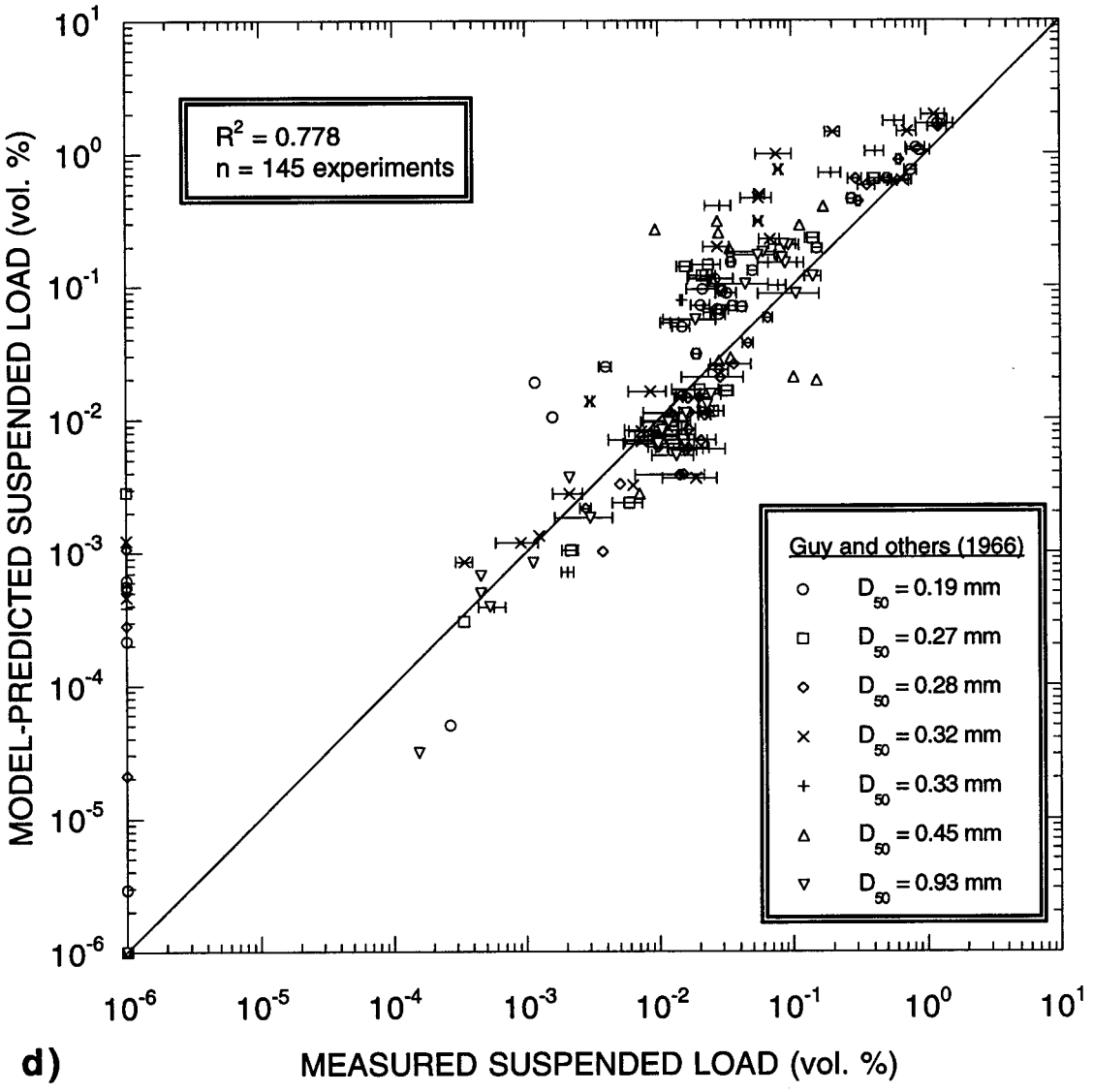

d)

Figure 3.16 (continued) (d) Model-predicted vs. measured suspended-load concentration for the Guy and others (1966) experiments; values appearing on either the x- or y-axis are zero values. Error bars for plus and minus one standard deviation of the measurements of Guy and others (1966) appear in this figure; no error bars are associated with the measurements of Kennedy (1961) since he did not report measurement error. R^2 value is that calculated for the line of perfect agreement between the model predictions and the measurements.

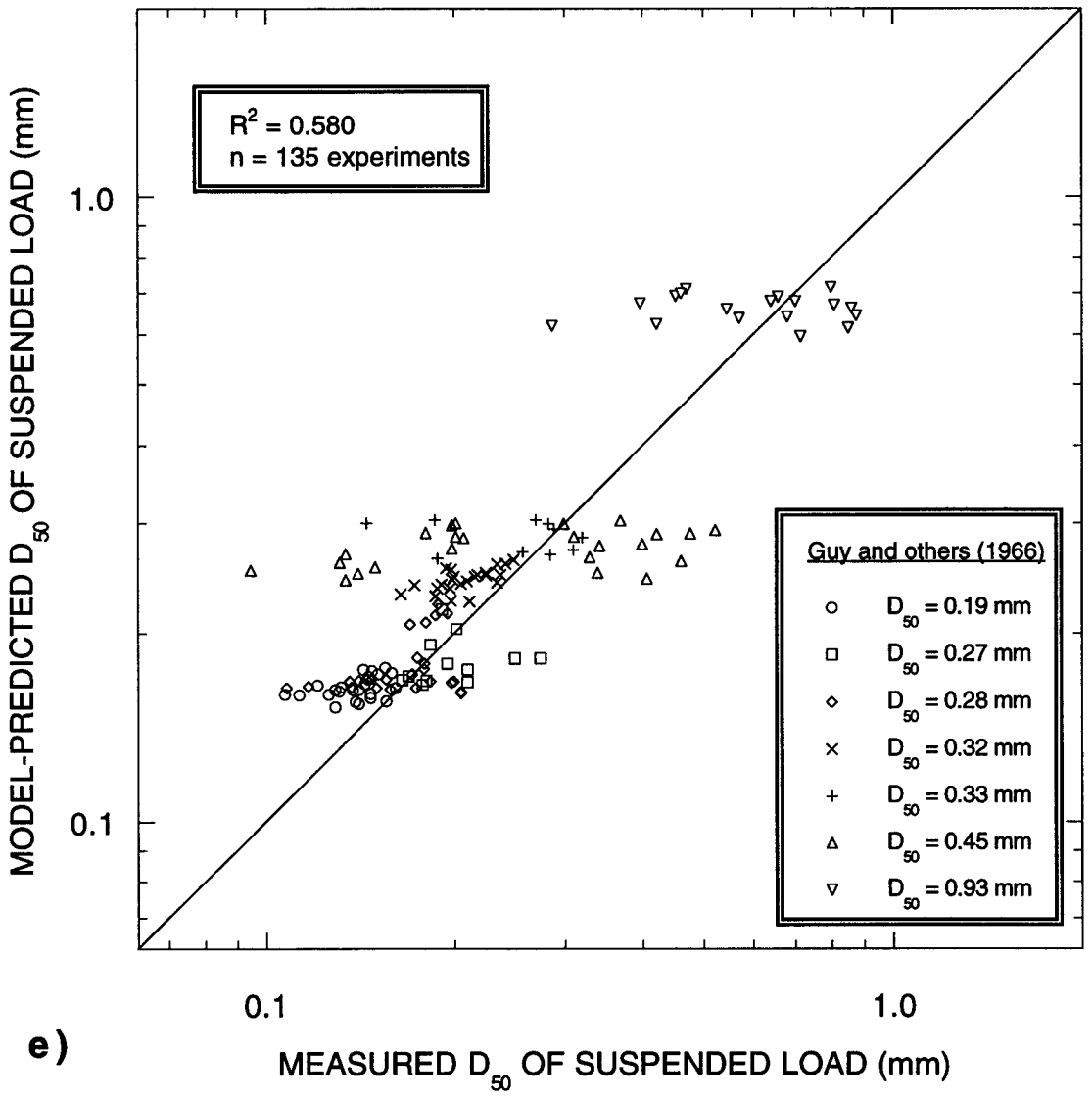

Figure 3.16 (continued): **(e)** Model-predicted vs. measured D50 of the suspended load for the Guy and others (1966) experiments. R^2 value is that calculated for the line of perfect agreement between the model predictions and the measurements.

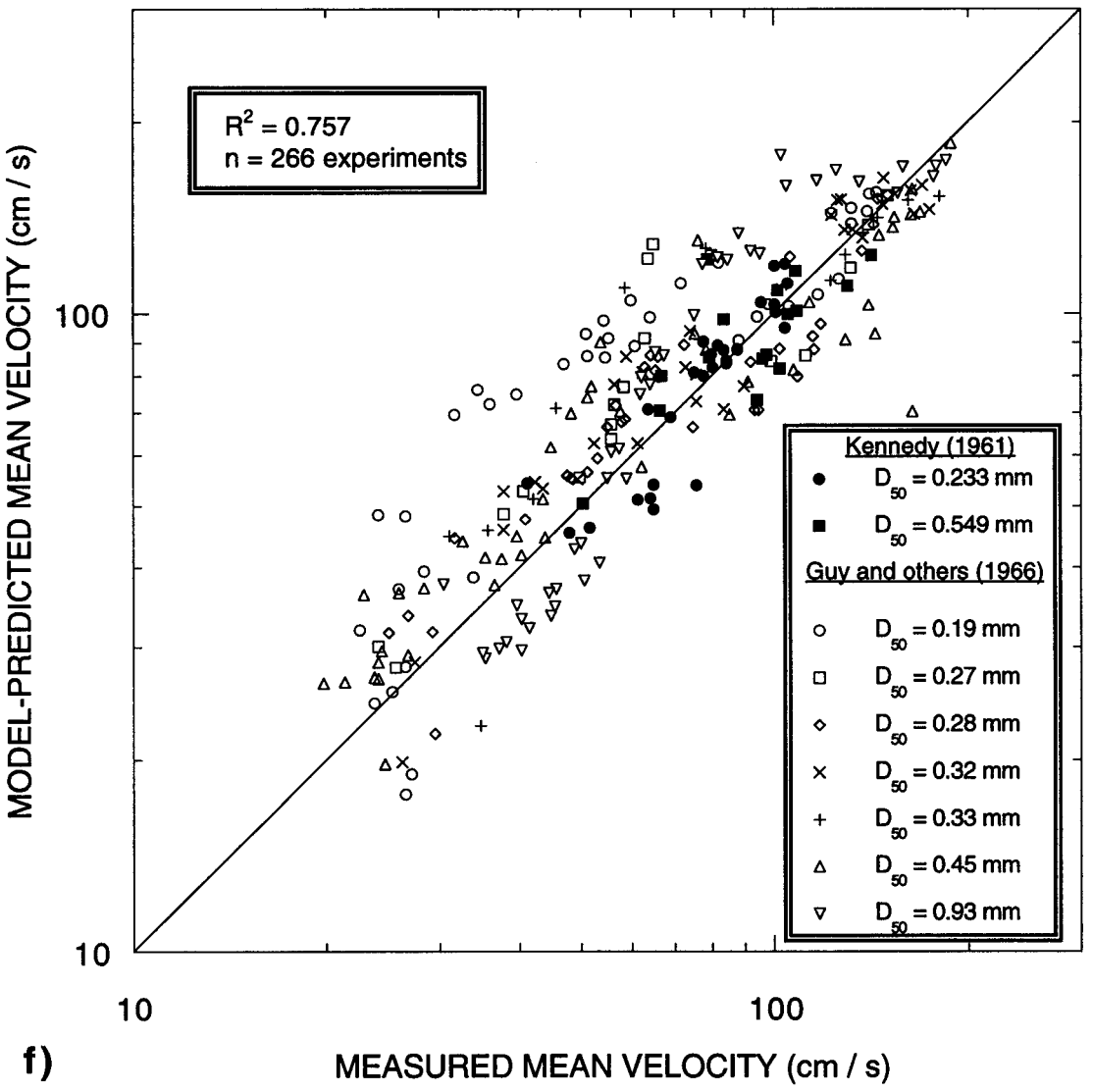

Figure 3.16 (continued): **(f)** Model-predicted vs. measured mean velocity for the Guy and others (1966) experiments. R^2 value is that calculated for the line of perfect agreement between the model predictions and the measurements.

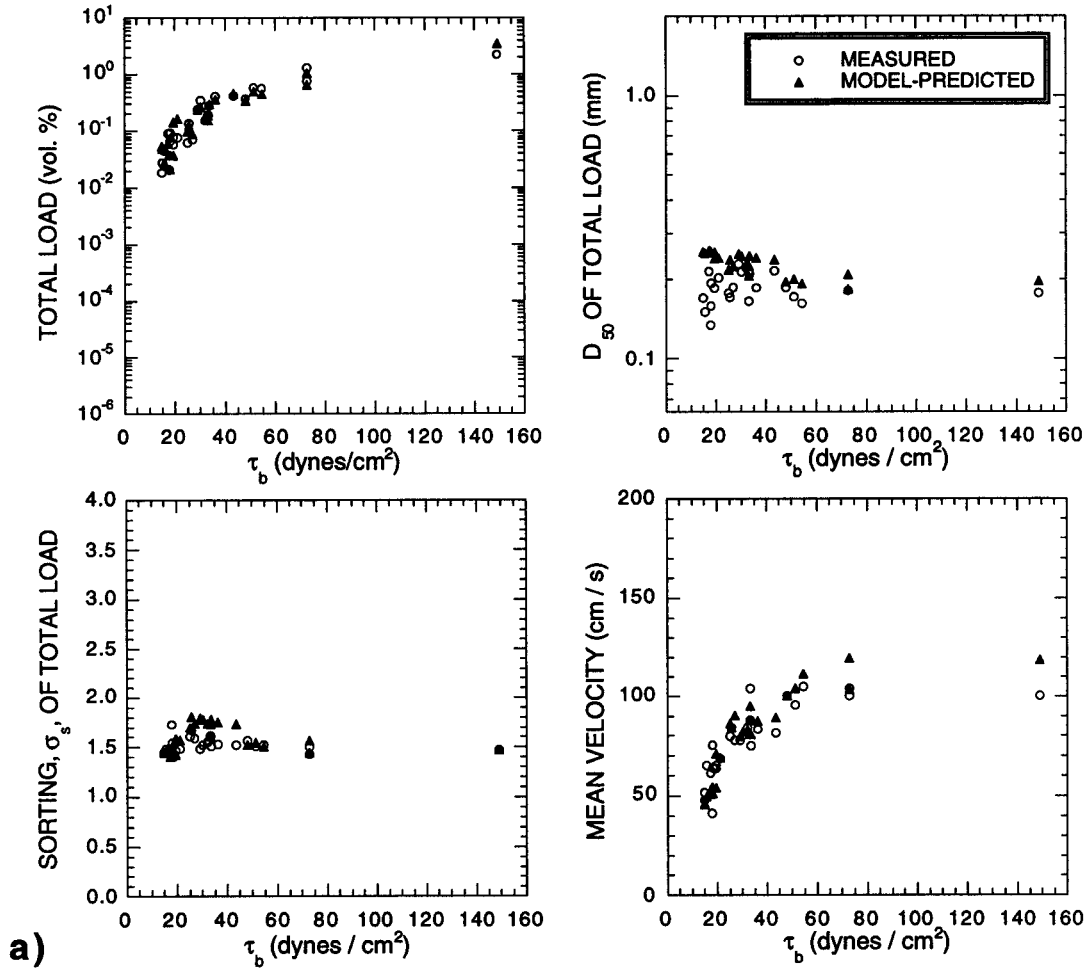

Figure 3.17: (a) Measured and model-predicted total-load concentration, D_{50} of the total load, sorting of the total load, and mean velocity as functions of the total boundary shear stress for the D_{50} = 0.233 mm experiments of Kennedy (1961).[7]

---

[7]In Figure 3.17, for each value of the total boundary shear stress, the range of measured and predicted values results from the range of flow depths and water temperatures used in the experiments. For example, for two flows of different depths with the same total boundary shear stress, the mean suspended-sediment concentration in a deeper flow will be less than that in a shallower flow.

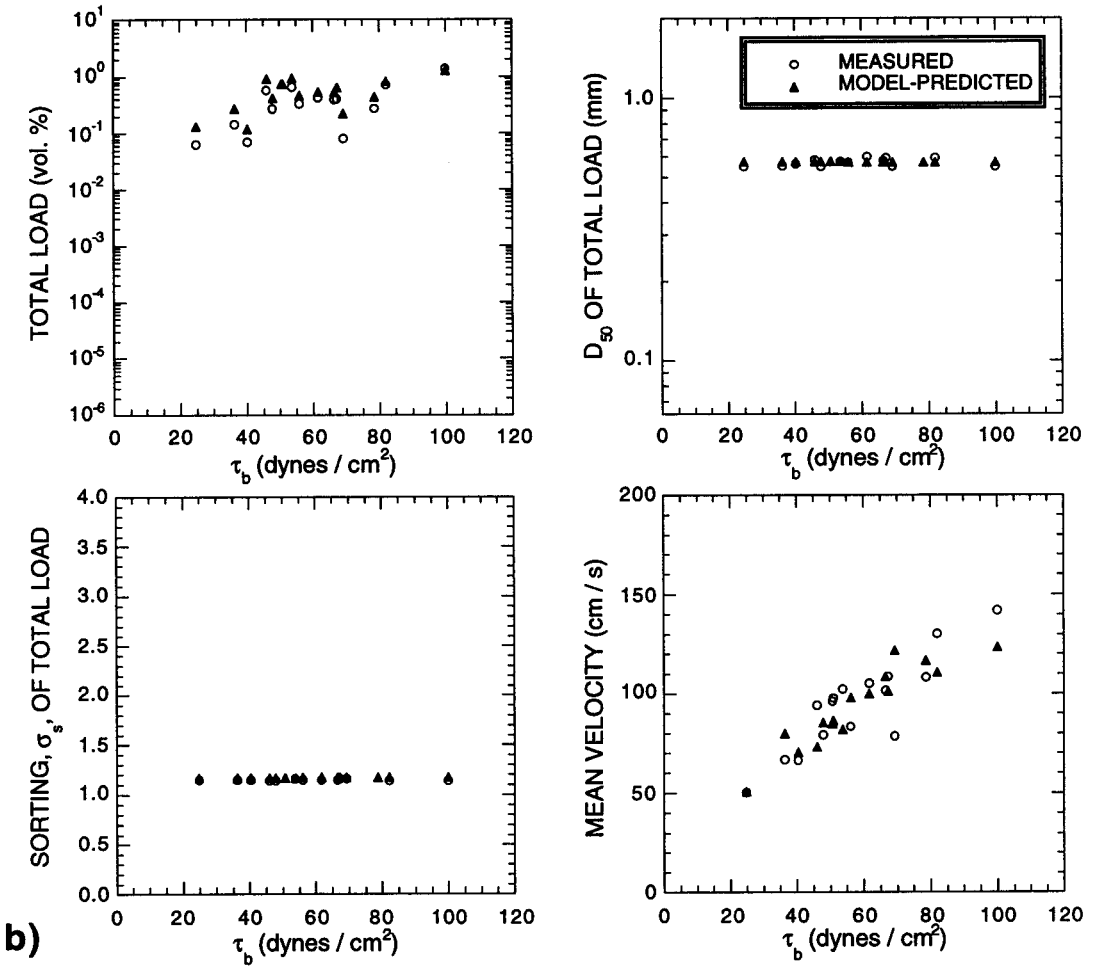

Figure 3.17 (continued): **(b)** Measured and model-predicted total-load concentration, D_{50} of the total load, sorting of the total load, and mean velocity as functions of the total boundary shear stress for the D_{50} = 0.549 mm experiments of Kennedy (1961).

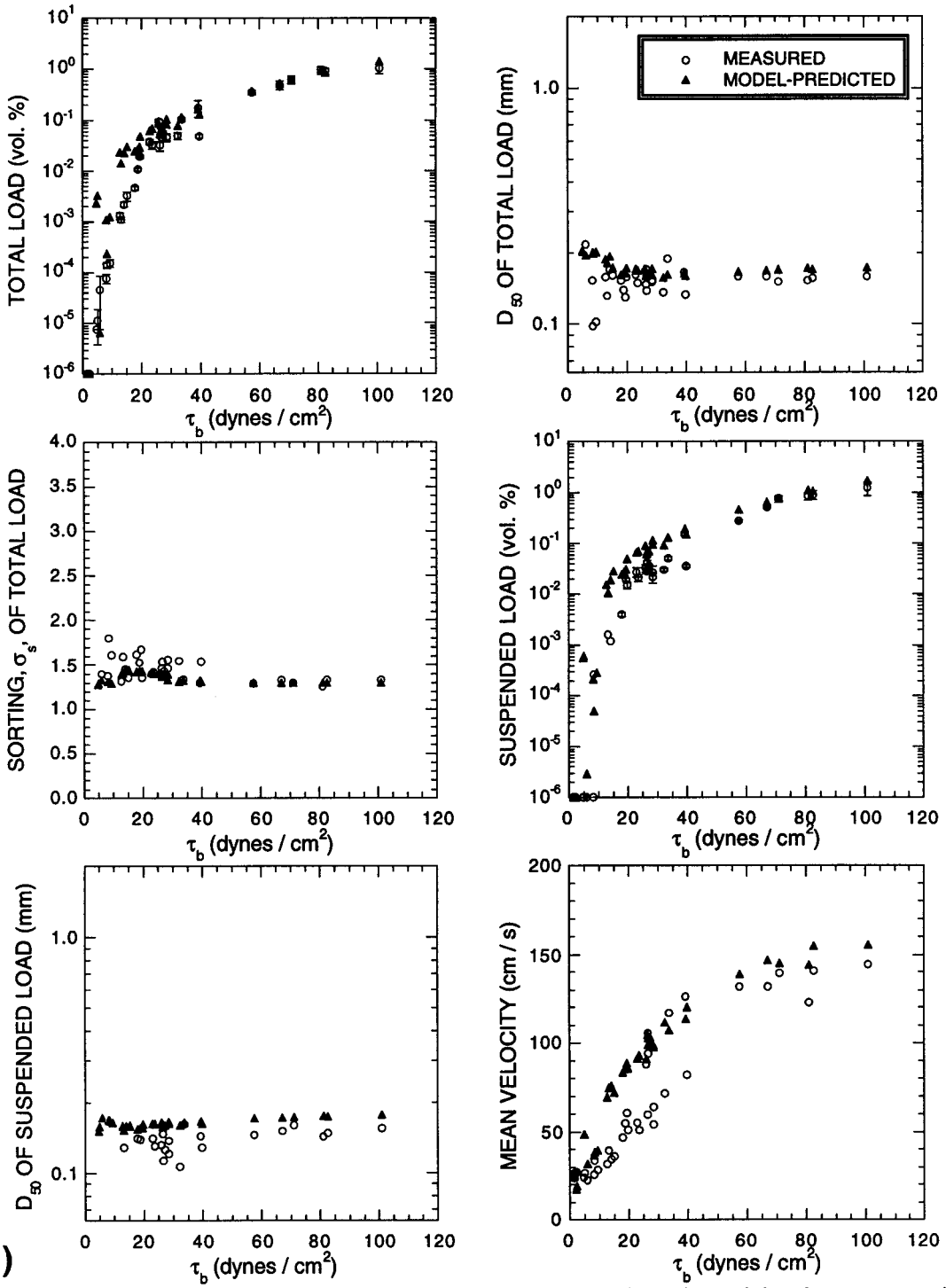

c)

Figure 3.17 (continued): (c) Measured and model-predicted total-load concentration, D_{50} of the total load, sorting of the total load, suspended-load concentration, D_{50} of the suspended load, and mean velocity as functions of the total boundary shear stress for the D_{50} = 0.19 mm experiments of Guy and others (1966). Error bars are plus and minus one standard deviation.

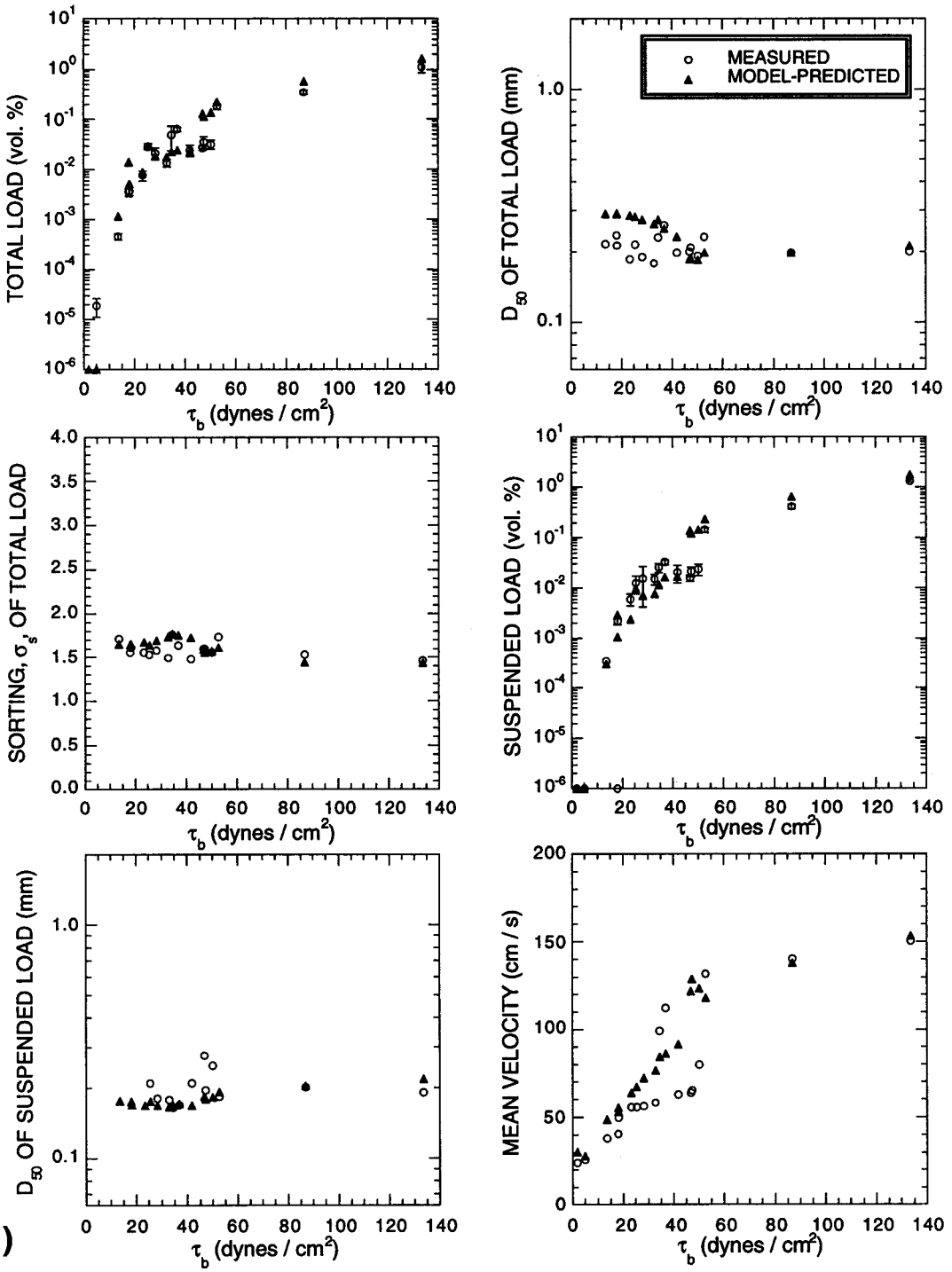

Figure 3.17 (continued): **(d)** Measured and model-predicted total-load concentration, D_{50} of the total load, sorting of the total load, suspended-load concentration, D_{50} of the suspended load, and mean velocity as functions of the total boundary shear stress for the D_{50} = 0.27 mm experiments of Guy and others (1966). Error bars are plus and minus one standard deviation.

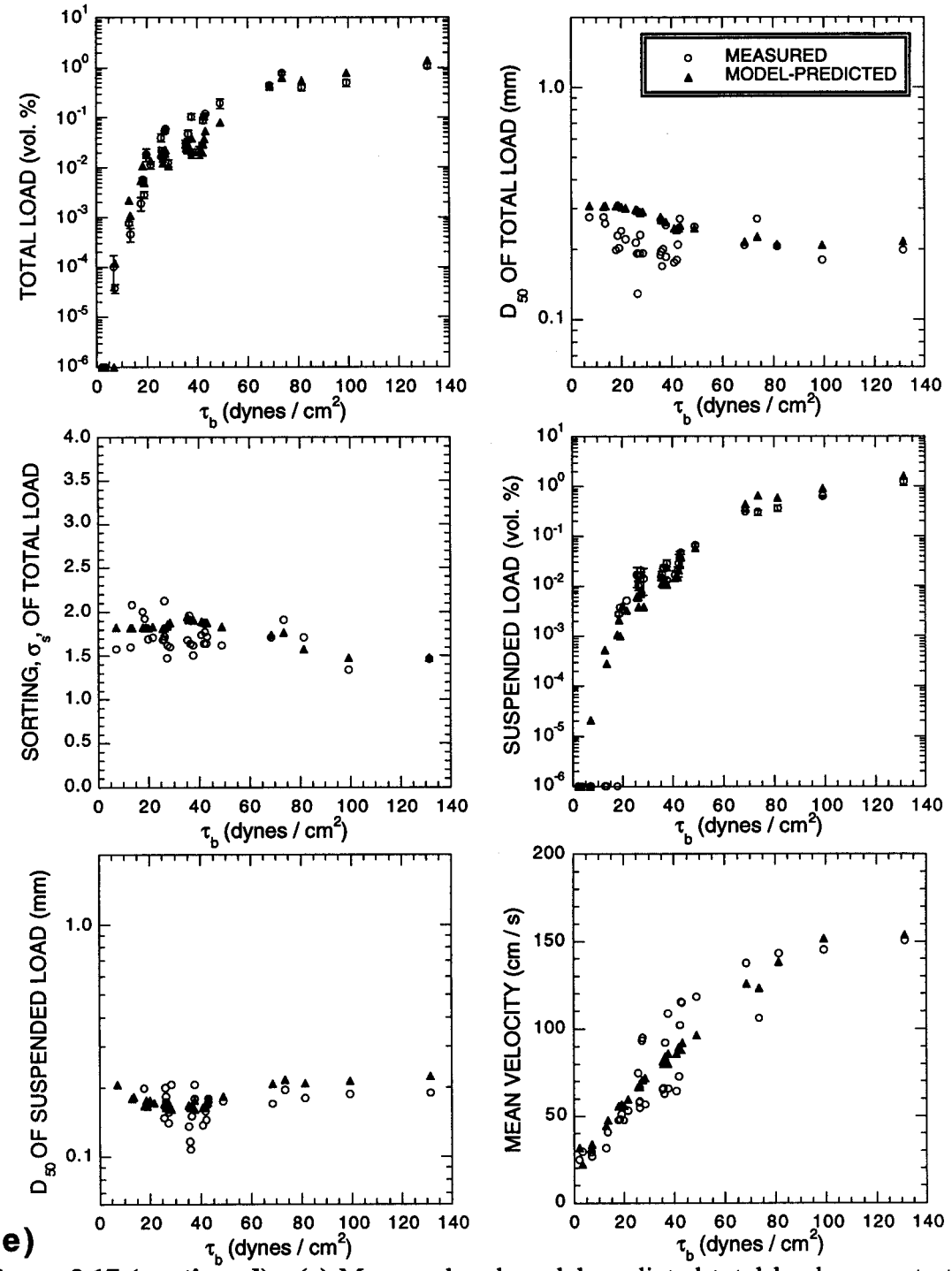

Figure 3.17 (continued): (e) Measured and model-predicted total-load concentration, D_{50} of the total load, sorting of the total load, suspended-load concentration, D_{50} of the suspended load, and mean velocity as functions of the total boundary shear stress for the D_{50} = 0.28 mm experiments of Guy and others (1966). Error bars are plus and minus one standard deviation.

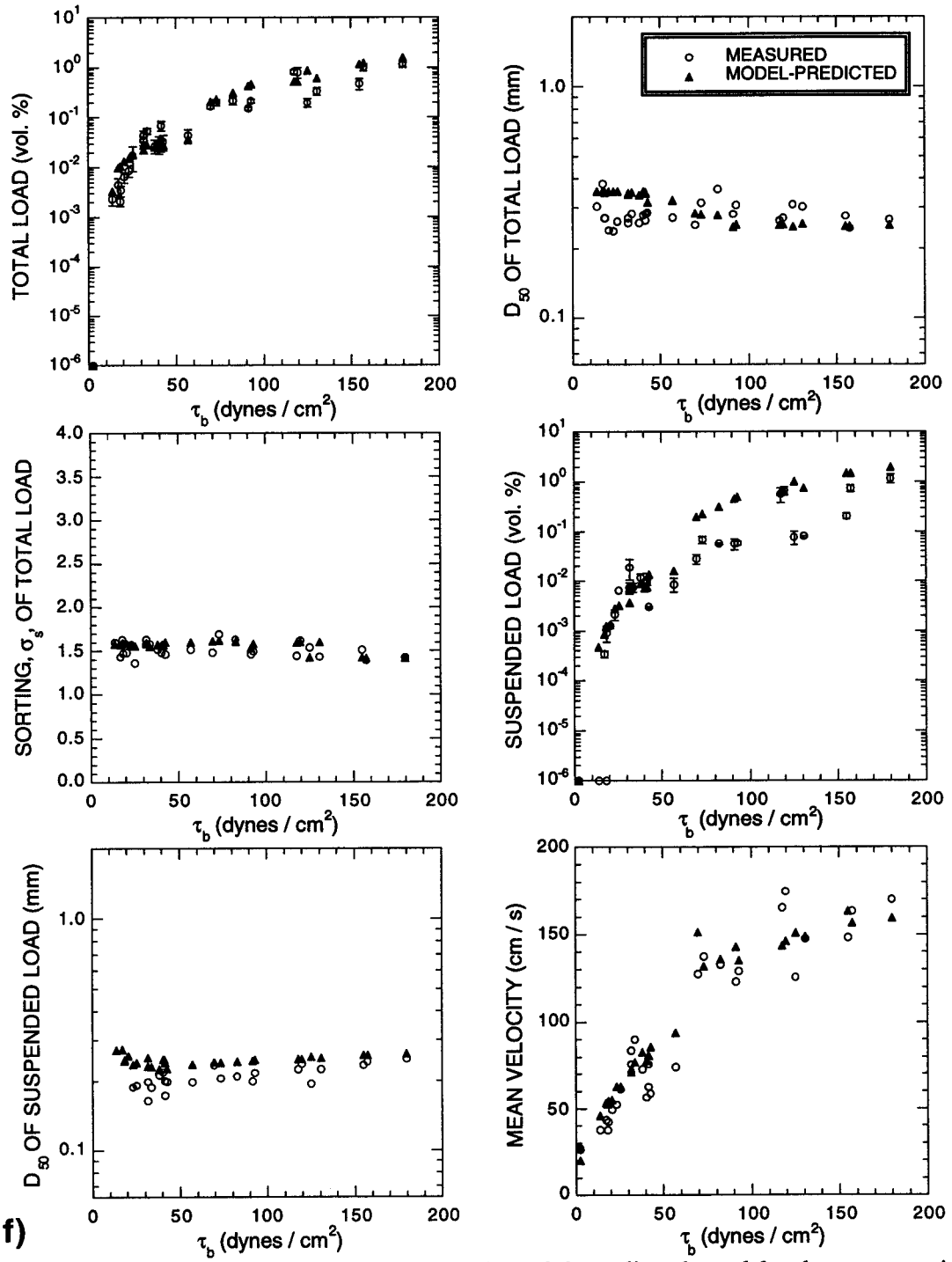

Figure 3.17 (continued): **(f)** Measured and model-predicted total-load concentration, D_{50} of the total load, sorting of the total load, suspended-load concentration, D_{50} of the suspended load, and mean velocity as functions of the total boundary shear stress for the D_{50} = 0.32 mm experiments of Guy and others (1966). Error bars are plus and minus one standard deviation.

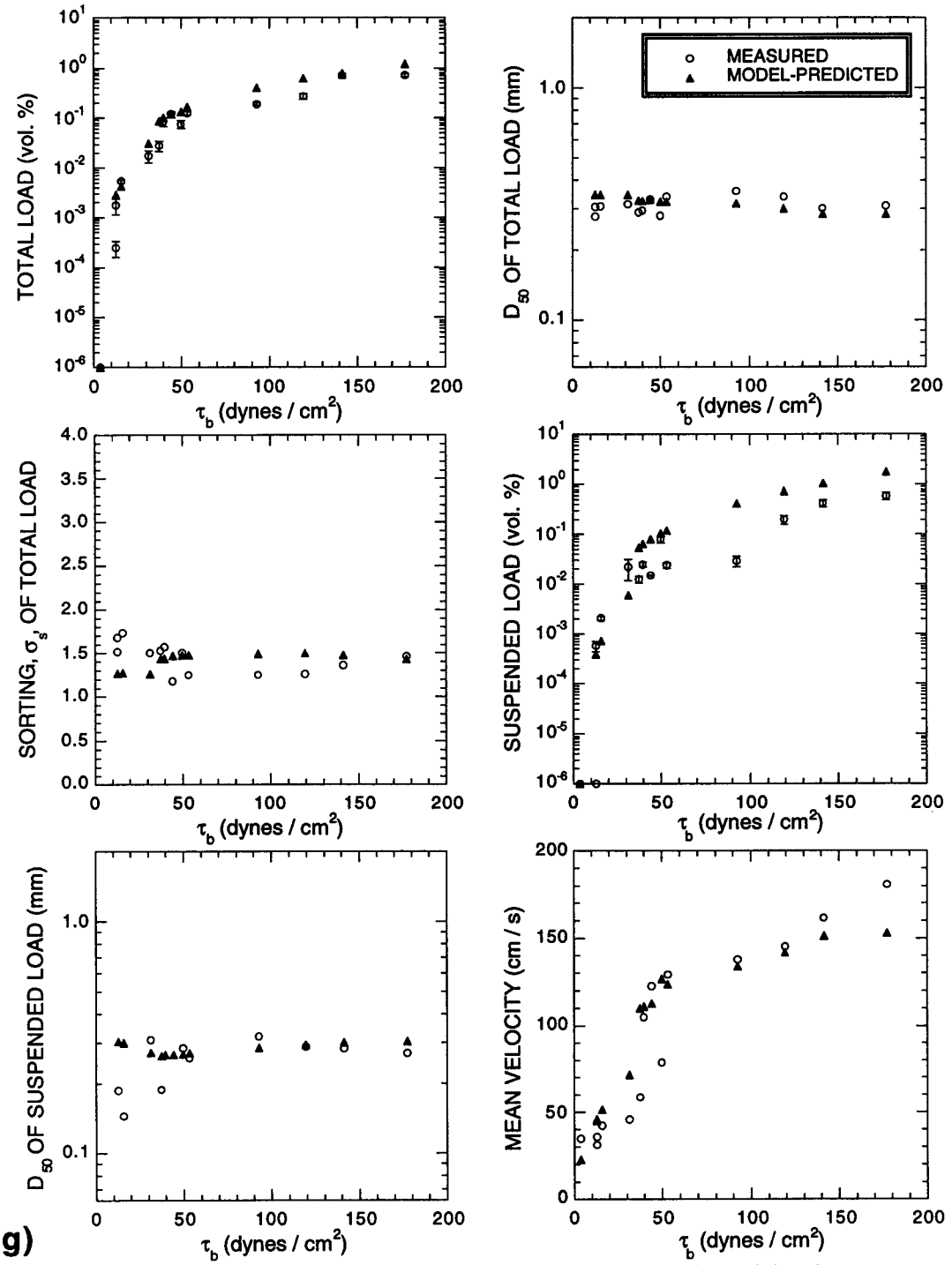

g)

Figure 3.17 (continued): **(g)** Measured and model-predicted total-load concentration, D_{50} of the total load, sorting of the total load, suspended-load concentration, D_{50} of the suspended load, and mean velocity as functions of the total boundary shear stress for the D_{50} = 0.33 mm experiments of Guy and others (1966). Error bars are plus and minus one standard deviation.

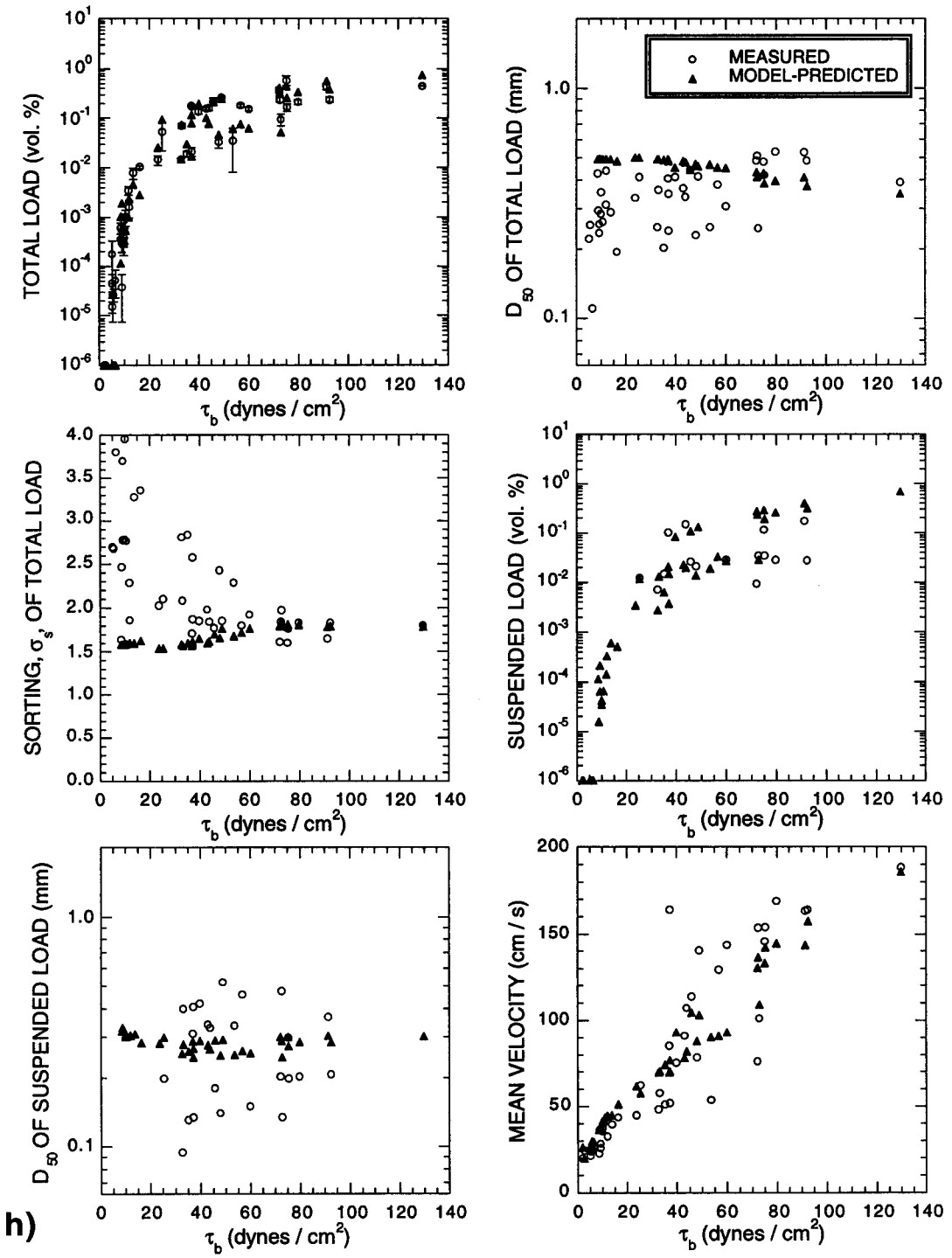

Figure 3.17 (continued): (h) Measured and model-predicted total-load concentration, D_{50} of the total load, sorting of the total load, suspended-load concentration, D_{50} of the suspended load, and mean velocity as functions of the total boundary shear stress for the D_{50} = 0.45 mm experiments of Guy and others (1966). Error bars are plus and minus one standard deviation.

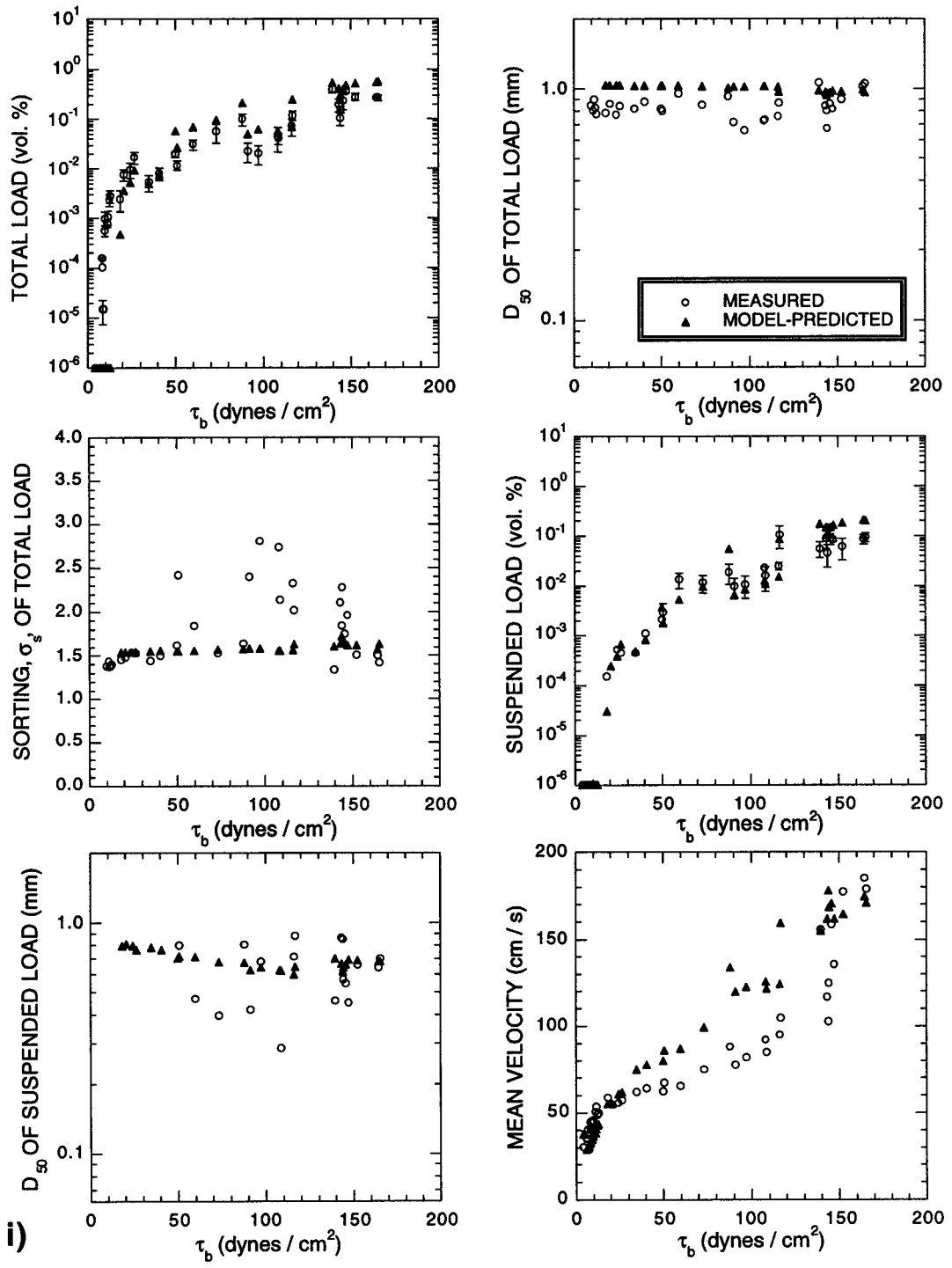

Figure 3.17 (continued): **(i)** Measured and model-predicted total-load concentration, D_{50} of the total load, sorting of the total load, suspended-load concentration, D_{50} of the suspended load, and mean velocity as functions of the total boundary shear stress for the D_{50} = 0.93 mm experiments of Guy and others (1966). Error bars are plus and minus one standard deviation.

with a pumping sampler. The slight tendency of the model to overpredict the suspended-load concentrations in Figure 3.16d is interpreted to arise from the difference in theoretical and measurable suspended load. Unlike total load, which is relatively easy to measure as it leaves the flume, suspended load, as it is defined theoretically (e.g., equation 3.112), is difficult to measure. The model, therefore, systematically predicts sediment to be in suspension for flume runs in which Guy and others (1966) measured no suspended load because their pumping sampler could not measure to the top of the saltation layer.

The model does reasonably well in predicting mean velocity for all 266 experiments (Figure 3.16f). As expected, since the effect of flume sidewall drag was not treated in the model, the model slightly overpredicts the measured mean velocity determined by dividing measured discharge by cross-section area of the flow in the flume.

Section 3.10: TEST OF THE FLOW AND SEDIMENT-TRANSPORT MODEL AGAINST DATA FROM THE RIO PUERCO

Since the model predictions favorably compare with the wide range of flow and sediment-transport conditions in the laboratory experiments of Kennedy (1961) and Guy and others (1966), the model was further tested against data that Nordin (1963) collected during flood on September 20, 1961 on the Rio Puerco near Bernardo, NM. Nordin's data set is unique in that it is the highest-sediment-concentration (i.e., 11% by volume) set of suspended-sediment-concentration and velocity measurements made in a natural river for which both: vertical profiles of sediment concentration by size class, and vertical profiles of velocity were measured. Furthermore, since the channel of the Rio Puerco in the Bernardo study reach during the measurements of September 20, 1961 was similar to the morphology of the equilibrium channel of the Paria River in the Lees Ferry study area, this data set should provide the best possible test of the model against data from a river.

For this comparison, the velocity and suspended-sediment data that were collected near the flat-bottomed, center portion of the river channel at stations 170 and 185 of Nordin (1963) have been combined in Figure 3.18. The measured water surface slope (0.00148), flow-depths (1.13 m for the velocity measurements and 1.02 m for the suspended-sediment measurements), water temperature (17.2°C), average bed grain-size distribution as measured during the flow (see Table 4 of Nordin (1963)), and the average D_{50} of the bed surface as measured during the flow (approximately 0.025 cm from Figure 16 of Nordin (1963)) were used as input into the model. Since Nordin measured the bed grain-size distribution during the flow event, it was not necessary to calculate the bed grain-size distribution by forcing local conservation of mass of each sediment size class in the bed.

Nordin (1963) measured the grain-size distribution of the bed material at 1ϕ increments, a size increment too coarse for suspended-sediment modeling; thus, for the purposes of modeling, the amount of sediment in each 1ϕ interval was subdivided into equal amounts of the finest grain size in each 1/2ϕ portion of the 1ϕ interval. For example, half of the measured amount of sediment in the 0.0625 to 0.125 mm size class was assumed to be composed of 0.0625 mm sediment and half was assumed to be composed of 0.088 mm sediment. Finally, since the silt and clay fraction would be in a flocculated state in the river and the grain-size distribution of the silt and clay fraction was only analyzed in a deflocculated state, the measured D_{50} of the Paria River silt and clay fraction (see Figure 3.4) was used to approximate the D_{50} of the flocculated Rio Puerco silt and clay.

The modeled and measured suspended-sediment size-class concentration profiles and velocity profile appear in Figure 3.18 both with and without: the density and viscosity correction from equations 3.86 and 3.87; and the density stratification correction. Inclusion of these two effects greatly improves the agreement between the model-predicted and measured velocity profiles and suspended-sediment concentration profiles. The density stratification correction preferentially has the largest impact on the coarsest sediment in suspension; it has no effect on the wash-load concentration profile, it improves the agreement between the model and the 0.0625-0.125 mm and 0.125-0.25 mm size-class concentration profiles. Inclusion of the density stratification correction also improves the agreement between the model and 0.25-0.50 mm size-class concentration profile at station 170, but not at station 185, possibly because of the reported presence of violent antidunes at station 185 (Nordin, 1963). The effect of density stratification on the structure of the turbulence results in increased velocities in the upper part of the flow; and, inclusion of the density stratification correction results in much better agreement between the model predicted velocity profile and the measured velocity profile in Figure 3.18b. In this case, exclusion of the effects of density stratification would lead to a 20% underprediction of the surface velocity of the flow.

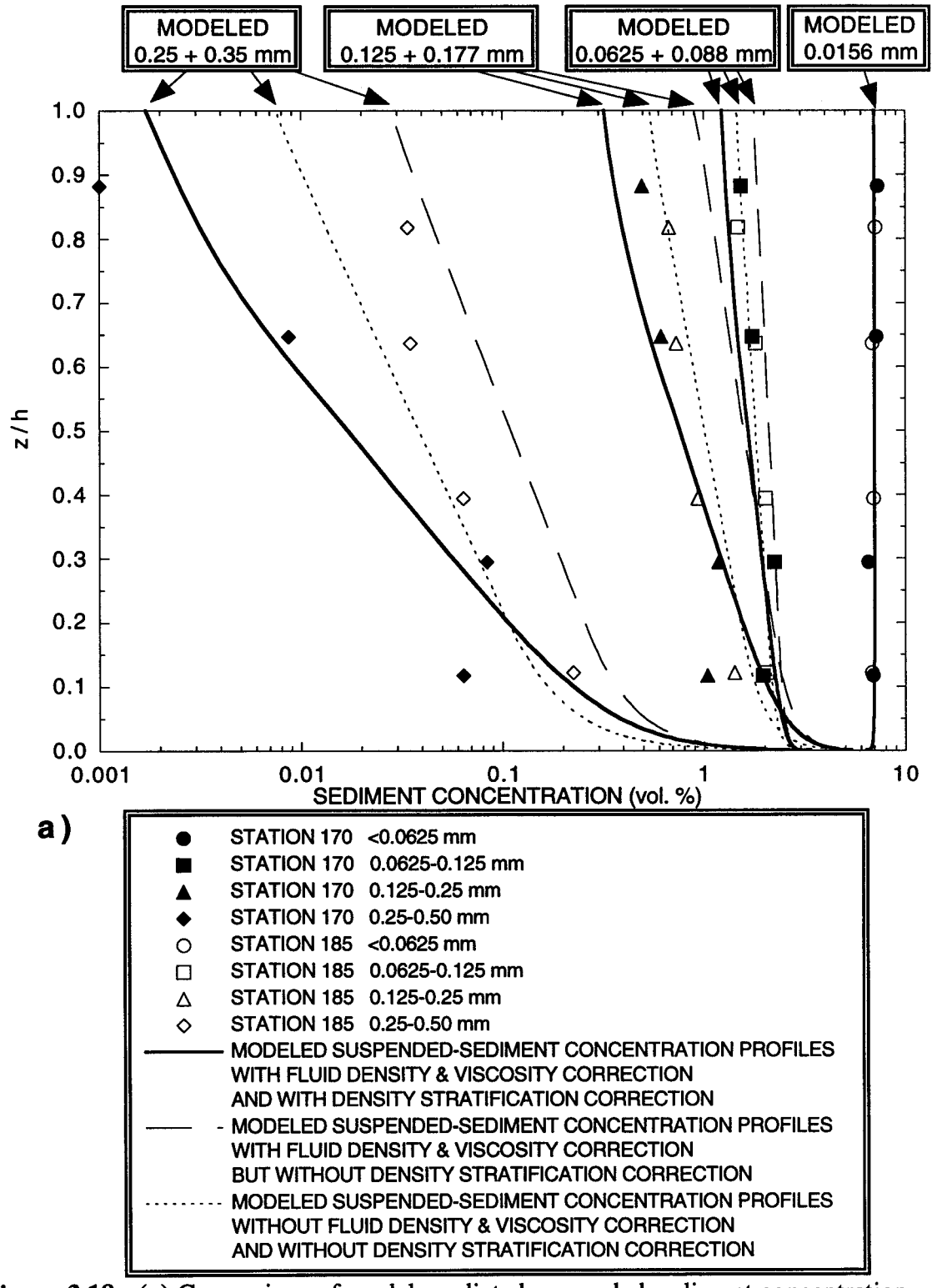

Figure 3.18: **(a)** Comparison of model-predicted suspended-sediment concentration profiles with the suspended-sediment concentration profiles measured by Nordin (1963) in the Rio Puerco near Bernardo, NM on September 20, 1961. The point plotted on the y-axis is a zero concentration measurement.

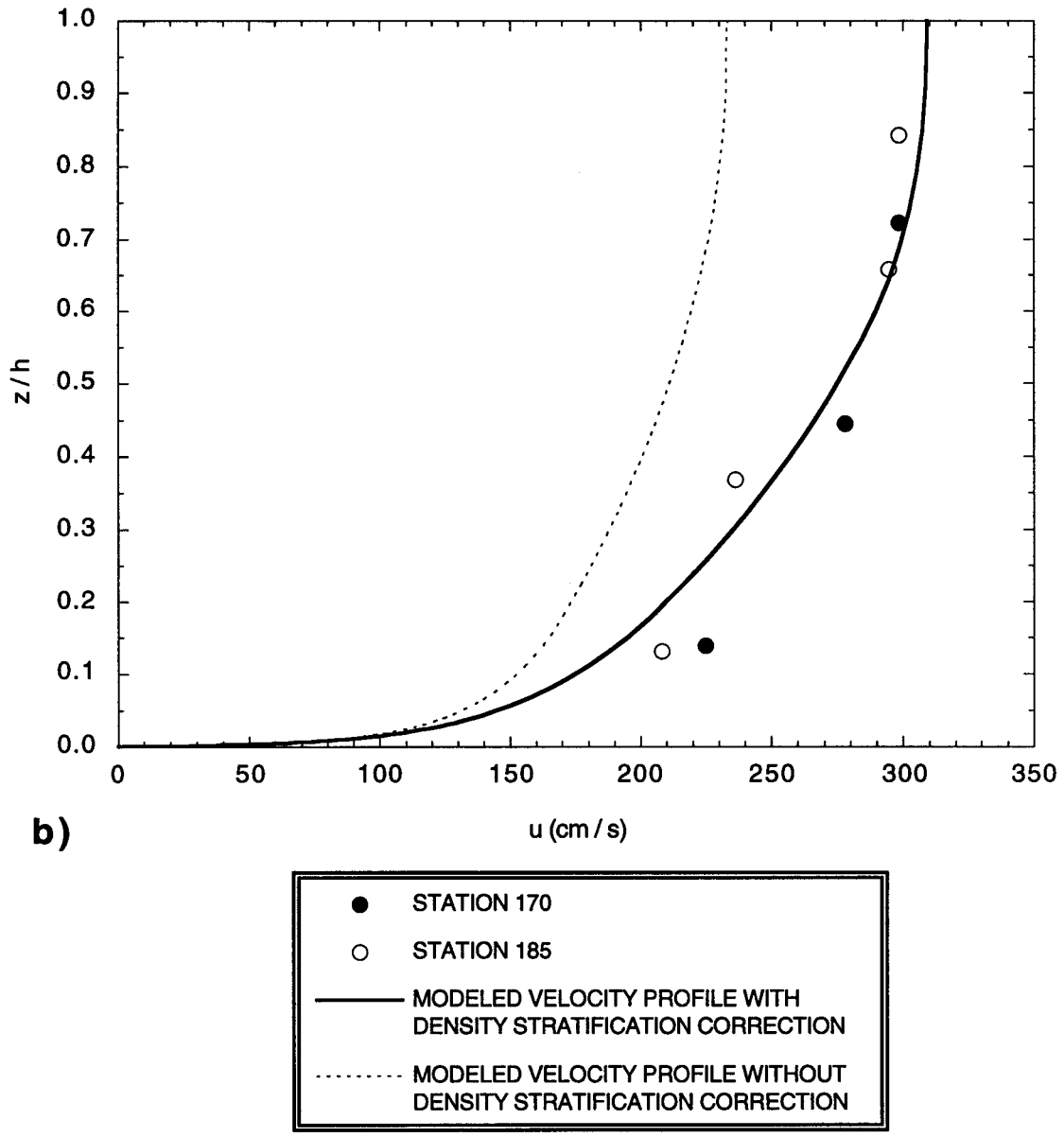

Figure 3.18 (continued): **(b)** Comparison of the model-predicted velocity profile with the velocity profiles measured by Nordin (1963) in the Rio Puerco near Bernardo, NM on September 20, 1961.

Chapter 4: APPLICATION OF THE GEOMORPHICALLY COUPLED FLOW AND SEDIMENT-TRANSPORT MODEL TO THE PARIA RIVER WITH TESTS OF THE MODEL PREDICTIONS AGAINST DATA

Section 4.1: INTRODUCTION

The major goal of work presented in this chapter is the application of the geomorphically coupled, flow and sediment-transport model to the Paria River. Model predictions are tested against data from the Paria River in seven different tests; these tests are designed to evaluate the two working hypotheses and five physical assumptions used in the development of the model in Chapter 3. In addition, because the Paria River is the "birthplace" of hyperconcentrated flows, the existence of a hyperconcentrated flow as a type of flow physically distinct from a turbulent suspension is investigated in this chapter. Work presented in Chapter 2 suggests strongly that climate changes, such as those inferred from regional tree-ring width records, are coupled relatively weakly to both the hydrology and geomorphology in the Paria River. Therefore, to investigate the coupling between climate and sediment transport in an ephemeral river, the geomorphically coupled flow and sediment transport model is used to calculate instantaneous loads of each sediment size class in the Paria River for the entire period of gage record. Finally, to determine if there is a meaningful relationship between long-term sediment transport and bankfull channel geometry in ephemeral rivers, the "effective discharge" and bankfull discharge of the Paria River are compared. To meet these goals, this chapter of the dissertation is divided into six major sections: introduction; description of the model inputs; presentation of the seven tests of the model predictions against measurements of channel geometry, flow, and suspended-sediment transport; discussion of hyperconcentrated flows; prediction of long-term sediment fluxes and discussion of the "effective discharge" for transporting each size range of sediment; and, summary and conclusions.

Section 4.2: MODEL INPUTS

To apply the model to the Lees Ferry reach, the following were used as the inputs into the geomorphically coupled flow and sediment-transport model. (1) Topography in the 1993 reach-averaged cross-section (Figure 2.24a) was used as the initial topography. (2) Reach-averaged, measured gravel grain-size distributions in the 1993 reach-averaged cross-section (Figure 2.24c & 2.24d) was used to set the gravel grain-size distribution at each cross-stream position. (3) Reach-averaged measured thicknesses of the sand, silt, and clay layer (Figure 2.24b) were used to set the initial thickness of the sand, silt, and clay layer at each cross-stream position. (4) Locations of the four sediment types in Figure 2.20

were used as the locations of these sediment types in the modeled cross-section. (5) The sand portion of the bed sediment in each of the four sediment types was broken into ten 1/2-ϕ sized bins (Table 2.3); since grain-size analyses determined by dry sieving are biased toward the size of the sieve on which each size class of sand is collected, each bin was treated as though it were composed entirely of the finest size in the bin. (6) The silt and clay portion of the bed sediment in each sediment type was treated as though it were entirely composed of the measured D_{50} of the flocculated silt and clay (Figure 3.4). (7) For each size class of sediment, the Corey shape factor was set equal to the "standard value" of 0.7 and the Powers index was set equal to the "standard value" of 3.5.[1] (8) The water temperature used to calculate the clear-water density and dynamic viscosity for the Paria River was chosen as 20° C. This choice is within one standard deviation of the mean annual water temperature of 16° C (Figure 4.1) and was made to bias the model slightly toward the higher water temperatures of the summer when most of the floods that transport large quantities of sediment occur. (9) The reach-averaged longitudinal slope of 0.004 from the 762-m-long, 3-reach composite was used as the water-surface slope for all flows. (10) For each modeled flow, the modeled cross-section was divided into computation verticals spaced 0.4 m apart.

Section 4.3: THE SEVEN TESTS OF THE MODEL

Seven tests were developed to test the geomorphically coupled, flow and sediment-transport model against data from the Lees Ferry reach of the Paria River and, therefore, also evaluate the two major working hypotheses and five physical assumptions (stated in Section 3.3) used in the development of the model.

4.3a: TEST 1: Magnitude of cross-section enlargement during a flood

The first test compares the model-predicted magnitude of reach-averaged cross-section enlargement of the channel during a flood with measurements. Results of this test indicate that for the entire discharge range during the period of gage record, the amount of

---

[1]Use of the "standard values" of 0.7 for the Corey shape factor and 3.5 for Powers index for the Paria River is supported by analyses that I subsequently conducted of the shape and roundness of sand from two sites on the Colorado Plateau, i.e., the Colorado River at the near Cisco, UT gage and the Colorado River at the near Grand Canyon, AZ gage. These analyses calculated the Corey shape factor and Powers index of a sand at half-ϕ size increments by comparing the grain-size distribution determined by dry sieving with the grain-size distribution determined by use of a visual accumulation tube. Results from these analyses indicate that the Corey shape factor for all sizes of sand is 0.7±0.2 and 0.7±0.1 (mean±one standard deviation) at the Cisco and Grand Canyon sites, respectively; and, the Powers index for all sizes of sand is 3.2±1.9 and 3.0±1.8 at the Cisco and Grand Canyon sites, respectively.

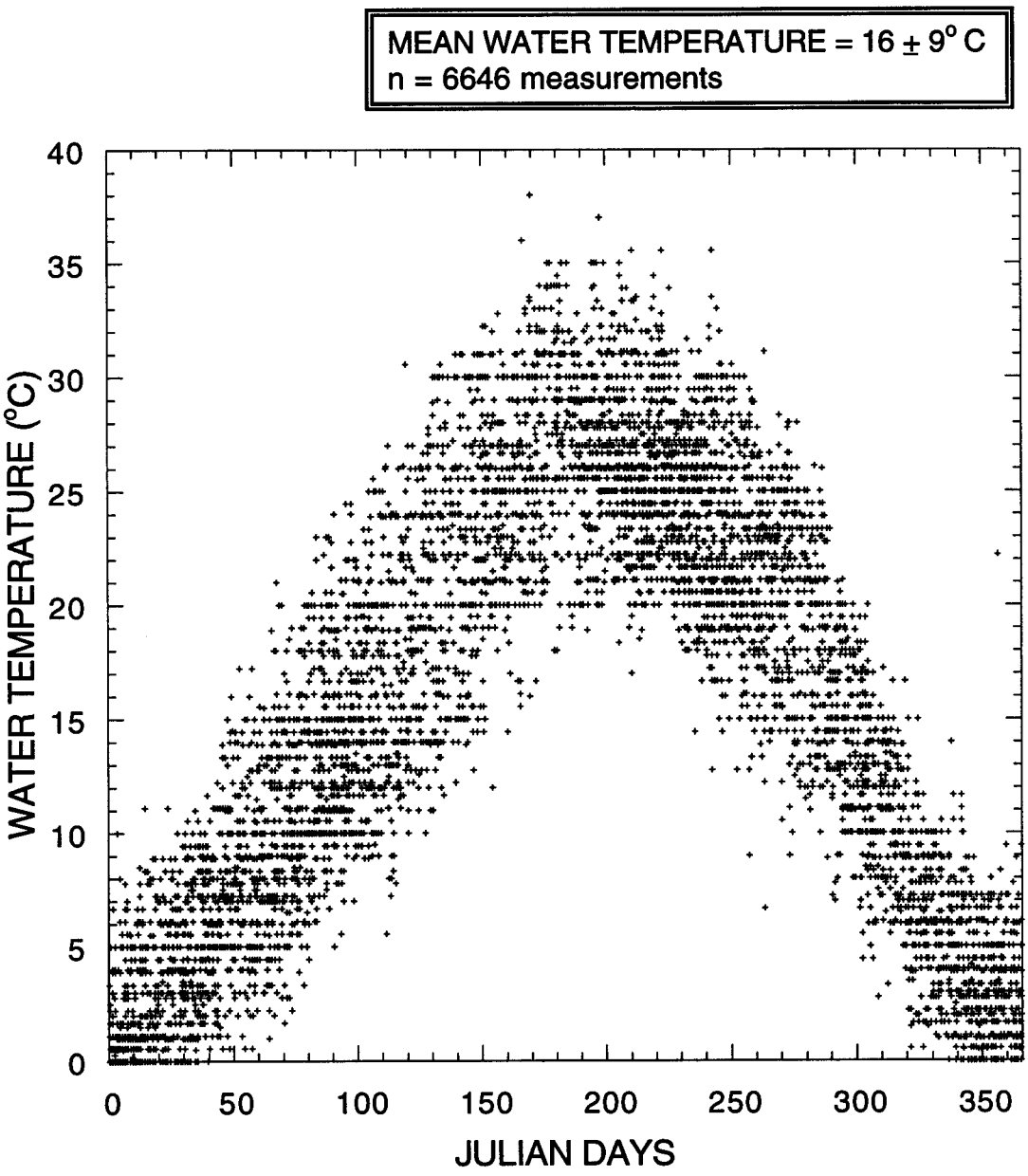

Figure 4.1: Water temperature of the Paria River at Lees Ferry, AZ as a function of Julian day; temperature measurements from both discharge and suspended-sediment concentration measurements.

cross-section enlargement predicted by the model is compatible with the measured maximum amount of cross-section enlargement at the peak discharge of floods. However, during the course of overbank floods, both the second working hypothesis that "the mass of each sediment grain size is conserved on the reach scale" and the first physical assumption that "the lateral advective transport of sediment in the reach-averaged cross-section can be ignored" may begin to break down. During overbank floods, slightly more sediment may be exported from a reach than is imported into it (as previously suggested by the statistical analysis in Section 3.2c), and the reach-averaged cross-section geometry may be altered by the net lateral transport of sediment.

Because lateral advective transport of sediment is prohibited in the model, the model predictions of cross-section enlargement provide a potential means of evaluating the importance of lateral advective transport of sediment on channel enlargement during floods in the river. If the lateral advective transport of sediment in the cross-section plays a relatively unimportant role in determining the magnitude of cross-section enlargement during floods, as shown in Figure 4.2, substantial channel widening should occur only when the banks are significantly overtopped by floods and sediment goes directly into suspension from the floodplains.[2] Figure 4.3 compares the model-predicted cross-section with the measured cross-section at Cableway 2 during the "highest high-confidence discharge measurement" made on the Paria River before the onset of post-1972 incision near the gage.[3] At a discharge of 38.2 m^3/s, the model-predicted enlarged channel cross-section geometry is in excellent agreement with the measured channel cross-section geometry (Figure 4.3).[4] Unfortunately, the relatively low discharge of 38.2 m^3/s, which is only 42% of the bankfull discharge and corresponds to only 75% of the bankfull stage, is the highest discharge for which the cross-section geometry during a flood is relatively well known.

Because the "highest high-confidence discharge measurement" was made at a relatively low discharge, the maximum amount of channel enlargement at the peak discharge of larger floods must be estimated from cross-sections surveyed after floods,

---

[2]Some of the steep margins in the model-predicted cross-sections in Figure 4.2, e.g., the stepped, steep margin on the lower right side of the model-predicted cross-section at 2.2 m stage, are artifacts of the vertical boundaries between sediment types in the initial cross-section (Figure 2.20).

[3]The phrase "highest high-confidence discharge measurement" means simply that this is the highest discharge measurement during which mean velocities were measured with a Price current meter and depths were determined by sounding.

[4]The two kinks in the bottom of the model-predicted cross-section in Figure 4.3 are artifacts of the boundaries between sediment types 1 and 2 in the initial cross-section (see Figure 2.20).

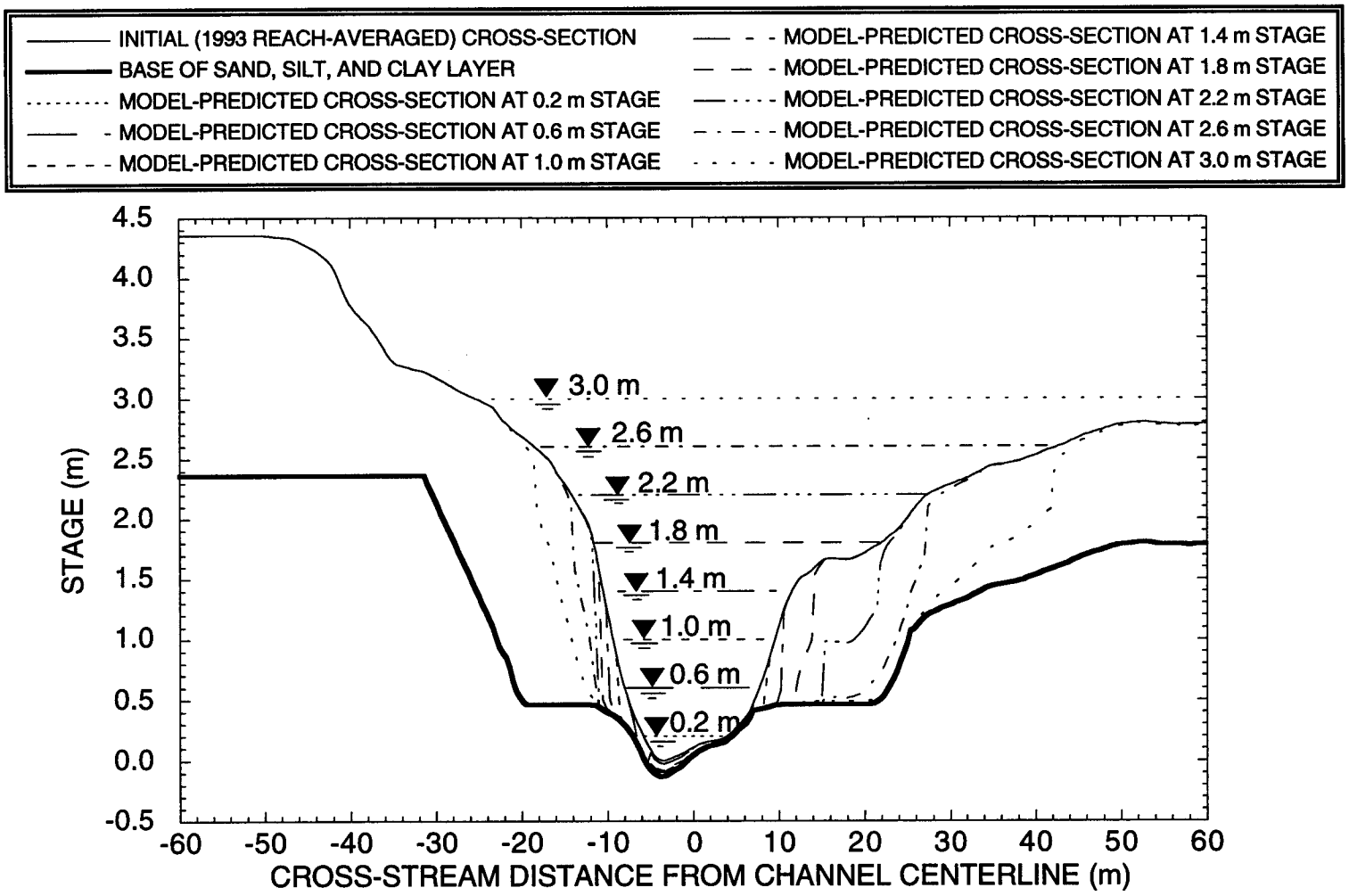

Figure 4.2: Model predictions of channel enlargement at eight different discharges; shown for reference are the 1993 reach-averaged cross-section and the base of the sand, silt, and clay layer used as inputs into the model. In this figure, stage is measured from the initial low point in the channel, prior to bed scour, to the water surface.

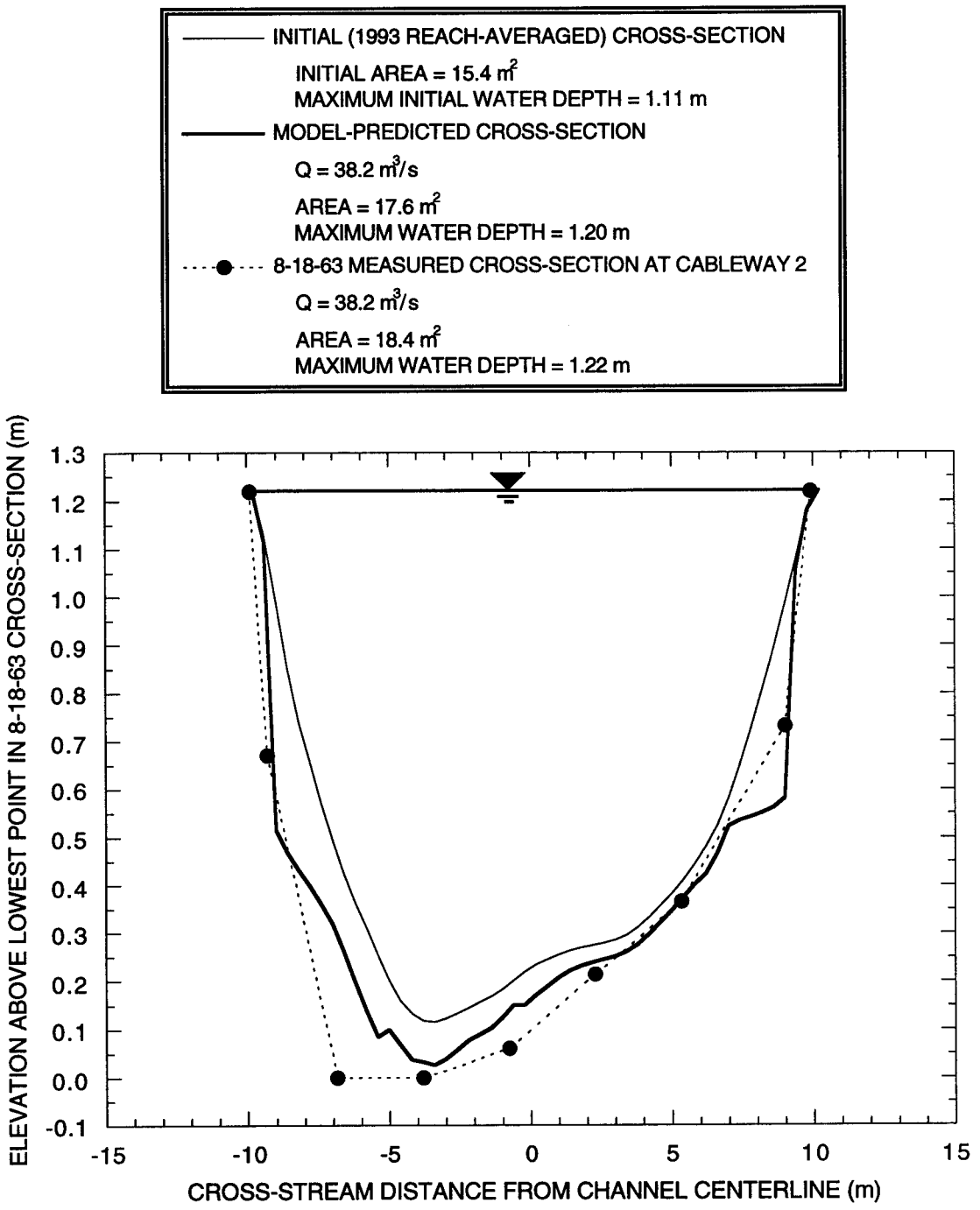

Figure 4.3: Comparison of the model-predicted cross-section with the measured cross-section at a discharge of 38.2 m^3/s; also shown is the channel topography from the 1993-reach-averaged cross-section used as model input. The August 18, 1963 discharge measurement was made between 10:55 and 11:10 a.m. at Cableway 2 (velocities from this measurement were shown in Figure 3.7).

i.e., cross-sections surveyed as part of the slope-area surveys (Figure 4.4). In Figure 4.4, cross-section areas determined from all standard and float-area discharge measurements made between 1923 and 1972 and cross-section area determined from all cross-sections surveyed after large floods in reaches with longitudinal bed slopes within 15% of the equilibrium slope of 0.0035 are compared with the initial (1993 reach-averaged) and model-predicted cross-section areas as functions of the maximum depth in the cross-section. Given that post-flood measurements of cross-section area are somewhat representative of cross-section areas during the peak of a flood (i.e., the cross-section area during the peak of a flood is not significantly larger than that measured after a flood), the comparison in Figure 4.4 suggests that the amount of cross-section enlargement predicted by the model is in agreement with that measured over the full discharge range of floods during the period of gage record. However, as explained in detail below, this comparison also indicates that either sediment is exported in a net sense or laterally redistributed during the falling limb of overbank floods.

If, during the course of a flood, the mass of sediment is conserved on the reach-scale (as hypothesized) and no lateral advective transport of sediment occurs in the reach-averaged cross-section (as assumed), the cross-section area, as a function of maximum depth, measured after floods should agree with the cross-section area, as a function of depth in the initial (1993 reach-averaged) cross-section. Results of the comparison in Figure 4.4 indicate, however, that the measured cross-section areas after overbank floods are generally intermediate between those associated with the initial (1993 reach-averaged) and the model-predicted cross-section. This observation suggests that either sediment mass is not be conserved on the reach-scale during the largest floods, lateral advective transport of sediment increases in relative importance during the larger floods, or both. As is shown below, support exists for the occurrence of both of these possibilities.

If the mass of sediment is not conserved on the reach scale during the largest floods (as has already been suggested by the results of the statistical analysis in Section 3.2c) and more sediment is exported from a reach than is replaced during the falling limb, the reach-averaged cross-section area will increase during the course of these floods. As shown in Section 3.2c, the significant depletion in the sand supply in the system following the largest 16% of the Paria River floods during the period of gage record may, in fact, manifest itself as the 15-20% larger cross-section areas measured after the largest floods. Thus, the largest (i.e., overbank) floods may cause true enlargement of the cross-section through reach-scale thinning of the sand, silt, and clay layer overlying the gravel, with (since the

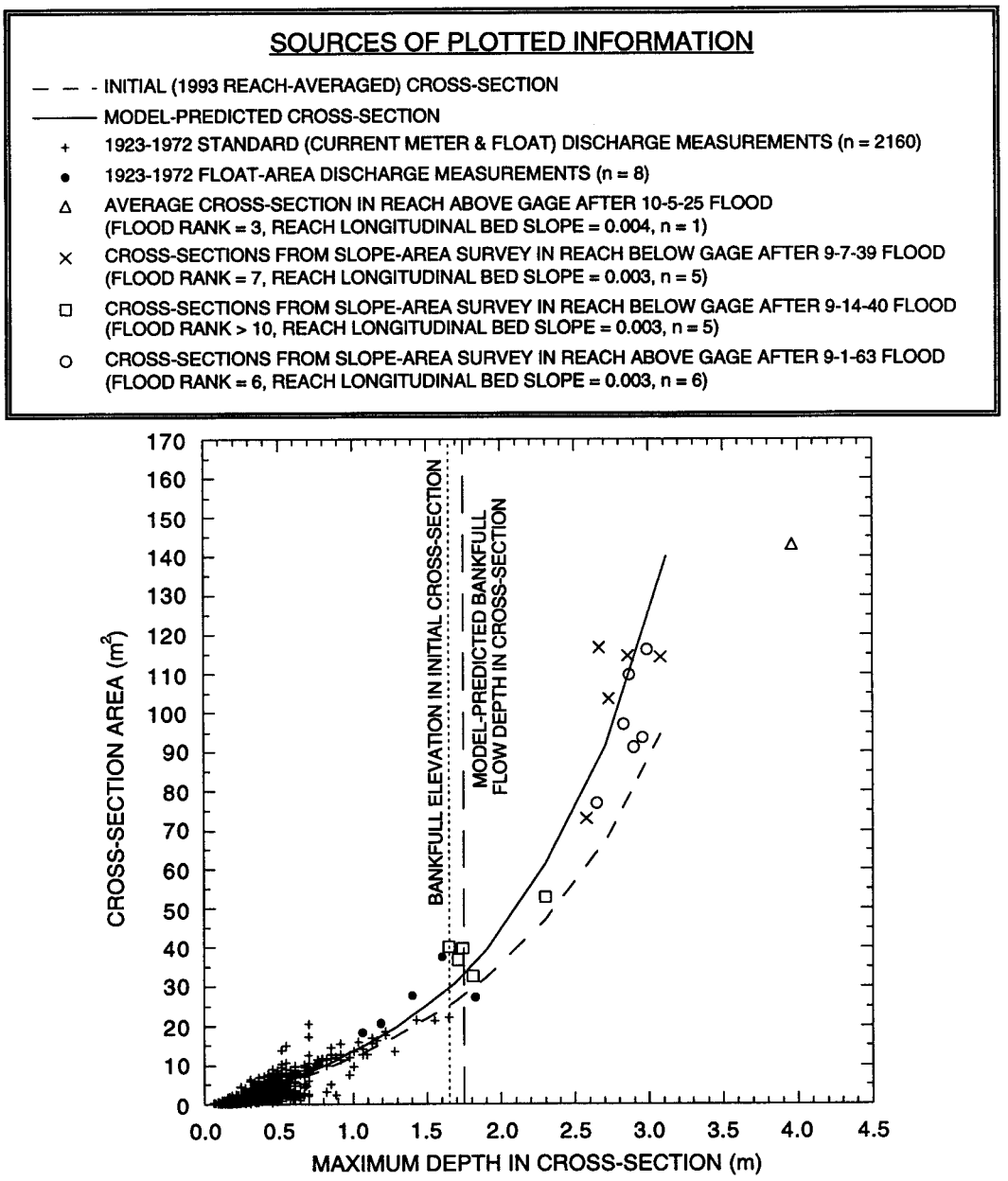

Figure 4.4: Cross-section area as a function of the maximum depth in the initial cross-section, the model-predicted cross-section, and the cross-sections from the pre-1972 standard discharge measurements, float-area discharge measurements, and all 1925-1963 surveys from reaches with longitudinal bed slopes within 15% of the equilibrium bed slope of 0.0035 (see Section 2.5b-4a). Flood ranks shown are those for the period of gage record in Table 2.1. Since ~10 cm of bed scour is predicted to occur in the modeled cross-section at bankfull flow, the model-predicted bankfull flow depth is shifted 10 cm to the right of the bankfull elevation in the initial (dry) cross-section.

measured cross-section areas after overbank floods are intermediate with respect to the areas associated with the initial and model-predicted cross-sections) approximately half of the volume of sand, silt, and clay eroded during the rising limb of a flood redeposited in a reach during the falling limb.

Alternatively, disagreement between the measured cross-section areas after overbank floods and the areas associated with the initial cross-section in Figure 4.4 may be explained by a temporary change in the reach-averaged cross-section geometry resulting from net lateral advective transport of sediment during the course of overbank flooding. In fact, lateral redistribution of sediment can occur while mass of sediment is still conserved on the reach scale. For example, fresh-appearing sand was deposited in the reach above the gage during the 200 m^3/s 1963 flood in the same locations where sand existed in February 1951 (Figure 4.5). This observation is surprising, given that 213 floods, five overbank floods, and two of the ten largest floods during the period of gage record occurred during the time between the two photographs in Figure 4.5.[5] Notes taken by the USGS technicians during the 1963 slope-area survey indicate that, on average, the amount of "redeposited" fresh, clean sand during the 1963 flood was 12 m^2 in the six cross-sections surveyed in the reach above the gage. This value agrees reasonably well with the model-predicted 15 m^2 of eroded sand, silt, and clay for a flow of 200 m^3/s, thus suggesting that the 15-20% apparent enlargement of the reach-averaged cross-section during overbank flooding can partially be explained as a change in cross-section geometry instead of only by a true enlargement of the cross-section.

4.3b: TEST 2: Magnitude of cross-section widening during a flood

The second test compares, as a function of discharge, the width of the model-predicted cross-section at seven different elevations with measurements of width determined from the discharge measurement cross-sections measured at Cableway 2 from July 16, 1953 through March 21, 1979 (Figure 4.6).[6] If for a given discharge, either the

---

[5]A flood is defined as an event with a peak discharge greater than one standard deviation above the mean instantaneous discharge, see Section 2.4e.

[6]Included in the comparison in Figure 4.6 are: widths from the cross-sections from the 61 discharge measurements made from 7-16-53 through 6-23-72 at Cableway 2, in which the geometry of the cross-section was determined by sounding during the flood; widths from the cross-section from the discharge measurement made at 12:45-1:15 p.m. on 9-18-61 at Cableway 2, in which the geometry of the cross-section was measured prior to the flood; widths from the cross-sections from the three discharge measurements made at 9:30-9:50 a.m. on 8-18-63, 12:30 p.m. on 9-23-67, and 1:45 p.m. on 9-25-67 at Cableway 2, in which the geometry of the cross-section was measured after the flood; and widths from the cross-sections from the nine discharge measurements made at Cableway 2 after the incision at the gage on August 15, 1972.

Figure 4.5: **(a)** Upstream view of the reach above the gage from the cliff above the gage after the 200 m^3/s flood of September 1, 1963; the locations marked **A** and **B** are the same as in Figure 4.5b. Note the freshly deposited sand on the right floodplain in the left side of the field of view. Photograph taken by USGS technician R.H. Roeske on September 18, 1963. **(b)** Upstream view of the right portion of the reach above the gage in February 1951; the locations marked **A** and **B** are the same as in Figure 4.5a. Note that sand between locations **A** and **B** in this photograph is occupying the same position as sand between **A** and **B** Figure 4.5a. The fence in the left portion of this photograph is not in the same location as the fence that appears in Figure 4.5a. Also, note the right A-frame of Cableway 1 in the left portion of the field of view; the dashed line was drawn on the photograph by USGS personnel in 1951 to indicate local bank erosion on the outside of a newly formed meander. Photograph taken by unnamed USGS technician.

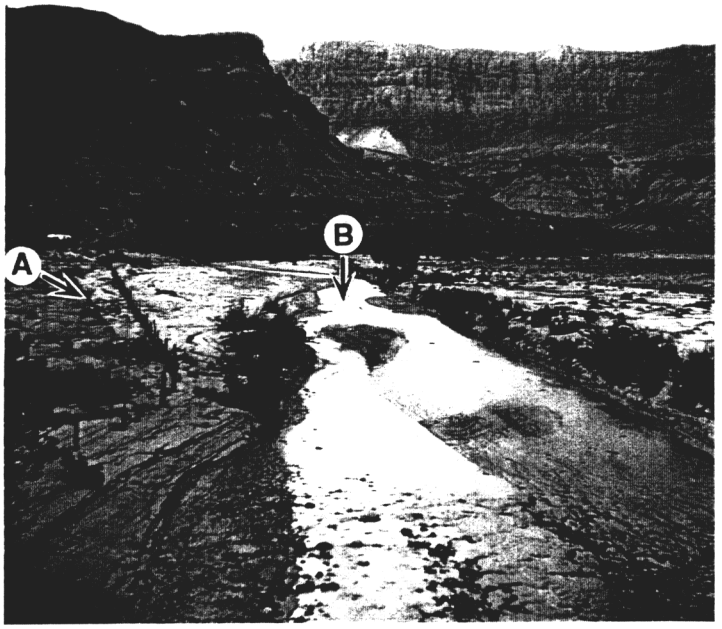

a)

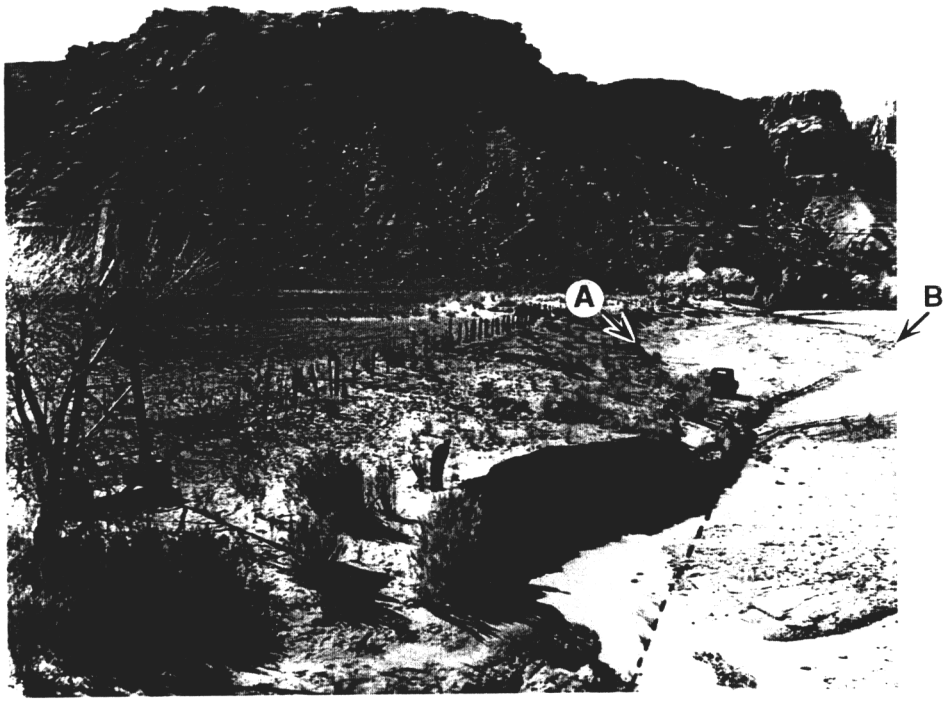

b)

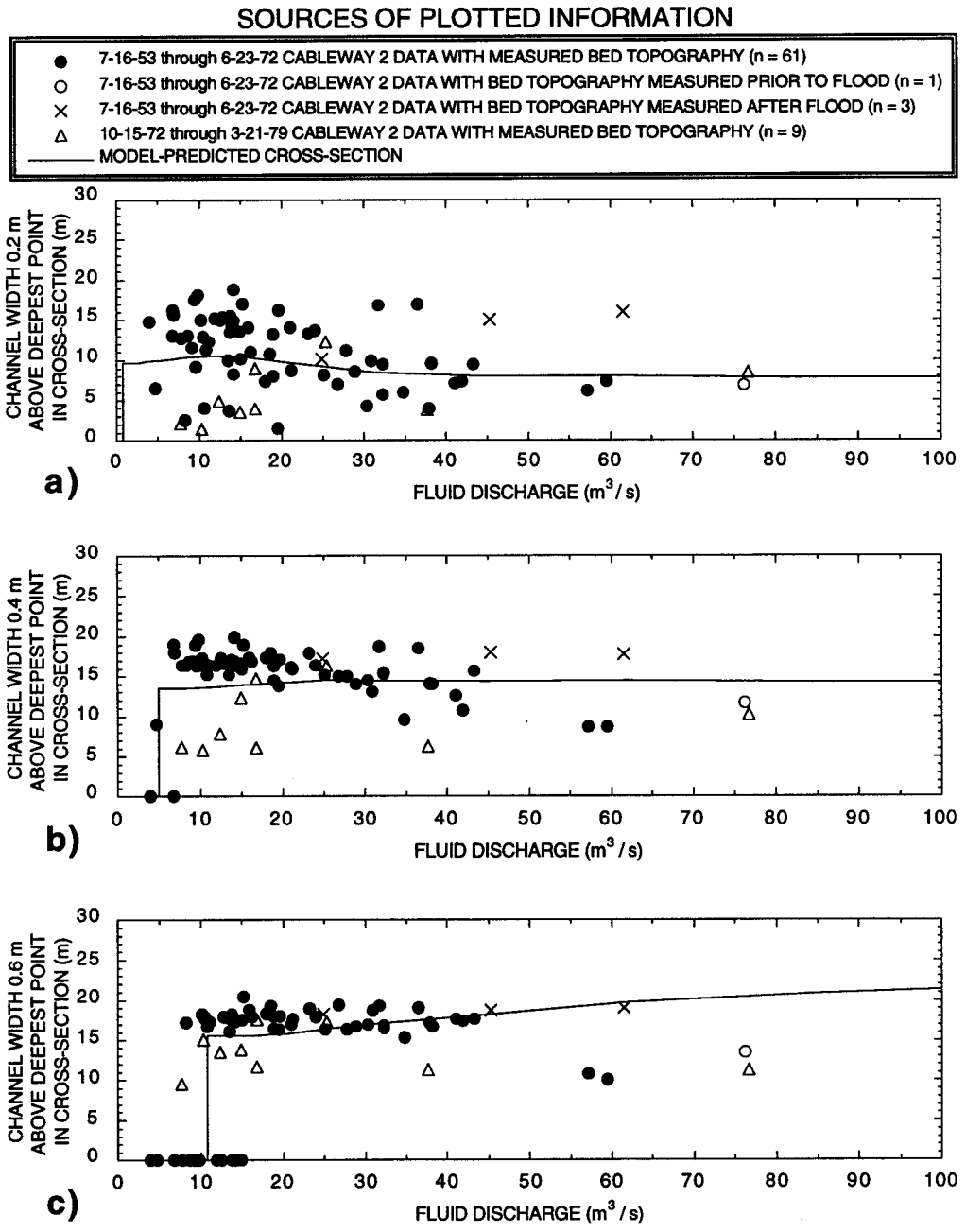

Figure 4.6: **(a)** Model-predicted and measured width of the flow at 0.2 m above the deepest point in the cross-section. **(b)** Model-predicted and measured width of the flow at 0.4 m above the deepest point in the cross-section. **(c)** Model-predicted and measured width of the flow at 0.6 m above the deepest point in the cross-section.

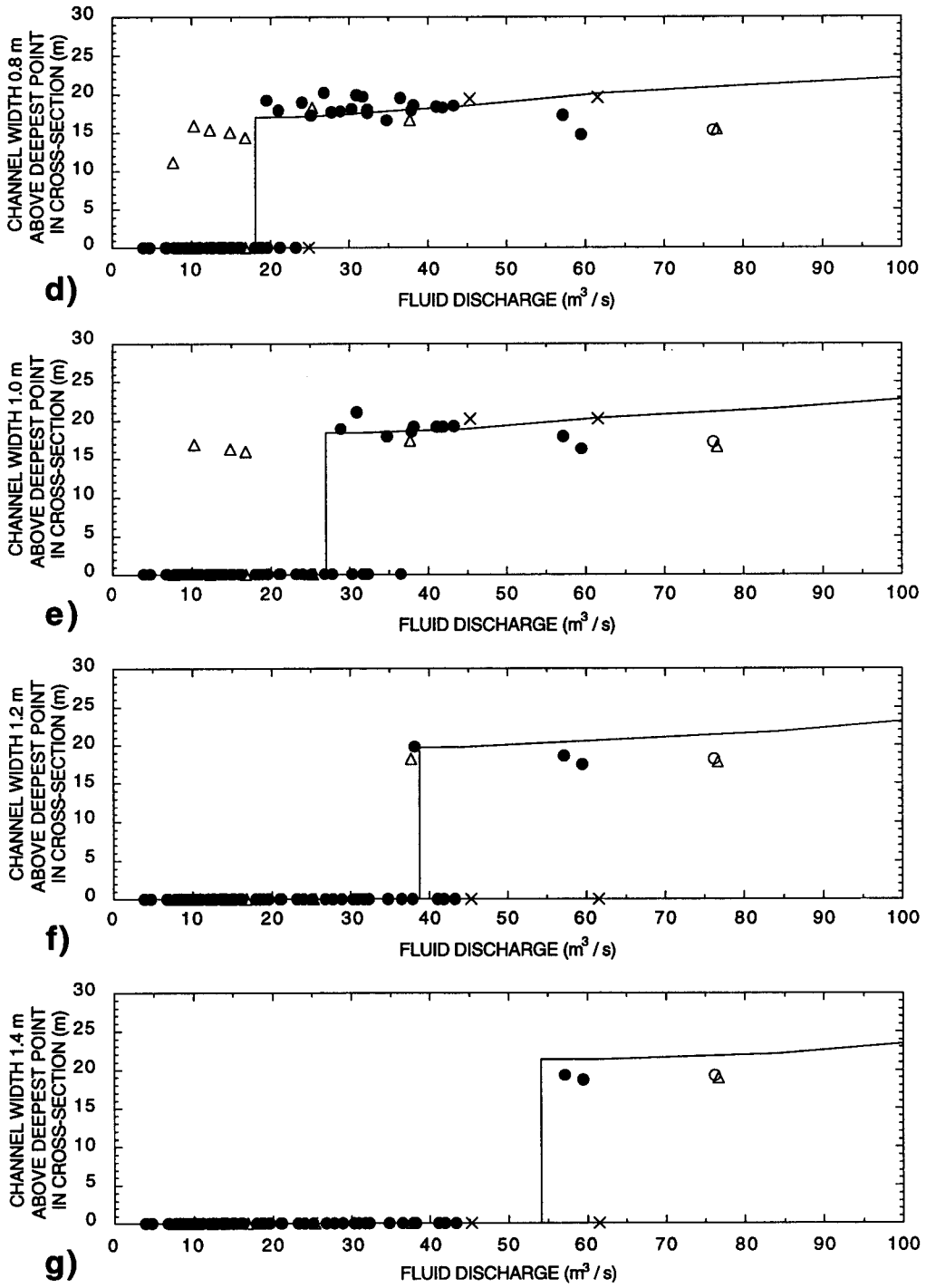

Figure 4.6 (continued): **(d)** Model-predicted and measured width of the flow at 0.8 m above the deepest point in the cross-section. **(e)** Model-predicted and measured width of the flow at 1.0 m above the deepest point in the cross-section. **(f)** Model-predicted and measured width of the flow at 1.2 m above the deepest point in the cross-section. **(g)** Model-predicted and measured width of the flow at 1.4 m above the deepest point in the cross-section.

model- predicted or measured water-surface elevation of a flow does not reach the elevation of a "width comparison", the width of the modeled or measured flow at that elevation is reported as zero in Figure 4.6. Agreement is excellent between modeled and measured widths for all of the pre-incision measurements and the model captures many of the subtleties of width variation as a function of discharge. For example, because of increasing scour of the sand, silt, and clay layer with increasing discharge, both the measured and the model-predicted width of the channel 0.2 m above the deepest point decrease after reaching a maximum between a discharge of 10 and 15 m^3/s (Figure 4.6a). The only notable disagreement between the model predictions and measurements of width occurs in the case of the post-incision cross-sections. Measurements of width in the post-incision cross-sections indicate that, after passage of the first headcut by the gage on August 15, 1972, for a given discharge, the channel at Cableway 2 became much narrower and deeper, corroborating results of the statistical analysis of cross-section geometry in Section 2.5b-4b.

Results from this test indicate conclusively that the model predictions of channel widening at discharges less than bankfull are in excellent agreement with all available measurements; thus, this test lends further support, for flows less than bankfull (i.e., 99.98% of all Paria River flows), to both the second working hypothesis that "the mass of each sediment grain size is conserved on the reach scale" and the first physical assumption that "lateral advective transport of sediment in the reach-averaged cross-section can be ignored". Results from this test, in conjunction with results from the previous test, strongly suggest that the dominant mechanism of channel widening during floods in ephemeral rivers is sediment going into directly into suspension from the bed, banks, and floodplains as they are locally overtopped by the flow. Furthermore, results from these first two tests show that lateral advective transport of sediment is only of secondary importance in determining the maximum amount of channel widening during a flood.

4.3c: TEST 3: Comparison of model-predicted and measured maximum depth, area, and mean velocity as a function of fluid discharge

The third test compares model-predicted maximum cross-section depth, cross-section area, and cross-section mean velocity with measurements of these quantities from all "non-ice-affected" discharge measurements made from November 22, 1923 through October 12, 1994 in the Lees Ferry reach (Figure 4.7). Results from this test show that the third physical assumption that "form drag from channel-scale features, i.e., bars and banks, is negligible" is appropriate at discharges greater than about 10 m^3/s. In contrast,

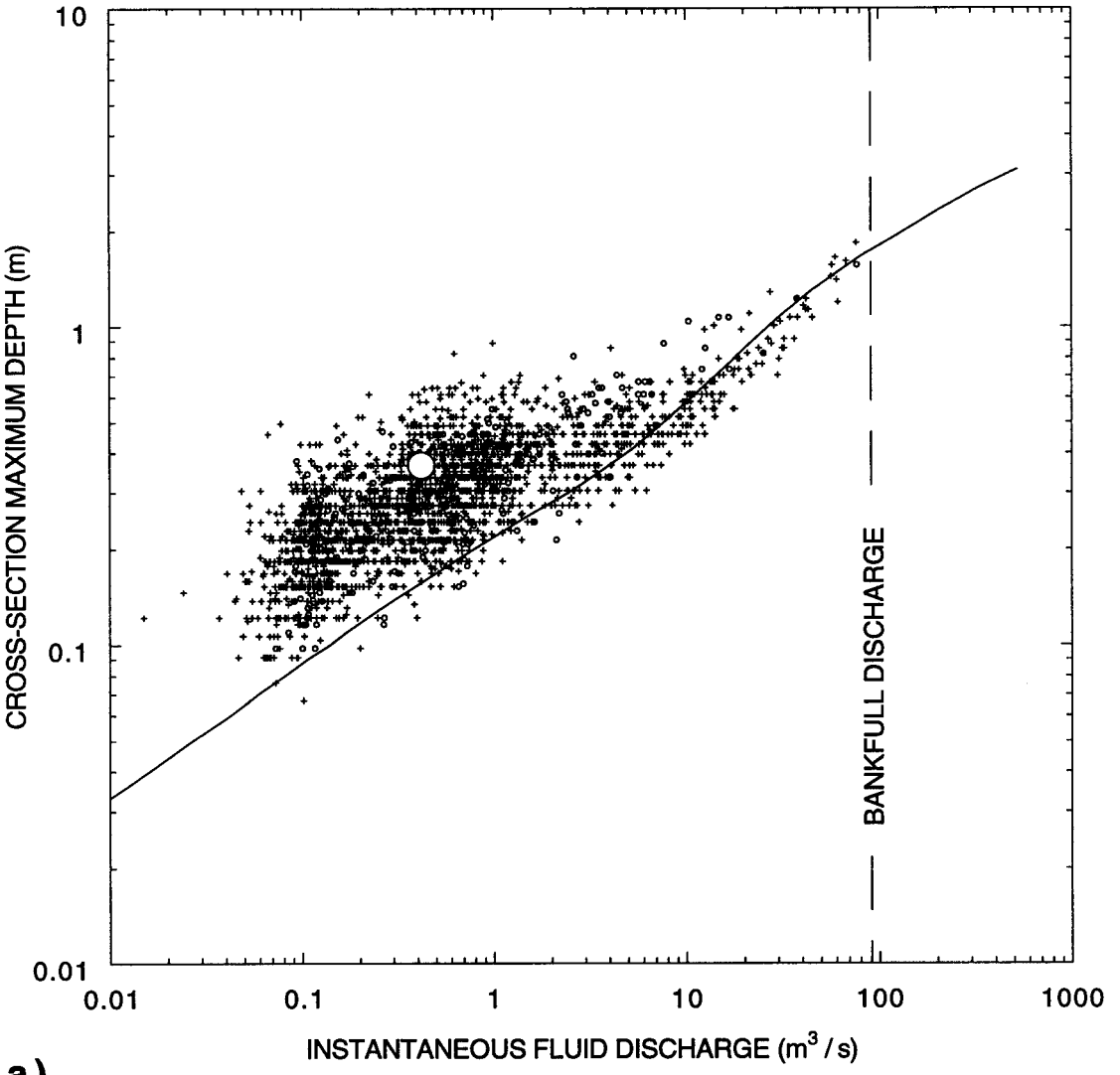

Figure 4.7: **(a)** Measured and model-predicted cross-section maximum depth as a function of instantaneous fluid discharge. Data from both pre- and post-incision discharge measurements (i.e., pre- and post-August 15, 1972 discharge measurements) are shown.

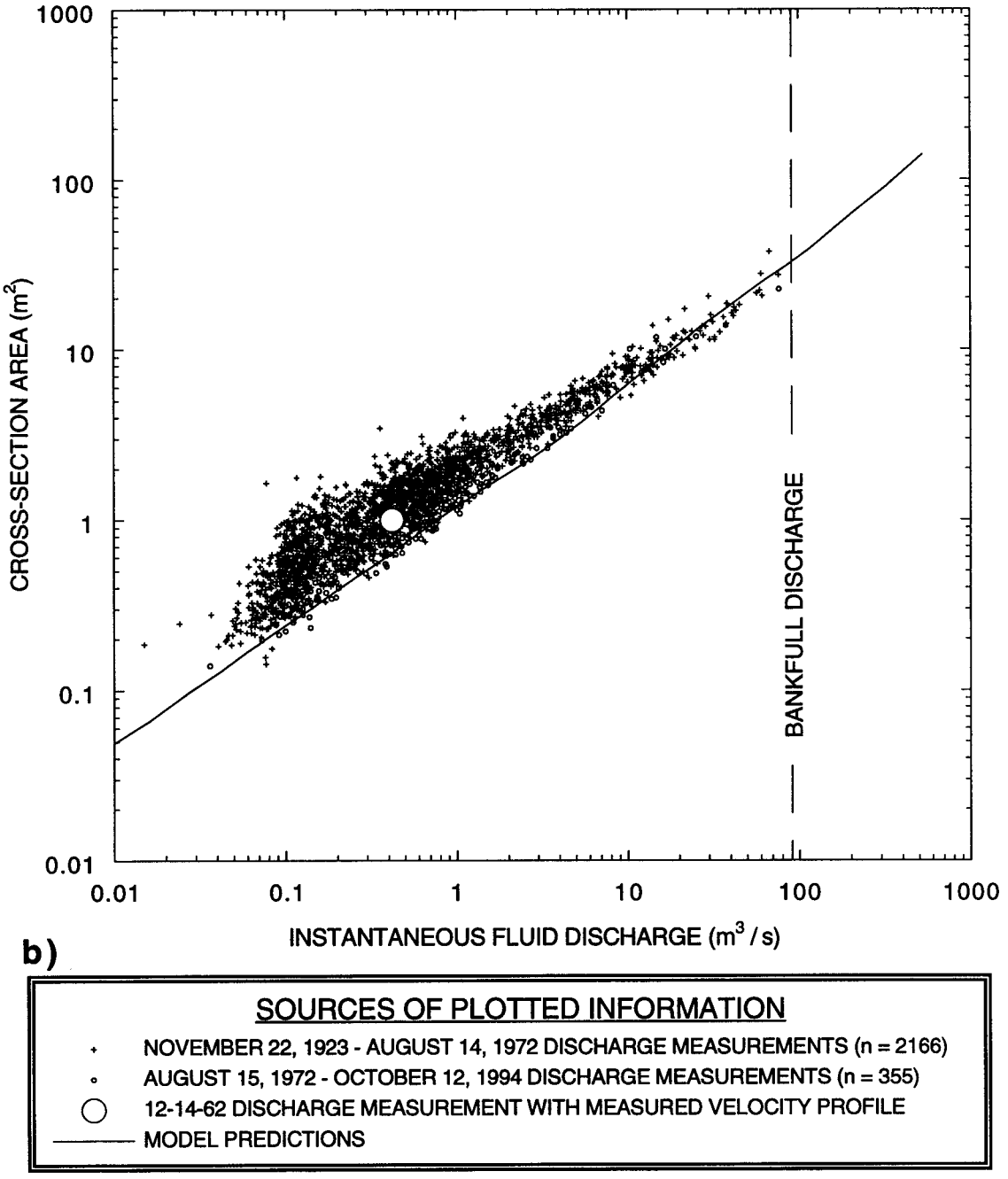

Figure 4.7 (continued): **(b)** Measured and model-predicted cross-section area as a function of instantaneous fluid discharge. Data from both pre- and post-incision discharge measurements (i.e., pre- and post-August 15, 1972 discharge measurements) are shown.

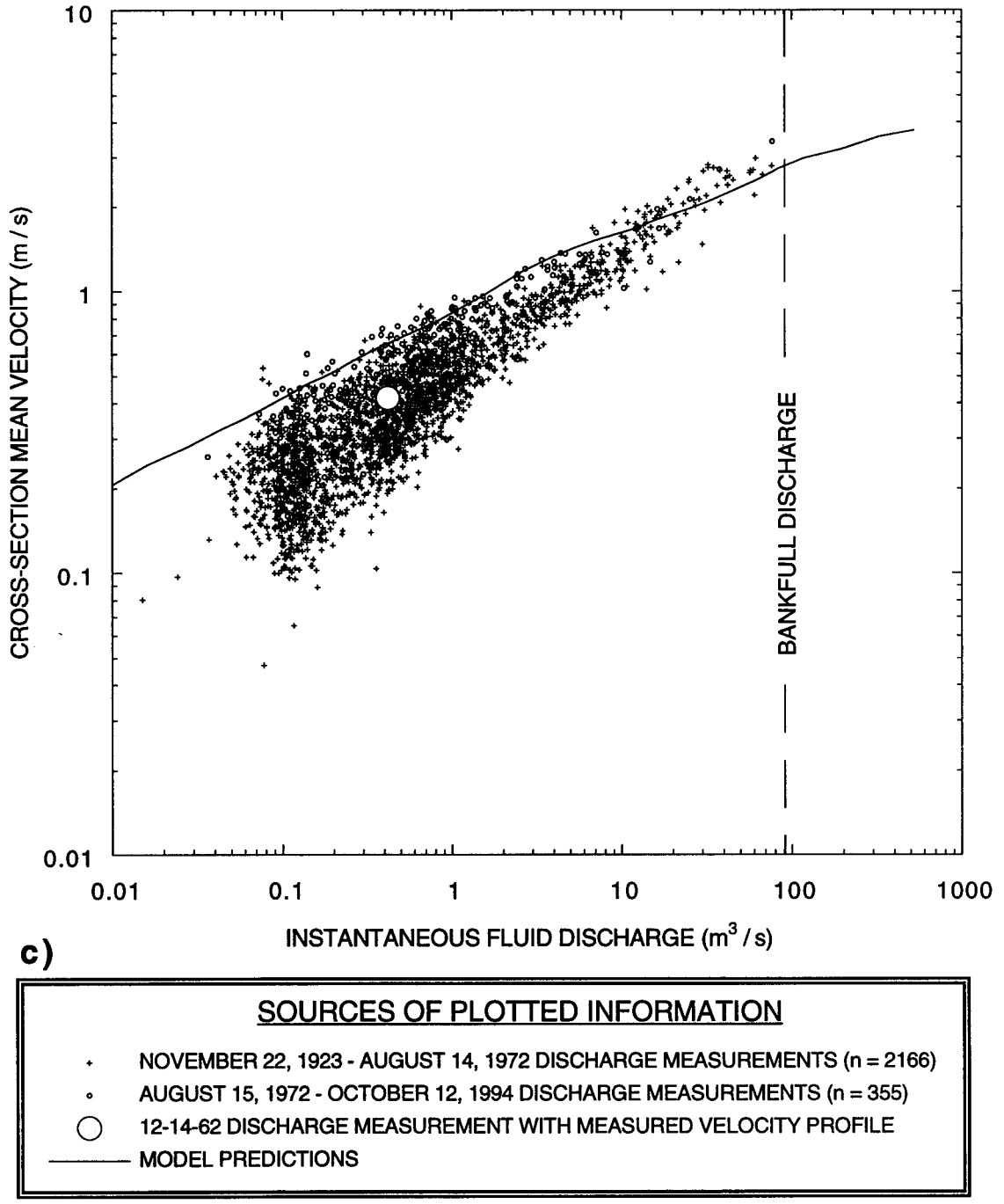

Figure 4.7 (continued): (c) Measured and model-predicted cross-section mean velocity as a function of instantaneous fluid discharge. Data from both pre- and post-incision discharge measurements (i.e., pre- and post-August 15, 1972 discharge measurements) are shown.

results from this test suggest that, though this physical assumption can also be valid at discharges less than about 10 m^3/s, it is not valid on average at low discharges.

At discharges greater than about 10 m^3/s, model predictions of maximum cross-section depth, cross-section area, and cross-section mean velocity fall in the middle of the measurements of these quantities (Figure 4.7), thus lending support to the physical assumption that "form drag from channel-scale features is negligible" at discharges from about 10 m^3/s up to bankfull (90 m^3/s). At discharges less than 10 m^3/s, however, model predictions do not fall in the middle of the measurements, but rather, fall on the appropriate "no channel-scale form drag" bound of the data. In Figure 4.7, the "no channel-scale form drag" bound is the lower bound of the data for maximum cross-section depth, the lower bound of the data for cross-section area and the upper bound of the data for cross-section mean velocity. This behavior of model predictions relative to measurements is seen again in Section 4.3e below, where, because of the use of the physical assumption that "form drag from channel-scale features is negligible", the model also predicts the upper bound of the measured suspended-sand concentrations at discharges less than about 10 m^3/s and predicts the mean of the measured suspended-sand concentrations at higher discharges.

The argument that channel-scale form drag is important on average in the Paria River at discharges less than about 10 m^3/s is supported by the data in Figure 4.7 from the one cross-section (measured as part of the discharge measurement on December 14, 1962), during which a velocity profile was measured in the middle of the channel (Figure 4.8). Relative to the model-predictions based on no channel-scale form drag, this cross-section has a larger maximum depth, larger area, and smaller mean velocity (Figure 4.7). Since discharge measurements made at low discharges are typically made in "backwatered" pools, in which the form-drag component of the stress typically dominates the total boundary shear stress, the majority of cross-sections from lower-flow discharge measurements would have larger maximum depths, larger areas, and lower mean velocities than those few cross-sections measured in portions of the channel in which channel-scale form drag is relatively unimportant. Thus, the skin-friction shear stress determined by assuming steady, uniform flow and fitting a velocity profile (using the 2-part eddy viscosity of Rattray and Mitsuda (1974)) to the velocity profile in Figure 4.8 is one order of magnitude lower (i.e., 9.92 $dynes/cm^2$) than that associated with the reach-averaged water-surface slope of 0.004 and no channel-scale form drag (i.e., 145 $dynes/cm^2$).

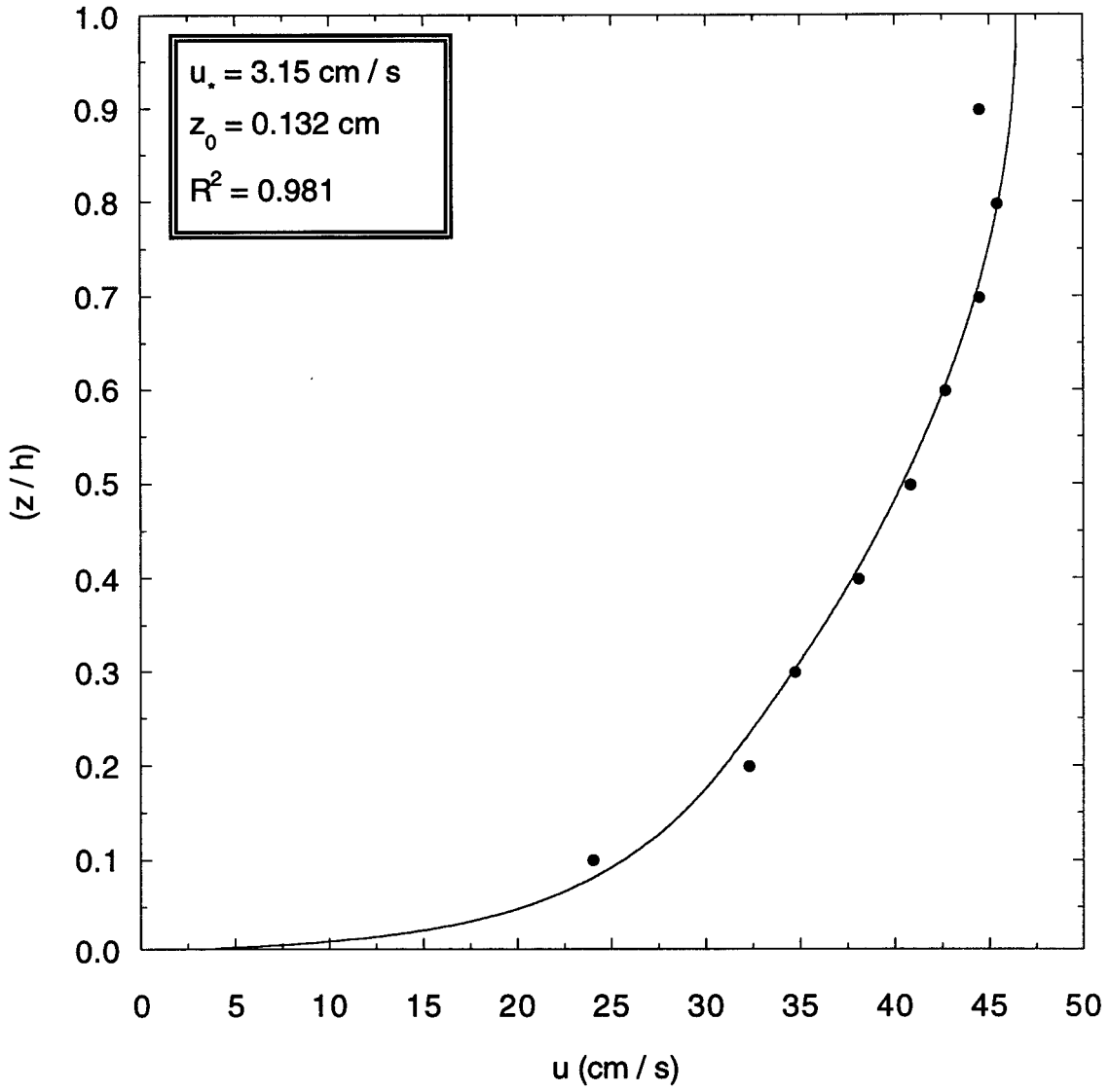

Figure 4.8: Velocity profile measured in the center of the channel on December 14, 1962 by USGS hydrologist Dallas Childers, Jr; depth of flow was 37 cm at this location. The line is the best-fit regression using the 2-part eddy viscosity of Rattray and Mitsuda (1974).

4.3d: TEST 4: Occurrence of dunes and antidunes in the channel

The fourth test compares the model predictions of bedform types in two portions the channel, the thalweg and bar surface, with field observations of the occurrence of dunes and antidunes. The two verticals selected for this test are located on either side of the channel centerline (Figure 4.9a); one in the deepest part of the thalweg (3.4 m left of the channel centerline) and the other on the bar surface (3.0 m right of the channel centerline). The bed at each vertical is composed of different grain-size distributions of sand, silt, and clay; the bed in the deepest part of the thalweg is composed of Type 1 sediment (D_{50} = 0.33 mm) overlying gravel, while bed on the bar surface is composed of finer (Type 2) sediment (D_{50} = 0.093 mm) overlying slightly finer gravel (see Section 2.5a). The model predicts that because the gravel is never completely covered on the bar surface, dunes and antidunes should only exist in the thalweg. In the thalweg, dunes are predicted to only exist in flow depths less than 25 cm, and antidunes are predicted to exist in flow depths ranging from about 27 to 73 cm. These predictions are in agreement with observations (presented in Section 2.5a) that dunes exist on the floor of the thalweg in flows less than 30 cm deep when D_{84} of the gravel is buried and that antidunes are present in the thalweg for flow depths ranging only from 30-80 cm.

In agreement with field observations, the model predicts that dunes should only be exist in the Paria River in the thalweg at low flows. In the thalweg, dunes are predicted to exist only in flow depths less than about 25 cm, accounting for a sizable reduction in the skin-friction boundary shear stress (Figure 4.9b). Because it is relatively coarse (Figure 4.9f), the bed in the thalweg is predicted to remain fairly sandy (i.e., 70 area-% sand, silt, and clay) even at the highest flows (Figure 4.9d); thus, the gravel form-drag stress at the bed is never predicted to be substantial in the thalweg (Figure 4.9b). The upper limit on dune occurrence on the floor of the thalweg, therefore, is not predicted to be the result of gravel being uncovered, but rather, the result of the dunes "washing out" as the coarser size classes of bed sediment progressively go into suspension (see Figure 3.12). On the bar surface, dunes are never predicted to exist because the sand, silt, and clay layer is both too fine and too thin; thus, as shown in Figure 4.9c, the dune form drag is always zero. Unlike in the thalweg, the model predicts that the area of the bar surface covered by sand, silt, and clay on decreases rapidly from 96 area-% to less than 2 area-% as the flow depth increases (Figure 4.9e) resulting in a substantial gravel form-drag stress (Figure 4.9c).

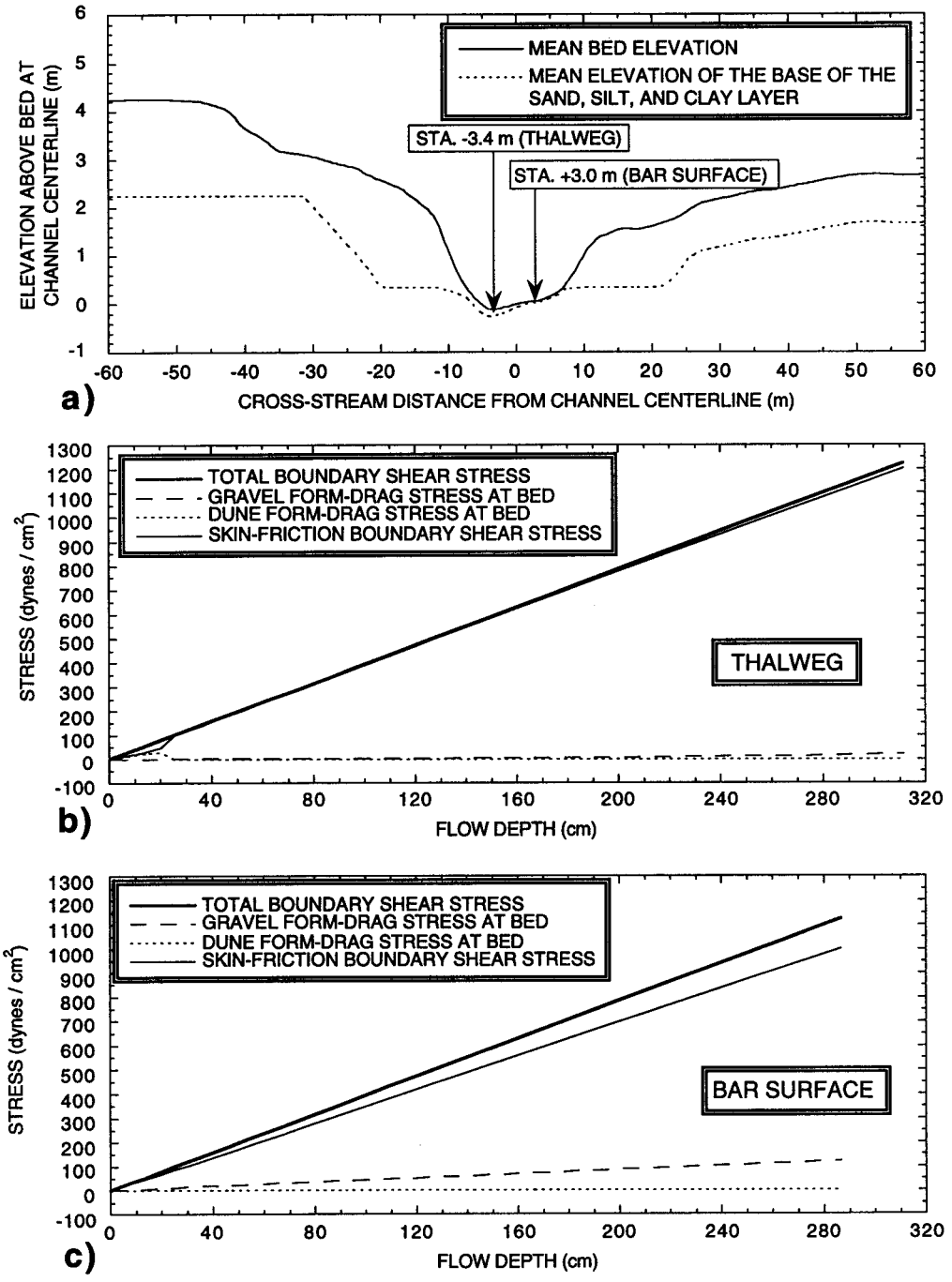

Figure 4.9: **(a)** The "thalweg" and "bar surface" test verticals located at stations -3.4 m and +3.0 m, respectively, in the cross-section. **(b)** Predicted total boundary shear stress, gravel form-drag stress at the bed, dune form-drag stress at the bed, and skin-friction boundary shear stress as functions of the model-predicted flow depth in the thalweg. **(c)** Predicted total boundary shear stress, gravel form-drag stress at the bed, dune form-drag stress at the bed, and skin-friction boundary shear stress as functions of the model-predicted flow depth on the bar surface.

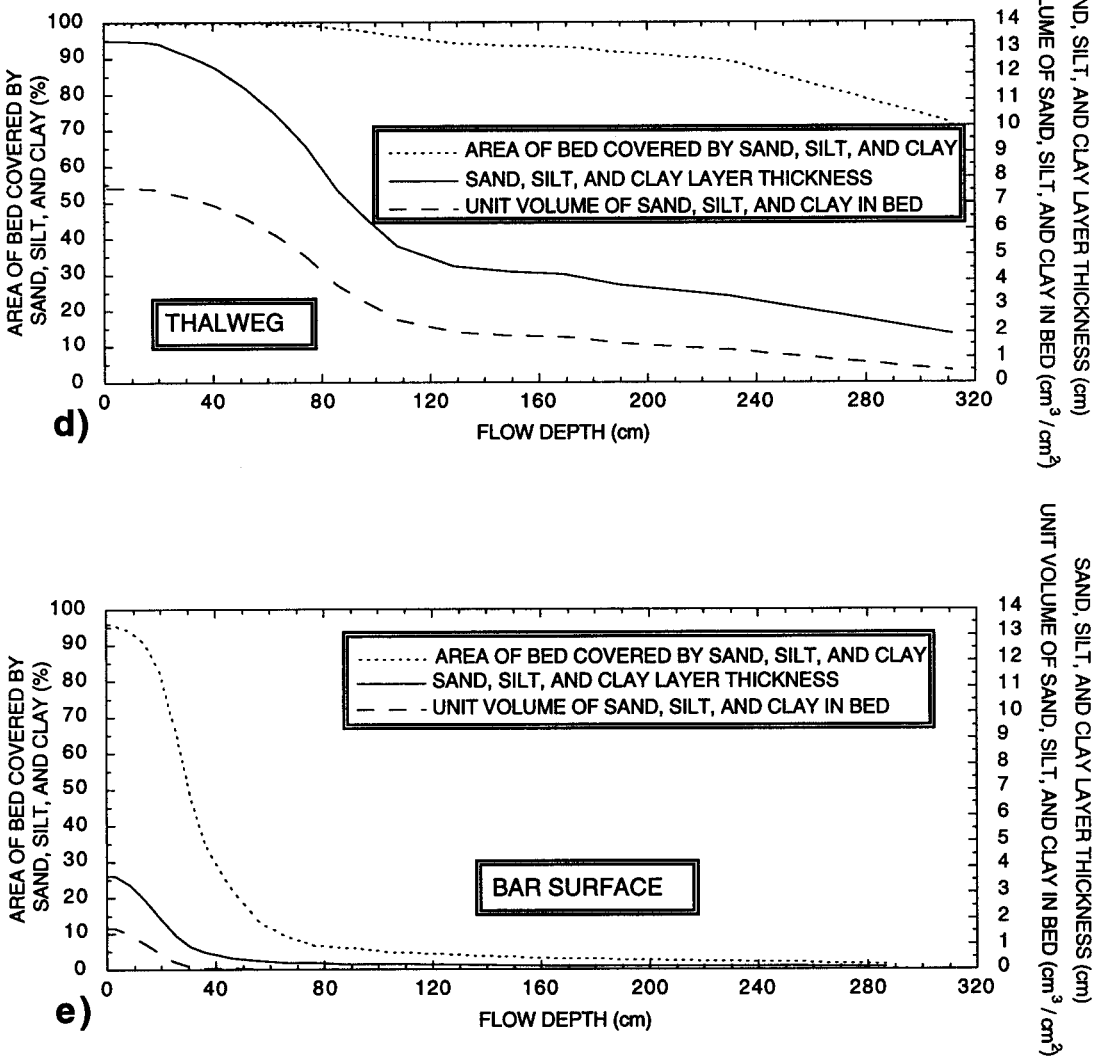

Figure 4.9 (continued): **(d)** Predicted area of the bed covered by sand, silt, and clay, predicted thickness of sand, silt, and clay, and predicted unit volume of sand, silt, and clay as functions of the model-predicted flow depth in the thalweg. **(e)** Predicted area of the bed covered by sand, silt, and clay, predicted thickness of sand, silt, and clay, and predicted unit volume of sand, silt, and clay as functions of the model-predicted flow depth on the bar surface.

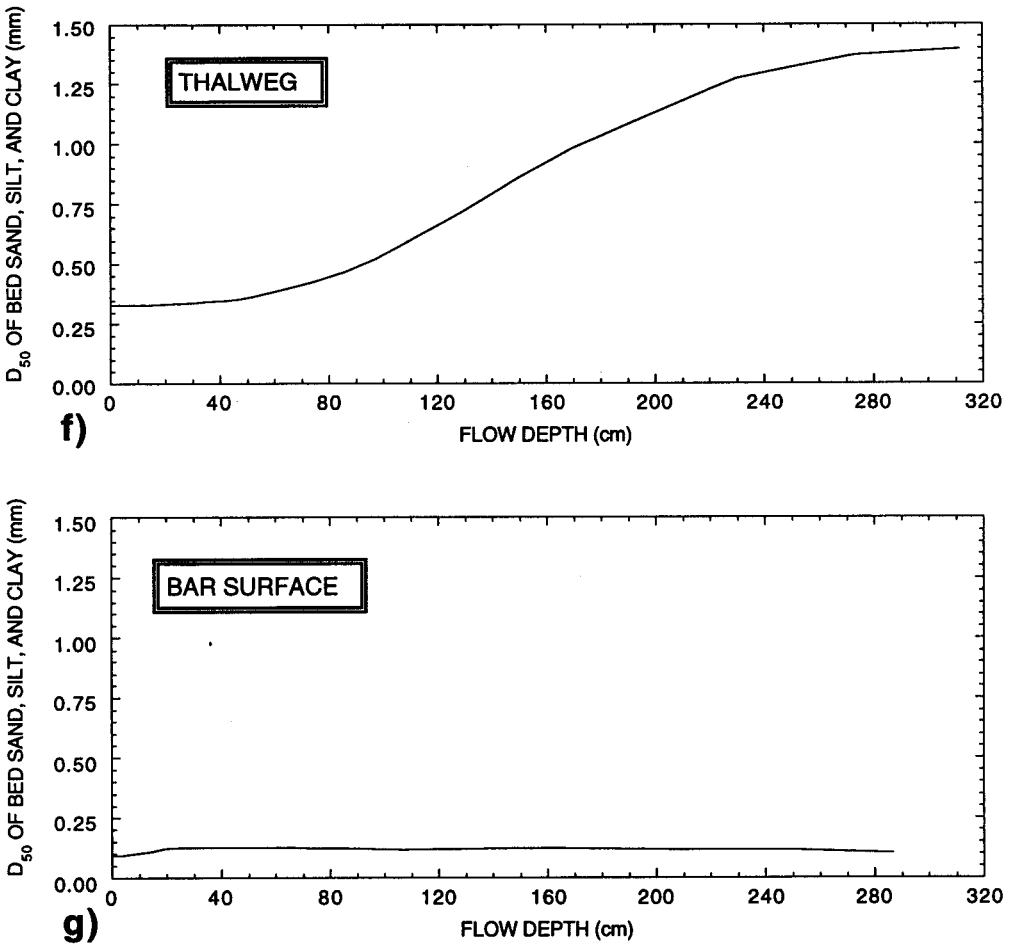

Figure 4.9 (continued): **(f)** Predicted D_{50} of the sand, silt, and clay on the bed as a function of the model-predicted flow depth in the thalweg. **(g)** Predicted D_{50} of the sand, silt, and clay on the bed as a function of the model-predicted flow depth on the bar surface.

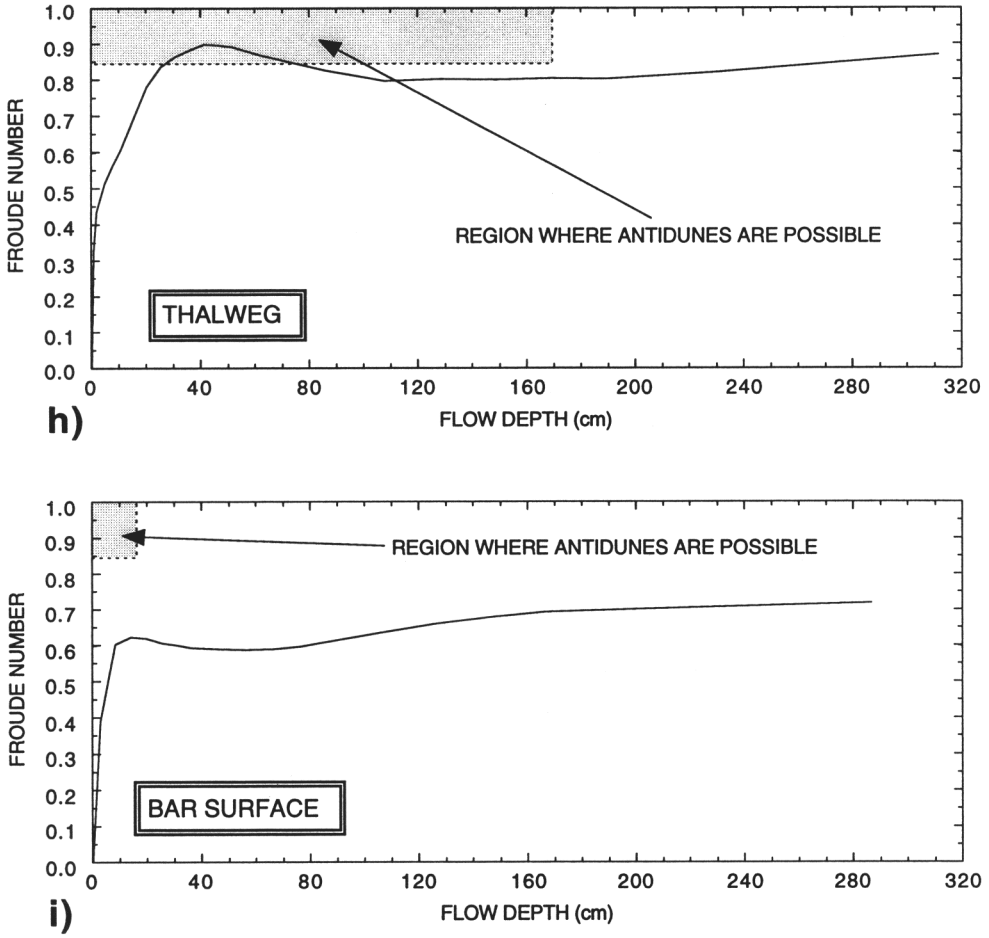

Figure 4.9 (continued): **(h)** Predicted Froude number as a function of the model-predicted flow depth in the thalweg. Antidunes are predicted to occur when the Froude-number curve intersects the "region where antidunes are possible". **(i)** Predicted Froude number as a function of the model-predicted flow depth on the bar surface; shown is the "region where antidunes are possible". Because the Froude-number curve does not intersect the "region where antidunes are possible", antidunes are never predicted to occur on the bar surface.

Also in agreement with field observations, the model predicts that antidunes will be only be present in the thalweg (Figures 4.9h and 4.9i).[7] The model predicts that D_{84} of the gravel will remain buried at flow depths up to about 200 cm in the thalweg; so, for flows less than bankfull (i.e., 180 cm) in the thalweg, the upper limit on antidune occurrence is only the Froude number criterion (Figure 4.9d). Antidunes are never predicted to exist on the bar surface because the sand, silt, and clay layer is too thin.

4.3e: TEST 5: Comparison of model-predicted and measured depth-integrated suspended-sediment concentrations in each size class

The fifth test compares model predictions to measurements of depth-integrated suspended-sediment concentration in each size class in the Lees Ferry, AZ reach of the Paria River.[8] As shown in this section, the model-predicted concentration of each size class of suspended sand is in good agreement with all measurements; and, the model-predicted concentration of suspended silt and clay is in reasonable agreement with the measured "non-monsoon" season concentrations. Furthermore, because the initial thickness of the sand, silt, and clay layer used as input into the model was that for a "replenished supply", model predicted suspended-sand concentrations are in the best agreement with those measured after smaller floods.[9] Results from this test provide general support for the two working hypotheses and five physical assumptions that were used to develop the model, with two minor exceptions. The second working hypothesis that "the mass of each sediment grain size is conserved on the reach scale" may begin to break down during the course of the largest floods (as suggested in Sections 3.2c and 4.3a), and the third physical assumption that "form drag from channel-scale features is negligible" is not true on average at discharges less than about 10 m^3/s (as suggested in Section 4.3c).

Differences between measurable and predictable suspended-sediment concentrations

Prior to comparing model predictions and measurements, it is important to distinguish between what a depth-integrated suspended-sediment sampler measures and

---

[7]The "region where antidunes are possible" in Figures 4.9h and 4.9i is defined as existing at a Froude number greater than the critical value of 0.844 for antidunes (Kennedy, 1963) and at a flow depth at which D_{84} of the gravel is still buried by the sand, silt, and clay.

[8]The data used in this comparison are presented in Section 3.2a.

[9]The model-input thickness of the sand, silt, and clay layer is interpreted to reflect a "replenished supply" because the thickness is based on measurements made in March-April 1993 after a series of small floods; see discussion in Section 3.2c.

what the model predicts. The concentrations of suspended sediment measured with such as sampler, even when used properly, differ from those predicted by suspended-sediment theory in three significant ways.

First, as mentioned in Chapter 3, depth-integrated suspended-sediment samplers cannot measure the true depth-integrated concentration in a river because they miss the lowest part of the flow where the concentrations of suspended sediment are the highest. The model, in contrast, can calculate the depth-integrated sediment concentration from the top of the bedload layer at z_a to the water surface (Figure 4.10). As shown in Figure 4.10, a depth-integrated suspended-sediment sampler can only measure the true depth-integrated concentration for the size class with no vertical concentration gradient, which, for this example, is only the suspended silt and clay.

The second difference between the suspended-sediment concentration measured by depth-integrated suspended-sediment samplers and that predictable by theory is due to the difference between a temporal and a spatial average of sediment concentration. Since depth-integrated samplers move through the flow at a constant transit velocity, they do not measure the temporal average of sediment concentration at each position in the flow. Thus, depth-integrated suspended-sediment samplers may spatially integrate potentially temporally anomalous concentrations. In contrast, the model is derived to predict the temporal average of sediment concentration over time scales long relative to the time scale of the turbulent velocity fluctuations. As defined in equation 3.66, the actual concentration of each sediment size-class m that the depth-integrated sampler is measuring at each point is $\epsilon_m = \bar{\epsilon}_m + \epsilon'_m$. The model, however, is only capable of predicting $\bar{\epsilon}_m$ at each level z in the flow and, in rivers, ϵ'_m may be as large or larger than $\bar{\epsilon}_m$. Also, since the sampler samples at the local flow velocity, the suspended-sediment sample is collected at the local velocity $u = \bar{u} + u'$ while the model can only predict $\bar{u}$ at each level z in the flow.

The third difference between the suspended-sediment concentration measured by depth-integrated suspended-sediment samplers and that predictable by theory arises from the discharge-weighted nature of samples collected with depth-integrated suspended-sediment samplers. Given the quasi-logarithmic shape of a velocity profile in a river and the fact that a depth-integrated sampler is sampling at the instantaneous flow velocity at each level z in the flow, the sample collected is not a true measure of the average concentration in the portion of the flow that the sampler traverses, but is a discharge-weighted concentration. Thus, for a full one-pint sample, more of the sample is from the upper part of the flow where the velocity is greatest, and where the sediment concentrations are lowest for most size classes of sediment.

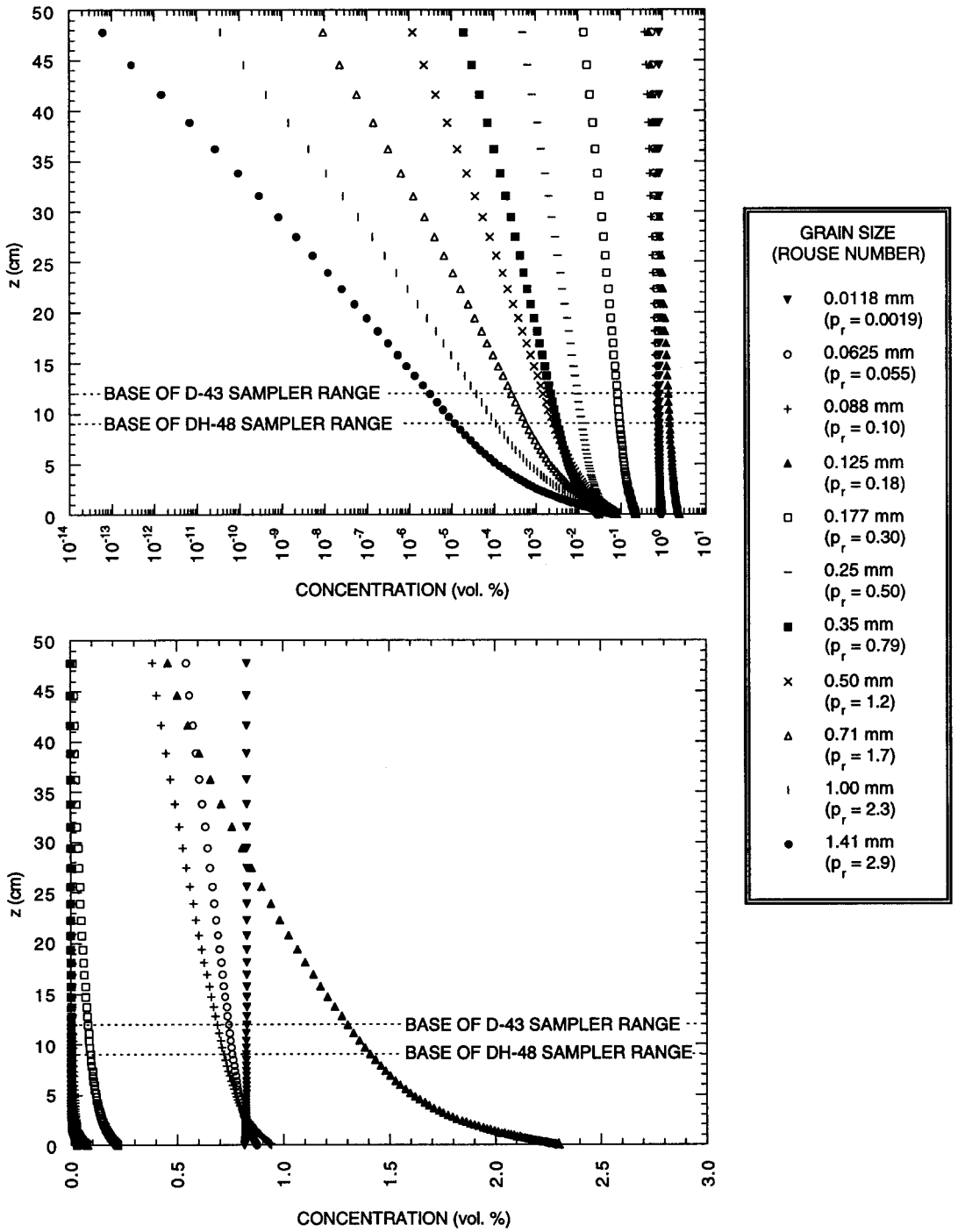

Figure 4.10: Log-linear and linear graphs of the model-predicted suspended-sediment concentration profiles for the 11 size classes of sand, silt, and clay in the Paria River at station +3.0 m for a flow depth of 50 cm; the Rouse numbers for each sediment size class are shown in parentheses in the legend. Superimposed on the graphs are the lower sampling limits for the D-43 and the DH-48 suspended-sediment samplers.

Modeling depth-integrated suspended-sediment samplers

With these three major differences clarified, an expression to model the behavior of a depth-integrated suspended-sediment sampler can be derived and then be used to compare model predictions to measurements. An equation describing the behavior of a depth-integrated sampler traveling at a constant velocity through the flow at one vertical is as follows:

$$(c_m)_{sampler} = \frac{1}{\langle u_{fill} \rangle} \frac{1}{(h-10)} \int_{10}^{h} (\bar{u} + u')(\bar{c}_m + c_m')dz, \tag{4.1}$$

where $(c_m)_{sampler}$ is the concentration of each size-class m that the sampler is measuring as it travels at a constant transit velocity through the flow and $\langle u_{fill} \rangle$ is the vertically averaged sampler filling velocity that can be defined as follows for an isokinetic nozzle:

$$\langle u_{fill} \rangle = \frac{\overline{dV_{sampler}/dt}}{A_{nozzle}} = \frac{1}{(h-10)} \int_{10}^{h} (\bar{u} + u')dz, \tag{4.2}$$

where $\overline{dV_{sampler}/dt}$ is the change in the volume of sampled material with respect to time averaged over the time of sampling, and A_{nozzle} is the cross-sectional area of the nozzle on the sampler. Therefore, by substituting equation 4.2 into equation 4.1, the final equation that defines the concentration of each size-class m measured by a depth-integrated sampler at one vertical is:

$$(c_m)_{sampler} = \frac{1}{(h-10)} \left(\frac{\int_{10}^{h} (\bar{u} + u')(\bar{c}_m + c_m')dz}{\frac{1}{(h-10)} \int_{10}^{h} (\bar{u} + u')dz} \right), \tag{4.3}$$

and the equation that defines the concentration of each size-class m in the cross-section as measured by a depth-integrated sampler is:

$$\left((c_m)_{sampler} \right)_{cs} = \frac{1}{\int_0^W \int_{10}^{h} dzdy} \left(\frac{\int_0^W \int_{10}^{h} (\bar{u} + u')(\bar{c}_m + c_m')dzdy}{\frac{1}{\int_0^W \int_{10}^{h} dzdy} \int_0^W \int_{10}^{h} (\bar{u} + u')dzdy} \right), \tag{4.4}$$

where W is the width of the cross-section.

Since the model cannot predict exactly what the depth-integrated sampler measures because the model predicts only the temporal average of u and c_m at each level z, the equation used to model the "sampled" mean concentration of each size-class m measured by the depth-integrated sampler at each vertical is:

$$(\epsilon_m)_{modeled\ sampler} = \frac{\int_{10}^{h} \bar{u}\bar{\epsilon}_m dz}{\frac{1}{(h-10)}\int_{10}^{h} \bar{u} dz}, \tag{4.5}$$

and the equation used to model the "sampled" mean concentration of each size-class m measured by the depth-integrated sampler in the cross-section is:

$$\left((\epsilon_m)_{modeled\ sampler}\right)_{cs} = \frac{1}{\int_0^W \int_{10}^{h} dz dy} \int_0^W \frac{\int_{10}^{h} \bar{u}\bar{\epsilon}_m dz}{\frac{1}{(h-10)}\int_{10}^{h} \bar{u} dz} dy. \tag{4.6}$$

The equation used to calculate the "true" mean concentration of each size-class m from the top of the bedload layer to the water surface at each vertical in the modeled cross-section is:

$$\langle \bar{\epsilon}_m \rangle = \frac{1}{h}\int_{z_a}^{h} \bar{\epsilon}_m dz, \tag{4.7}$$

and the equation used to calculate the "true" mean concentration of each size class m from the top of the bedload layer z_a to the water surface in the modeled cross-section, $(\bar{\epsilon}_m)_{cs}$, is:

$$(\bar{\epsilon}_m)_{cs} = \frac{1}{\int_0^W \int_{z_a}^{h} dz dy} \int_0^W \int_{z_a}^{h} \bar{\epsilon}_m dz dy. \tag{4.8}$$

Comparison of model-predicted and measured depth-integrated concentrations of suspended sand

Comparison of the model-predicted depth-integrated suspended-sand concentrations by size-class to the 1954-1976 and 1983 USGS measured depth-integrated suspended-sand concentrations by size-class appear in Figures 4.11a through 4.11k. Because the 1954-1976 and 1983 suspended-sand data sets differ (see Section 3.2c), they are plotted with different symbols. Because the input cross-section geometry for the model is similar to the shape of the cross-section in which the majority of 1954-1976 suspended sediment data were measured, model predictions should agree more closely with the 1954-1976 measurements than the 1983 measurements. Furthermore, because the initial thickness of the sand, silt, and clay layer used as input into the model is that for a "replenished supply", the model predicted suspended-sand concentrations should be in the best agreement with suspended-sand concentrations measured after smaller floods (Figure 4.11b).

The total suspended-sand concentration data in Figure 4.11a and the suspended-sand size-class concentration data in Figures 4.11c through 4.11k have considerable spread, i.e., from one to four orders of magnitude in volume concentration for each value of instantaneous fluid discharge. The 1983 data collected in the incised channel near the gage have higher concentrations of suspended sand in each size class as a function of fluid

Figure 4.11 (a): Comparison of: model predictions of the "true" mean and maximum depth-integrated concentrations of suspended total sand (0.0625-2.0 mm); model predictions of the "sampled" mean and maximum depth-integrated concentrations of suspended total sand; and the 1954-1976, and 1983 measurements of depth-integrated concentration of suspended total sand. The solid, thin "model-predicted true mean concentration" line is calculated by summing equation 4.8 over all 10 sand size classes; the dashed, thin "model-predicted true maximum concentration" line is the maximum value in the cross-section of equation 4.7 summed over all ten sand size classes; the solid, thick "model-predicted sampled mean concentration" line is calculated by summing equation 4.6 over all ten size-classes; and, the dashed thick "model-predicted sampled maximum concentration" line is the maximum value in the cross-section of equation 4.5 summed over all ten size classes of sand. So that zero values of concentration appear in the log-log plots, zero concentrations are plotted as being equal to 1×10^{-7} %. The thick, vertical "model-predicted sampled mean and maximum concentration" line intersecting the x-axis at a discharge of 0.173 m^3/s indicates the discharge at which the flow is too shallow in the modeled cross-section to sample suspended sediment with the depth-integrated suspended-sediment samplers; and, the thin, vertical "model-predicted true mean and maximum concentration" line intersecting the x-axis at a discharge of 0.00059 m^3/s indicates the discharge at which no sand is in transport in the modeled cross-section. Kinks in the model-predicted concentrations are due to the geometric properties of the 1993 reach-averaged cross-section and the local supply of each sediment type in the 1993 reach-averaged cross-section.

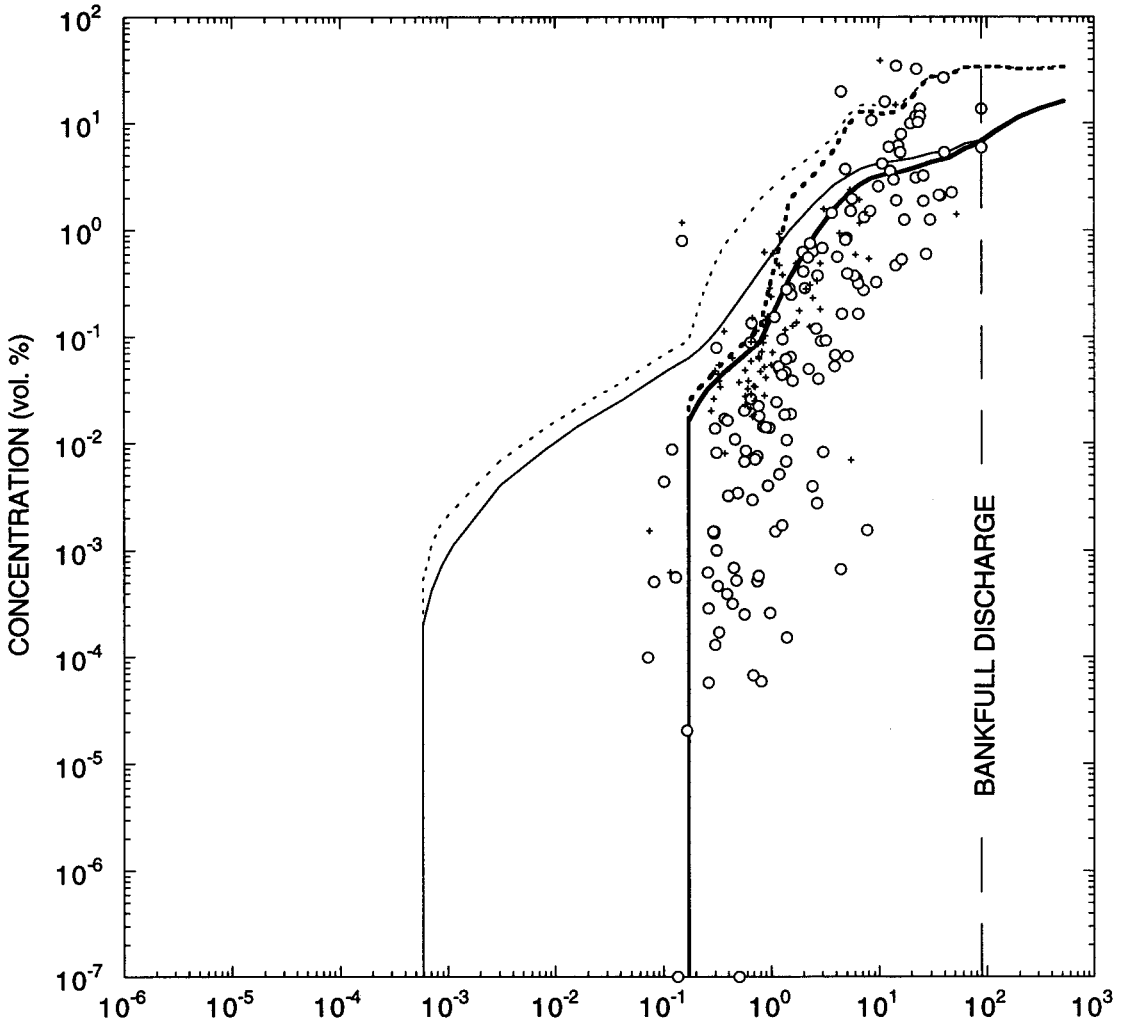

a)

- 1954-1976 MEASUREMENTS (n = 145)
- MODEL-PREDICTED "TRUE" MEAN CONCENTRATION IN THE CROSS-SECTION
- MODEL-PREDICTED "SAMPLED" MEAN CONCENTRATION IN THE CROSS-SECTION
- MODEL-PREDICTED "TRUE" MAXIMUM DEPTH-INTEGRATED CONCENTRATION IN THE CROSS-SECTION
- MODEL-PREDICTED "SAMPLED" MAXIMUM DEPTH-INTEGRATED CONCENTRATION IN THE CROSS-SECTION
- 1983 MEASUREMENTS (n = 81)

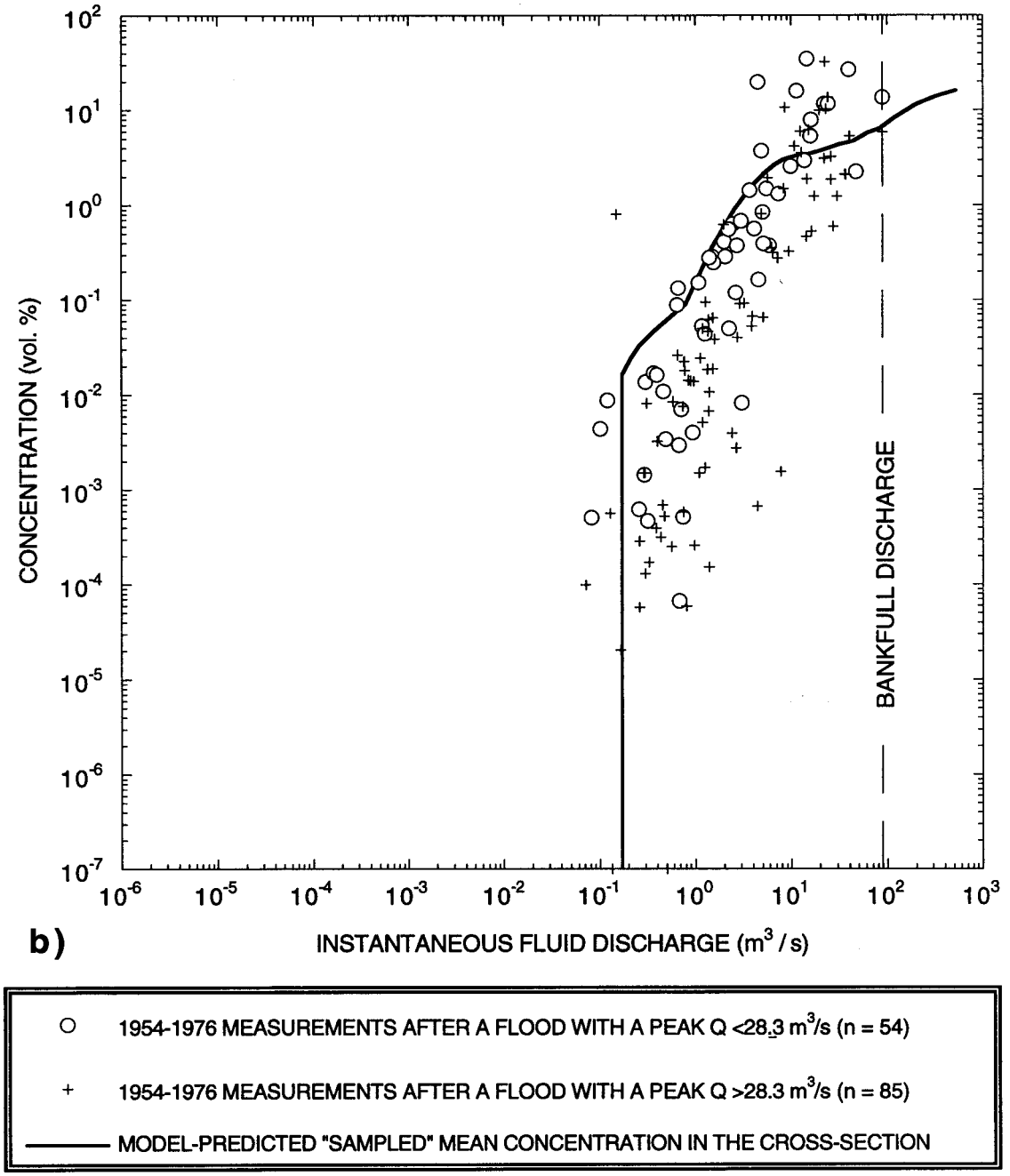

Figure 4.11 (continued): **(b)** Model-predicted "sampled" mean depth-integrated suspended-sand concentrations in the model-predicted cross-section and the 1954-1976 depth-integrated suspended-sand concentrations measured after smaller and larger floods. See caption for Figure 4.11a for further explanation of notation.

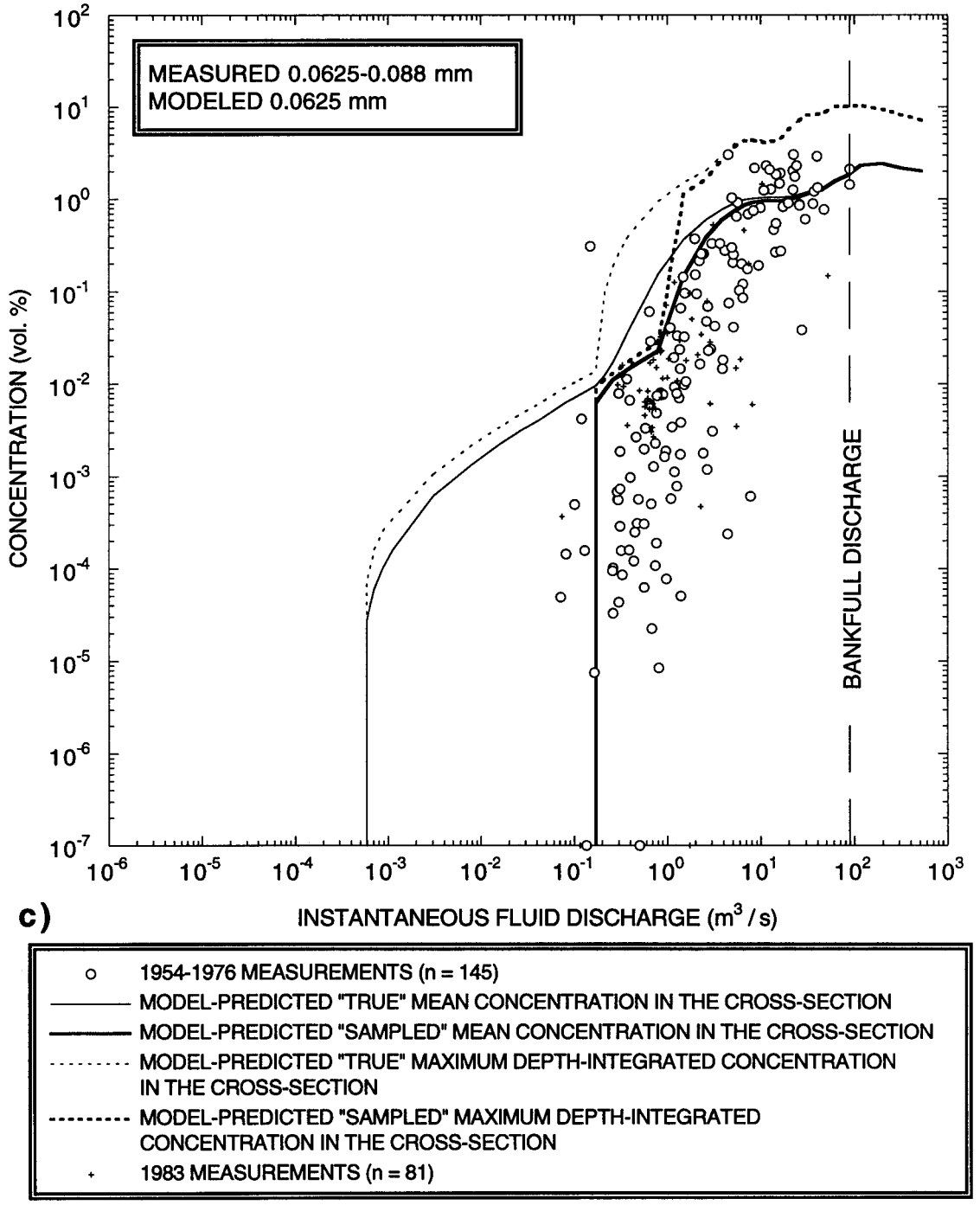

Figure 4.11 (continued): **(c)** Model-predicted "true" and "sampled" mean and maximum depth-integrated concentrations of 0.0625 mm suspended sand in the model-predicted cross-section and 1954-1976 & 1983 measured depth-integrated concentrations of suspended sand $\geq$0.0625 mm and <0.088 mm. See caption for Figure 4.11a for further explanation of notation.

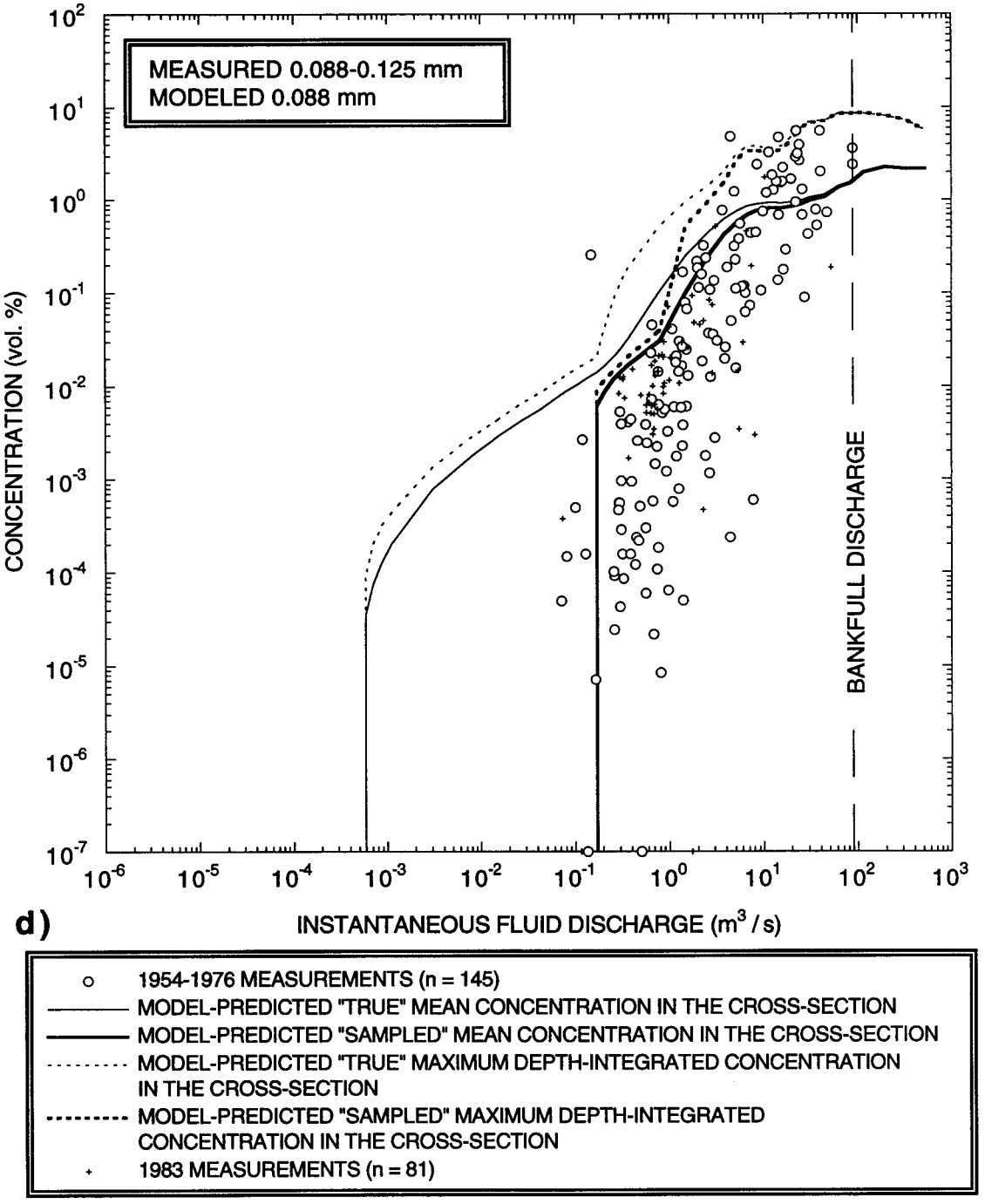

Figure 4.11 (continued): **(d)** Model-predicted "true" and "sampled" mean and maximum depth-integrated concentrations of 0.088 mm suspended sand in the model-predicted cross-section and 1954-1976 & 1983 measured depth-integrated concentrations of suspended sand $\geq$0.088 mm and <0.125 mm. See caption for Figure 4.11a for further explanation of notation.

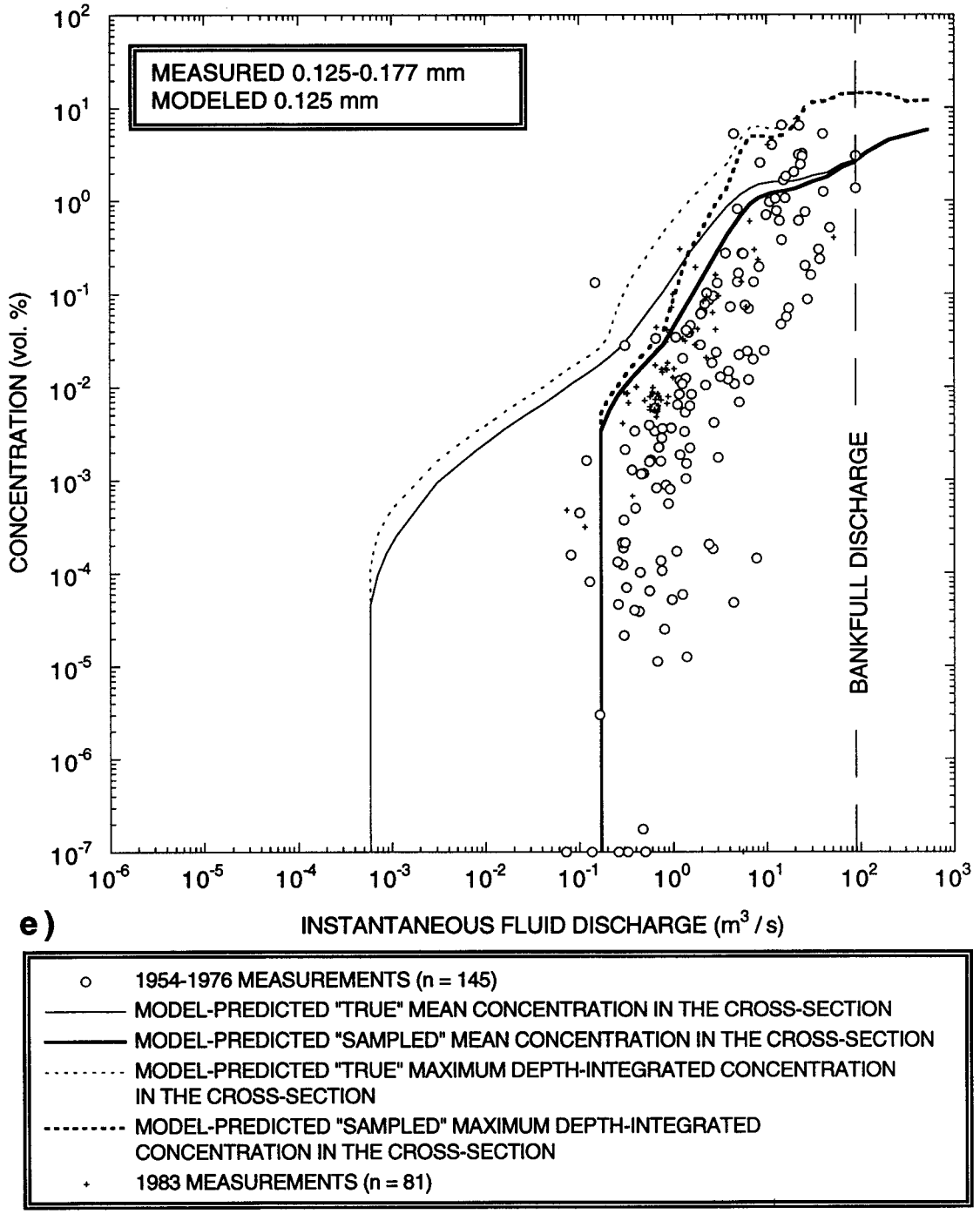

Figure 4.11 (continued): **(e)** Model-predicted "true" and "sampled" mean and maximum depth-integrated concentrations of 0.125 mm suspended sand in the model-predicted cross-section and 1954-1976 & 1983 measured depth-integrated concentrations of suspended sand $\geq$0.125 mm and <0.177 mm. See caption for Figure 4.11a for further explanation of notation.

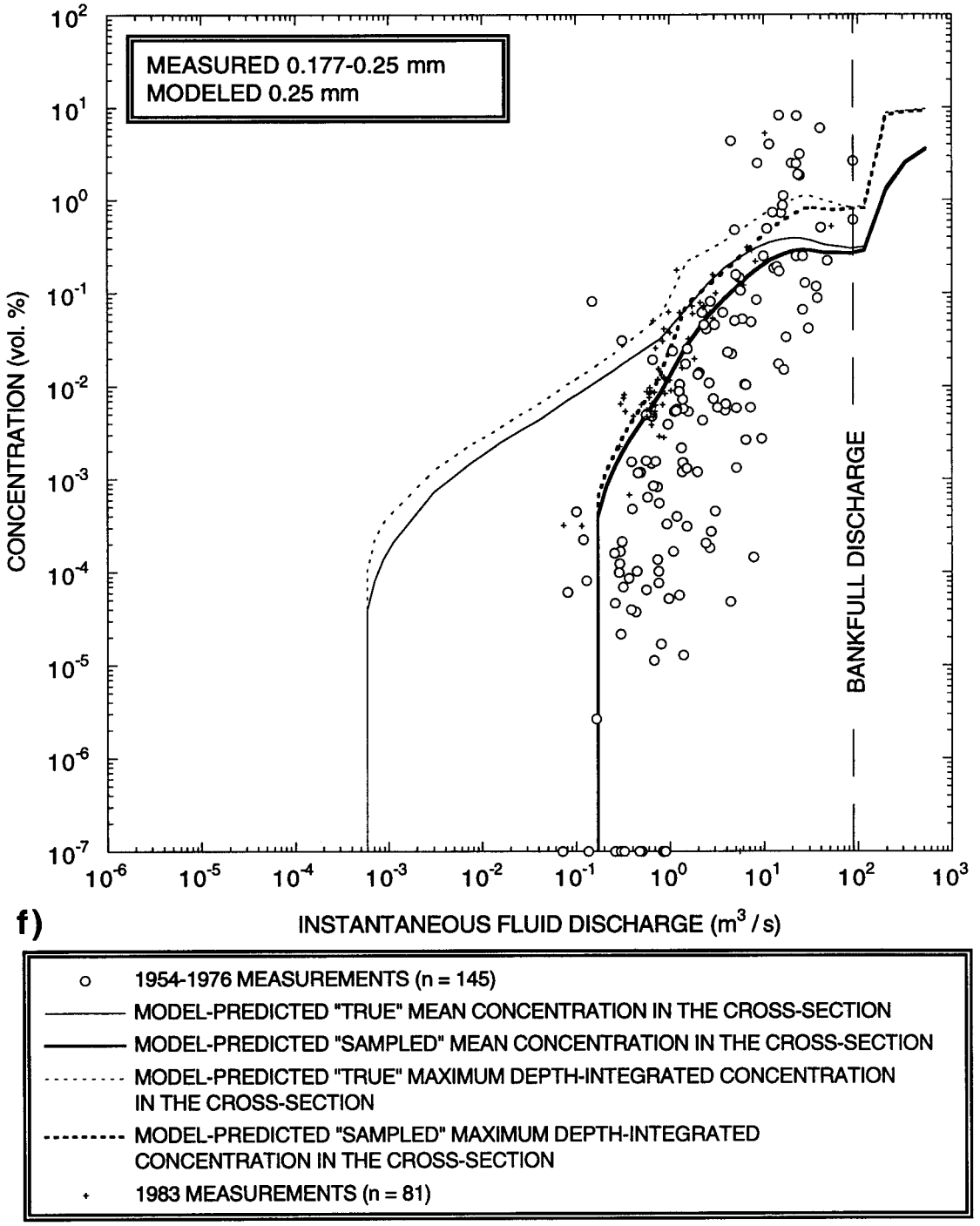

Figure 4.11 (continued): **(f)** Model-predicted "true" and "sampled" mean and maximum depth-integrated concentrations of 0.177 mm suspended sand in the model-predicted cross-section and 1954-1976 & 1983 measured depth-integrated concentrations of suspended sand $\geq$0.177 mm and <0.25 mm. See caption for Figure 4.11a for further explanation of notation.

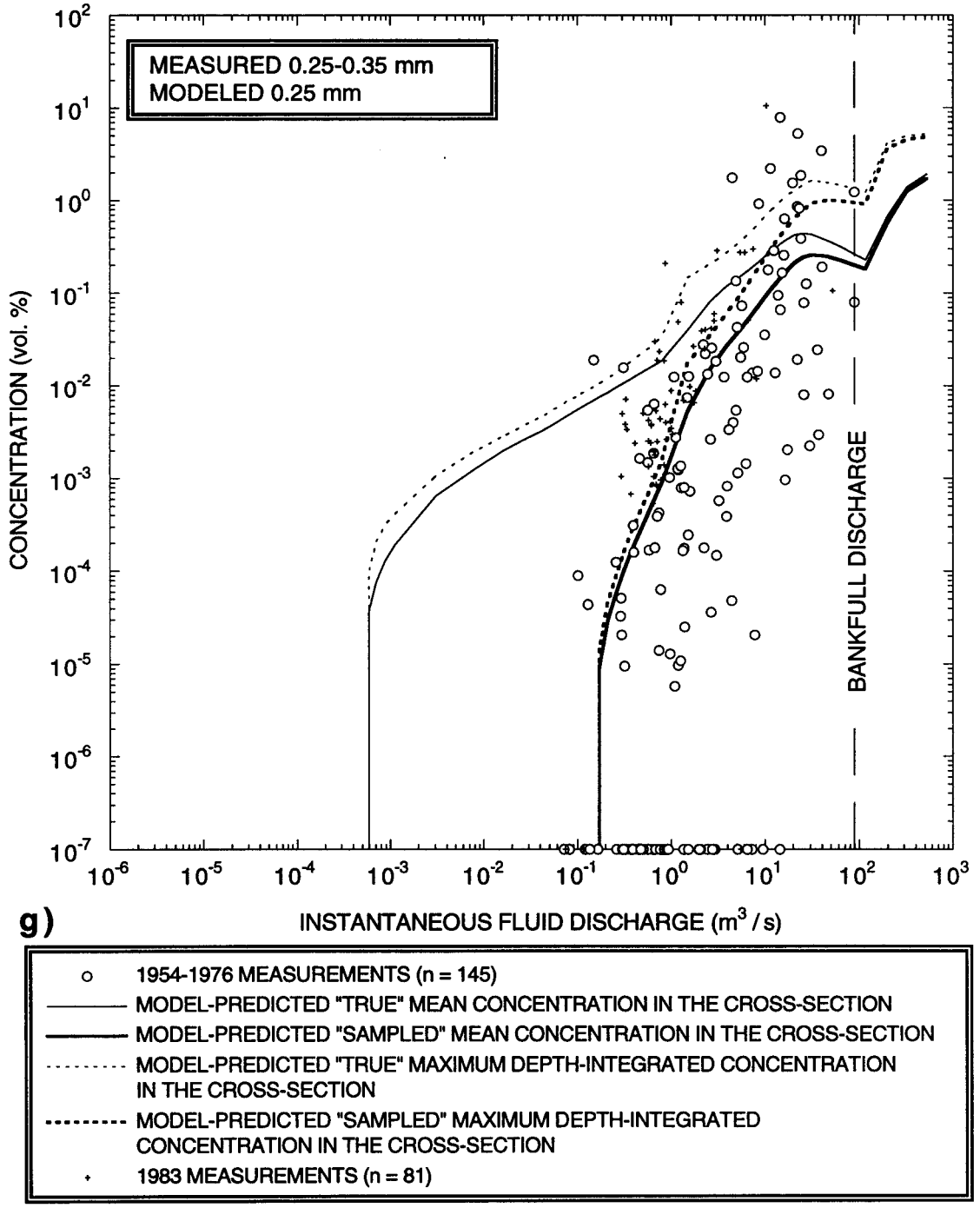

Figure 4.11 (continued): (g) Model-predicted "true" and "sampled" mean and maximum depth-integrated concentrations of 0.25 mm suspended sand in the model-predicted cross-section and 1954-1976 & 1983 measured depth-integrated concentrations of suspended sand $\geq$0.25 and <0.35 mm. See caption for Figure 4.11a for further explanation of notation.

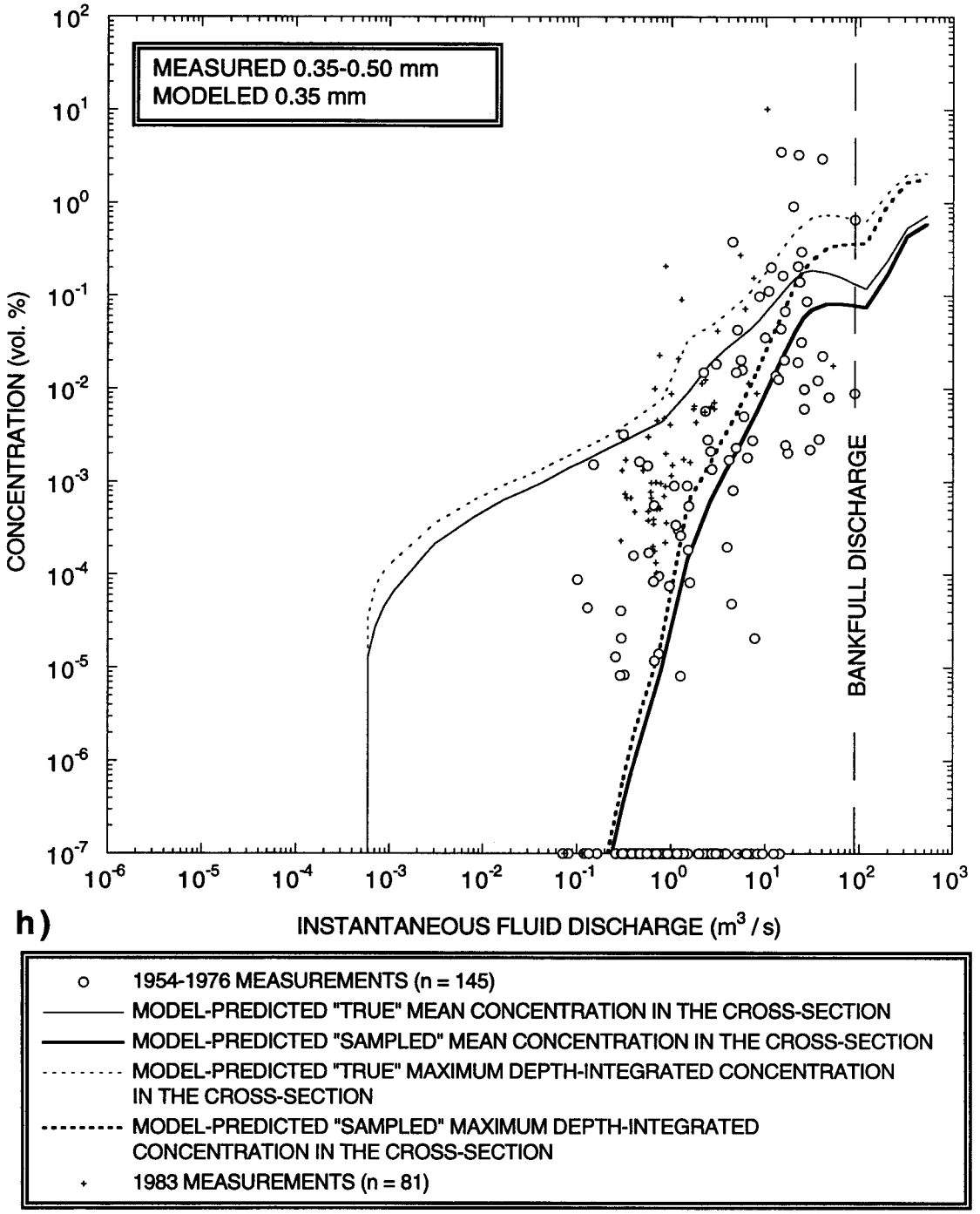

Figure 4.11 (continued): **(h)** Model-predicted "true" and "sampled" mean and maximum depth-integrated concentrations of 0.35 mm suspended sand in the model-predicted cross-section and 1954-1976 & 1983 measured depth-integrated concentrations of suspended sand $\geq$0.35 mm and <0.50 mm. See caption for Figure 4.11a for further explanation of notation.

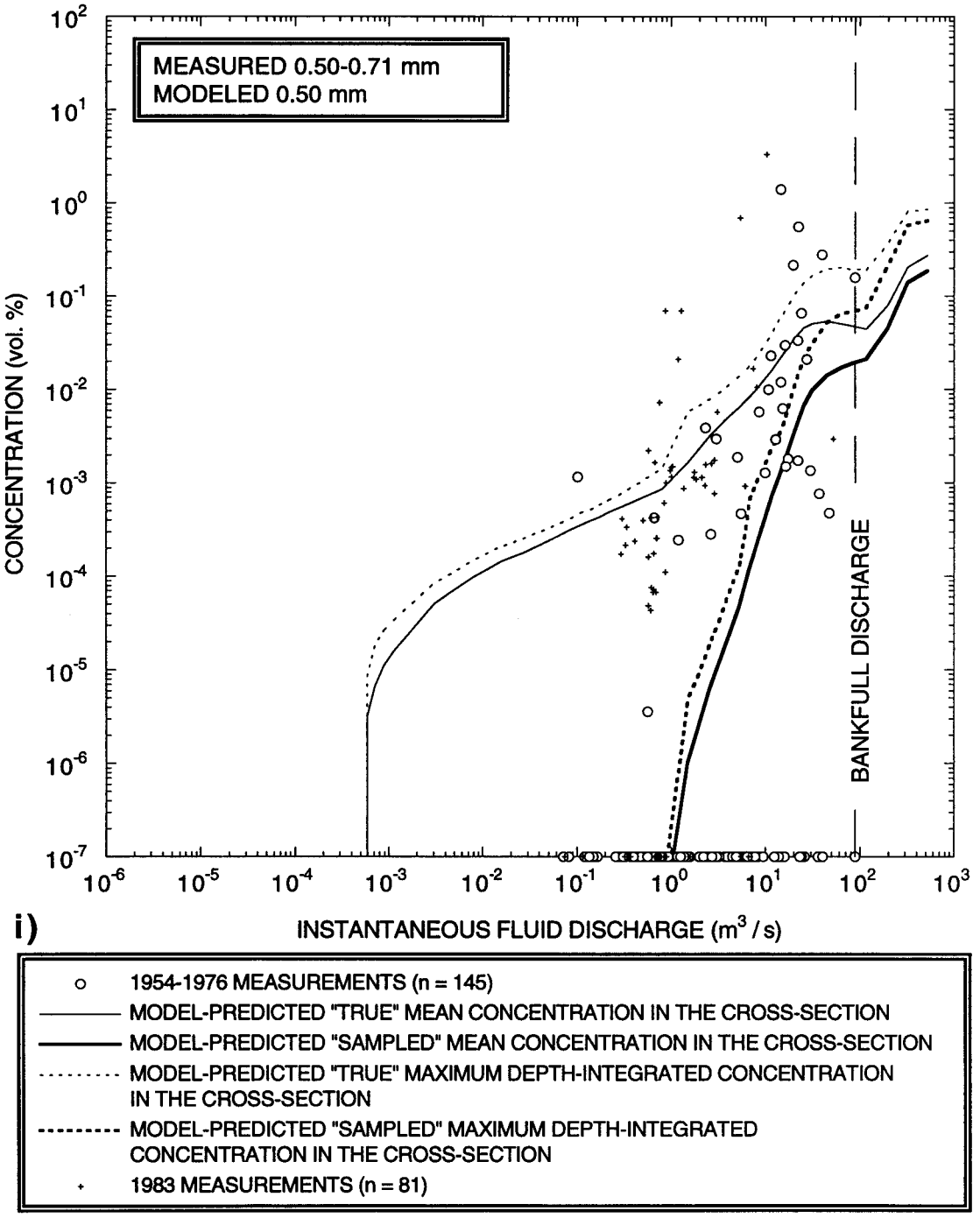

Figure 4.11 (continued): (i) Model-predicted "true" and "sampled" mean and maximum depth-integrated concentrations of 0.50 mm suspended sand in the model-predicted cross-section and 1954-1976 & 1983 measured depth-integrated concentrations of suspended sand $\geq$0.50 mm and <0.71 mm. See caption for Figure 4.11a for further explanation of notation.

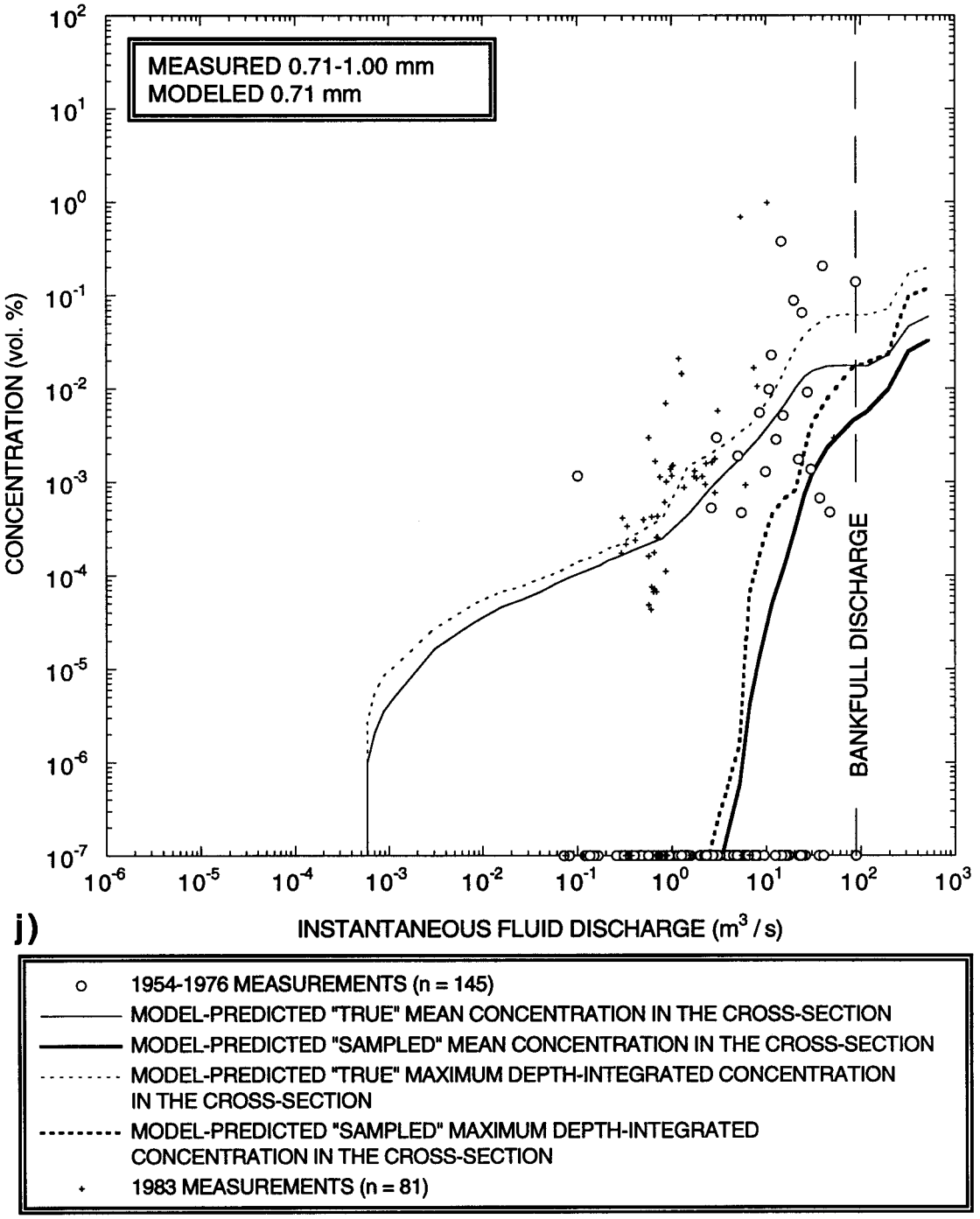

Figure 4.11 (continued): **(j)** Model-predicted "true" and "sampled" mean and maximum depth-integrated concentrations of 0.71 mm suspended sand in the model-predicted cross-section and 1954-1976 & 1983 measured depth-integrated concentrations of suspended sand $\geq$0.71 mm and <1.00 mm. See caption for Figure 4.11a for further explanation of notation.

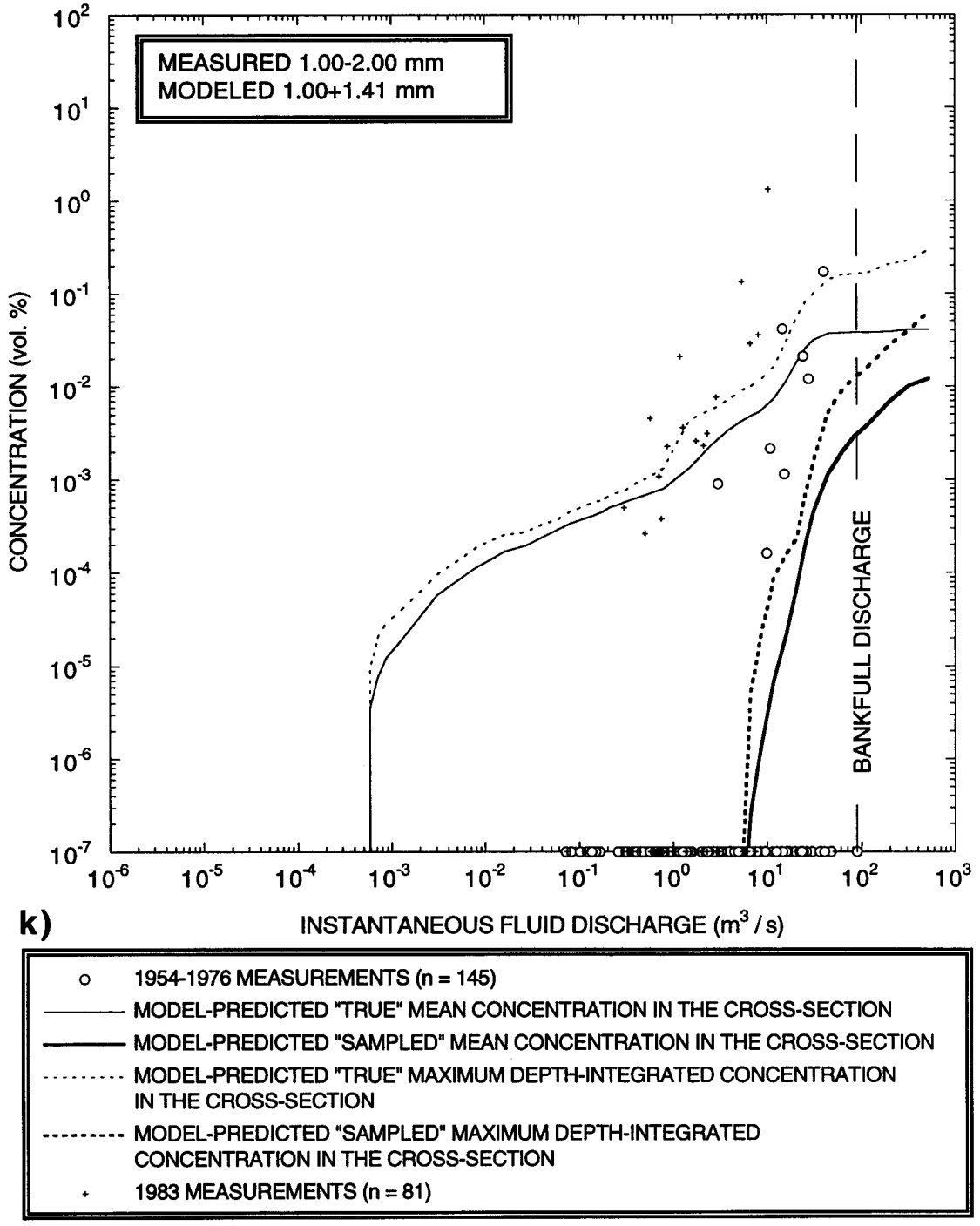

Figure 4.11 (continued): **(k)** Model-predicted "true" and "sampled" mean and maximum depth-integrated concentrations of combined 1.00 & 1.41 mm suspended sand in the model-predicted cross-section and 1954-1976 & 1983 measured depth-integrated concentrations of suspended sand ≥1.00 mm and <2.00 mm. See caption for Figure 4.11a for further explanation of notation.

discharge; and, this effect is enhanced for the coarser size classes (Figures 4.11f through 4.11k). This effect is attributed to the fact that for each value of fluid discharge, the flow depths are greater in the incised channel than they are in the equilibrium channel. Thus, for the same discharge, the values of total boundary shear stress are higher in the incised channel than in the equilibrium channel, resulting in higher concentrations of suspended sediment; and, since the advection length of a particle (defined in equation 3.1) gets progressively shorter as grain size increases, the coarsest sizes of sediment will show the greatest changes in concentration as a function of changes in the boundary shear stress due to changes in local channel geometry.

As shown in Figures 4.11a and 4.11b (and in a manner similar to the model predictions of cross-section maximum depth, cross-section area, and cross-section mean velocity in Section 4.3c), the model-predicted "sampled" concentrations fall in the middle of the 1954-1976 measured concentrations of suspended sand only for discharges in excess of about 10 m^3/s (for both all of the 1954-1976 measurements and the subset of these measurements made after floods with peak discharges less than or equal to 28.3 m^3/s). Likewise, just as the model predictions of maximum depth and cross-section area fell at the lower bound and the model predictions of mean velocity fell at the upper bound of the lower-flow data in Section 4.3c, the model-predicted "sampled" concentrations of suspended sand fall at the upper bound of the 1954-1976 measured concentrations of suspended sand for flows less than about 10 m^3/s. Furthermore, at flows less than about 10 m^3/s, the model also predicts the upper bound of the 1954-1976 measured suspended-sand concentration for the 0.0625-0.088 mm, 0.088-0.125 mm, 0.125-0.177 mm, and 0.177-0.25 mm, and 0.25-0.35 mm size classes. This behavior of the model can be explained by the fact that, at flows less than 10 m^3/s, suspended-sediment measurements (like the discharge measurements in Section 4.3c) are typically made in "backwatered" pools in which the assumption that "form drag from channel-scale features is negligible" is not valid.

Because the thicknesses of the sand, silt, and clay layer used as model input were measured in March-April 1993 after a series of floods with peak discharges less than 30% of the bankfull discharge, the model predictions of suspended-sand concentrations should be those associated with a "replenished state" of sand, silt, and clay supply (see Section 3.2c). Thus, as expected, the model-predicted "sampled" concentrations of suspended sand are in best agreement with the 1954-1976 concentrations of suspended sand measured after smaller floods, i.e., floods with peak discharges less than about 28.3 m^3/s (Figure 4.11b). Agreement between the model predictions and "replenished state" measurements is

the desired relationship for the majority of the time in the Paria River because 84% of all floods during the period of gage record at Lees Ferry, AZ have had peak discharges less than 28.3 m^3/s; thus, for 84% of the time, the Paria River is in a replenished, not a depleted, state with respect to the supply of sand, silt, and clay on the bed.

With regard to the coarser size classes of sand (Figures 4.11h through 4.11k), the predicted depth-integrated "sampled" concentration is below the non-zero measured concentrations. This apparent disagreement between model and measurements that progressively grows as a function of grain size is, in fact, not real, but merely an artifact of graphing the comparison in log-log space. For example, only 54% of the 0.35-0.50 mm, only 21% of the 0.50-0.71 mm, only 14% of 0.71-1.0 mm, and only 6% of the 1.0-2.0 mm measured concentrations are greater than zero. Therefore, the model predictions of "sampled" concentrations are actually in excellent agreement with the majority of the 145 measurements of concentration, which are zero values falling on the x-axes in Figures 4.11h through 4.11k.

Comparison of model-predicted and measured sorting of suspended sand

Another way to evaluate the model predictions of suspended-sand concentration, is to compare the model-predicted with the measured grain-size distribution of the suspended sand (Figure 4.12). As with the model predictions of suspended-sand concentration for each size class, the model predictions of the "sampled" D_{16}, D_{50}, and D_{84} of the suspended sand are in good agreement with the measurements. Again, since the total boundary shear stresses are higher in the incised channel than in the equilibrium channel for the same fluid discharge, the 1983 measurements of the grain-size distribution of the suspended sand are coarser than the 1954-1976 measurements.

Comparison of model-predicted and measured concentration of suspended silt and clay

Model predictions of the concentration of suspended silt and clay based on the local supply in the 1993 reach-averaged cross-section agree reasonably well (i.e., within a factor of two of the highest values) with the "non-monsoon" season measurements of suspended silt and clay concentration (Figure 4.13a). Because the model forces the local mass conservation of each size class of sediment between the bed and the flow, this level of agreement lends further support to the interpretation made in Section 2.3c that the "non-monsoon" season silt and clay concentration is largely in equilibrium with the supply on the bed in the Lees Ferry reach. As demonstrated in Section 3.2c, the suspended-silt and clay concentration in the monsoon season (July 1 through October 31) is statistically distinct

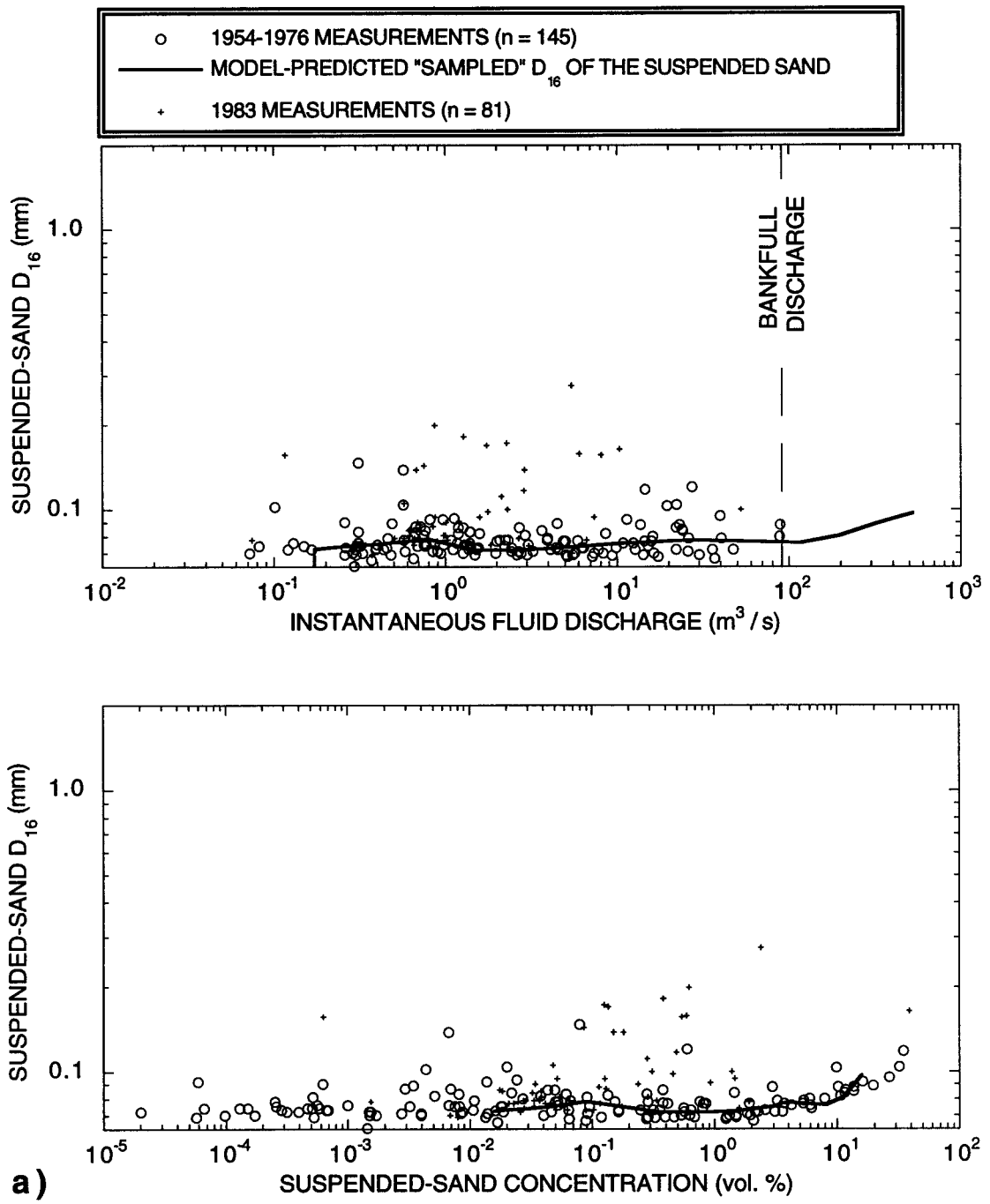

Figure 4.12: **(a)** D_{16} of the 1954-1976 sampled suspended sand, the model prediction of the "sampled" suspended sand, and the 1983 sampled suspended sand functions of both instantaneous fluid discharge and mean "sampled" suspended-sand concentration in the cross-section. A zero value of grain size in means that no sand was predicted to be sampled by the depth-integrated sampler because of predicted flow depths less than 10 cm.

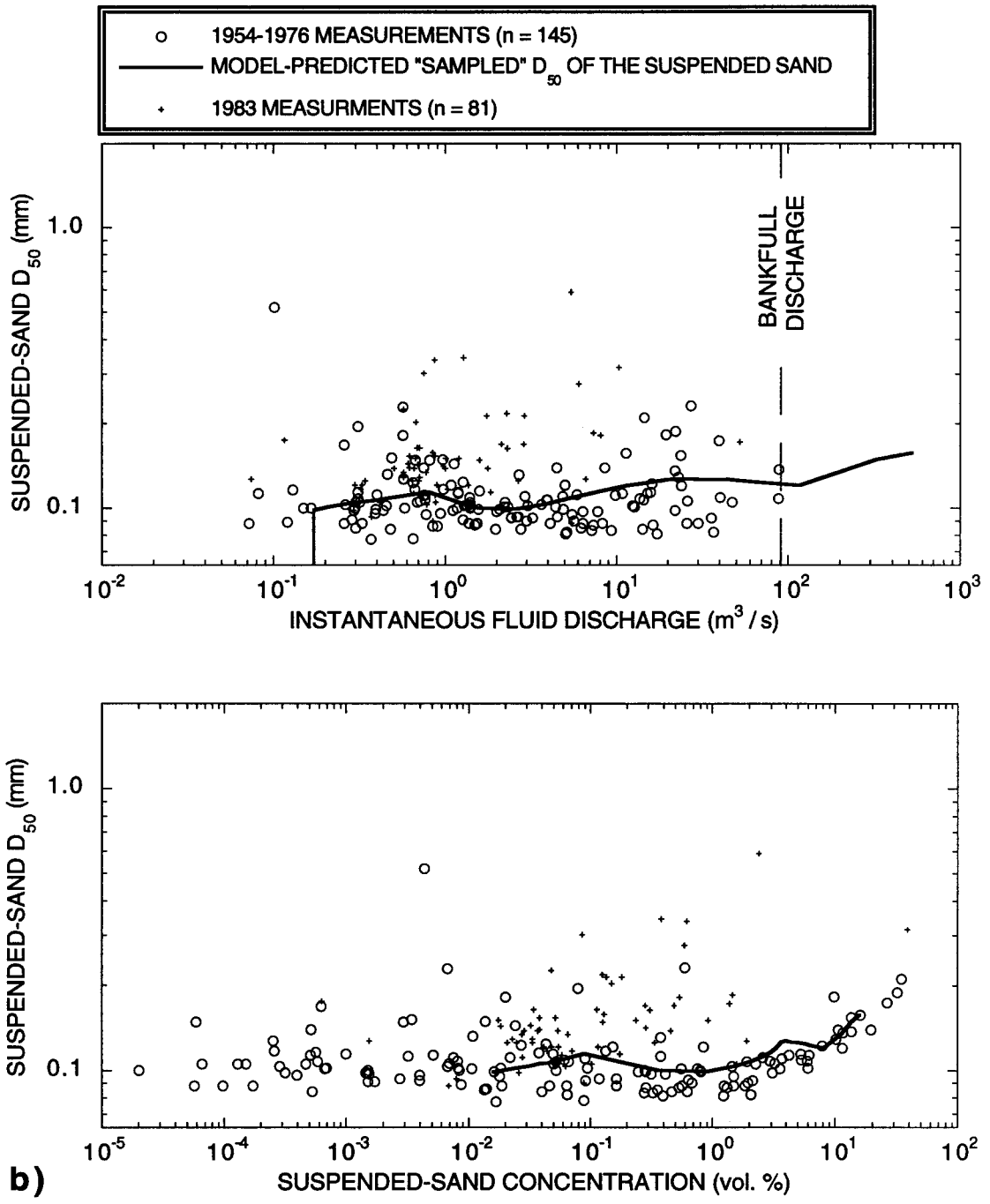

Figure 4.12 (continued): **(b)** D_{50} of the 1954-1976 sampled suspended sand, the model prediction of the "sampled" suspended sand, and the 1983 sampled suspended sand functions of both instantaneous fluid discharge and mean "sampled" suspended-sand concentration in the cross-section. A zero value of grain size in means that no sand was predicted to be sampled by the depth-integrated sampler because of predicted flow depths less than 10 cm.

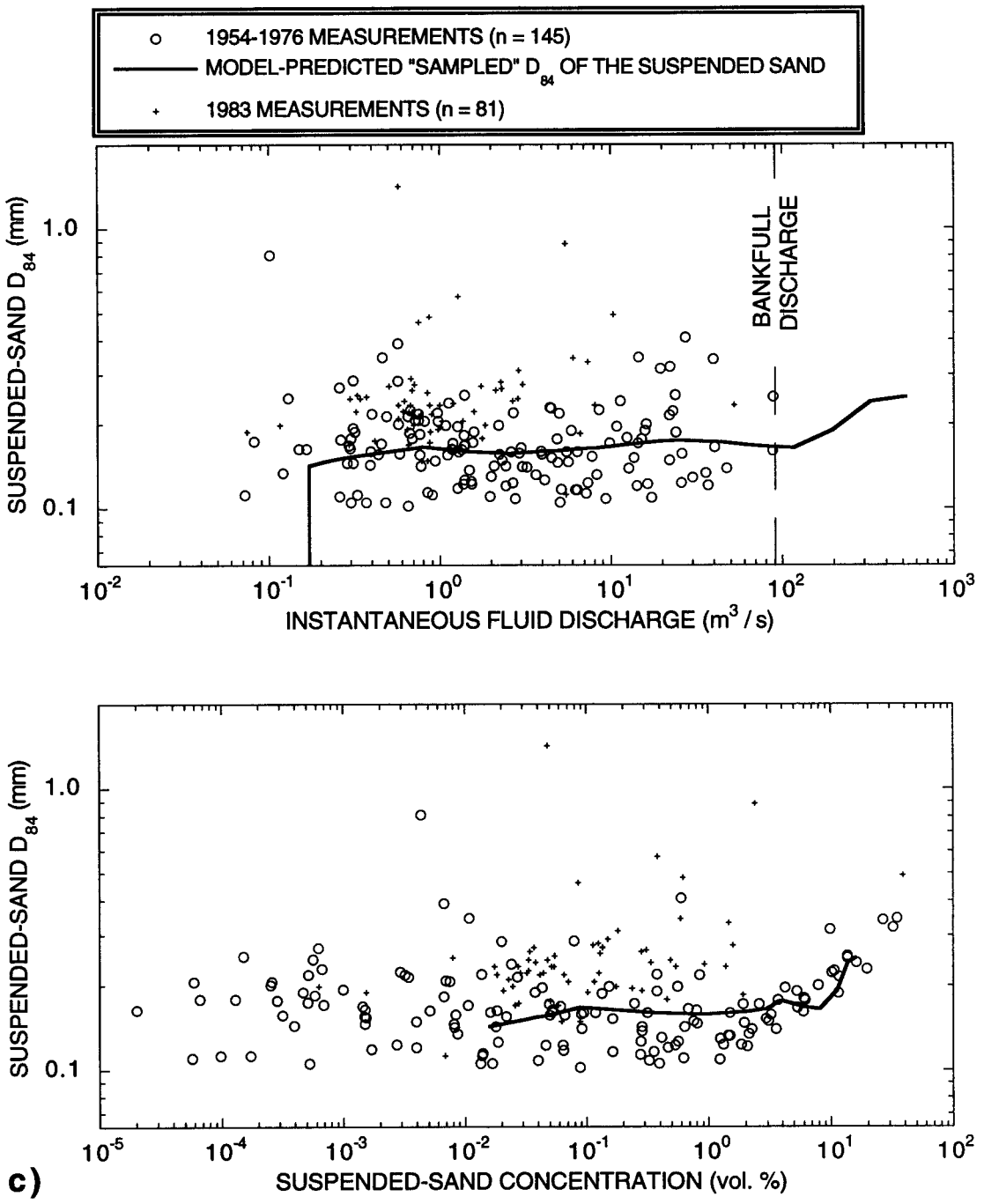

Figure 4.12 (continued): (c) D_{84} of the 1954-1976 sampled suspended sand, the model prediction of the "sampled" suspended sand, and the 1983 sampled suspended sand functions of both instantaneous fluid discharge and mean "sampled" suspended-sand concentration in the cross-section. A zero value of grain size in means that no sand was predicted to be sampled by the depth-integrated sampler because of predicted flow depths less than 10 cm.

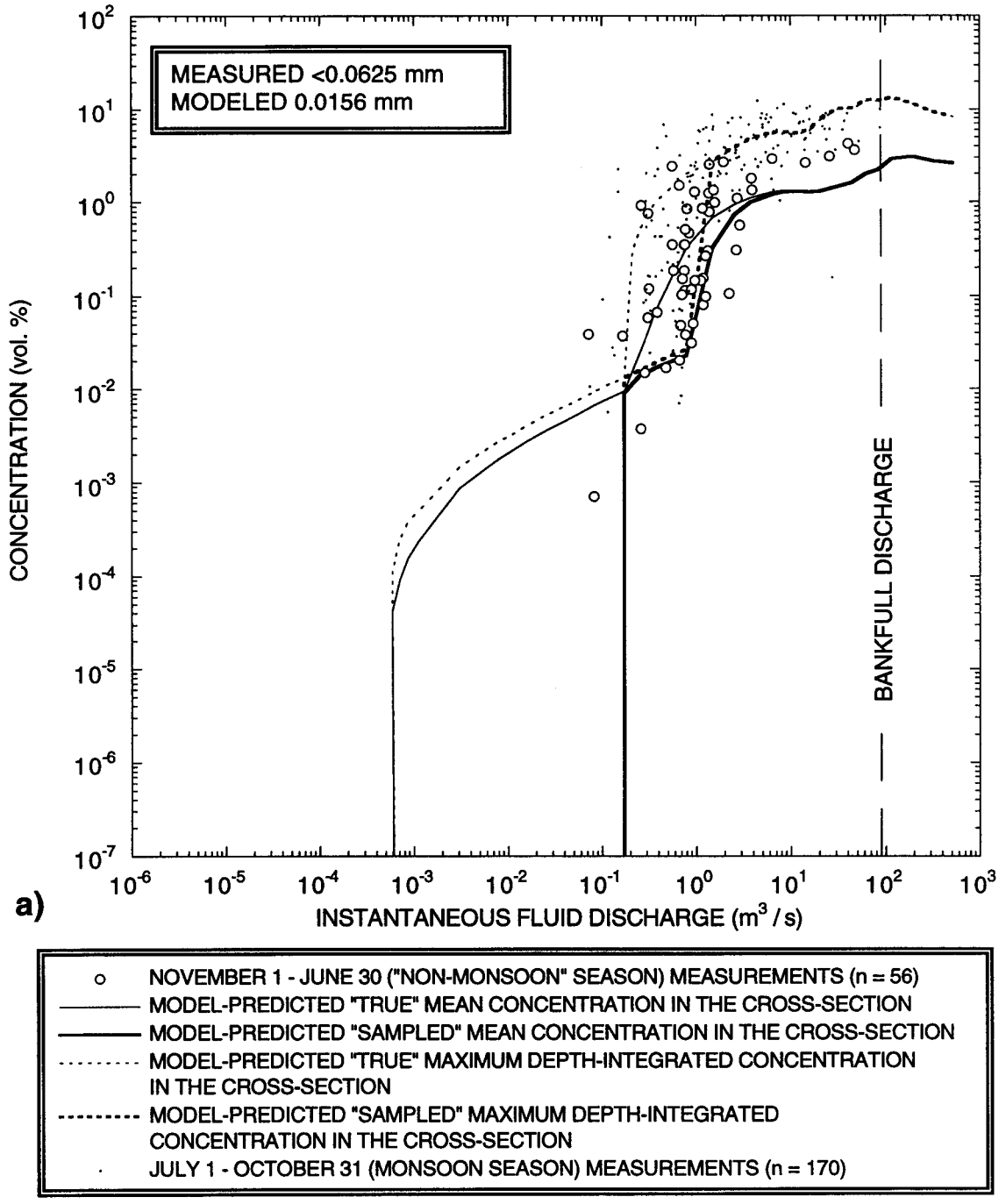

Figure 4.13: (a) Model-predicted "true" and "sampled" mean and maximum depth-integrated concentrations of suspended silt and clay in the model-predicted cross-section and measured depth-integrated concentrations of suspended silt and clay in the "non-monsoon" season and monsoon season.

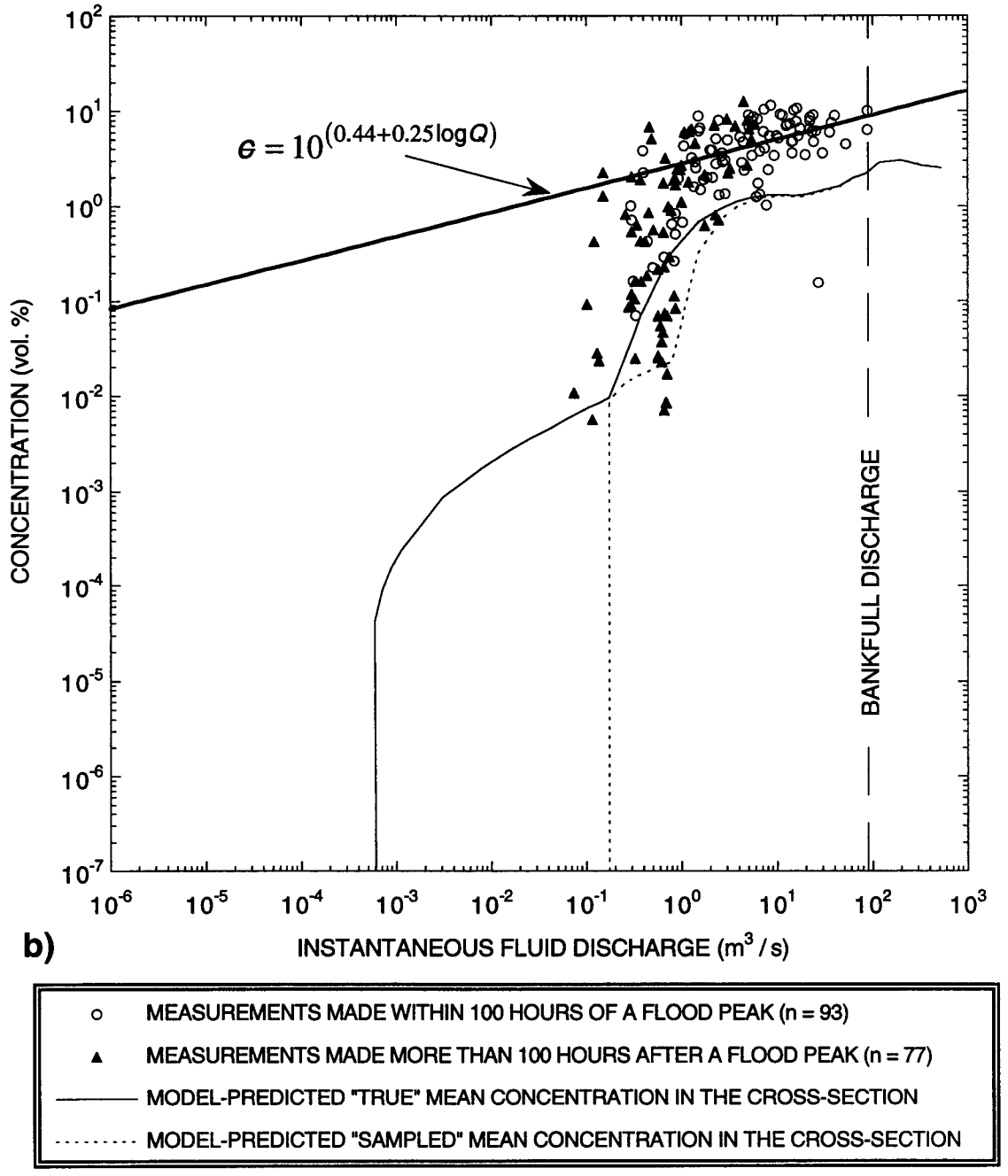

Figure 4.13 (continued): **(b)** Monsoon-season measurements of suspended-silt and clay concentration made within 100 hours of a flood peak and monsoon-season measurements of suspended-silt and clay concentration made more than 100 hours after a flood peak. The solid thick line is the best-fit log-linear regression to the monsoon season measurements of >1% silt and clay concentration made within 100 hours of a flood peak as a function of instantaneous fluid discharge. Model-predicted "true" and "sampled" mean depth-integrated concentrations of suspended silt and clay in the model-predicted cross-section are also shown.

from that in the "non-monsoon" season with the main difference being the enhanced maximum concentration of suspended silt and clay during the monsoon season. Not only is the monsoon season concentration of suspended-silt and clay statistically different from the "non-monsoon" season concentration of silt and clay, but the concentration of suspended-silt and clay within 100 hours of a flood peak during the monsoon season is statistically different from the concentration of suspended-silt and clay more than 100 hours after a flood peak. Thus, the magnitude of the difference between the log-linear regression fit to the "enhanced" monsoon season suspended-silt and clay concentration within 100 hours of a flood peak and the model-predicted "sampled" suspended-silt and clay concentration in Figure 4.13b is interpreted to equal the magnitude of the suspended-silt and clay concentration advected into the lower Paria River from hillslopes in the upper portion of the drainage basin during monsoon season floods.

4.3f: TEST 6: Comparison of model-predicted and quasi-daily measured depth-integrated suspended-sediment concentrations

The sixth test compares the model-predicted concentrations of total suspended sediment with the 7756 measured concentrations of total suspended sediment from 10-1-47 through 9-30-75 (see Figure 3.1). Results from this test indicate that the model predictions are in agreement, on average, with all of the measured concentrations of suspended sediment. Agreement between model and measurement increases as a function of discharge; and, the model prediction and measurements are in excellent agreement during the flood flows that transport especially large quantities of sediment. No grain-size analyses were performed by the USGS on the 7756 measurements used in this comparison; so, to test the model against this vast data set, the modeled "sampled" concentration of suspended sediment at each fluid discharge was treated as the sum of the modeled "sampled" sand concentration at each discharge and the modeled "sampled" seasonally adjusted silt and clay concentration at each discharge. The seasonally adjusted concentration of silt and clay is defined for the "non-monsoon" season as the modeled "sampled" concentration of silt and clay concentration and for the monsoon season as the modeled "sampled" silt and clay concentration enhanced by the empirically determined advected silt and clay concentration from Figure 4.13b for fluid discharges in excess of 1.51 m^3/s within 100 hours of a flood peak.

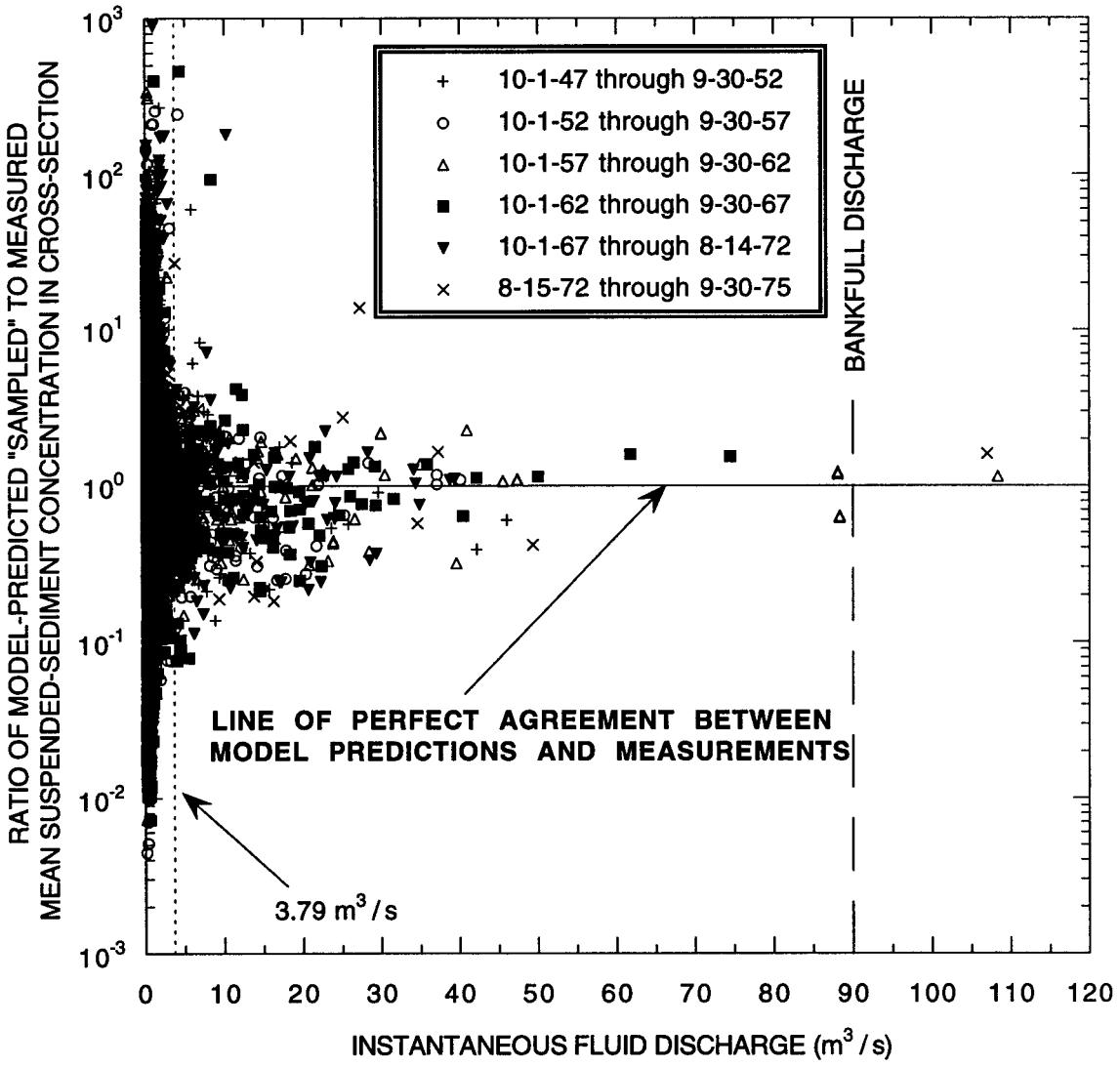

Figure 4.14: Comparison of the model-predictions with the quasi-daily 7756 measurements of suspended-sediment concentration; shown is the ratio of the model-predicted "sampled" to measured mean suspended-sediment concentration in the cross-section as a function of the instantaneous fluid discharge in the Paria River. Also shown is the base discharge of 3.79 m^3/s used to define floods in Section 2.4e, i.e., the discharge one standard deviation above the mean instantaneous discharge of the river.

Table 4.1: Comparison of model-predicted "sampled" depth-integrated suspended-sediment concentrations to the USGS depth-integrated suspended-sediment concentration measurements made from October 1, 1947 through September 30, 1975.

TIME PERIOD	FLUID DISCHARGE RANGE	log (RATIO OF *MODEL-PREDICTED "SAMPLED" MEAN SUSPENDED-SEDIMENT CONCENTRATION IN THE CROSS-SECTION* TO *MEASURED MEAN SUSPENDED-SEDIMENT CONCENTRATION IN THE CROSS-SECTION*)*		NUMBER OF NONZERO MODEL PREDICTIONS	NUMBER OF NONZERO MEASURE-MENTS
		MEAN VALUE	STANDARD DEVIATION		
10-1-47 through 9-30-75	**ALL FLOWS**	**0.14**	**0.79**	**6193**	**7756**
10-1-47 through 9-30-75	**FLOWS > 3.79 m^3/s**	**-0.067**	**0.40**	**568**	**568**
10-1-47 through 9-30-52	ALL FLOWS	0.17	0.82	1251	1490
10-1-47 through 9-30-52	FLOWS > 3.79 m^3/s	-0.020	0.39	97	97
10-1-52 through 9-30-57	ALL FLOWS	0.23	0.87	1075	1308
10-1-52 through 9-30-57	FLOWS > 3.79 m^3/s	-0.12	0.43	76	76
10-1-57 through 9-30-62	ALL FLOWS	0.14	0.75	955	1150
10-1-57 through 9-30-62	FLOWS > 3.79 m^3/s	-0.0099	0.29	116	116
10-1-62 through 9-30-67	ALL FLOWS	0.000015	0.76	974	1230
10-1-62 through 9-30-67	FLOWS > 3.79 m^3/s	-0.13	0.45	135	135
10-1-67 through 8-14-72	ALL FLOWS	0.24	0.75	1225	1627
10-1-67 through 8-14-72	FLOWS > 3.79 m^3/s	-0.086	0.40	110	110
8-15-72 through 9-30-75	ALL FLOWS	0.0044	0.71	713	951
8-15-72 through 9-30-75	FLOWS > 3.79 m^3/s	0.038	0.39	34	34

Notes:
* A mean value of zero indicates perfect agreement between model predictions and measurements.

Results of this comparison are shown in Figure 4.14.[10] To allow the detection of any trends with respect to time, comparisons in Figure 4.14 were broken into six time periods: five time periods covering the period from October 1, 1947 to the onset of channel incision near the gage on August 15, 1972; and one time period from August 15, 1972 through September 30, 1975. In Table 4.1, values of the log-transformed mean and standard deviation of the ratio of the model-predicted "sampled" to measured mean suspended-sediment concentration in the cross-section are shown for each time period for both all discharges and "flood" discharges above 3.79 m^3/s.

The model predictions of the "sampled" mean concentration of suspended sediment in the cross-section are in good agreement with the 7756 measurements of the mean concentration of suspended sediment in the cross-section. Furthermore, the magnitude of disagreement between the model and the measurements decreases substantially for flood flows. At all discharges, the ratio of model predictions to measurements is approximately log-normally distributed about the line of perfect agreement indicating that the magnitudes of positive and negative disagreement between the model and the measurements are equal. As expected, based on results from Chapter 2 that show that the equilibrium hydraulic geometry of the Paria River has been constant and that the hydrology has been approximately stationary over the period of record, no trend exists in the ratio of model predictions to measurements in Table 4.1. Significant overlap between the ratio of model-predicted "sampled" to measured suspended sediment concentrations exists at one standard deviation.

4.3g: TEST 7: Comparison of model-predicted and measured cross-stream differences in depth-integrated sediment concentration

The seventh test compares the model-predicted cross-stream gradients in "sampled" sediment concentration with measured cross-stream differences in depth-integrated sediment concentration. Because the model includes no lateral transport of suspended sediment and calculates the concentration of suspended-sediment at each computation vertical independently by forcing the local mass conservation of each sediment size class between the bed and the flow, this test allows the importance of lateral advective suspended-sediment transport in the Paria River to be evaluated. Results from this test

---

[10]Logarithmic transformation of the ratio of the model-predicted "sampled" to measured mean suspended-sediment concentration in the cross-section allows the magnitude of disagreement between the model and the measurements to be easily depicted in Figure 4.14; thus, a point falling the same distance above or below the line of perfect agreement in Figure 4.14 represents the same absolute value of the magnitude of disagreement between the model predictions and the measurements.

indicate that the measured cross-stream gradients are consistent with those predicted by the model, therefore, results from this test lend support to the first physical assumption that "lateral advective transport of sediment in the reach-averaged cross-section can be ignored"

Figure 4.15 shows, for three different discharges: the initial and model-predicted bed, and the model-predicted "sampled" depth-integrated concentration of total suspended sediment (sand, silt, and clay). The discharges chosen for this comparison were: 0.801 m^3/s (with a model-predicted maximum depth of 20.1 cm), 8.30 m^3/s (with a model-predicted maximum depth of 51.8 cm), and 31.1 m^3/s (with a model-predicted maximum depth of 108 cm). No higher discharges were chosen for this comparison because of the scarcity of suspended-sediment data at higher discharges; only 32 of the 7756 measurements were made at discharges in excess of 31.1 m^3/s. Also shown in Figure 4.15 are the ranges of the measured maximum cross-stream difference in suspended-sediment concentration for these three discharges; these values are taken from Figure 3.1b, and the base values of the cross-stream range in sediment concentration are matched to the minimum model-predicted "sampled" concentrations in Figure 4.15. Most probable locations of sampling verticals are indicated in the modeled cross-sections for the suspended-sediment measurements with both two and three sampling verticals. For measurements with two verticals, these would be located at 1/3 and 2/3 of the width of the portion of the channel deeper than the minimum sampling depth of 10 cm; and, for measurements with three verticals, these would be located at 1/4, 1/2, and 3/4 of the width of the portion of the channel deeper than the minimum sampling depth of 10 cm. Because the model predictions of "sampled" depth-integrated sediment concentration fall well within the measured maximum range of depth-integrated suspended-sediment concentrations at the probable positions of the measurement verticals, the importance of lateral advective transport of suspended sediment on the resultant suspended-sediment concentration fields in the Paria River is indicated to be minimal, thus the exclusion of lateral transport of sediment in the model is justified.

Section 4.4: HYPERCONCENTRATED FLOWS

Since the Paria River was the birthplace of the term "hyperconcentrated flow", it is appropriate that the existence of hyperconcentrated flows as a flow type physically distinct from turbulent suspensions be re-evaluated as part of this study. As mentioned in Section 3.2a, the term "hyperconcentrated flow" was introduced by Beverage and Culbertson (1964) to describe the high concentrations of suspended sediment measured on the Paria River, Rio Puerco, and Little Colorado River. Their original definition of

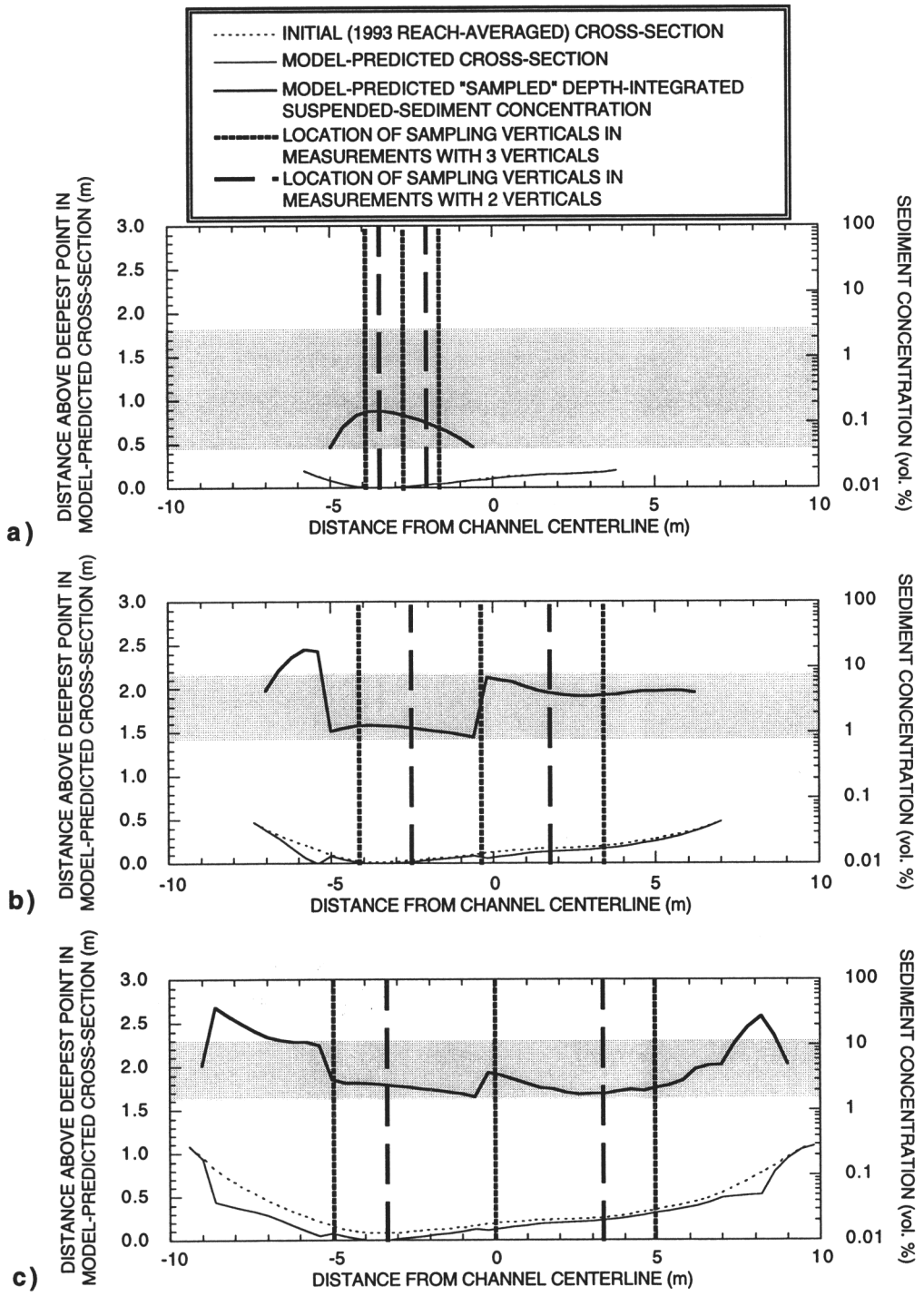

Figure 4.15: **(a)** Model-predicted "sampled" and measured range in depth-integrated suspended-sediment concentration for a flow of 0.801 m^3/s. **(b)** Model-predicted "sampled" and measured range in depth-integrated suspended-sediment concentration for a flow of 8.30 m^3/s. **(c)** Model-predicted "sampled" and measured range in depth-integrated suspended-sediment concentration for a flow of 31.1 m^3/s. Shown, for each case, are the initial and model-predicted cross-section geometry and the most probable locations of the suspended-sediment sampling verticals.

hyperconcentrated flow was developed to describe depth-integrated mass concentrations in excess of 40%, which are equivalent of volume concentrations in excess of 20%. Beverage and Culbertson (1964) postulated that the physical mechanism responsible for hyperconcentration was somehow different than that responsible for normal turbulent suspensions and that hyperconcentrated flows were transitional between normal turbulent suspensions and debris flows. Beverage and Culbertson (1964) hypothesized, based on Paria River data, that, at a concentration of about 6% by volume silt and clay, the proportion of sand in a suspension increased dramatically as the process responsible for hyperconcentration started to become dominant. They did neither a rigorous theoretical analysis nor did they present any measurements indicating that hyperconcentrations were anything but the high-concentration end-member of normal turbulent suspensions.

Unfortunately, the term "hyperconcentrated flow" has taken on a life of its own in the geomorphological community to describe a to-date unverified process, and its use has become widespread (e.g. Pierson and Scott, 1985; Janda and Meyer, 1986; Pierson and Costa, 1987; Webb, 1987). Pierson and Scott (1985) claimed that hyperconcentrated flows were not turbulent because the surface of the flows were glassy. This argument is misguided because the water surface of a flow cannot be used to determine if it is turbulent. In fact, Bondurant (1951) stated that the flow in the Rio Puerco during the highest depth-integrated-concentration measurement ever made in a river possessed all of the characteristics of a turbulent flow. The so-called hyperconcentrated flow process has even taken on geomorphic implications. Janda and Meyer (1986) stated that, on the Toutle River, hyperconcentrated flows caused channel narrowing while normal turbulent suspensions caused channel widening. However, to date, no one has demonstrated with either experiments or theory that hyperconcentrated flows exist as a process physically distinct from turbulent suspensions.

Figure 4.16 is a updated version of a graph originally presented by Beverage and Culbertson (1964) showing the volume percent sand concentration as a function of the volume percent total suspended sediment. Included in this graph are data from all of the grain-size analyzed monsoon season and "non-monsoon" season suspended-sediment samples collected in the Paria River between 1954 and 1976. Also shown are values from the monsoon season and "non-monsoon" season model predictions of "sampled" suspended sediment in the 648 total individual computation verticals in the 20 different modeled flows that cover a discharge range from zero to bankfull flow. Agreement between the "data" from the model and measurements is exceptional for both the monsoon and "non-monsoon" season. Unlike the interpretation of Beverage and Culbertson (1964),

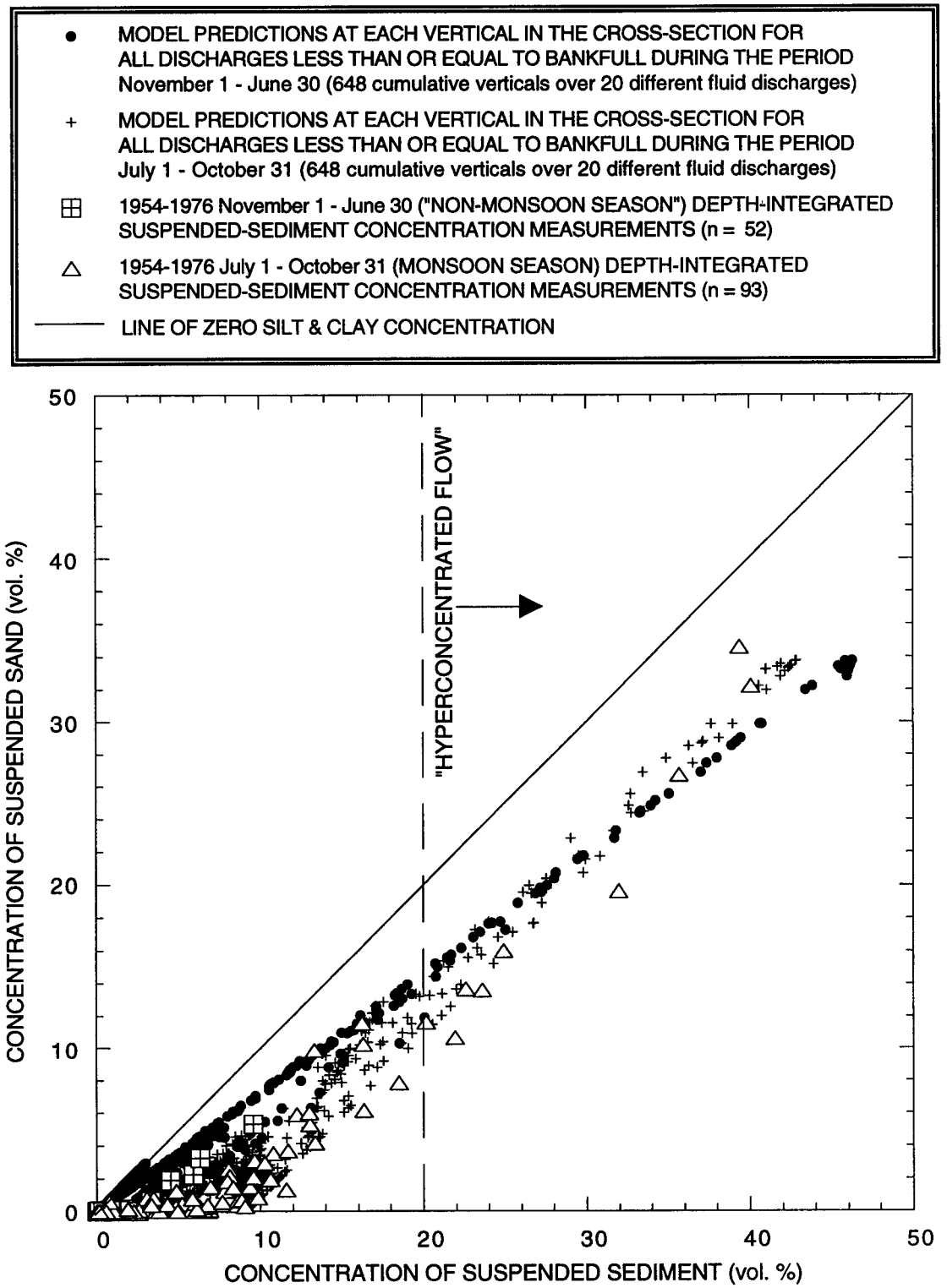

Figure 4.16: Measured and model-predicted "sampled" depth-integrated concentration of suspended sand as a function of the depth-integrated concentration of suspended sediment. The so-called lower limit of hyperconcentration and the line of zero silt and clay concentration are also shown

the behavior depicted in Figure 4.16 is not unique for "hyperconcentrated flows", but is typical for all rivers with a fixed amount of silt and clay in the system. The process that controls the concentration of suspended sand as a function of suspended sediment in Figure 4.16 is simply a balance between supply, hydraulics, and settling velocity. As sediment goes into suspension from the bed of the river, the silt and clay on the bed, by virtue of its extremely slow settling velocity, quickly goes into suspension until its supply on the bed is exhausted; and, as the boundary shear stress continues to rise, the concentration of sand in suspension continues to increase.

This analysis shows that a "normal" turbulent-flow suspended-sediment theory that accounts for the salient physics associated with turbulence damping caused by the high-density gradients associated with high suspended-sediment-concentration gradients can adequately predict concentrations in the "hyperconcentrated range". Thus, until the existence of a distinct hyperconcentrated flow process is physically documented, hyperconcentrated flows should be treated as an upper extent of turbulent suspensions, and the term should not have any special geomorphic implications.

Section 4.5: MODEL-PREDICTED SEDIMENT FLUXES THROUGH THE MODEL-PREDICTED CROSS-SECTION

Suspended-load transport of sand, silt, and clay is predicted to dominate over bedload transport of sand, silt, and clay in the Paria River for virtually all but the lowest flows (Figure 4.17). Decrease in the bedload flux of a certain size class with increasing discharge, as shown in Figure 4.17c, occurs when the settling velocity of that size class is greater than the skin-friction shear velocity at progressively fewer computation verticals. Likewise, "dropouts" in the bedload flux of a certain size class occur in Figure 4.17c when the settling velocity of that size class is less than the skin-friction shear velocity at all computation verticals in the cross-section. Since the settling velocity of the silt and clay fraction, the 0.0625 mm sand size class, and the 0.088 mm sand size class are never greater than the skin-friction shear velocity at any computation vertical in any flow, these sizes are never predicted to move as bedload in the Paria River. Model predictions of total load by size class and season for each value of modeled fluid discharge appear in Table 4.2.

Application of the model to the period of gage record

Given that, over the period of gage record, the hydraulic geometry of equilibrium reaches in the Lees Ferry study area has been constant (see Sections 2.5 and 2.6), the hydrology has been approximately stationary (see Section 2.4), and the geomorphically

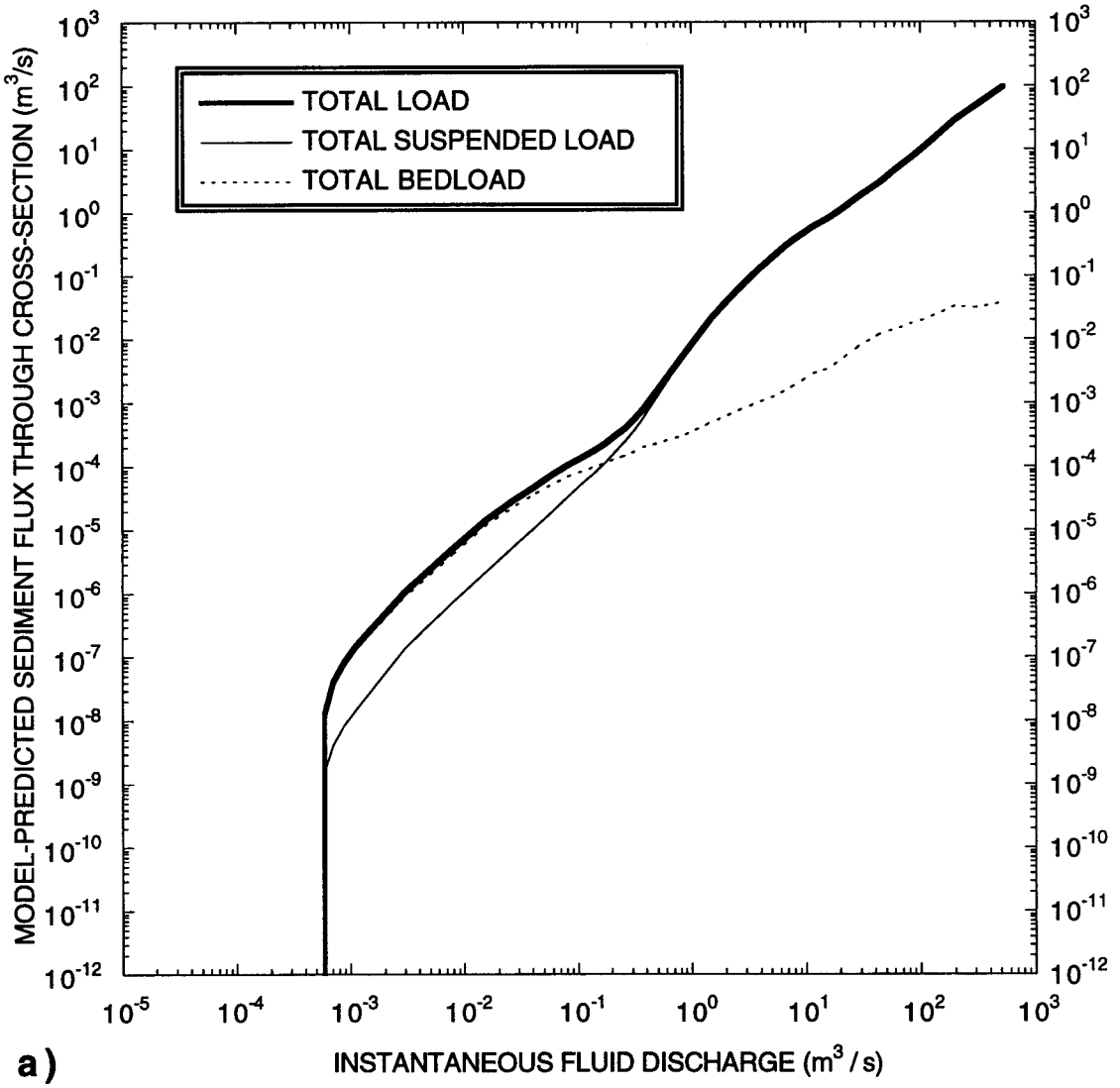

Figure 4.17: **(a)** Model-predicted fluxes of total load, total suspended load, and total bedload through the model-predicted cross-section as a function of fluid discharge.

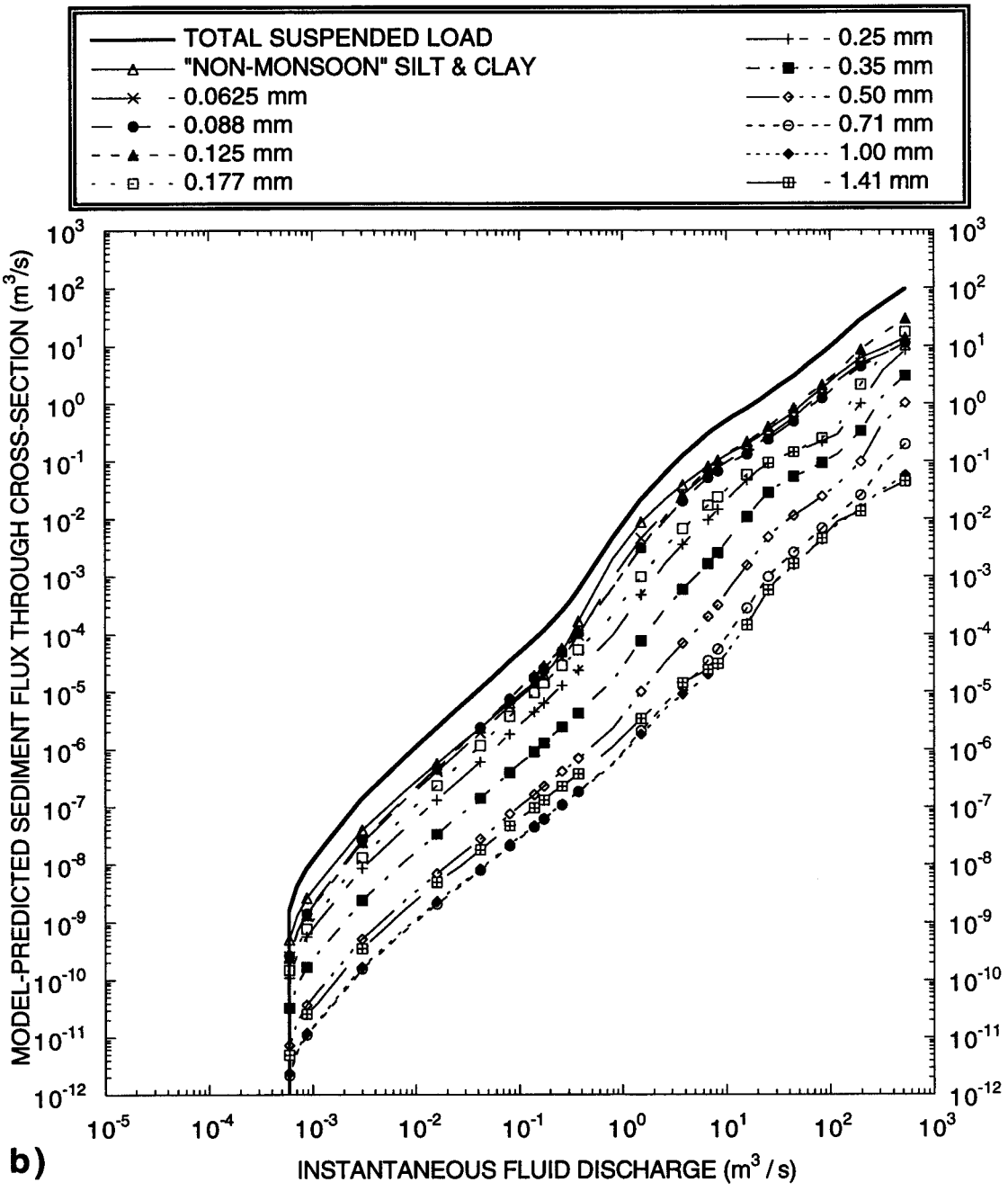

Figure 4.17 (continued): **(b)** Model-predicted fluxes of each size class of the suspended load through the model-predicted cross-section as a function of fluid discharge.

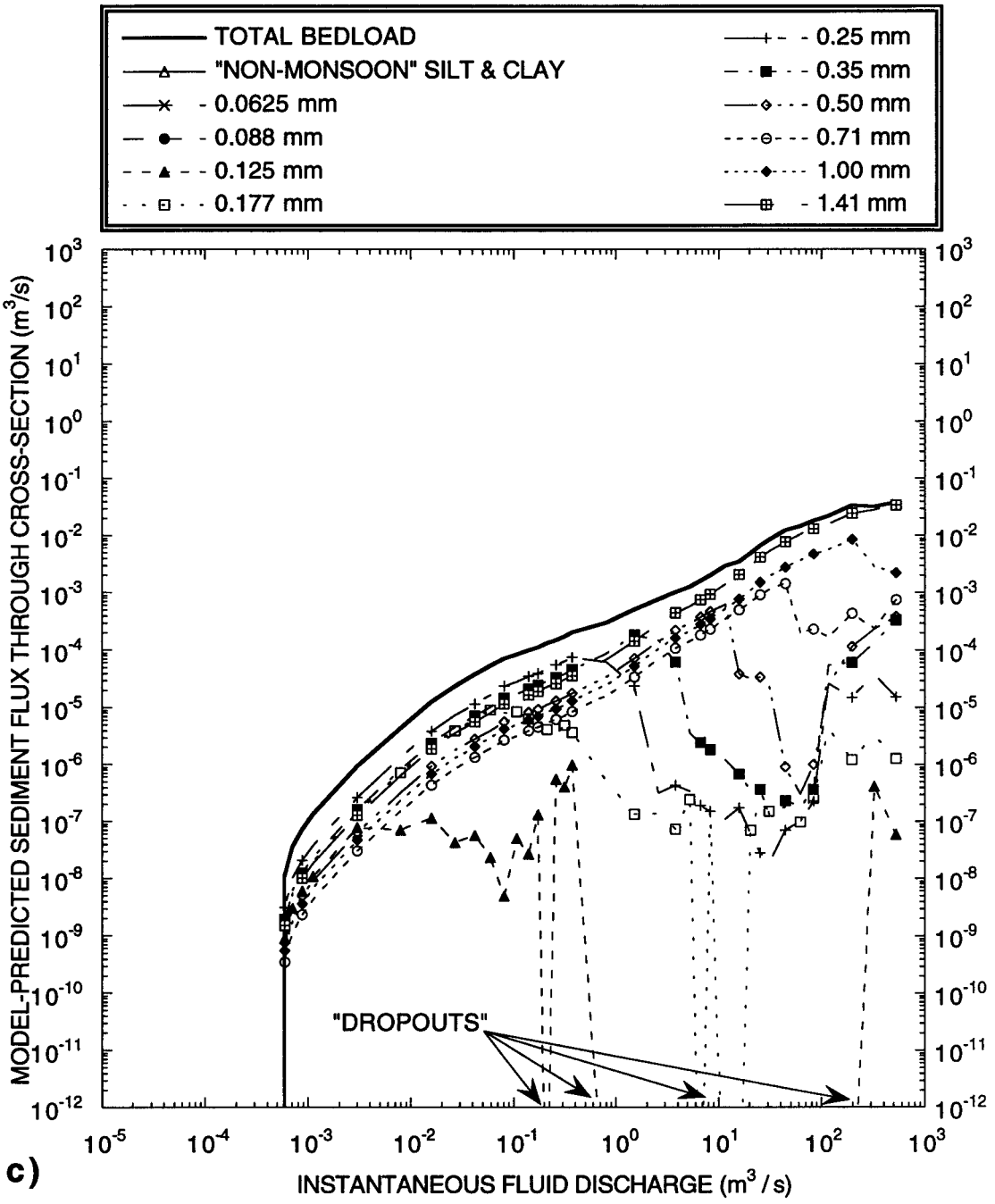

Figure 4.17 (continued): (c) Model-predicted fluxes of each size class of the bedload through the model-predicted cross-section as a function of fluid discharge. See text for explanation of the decreases and "dropouts" in bedload flux.

Table 4.2: Model-predicted sediment flux by size class and time within season through the model-predicted cross-section.

FLUID DIS. (m^3/s)	FLUX THROUGH MODEL-PREDICTED CROSS-SECTION (m^3/s)														
	TOTAL SED. LOAD (Nov. 1 - June 30 or >100 hrs. after flood peak)	TOTAL SED. LOAD (July 1 - Oct. 31 & ≤100 hrs. after flood peak)	TOTAL SAND (0.0625-2.0 mm)	SAND BY SIZE CLASS										SILT & CLAY (Nov. 1 - June 30 or >100 hrs. after flood peak)	SILT & CLAY (July 1 - Oct. 31 & ≤100 hrs. after flood peak)
				0.0625 mm	0.088 mm	0.125 mm	0.177 mm	0.25 mm	0.35 mm	0.50 mm	0.71 mm	1.00 mm	1.41 mm		
<5.90e-4	0	0	0	0	0	0	0	0	0	0	0	0	0	0	0
5.90e-4	1.23e-8	1.23e-8	1.18e-8	2.56e-10	2.59e-10	1.14e-9	1.84e-9	3.22e-9	1.94e-9	7.51e-10	3.55e-10	5.50e-10	1.51e-9	5.02e-10	5.02e-10
7.11e-4	3.93e-8	3.93e-8	3.80e-8	6.83e-10	6.98e-10	3.58e-9	5.94e-9	1.05e-8	6.31e-9	2.45e-9	1.16e-9	1.79e-9	4.96e-9	1.31e-9	1.31e-9
8.73e-4	7.92e-8	7.92e-8	7.66e-8	1.38e-9	1.42e-9	7.22e-9	1.19e-8	2.11e-8	1.27e-8	4.94e-9	2.34e-9	3.63e-9	9.99e-9	2.60e-9	2.60e-9
1.12e-3	1.44e-7	1.44e-7	1.40e-7	2.50e-9	2.59e-9	1.32e-8	2.17e-8	3.85e-8	2.32e-8	9.01e-9	4.28e-9	6.62e-9	1.82e-8	4.53e-9	4.53e-9
3.03e-3	1.06e-6	1.06e-6	1.02e-6	2.41e-8	2.59e-8	1.00e-7	1.57e-7	2.74e-7	1.65e-7	6.39e-8	3.03e-8	4.70e-8	1.29e-7	3.96e-8	3.96e-8
7.99e-3	5.01e-6	5.01e-6	4.81e-6	1.31e-7	1.48e-7	2.07e-7	7.92e-7	1.37e-6	8.23e-7	3.18e-7	1.51e-7	2.34e-7	6.43e-7	1.93e-7	1.93e-7
0.0160	1.47e-5	1.47e-5	1.41e-5	4.11e-7	4.83e-7	5.65e-7	2.33e-6	4.02e-6	2.40e-6	9.31e-7	4.40e-7	6.82e-7	1.88e-6	5.62e-7	5.62e-7
0.0267	2.89e-5	2.89e-5	2.77e-5	9.55e-7	1.17e-6	1.16e-6	4.56e-6	7.70e-6	4.60e-6	1.78e-6	8.46e-7	1.31e-6	3.60e-6	1.24e-6	1.24e-6
0.0421	4.80e-5	4.80e-5	4.57e-5	1.90e-6	2.38e-6	2.40e-6	7.50e-6	1.23e-5	7.31e-6	2.82e-6	1.33e-6	2.06e-6	5.68e-6	2.34e-6	2.34e-6
0.0594	7.26e-5	7.26e-5	6.86e-5	3.40e-6	4.38e-6	4.40e-6	1.12e-5	1.78e-5	1.05e-5	4.05e-6	1.91e-6	2.95e-6	8.14e-6	4.04e-6	4.04e-6
0.0808	1.04e-4	1.04e-4	9.74e-5	5.62e-6	7.40e-6	7.63e-6	1.18e-5	2.57e-5	1.50e-5	5.77e-6	2.73e-6	4.21e-6	1.16e-5	6.45e-6	6.45e-6
0.107	1.35e-4	1.35e-4	1.25e-4	8.75e-6	1.18e-5	1.24e-5	1.46e-5	3.11e-5	1.79e-5	6.83e-6	3.23e-6	4.98e-6	1.37e-5	9.74e-6	9.74e-6
0.140	1.76e-4	1.76e-4	1.62e-4	1.31e-5	1.78e-5	1.91e-5	1.58e-5	3.91e-5	2.21e-5	8.43e-6	3.97e-6	6.12e-6	1.69e-5	1.41e-5	1.41e-5
0.173	2.24e-4	2.24e-4	2.04e-4	1.86e-5	2.57e-5	2.82e-5	2.03e-5	4.57e-5	2.54e-5	9.62e-6	4.55e-6	7.01e-6	1.93e-5	1.96e-5	1.96e-5
0.212	2.94e-4	2.94e-4	2.64e-4	2.66e-5	3.65e-5	4.04e-5	2.44e-5	5.67e-5	3.09e-5	1.17e-5	5.48e-6	8.46e-6	2.33e-5	2.98e-5	2.98e-5
0.260	3.90e-4	3.90e-4	3.39e-4	3.92e-5	5.13e-5	5.75e-5	3.21e-5	6.71e-5	3.57e-5	1.34e-5	6.26e-6	9.66e-6	2.66e-5	5.06e-5	5.06e-5
0.312	5.36e-4	5.36e-4	4.46e-4	6.04e-5	7.28e-5	8.08e-5	4.45e-5	8.05e-5	4.17e-5	1.56e-5	7.31e-6	1.12e-5	3.09e-5	8.98e-5	8.98e-5
0.372	7.63e-4	7.63e-4	5.96e-4	9.58e-5	1.03e-4	1.14e-4	5.77e-5	9.81e-5	4.99e-5	1.85e-5	8.67e-6	1.33e-5	3.65e-5	1.67e-4	1.67e-4
0.801	4.81e-3	4.81e-3	2.81e-3	9.13e-4	6.45e-4	6.26e-4	2.19e-4	1.58e-4	1.02e-4	3.64e-5	1.69e-5	2.57e-5	7.02e-5	1.99e-3	1.99e-3
1.51	0.0215	0.0589	0.0128	4.49e-3	3.09e-3	3.16e-3	9.77e-4	5.03e-4	2.59e-4	8.13e-5	3.63e-5	5.47e-5	1.47e-4	8.72e-3	0.0461
2.59	0.0604	0.130	0.0390	0.0128	9.47e-3	0.0108	3.18e-3	1.69e-3	4.30e-4	1.75e-4	7.49e-5	1.10e-4	2.95e-4	0.0214	0.0905
3.83	0.122	0.231	0.0833	0.0257	0.0202	0.0255	6.60e-3	3.59e-3	6.59e-4	2.90e-4	1.19e-4	1.72e-4	4.56e-4	0.0389	0.148
5.26	0.204	0.364	0.145	0.0419	0.0346	0.0483	0.0112	6.15e-3	1.05e-3	4.16e-4	1.65e-4	2.32e-4	6.05e-4	0.0592	0.219
6.73	0.298	0.515	0.216	0.0600	0.0509	0.0755	0.0169	9.62e-3	1.67e-3	5.73e-4	2.19e-4	2.99e-4	7.68e-4	0.0811	0.299
8.30	0.393	0.679	0.291	0.0774	0.0668	0.103	0.0237	0.0143	2.58e-3	7.82e-4	2.87e-4	3.80e-4	9.59e-4	0.102	0.388
11.7	0.596	1.05	0.449	0.113	0.0992	0.160	0.0396	0.0277	5.62e-3	1.37e-3	4.80e-4	5.97e-4	1.46e-3	0.146	0.596
15.8	0.814	1.49	0.619	0.150	0.132	0.217	0.0574	0.0464	0.0108	1.60e-3	7.82e-4	9.25e-4	2.20e-3	0.194	0.868
20.4	1.11	2.04	0.848	0.202	0.177	0.295	0.0762	0.0694	0.0187	2.98e-3	1.26e-3	1.42e-3	3.30e-3	0.259	1.19
25.4	1.48	2.71	1.14	0.272	0.237	0.400	0.0943	0.0921	0.0278	4.83e-3	1.88e-3	2.06e-3	4.69e-3	0.346	1.57
31.1	1.92	3.49	1.47	0.355	0.312	0.525	0.111	0.112	0.0366	6.85e-3	2.58e-3	2.75e-3	6.17e-3	0.449	2.02
44.5	2.97	5.42	2.26	0.566	0.491	0.830	0.144	0.145	0.0536	0.0113	4.09e-3	4.36e-3	9.49e-3	0.709	3.17
62.1	4.93	8.52	3.72	0.970	0.842	1.43	0.193	0.179	0.0709	0.0168	4.43e-3	6.28e-3	0.0132	1.20	4.80
84.1	7.28	12.5	5.46	1.46	1.25	2.13	0.252	0.221	0.0928	0.0244	7.02e-3	8.94e-3	0.0177	1.81	7.01
117	12.3	19.8	9.18	2.49	2.18	3.63	0.368	0.291	0.130	0.0381	0.0118	0.0135	0.0249	3.12	10.6
197	27.8	42.0	21.7	4.94	4.45	8.64	2.14	1.00	0.331	0.0967	0.0259	0.0232	0.0378	6.15	20.3
325	53.1	82.1	44.1	7.21	7.09	16.3	7.58	3.85	1.39	0.461	0.0916	0.0354	0.0559	9.06	38.0
524	95.8	151	82.0	10.7	11.4	29.6	17.2	8.60	3.05	1.02	0.195	0.0592	0.0779	13.8	69.1

coupled flow and sediment-transport model has been found to work well (see Section 4.3), the fluxes of each grain size of sand and the silt and clay should be predictable with reasonable precision by application of the model to the period of gage record. This allows the analysis of whether any of the subtle trends in hydrology or clustering of hydrologic events described in Section 2.4 can produce significant trends in sediment transport. Also, this exercise allows the evaluation of which discharges over time are the most important for moving sediment and therefore which discharges most heavily influence the stability of the channel.

For this calculation, the instantaneous discharge time series presented in Section 2.4d is used as the model input. The total flux (bedload and suspended load) of each size class of sand and the silt and clay is then calculated as a function of the instantaneous fluid discharge using the information in Table 4.2. Cumulative volumes, over the period of gage record, of fluid (water + suspended sediment), model-predicted sediment (sand, silt, and clay), silt & clay and sand, and each of the ten size classes of sand are shown in Figure 4.18. Variation and trends in the annual loads with respect to time progressively diminish with increasing grain size. As illustrated in Figure 4.19, the silt and clay fraction is most sensitive and the coarsest sand fraction least sensitive to hydrologic variation. F-statistic trend analyses of the model predictions presented in Figure 4.19 show that trends with respect to time in the total sand fraction, the finest sand fraction, and the coarsest sand fraction exist at only the 0.32, 0.43, and 0.81 levels of significance, respectively. So, just as with the hydrology, even though there has been decade-scale variability, the sand loads have been approximately stationary with respect to the period from 1923 through 1996. However, since the silt and clay fraction is the most sensitive to the subtle changes in the hydrology of the river that have occurred since 1923 (see Sections 2.4e-g), the silt and clay load is predicted to decrease, at the marginal 0.055 level of significance, by 65% over the period from November 22, 1923 through September 30, 1996.

Comparison of the model predictions with previously published estimates of sediment loads

Prior to this study, Paria River mean-annual sediment loads have been calculated by Randle and Pemberton (1987), Andrews (1990), and Smillie and others (1993). Mean-annual sediment loads predicted by this study are compared to these three previously published sediment-load estimates in Table 4.3; also shown in Table 4.3 are the model-predicted mean-annual loads of silt and clay, total sand, and each size class of sand.

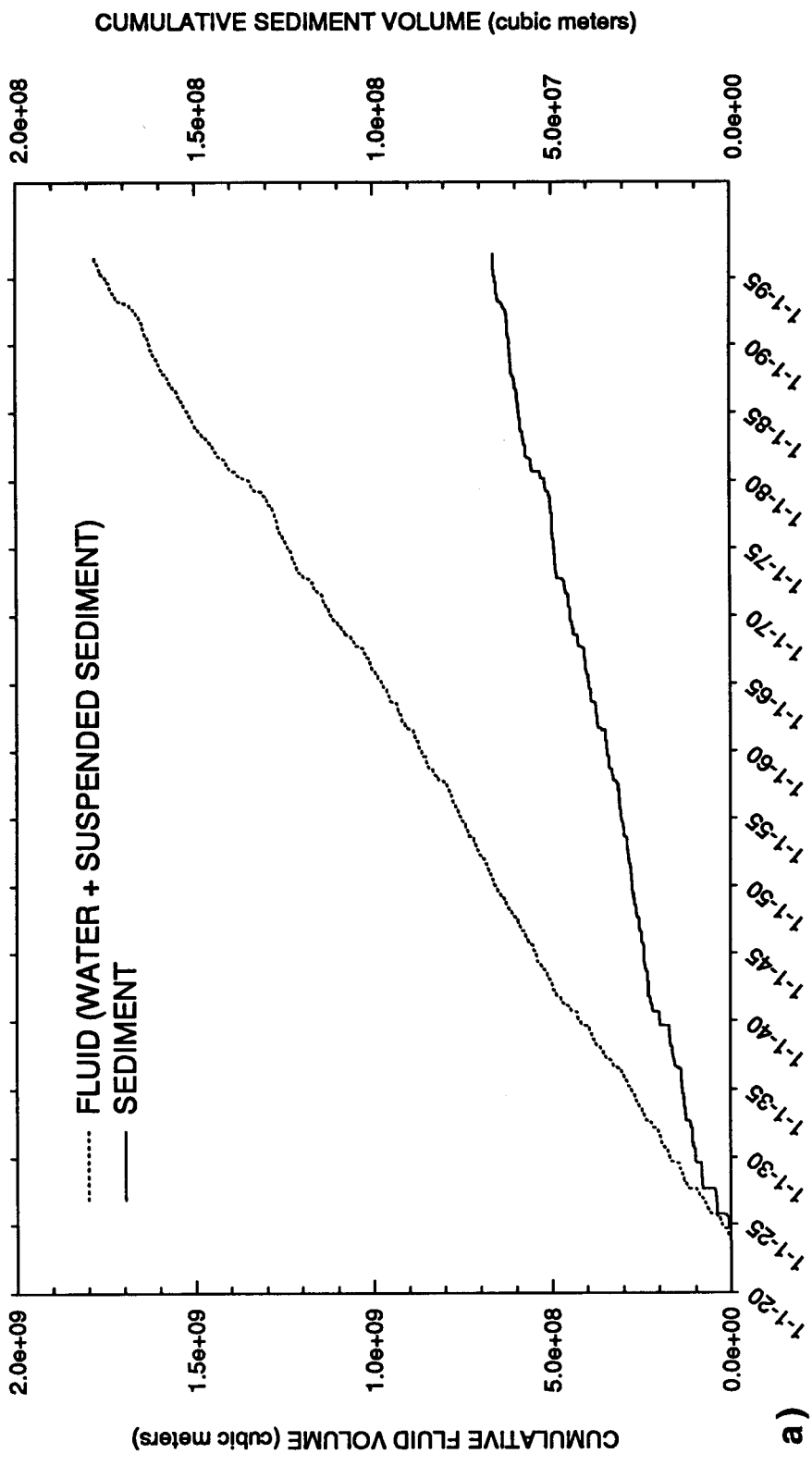

Figure 4.18: (a) Cumulative volume of fluid (water + suspended sediment) and model-predicted cumulative volume of sediment (sand, silt, and clay) passing the Paria River gage at Lees Ferry, AZ over the period from November 22, 1923 through September 30, 1996.

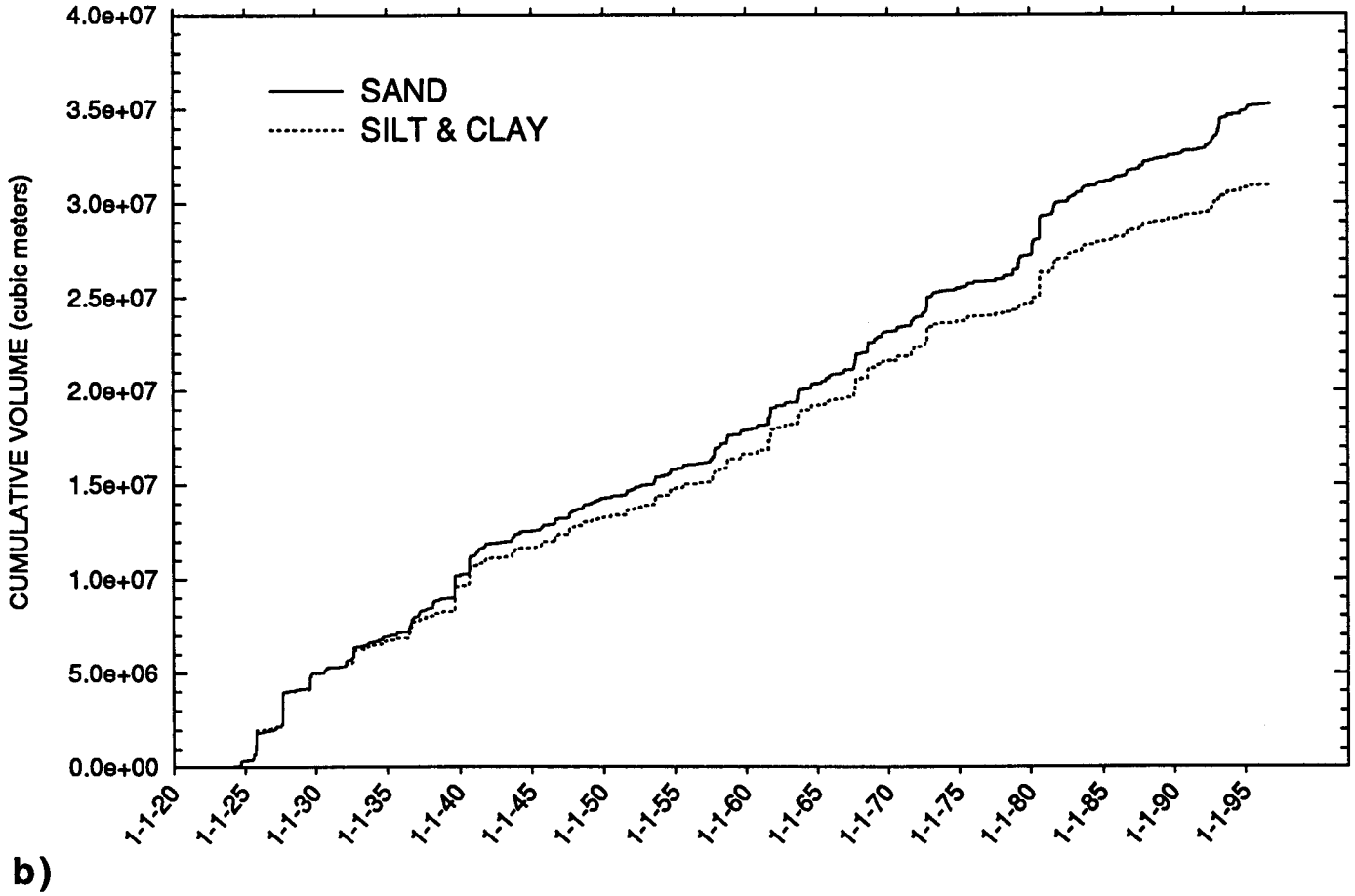

b)

Figure 4.18 (continued): **(b)** Model-predicted cumulative volume of sand and silt & clay passing the Paria River gage at Lees Ferry, AZ over the period from November 22, 1923 through September 30, 1996.

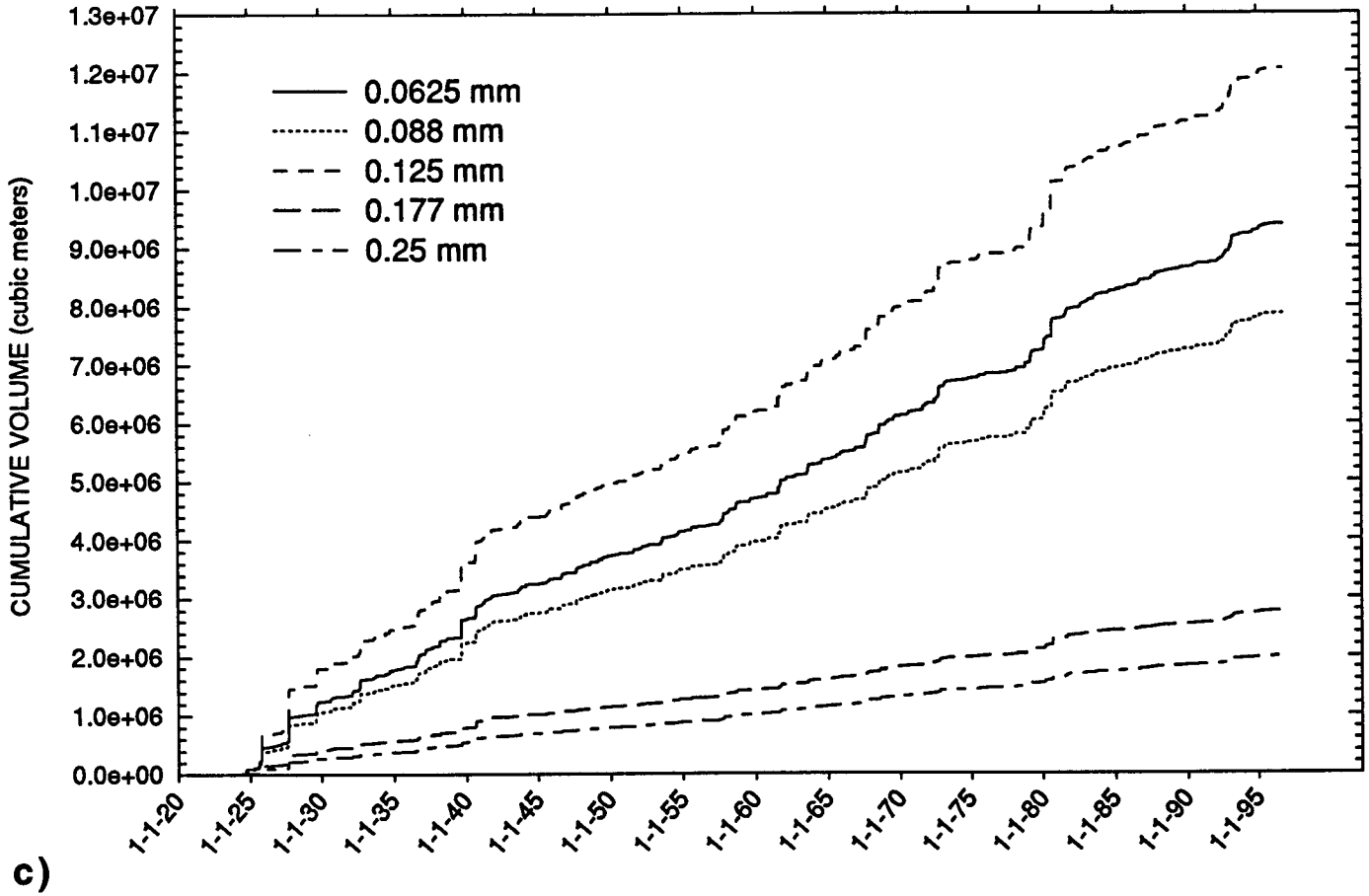

c)

Figure 4.18 (continued): (c) Model-predicted cumulative volume of 0.0625 mm, 0.088 mm, 0.125 mm, 0.177 mm, and 0.25 mm sand passing the Paria River gage at Lees Ferry, AZ over the period from November 22, 1923 through September 30, 1996.

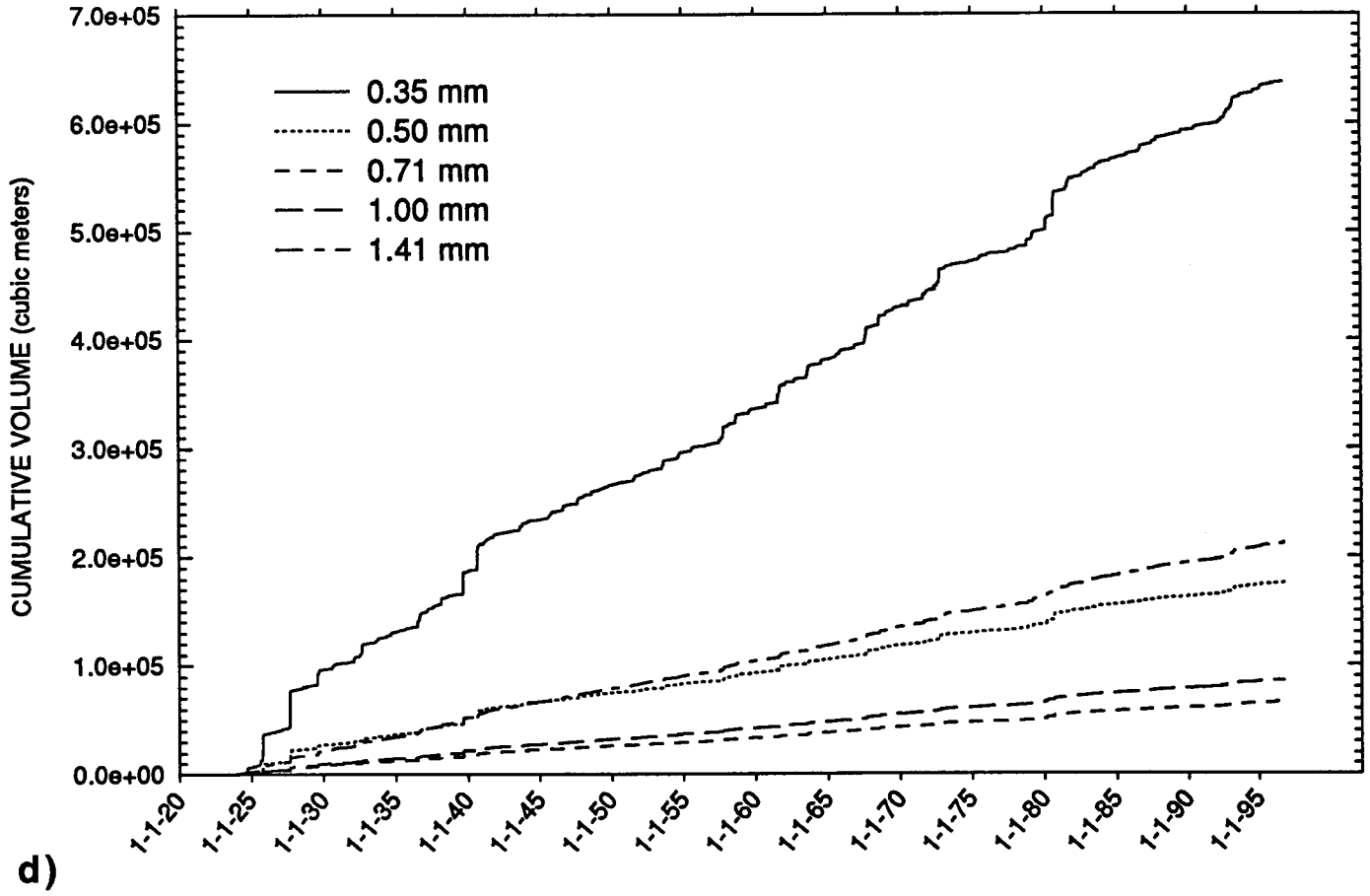

d)

Figure 4.18 (continued): **(d)** Model-predicted cumulative volume of 0.35 mm, 0.50 mm, 0.71 mm, 1.00 mm, and 1.41 mm sand passing the Paria River gage at Lees Ferry, AZ over the period from November 22, 1923 through September 30, 1996.

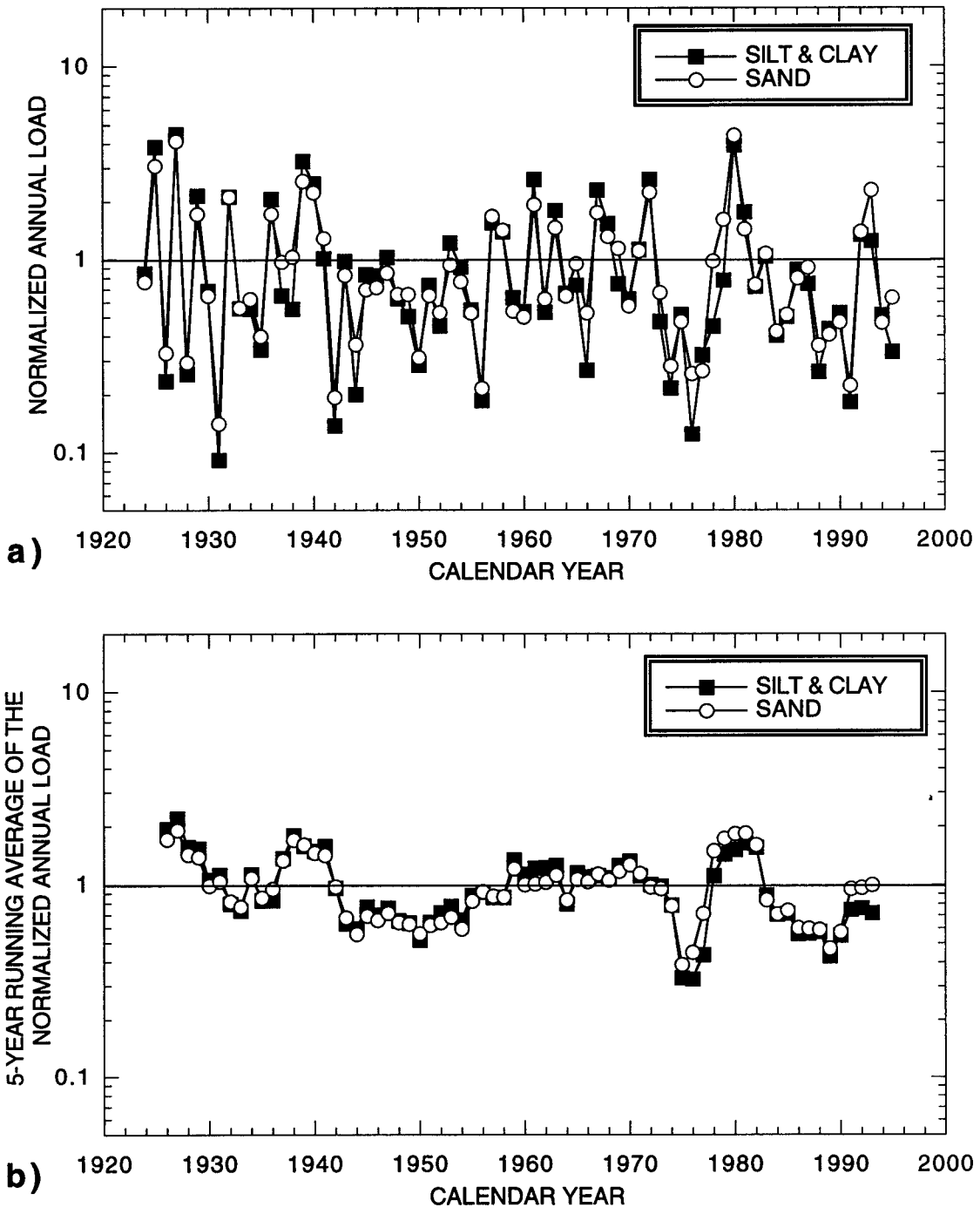

Figure 4.19: **(a)** Model-predicted normalized annual loads of silt & clay and sand for the period of gage record. **(b)** Model-predicted 5-year running average of the normalized annual loads of silt & clay and sand for the period of gage record.

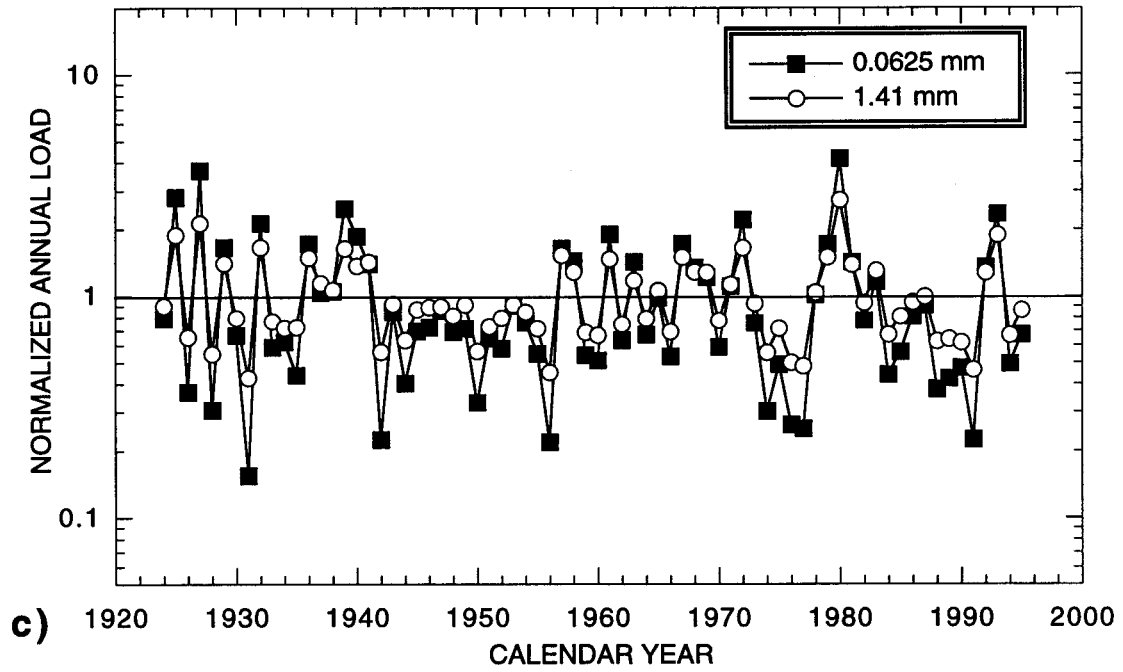

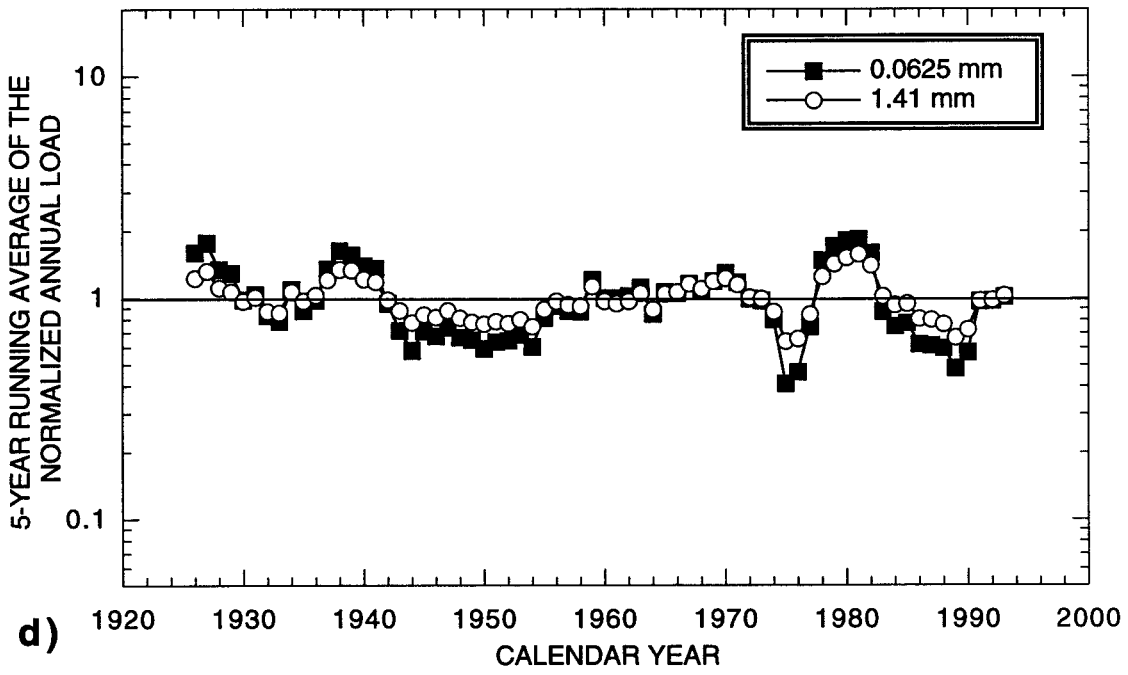

Figure 4.19 (continued): **(c)** Model-predicted normalized annual loads of 0.0625 and 1.41 mm sand for the period of gage record. **(d)** Model-predicted 5-year running average of the normalized annual loads of 0.0625 and 1.41 mm sand for the period of gage record.

Table 4.3: Model-predicted mean-annual sediment loads of the Paria River for the entire period of gage record and comparison of the model-predicted mean-annual sediment loads with previously published estimates of the mean-annual sediment loads.

	TIME PERIOD	TOTAL SED. (m^3/yr)	SILT & CLAY (m^3/yr)	TOTAL SAND (m^3/yr)	SAND BY SIZE CLASS (m^3/yr)									
					0.0625 mm	0.088 mm	0.125 mm	0.177 mm	0.25 mm	0.35 mm	0.50 mm	0.71 mm	1.00 mm	1.41 mm
THIS STUDY	**11-22-23 through 9-30-96**	**9.09e+05**	**4.25e+05 ***	**4.84e+05**	**1.29e+05**	**1.08e+05**	**1.65e+05**	**3.79e+04**	**2.73e+04**	**8740**	**2410**	**904**	**1180**	**2910**
THIS STUDY	11-22-23 through 9-30-84	9.70e+05	4.59e+05	5.11e+05										
Randle and Pemberton (1987)	11-22-23 through 9-30-84	1.46e+06	10.9e+05	3.70e+05										
THIS STUDY	10-1-47 through 9-30-76	8.12e+05	3.88e+05	4.24e+05										
Andrews (1990)	10-1-47 through 9-30-76	1.03e+06												
Smillie and others (1993)	10-1-47 through 9-30-76	1.13e+06	8.60e+05	2.70e+05										

Notes:
* This value may represent the mean of a value that has decreased over the period of gage record; the silt and clay load is predicted to have decreased by 65%, at the 0.055 level of significance, over the period of gage record.

Each of these three previously published load estimates was calculated by a different method. Randle and Pemberton (1987) calculated their value of the mean-annual sediment and sand loads through a 3-step process. They first computed a rating curve to relate daily suspended-sediment load to the daily mean discharge by fitting a 2-part log-linear regression to the quasi-daily suspended-sediment data collected by the USGS from October 1, 1947 through September 30, 1976 (see Figure 3.1). To determine the magnitude of sand fraction of the total suspended sediment, they calculated a mean sand to total suspended-sediment ratio of 19.4% based on the average fraction of sand in the 1954-1976 and 1983 grain-size analyzed suspended-sediment samples (see Figure 3.2). Since, the depth-integrated suspended-sediment samplers used by the USGS do not sample to the bed (e.g., Figure 4.10), they assumed that an additional sand load equal to 7.5% of the total load was unmeasured load. Finally, they calculated the mean-annual sediment and sand loads by using their rating curves for sediment and sand in conjunction with the daily flow duration curves for water years 1924 through 1984.

The method of Randle and Pemberton (1987) produces a misleading result for four reasons. First, as demonstrated in this study (e.g., Figures 4.16), the ratio of sand to silt and clay is not constant, with sand increasing in proportion to the silt and clay as discharge increases. Second, suspended-silt and clay concentration, unlike suspended-sand concentration, does not vary only as a function of discharge and is also a function of time since the last flood during the monsoon season. Third, a regression fit to suspended-sediment data not separated by season will be heavily biased toward the enhanced concentrations of suspended sediment (due to enhanced concentration of silt and clay) during the monsoon season and will, therefore, overpredict the concentrations of suspended sediment during the remaining eight months of the year. Finally, because the USGS overestimated the overbank discharges prior to September 1963 (see Section 2.4c-1), loads based on published daily discharges before September 1, 1963 will be much too high. For these four reasons, Randle and Pemberton (1987), for the period from November 22, 1923 through September 30, 1984, overpredict the mean-annual sediment load relative to the model prediction by 51% and underpredict the mean-annual sand load relative to the model prediction by 28%.

Andrews (1990) calculated his value of the mean-annual sediment load by dividing the cumulative sediment loads "measured" by the USGS in the Paria River at Lees Ferry, AZ from October 1, 1947 through September 30, 1976 by the 29 years of record. The model predicts a slightly lower mean-annual sediment load than that reported by Andrews (1990) for the period of sediment record, not because of disagreement between the model-

predictions and measurements of sediment concentration (e.g., Figure 4.14), but because the USGS overestimated the discharges of the overbank flows prior to September 1963 (see Section 2.4c-1). These overestimations of overbank discharge over the first 16 years of the period of suspended-sediment record account for the 27% higher mean-annual sediment load reported by Andrews (1990).

Smillie and others (1993) used a hybrid of the methods of Andrews (1990) and Randle and Pemberton (1987) in their calculation of the mean-annual sediment and sand loads. They calculated the mean-annual sediment load by first dividing the cumulative sediment loads "measured" by the USGS in the Paria River at Lees Ferry, AZ from October 1, 1947 through September 30, 1976 by the 29 years of record and then assuming that 20% of the measured suspended-sediment load was sand and that an additional sand load equal to 20% of their assumed suspended-sand load occurred as unmeasured load. Because they used the published daily discharges that include overbank discharges that are too high prior to September 1963 [like Randle and Pemberton (1987) and Andrews (1990)] and their unmeasured load assumption is somewhat ad hoc, they overpredict the mean-annual sediment load by 39% relative to the model prediction for the period of October 1, 1947 through September 30, 1976. The major flaw in the methodology of Smillie and others (1993) is that, as already mentioned, the sand fraction of the suspended load is not constant, but varies as the silt and clay concentration varies with time after a flood in the monsoon season and, for the same concentration of silt and clay, increases with discharge. Because of this flaw, Smillie and others (1993) calculated a mean-annual sand load that was 36% less than the model-predicted value for the period of October 1, 1947 through September 30, 1976.

The effective discharge of the Paria River at Lees Ferry, AZ with implications for the stability of the equilibrium bankfull channel geometry since 1872

As defined by Wolman and Miller (1960) and used by Andrews (1980), the effective discharge of a river is that discharge that transports the most sediment over time and is a combination of the magnitude and frequency of sediment-transporting events. In rivers carrying a bimodal distribution of grain-sizes, it is useful to determine the effective discharge for each size range of sediment. Figure 4.20 thus illustrates the effective discharges of the Paria River at Lees Ferry, AZ with respect to sand, silt & clay, and gravel. Figure 4.20 was constructed by binning the instantaneous discharge into equal-dimensioned 0.2 m^3/s bins and summing, at five-minute intervals over the period from November 22, 1923 through September 30, 1996: (1) the model-predicted sand and silt &

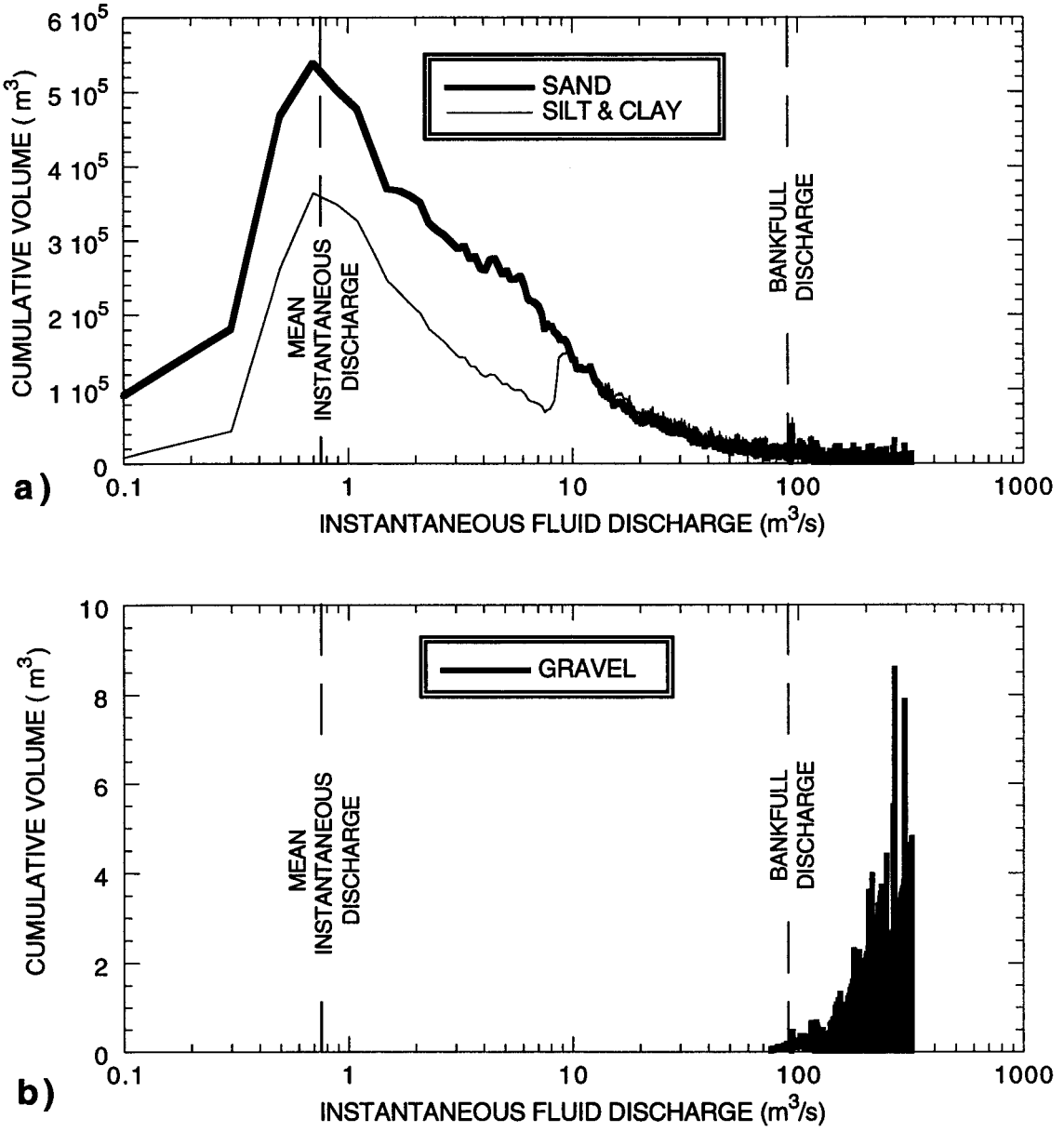

Figure 4.20: **(a)** Cumulative volume of sand and silt & clay transported by the Paria River from November 22, 1923 through September 30, 1996. The secondary peak in the silt and clay at 8.5 m^3/s is an artifact of the modeled enhancement of silt and clay concentrations within 100 hours of a flood peak in excess of 8.5 m^3/s during the monsoon season. **(b)** Cumulative volume of gravel and silt & clay transported by the Paria River from November 22, 1923 through September 30, 1996.

clay loads; and (2) the gravel loads predicted by the equation of Parker and others (1982). Some discharge bins have zero values of cumulative sediment volume because, especially during the highest flows, the instantaneous discharge changes faster than 0.2 m^3/s over 5 minutes. Thus, at the highest flows, the cumulative sediment volume as a function of instantaneous discharge alternates between high values and zero values.

The effective discharge of a river is not necessarily related to the bankfull discharge. Andrews (1980) showed that, in perennial rivers in which the bankfull discharge is equaled or exceeded every 0.9 years in the partial-duration series and is equaled or exceeded 1.5% of the time, the effective discharge is approximately equal to the bankfull discharge. This relationship does not hold true for "duration-limited" rivers like the Paria River, in which the bankfull discharge is still equaled or exceeded every 2.2 years on the partial duration series but is equaled or exceeded only 0.021% of the time. Thus, even though bankfull discharges occur with a reasonable frequency, because their duration is three orders of magnitude less than the duration of the mean instantaneous discharge (see Section 2.4g), over time very little sediment moves at the bankfull discharge. Because of the dominance of the mean instantaneous discharge, the most sand and the most silt and clay move over time at the mean instantaneous discharge of 0.77 m^3/s. As in most gravel rivers, substantial gravel transport in the Paria River is predicted to occur at discharges in excess of about 80% of the bankfull discharge, but because these flows are equaled or exceeded only 0.03% of the time, gravel rarely moves in the equilibrium reaches of the Paria River.

Andrews (1980) argued that the stable bankfull channel geometry of a river was formed by the flows that transported the most sediment over time. In contrast, one could also argue that a channel should be the most stable for the discharge range that transports the least amount of sediment over time. In the Paria River, the bankfull discharge is the discharge that effectively transports the least amount of sediment over time; that is, in the Paria River, the bankfull discharge is 117 times greater than the flow that transports the most sand and the most silt and clay over time, and the bankfull discharge is well below the rarest, largest, discharges that transport the most gravel over time. Furthermore, the observation that the bankfull discharge of the Paria River transports the least amount of sediment over time illustrates why, as shown in Chapter 2, the bankfull channel geometries of equilibrium reaches with similar longitudinal slopes have been stable from 1872 to the present.

Section 4.6: SUMMARY AND CONCLUSIONS

In this chapter, the geomorphically coupled flow and sediment transport model developed and tested in Chapter 3 has been rigorously tested against extensive channel-geometry, flow, and sediment-transport data from the Lees Ferry, AZ reach of the Paria River. In all tests, the model was found to work well, lending support to the two working hypotheses and five physical assumptions used in the development of the model. Though in specific cases, some of the hypotheses and assumptions may not be completely valid (e.g., in contrast to the third physical assumption, channel-scale form drag is important on average at low discharges), the model does capture the essence of the physical coupling between the in-channel flow and sediment-transport processes and channel geomorphic adjustment during floods.

Enforcement of the reach-scale mass conservation of each sediment size class between the bed and the flow was found to work well in predicting both magnitude of channel enlargement during a flood and measured concentrations of each size class of suspended sand, suggesting that, on average, mass of each size class of sand is conserved on the reach scale in the equilibrium reaches of the Paria River. Exclusion of lateral advective transport of sediment was also found to work well in predicting both magnitude of cross-section enlargement during floods and measured cross-stream differences in depth-integrated sediment concentration; comparison of model predictions to measurements of cross-section shape suggest that only during overbank flows does significant lateral transport occur, thus changing the ultimate shape of the cross-section after a flood, but not changing the amount of widening during a flood. Furthermore, the model includes the relevant physics associated with the high fluid densities, high fluid viscosities, and high density gradients that partially damp the turbulence, and was found to predict adequately the measured depth-integrated sediment concentrations in the "hyperconcentrated" range, thus suggesting that "hyperconcentrated" flows are merely the upper endmember of turbulent suspensions and not a physically distinct process.

The model was found to work well in predicting all of the quasi-daily suspended-sediment data collected from October 1, 1947 through September 30, 1975. Therefore, because the hydraulic geometry of equilibrium reaches of the Paria River has been stable since 1872 (see Sections 2.5 and 2.6), and the hydrology has been approximately stationary since at least 1923 (see Section 2.4), the sediment-transport predictions of the model were applied to the instantaneous discharge time series for the entire period of record from November 22, 1923 through September 30, 1996. Though decadal variation is predicted to exist in sand load, trends at the 0.05 level of significance are not predicted for

any of the sizes of sand over this time period. The finest sizes of sediment are predicted to be most affected by subtle changes in the hydrology of the system because they are largely advected through the Paria River from hillslopes and not tightly coupled to the fluvial geomorphology (see Section 3.2c). Thus, because of subtle trends in the hydrology, the silt and clay load is predicted to have decreased, at the marginal 0.055 level of significance, by 65% over the period from November 22, 1923 through September 30, 1996.

Application of the geomorphically coupled flow and sediment transport model to the period of record results in predictions of substantially higher sand loads than previously predicted by empirically based studies. In contrast to assumptions used in these previous studies, this study has illustrated that the sand fraction of the suspended load is not constant; sand concentration greatly increases with discharge while silt and clay concentration does not. Furthermore, the silt and clay concentration varies greatly by season and is the highest within 100 hours of a monsoon season flood. Slightly more sand than silt and clay is transported by the Paria River over time; sand transport dominates all of the low flows within about 100 hours of a flood during the monsoon season.

This study shows that ephemeral rivers, because of their "duration-limited" nature, may have the most stable channel geometry of all rivers; channels of these rivers are effectively built on top of a relatively stable gravel carpet. In the absence of channel perturbations due to catastrophic floods that mobilize substantial amounts of gravel and may destabilize the floor of the channel, or to natural or human-caused base level changes that generate headcuts, channels of ephemeral rivers should change very slowly because significant gravel-transporting events occur less than 0.03% of the time. The stable bankfull geometry of the Paria River is not set by the flows that transport the most sediment over time, but is probably set by the interplay between hydrology and vegetation (see Section 2.6a). Phreatophytes that line the channel attempt colonization of the upper parts of the channel down to the low-flow water surface and are occasionally removed by floods. Thus, the bankfull channel geometry will be maintained by floods that occur frequently enough to remove seedlings on the bars before they become firmly established, promote the trapping of sand, and begin the formation of new floodplains. Though the largest floods may heavily perturb channel geometry over short time scales, these floods are geomorphically unimportant to the long-term geometry of the river system.

Chapter 5: CONCLUSIONS

Work presented in this dissertation addresses the physics associated with flow, sediment transport, and channel geometry in flash-flood-dominated, ephemeral river systems. Since the Paria River is typical of ephemeral rivers on the Colorado Plateau, this work shows that the classic "arroyo problem" in southwestern geomorphology may not be a truly regional problem, but, rather, maybe a regional combination of local problems associated with locally perturbed reaches of channel. All channel changes that have occurred on the Paria River since the 1870's have been driven by changes in either local base level or channel longitudinal slope, rather than major changes in hydrology and sediment transport, i.e., climate. Therefore, my work illustrates that changes in climate over the last 120 years, such as those inferred from regional tree-ring width records, are much more weakly coupled to the geomorphology than assumed by many previous workers on fluvial channel change on the Colorado Plateau. Furthermore, my work demonstrates that the salient physical principles that determine channel geometry in alluvial rivers are the conservation of water and the conservation of sediment mass. The hydraulic geometry model that I have developed using these principles and have shown to work well in the Paria River system is applicable to all rivers with banks that are more easily erodible than the bed; the Paria River was simply the ideal laboratory to apply and test the model because the bankfull discharge, bankfull sediment load, and bed grain-size distribution are constant over the lower 81% of the river while the longitudinal slope of the channel decreases by about a factor of two.

The hydrology of the Paria River has been effectively stationary since the beginning of gage record on November 22, 1923. Trends in the published discharge record of the Paria River are not real, but are due to changing methods used by the USGS in determining peak discharges. For the period from November 22, 1923 through September 30, 1996 (the period of gage record), the mean instantaneous discharge, mean annual discharge, bankfull discharge, and largest peak flood discharge have been 0.77 m^3/s, 88 m^3/s, 90 m^3/s, and 320 m^3/s, respectively. Furthermore, during the period from about 1880 to September 1996, the largest known flood occurred in September 1909, and had a peak discharge no greater than about 400 m^3/s, i.e., only about 25% larger than the largest flood during the period of record. For the period of gage record, the mean instantaneous discharge was only equaled or exceeded 20.6% of the time, and the bankfull discharge was equaled or exceeded only 0.021% of the time. Furthermore, for the period of gage record, the flood-frequency distribution has been stable, at the 0.05 level of significance, with the

bankfull discharge being equaled or exceeded every 2.9 years in the annual-maximum flood series and every 2.2 years in the partial-duration flood series.

Lack of significant trends in the Paria River hydrologic data suggests that the hydrology of an ephemeral river is more weakly coupled to changes in climate over the last century, such as those inferred from tree-ring width data, than assumed by previous workers. Only two trends were detected in the hydrologic data during the period of gage record: the mean instantaneous discharge has decreased by 6% or 0.049 m^3/s; and the peak discharge of floods has also decreased slightly. This decreasing trend in peak flood discharge, however, is due only to the timing of the three largest of the 1308 floods above a base flow of 3.79 m^3/s; no trends in peak discharge exist for floods with peaks less than or equal to 2.8x bankfull discharge. Furthermore, during the period of gage record, no trends, at the 0.05 level of significance, exist in flood volume or flood duration for either the 1308 floods or the 33 overbank floods above a base flow of 3.79 m^3/s; and, no trends, at the 0.05 level of significance, exist in the discharge of overbank peaks or the duration of overbank flows for the 37 flood peaks above a bankfull base flow.

Channel incision and aggradation are currently, and have been in the past, only local features related to variation in local base level in the Paria River basin. In reaches of the river examined in this study, incision and aggradation have been driven by base-level changes at the confluence with the Colorado River; aggradation and subsequent incision have been associated with base-level changes associated with emplacement and subsequent breaching of rockfall/landslide dams; and incision has been associated with the effective decrease in base level following cutoff of meanders in the alluvial reach above Rock House, UT. No significant change in the minimum bed elevation of the channel has occurred: in excess of 3.9 km above the confluence with the Colorado River since 1872; at the site of the Paria, UT diversion dam since 1877; at the near Cannonville, UT gage since 1951; or at the site of the near Kanab, UT gage since 1971.

Placement of modern equilibrium reaches between Cannonville and Lees Ferry in the context of the hydraulic geometry model that I have developed indicates that the steep, wide, shallow, quasi-braided reaches near Cannonville and the more gently sloping, narrower, deeper, single-thread reaches near Lees Ferry have an equivalent hydraulic geometry. Moreover, in the Lees Ferry study area, channel cross-section geometry of equilibrium reaches of the Paria River has been stable for reaches of similar longitudinal slope over the last 120 years; channel widening or narrowing has occurred only as a function of a reach-scale change in channel longitudinal slope. In contrast to the conclusions of Hereford (1986, 1987a, 1987b) and W. Graf (1987), I could find no major

increase in floodplain volume since 1940 in the Paria River system. Both smaller-scale USGS slope-area surveys and large-scale cadastral and topographic maps indicate that the channel of the Paria River has laterally migrated over large portions of the valley floor, thus reworking previously deposited floodplain sediment. The assumption that no floodplain sediment existed between terrace margins prior to 1940, used by Hereford (1987b) and W. Graf (1987) to calculate new floodplain volume, is incorrect. Floodplains are prominent in old photographs dating from 1873, 1911, 1915, 1918, and 1939.

No hydrologic or sediment-transport change (i.e., no change in climate) is required to explain the channel changes that have occurred in the Paria River since the 1870's. Application of the hydraulic geometry model to the channel cross-section geometries and longitudinal slopes that have existed in Lees Ferry and Paria-Adairville reaches indicates that equilibrium channel geometries that have existed in these two reaches from the 1870's to the present have had an equivalent hydraulic geometry. The "arroyo-type" channel changes that occurred during the late 19th and earliest 20th centuries in the Paria-Adairville reach occurred within the same hydraulic geometry and were driven by human-induced changes in channel longitudinal slope. These "arroyo-type" channel changes were most prevalent in reaches that were most perturbed by human settlement. Because no major change in Paria River hydrology from 1880 to the present is documented, it is likely that increases in slope associated with meander cutoffs that triggered channel widening in the 1880's near the settlement of Paria, UT were not caused by catastrophic flooding, but by smaller floods encountering a reach heavily perturbed by the Mormon pioneers. By 1877, in the reach near Paria, UT: a major irrigation dam was constructed; a road ran straight down the valley cutting across meanders (this road eventually became the 1917 course of the river); and virtually all native vegetation on the floodplain was removed for the purpose of agriculture.

In the Paria River, the amount of sand in transport during the entire year and the amount of silt and clay in transport during the "non-monsoon" season are largely in equilibrium with the reach-scale hydraulics and supply in the bed. In contrast , the amount of silt and clay in transport during the monsoon season, because of its low settling velocity and thus long advection length, can be enhanced by a factor of three within 100 hours after a flood peak. Thus, the sand load is more tightly coupled to the reach-scale geomorphology than the silt and clay load, which largely reflects variation in the seasonal intensity of precipitation on hillslopes in the upper portion of the drainage basin. Application of the geomorphically coupled, flow and sediment transport model to the Paria River suggests that the amount of channel cross-section enlargement during a flood is

determined by the reach-scale mass conservation of each sediment size class between the bed and the flow. Furthermore, modeling suggests that the lateral advective transport of sediment is relatively unimportant to the geomorphic adjustment of the reach-averaged channel cross-section during floods, except perhaps during the largest floods; and, modeling suggests that channel-scale form drag is only important in the Paria River at discharges less than about 10 m^3/s.

The subtle changes in hydrology that have occurred over the last century (i.e., the 6% decrease in mean instantaneous discharge and the slight decrease in peak flood discharge) have not greatly affected the geomorphology of the Paria River channel and are not predicted to have caused major changes in the mean-annual load of sand. No trends, at the 0.05 level of significance, are predicted to exist in the annual loads of any of the ten size classes of sand for the period of gage record. In contrast, since the silt and clay load is not greatly coupled to the reach-scale geomorphology and is more sensitive to subtle changes in hydrology, the silt and clay load is predicted to have decreased by about 65% (at the marginal 0.055 level of significance) over the period of gage record. Given that, to a large extent, the hydrology, and to a larger extent, the fluvial geomorphology and sand load, are not greatly affected by the largest tree-ring width "climatic" anomaly in 1700 years, the mean-annual sand load is probably effectively constant with respect to time and should be predictable over the several-hundred-year time scale. Thus, this study suggests that climatic variability in the southwestern United States is coupled more tightly to hillslope processes, which control silt and clay loads, than it is coupled to in-channel fluvial processes that control the geomorphology of the river channel.

Finally, channel geometries of ephemeral rivers like the Paria River are not maintained by the "effective discharge" that transport the most sediment over time, but are probably maintained by the interplay between hydrology and phreatophyte vegetation that can trap sand along the banks. Bankfull floods may possibly set the channel geometry in an ephemeral river only because they occur frequently enough to remove vegetation before it gets firmly established in the higher portions of the channel. Over time, the least amount of sediment has been moved by bankfull discharges in the Paria River. The most sand and the most silt and clay have been transported over time by the mean instantaneous discharge; conversely, the most gravel has been moved over time at the most extreme discharges. Because ephemeral rivers are "duration-limited" with regard to sediment transport (i.e., sediment transport at higher discharges has been small over time because the duration of higher discharges has been short) and because gravel on the bed rarely moves, these rivers should be the most geometrically stable of all rivers over the longest time scales.

REFERENCES

Andrews, E.D., 1980, Effective and bankfull discharges of streams in the Yampa River basin, Colorado and Wyoming: Journal of Hydrology, v. 46, p. 311-330.

Andrews, E.D., 1984, Bed-material entrainment and hydraulic geometry of gravel-bed rivers in Colorado: Geological Society of America Bulletin, v. 95, p. 371-378.

Andrews, E.D., 1990, The Colorado River; A perspective from Lees Ferry, Arizona, *in* Wolman, M.G., Church, M., Newbury, R., Lapointe, M., Frenette, M., Andrews, E.D., Lisle, T.E., Buchanan, J.P., Schumm, S.A., and Winkley, B.R., The riverscape, *in* Wolman, M.G., and Riggs, H.C., eds., Surface water hydrology, The Geology of North America, v. O-1: Boulder, Colorado, Geological Society of America, p. 281-328.

Bailey, R.W., 1935, Epicycles of erosion in the valleys of the Colorado Plateau province: Journal of Geology, v. 43, p. 337-355.

Bailey, T.C., and Burrill, J.G., 1877, Cadastral survey of township no. 41 south, range no. 2 west of the Salt Lake meridian, Utah and township nos. 41, 42, and 43, range no. 1 west of the Salt Lake meridian, Utah: Denver, Colorado, U.S. Bureau of Land Management Archives.

Batchelor, G.K., and Green, J.T., 1972, The determination of the bulk stress in a suspension of spherical particles to order c^2: Journal of Fluid Mechanics, v. 56, part 3, p. 401-427.

Bejan, A., 1984, Convection heat transfer: New York, John Wiley and Sons, Inc, 477 p.

Beverage, J.P., and Culbertson, J.K., 1964, Hyperconcentrations of suspended sediment: Journal of the Hydraulics Division, Proceedings of the American Society of Civil Engineers, v. 90, p. 117-128.

Bondurant, D.C., 1950, Sedimentation studies at Conchas Reservoir in New Mexico: Transactions of the American Society of Civil Engineers, v. 76, n. 29, p. 1-10.

Bondurant, D.C., 1951, Discussion of "Sedimentation studies at Conchas Reservoir in New Mexico": Transactions of the American Society of Civil Engineers, v. 77, n. D-29, p. 1-3.

Brian, N., 1992, River to rim, A guide to place names along the Colorado River in Grand Canyon from Lake Powell to Lake Mead: Flagstaff, Arizona, Earthquest Press, 176 p.

Bryan, K., 1925, Date of channel trenching (arroyo cutting) in the arid southwest: Science, v. 62, p. 338-344.

Bureau of Reclamation, 1990, Glen Canyon Environmental Studies, Area 2, River Mile -4.0 to +2.0, Contract No. 8-CS-40-0527B D008: Rapid City, South Dakota, Horizons, Inc., Scale 1:2400, 5 sheets.

Burkham, D.E., 1972, Channel changes of the Gila River in Safford Valley, Arizona 1846-1970: U.S. Geologic Survey Professional Paper 655-G, 24 p.

Burkham, D.E., 1986, Trends in selected hydraulic variables for the Colorado River at Lees Ferry and near Grand Canyon, Arizona--1922-1984: Glen Canyon Environmental Studies Report No. PB88-216098, 58 p.

Businger, J.A., Wyngaard, J.C., Izumi, Y., and Bradley, E.F., 1971, Flux-profile relationships in the atmospheric surface layer: Journal of Atmospheric Science, v. 28, p. 181-189.

Chow, V.T., 1959, Open-channel hydraulics: New York, McGraw-Hill, 680 p.

Church, M., and Rood, K., 1983, Catalogue of Alluvial River Channel Regime Data: Vancouver, B.C., University of British Columbia, Department of Geography, 99p.

Cleland, R.G., and Brooks, J., eds., 1983, A Mormon chronicle: The diaries of John D. Lee, 1848-1876, v. 2: Salt Lake City, Utah, University of Utah Press, 480 p.

Dalrymple, T., and Benson, M.A., 1967, Techniques of water-resources investigations of the United States Geological Survey, Book 3, Chapter A2, Measurement of peak discharge by the slope-area method, 12 p.

Dean, J.S., Euler, R.C., Gumerman, G.J., Plog, F., Hevly, R.H., and Karlstrom, T.N.V., 1985, Human behavior, demography, and paleoenvironment on the Colorado Plateaus: American Antiquity, v. 50, p. 537-554.

Dietrich, W.E., 1982a, Settling velocity of natural particles: Water Resources Research, v. 18, p. 1615-1626.

Dietrich, W.E., 1982b, Flow, boundary shear stress and sediment transport in a river meander: University of Washington, unpublished Ph.D. thesis, 261 p.

Dietrich, W.E., and Whiting, P., 1989, Boundary shear stress and sediment transport in river meanders of sand and gravel, *in* Ikeda, I., and Parker, G., eds., River Meandering: Washington, D.C., American Geophysical Union Monograph 12, p. 1-50.

Dodge, R.E., 1902, Arroyo formation: Science, v. 15, p. 746.

Dunne, T., and Leopold, L.B., 1978, Water in environmental planning: New York, W.H. Freeman and Company, 818 p.

Dutton, C.E., 1882, Tertiary history of the Grand Canyon District: U.S. Geological Survey Monograph 2, 264 p.

Edwards, T.K., and Glysson, G.D., 1988, Field methods for measurement of fluvial sediment: U.S. Geologic Survey Open-File Report 86-531, 118 p.

Egiazaroff, I.V., 1965, Calculations of nonuniform sediment concentrations: Journal of the Hydraulics Division, American Society of Civil Engineers, v. 91, n. HY4, p. 225-247.

Einstein, A., 1906, Eine neue Bestimmung der Mölekuledimensionen: Annln. Phys., v. 19, p. 289 (and v.34, p. 591).

Einstein, H.A., and Chien, N., 1955, Effects of heavy sediment concentration near the bed on velocity and sediment distribution: University of California, Berkeley, Institute of Engineering Research, no. 8.

Ely, L.L., Enzel, Y., Baker, V.R., and Cayan, D.R., 1993, A 5000-year record of extreme floods and climate change in the southwestern United States: Science, v. 262, p. 410-412.

Emmett, W.W., 1975, The channels and waters of the upper Salmon River area, Idaho: U.S. Geological Survey Professional Paper 870A, p. 1-116.

Fernandez Luque, R., and van Beek, R., 1976, Erosion and transport of bed-load sediment: Journal of Hydraulic Research, v. 14, p. 127-144.

Fischer, H.B., 1963, Longitudinal dispersion and turbulent mixing in open channel flow: Annual Review of Fluid Mechanics, v.5, p. 289-302.

Flammer, G.H., Tullis, J.P., and Mason, E.S., 1970, Free surface, velocity gradient flow past hemisphere: Journal of the Hydraulics Division, Proceedings of the American Society of Civil Engineers, v. 96, 1485-1502.

Garrett, W.B., Van De Vanter, E.K., and Graf, J.B., 1993, Streamflow and sediment-transport data, Colorado River and three tributaries in Grand Canyon, Arizona, 1983 and 1985-86: U.S. Geologic Survey Open-File Report 93-174, 624 p.

Gelfenbaum, G., and Smith, J.D., 1986, Experimental evaluation of a generalized suspended-sediment transport theory: *in* Knight, R.J., and McLean, J.R., eds., Shelf sands and sandstones, Canadian Society of Petroleum Geologists, Memoir II, p. 133-144.

Gould, O.O., 1928, Cadastral survey of township no. 40 north, range no. 7 east of the Gila and Salt River meridian, Utah: Denver, Colorado, U.S. Bureau of Land Management Archives.

Graf, J.B., Webb, R.H., and Hereford, R., 1991, Relation of sediment load and flood-plain formation to climatic variability, Paria River drainage basin, Utah and Arizona: Geological Society of America Bulletin, v. 103, p. 1405-1415.

Graf, J.B., Marlow, J.E., Fisk, G.G., and Jansen, S.M.D., 1995, Sand-storage changes in the Colorado River downstream from the Paria and Little Colorado Rivers, June 1992 to February 1994: U.S. Geological Survey Open-File Report 95-446, 61 p.

Graf, W.H., 1971, Hydraulics of sediment transport: New York, McGraw-Hill Book Company, 509 p.

Graf, W.L., 1983, The arroyo problem - palaeohydrology and palaeohydraulics in the short term, *in* Gregory, K.J., ed., Background to palaeohydrology: New York, John Wiley and Sons Ltd., p. 279-302.

Graf, W.L., 1987, Late Holocene sediment storage in canyons of the Colorado Plateau: Geological Society of America Bulletin, v. 99, p. 261-271.

Gregory, H.E., 1951, The geology and geography of the Paunsaugunt region, Utah: U.S. Geological Survey Professional Paper 226, 116 p.

Gregory, H.E., and Moore, R.C., 1931, The Kaiparowits region: A geographic and geologic reconnaissance of parts of Utah and Arizona: U.S. Geologic Survey Professional Paper 164, 161 p.

Griffiths, J.C., 1967, Scientific method in analysis of sediments: New York, McGraw-Hill Book Company, 508 p.

Guy, H.P., 1969, Laboratory theory and methods for sediment analysis: United States Geological Survey techniques of water-resources investigations, Book 5, Chapter C1, 58 p.

Guy, H.P., and Norman, V.W., 1970, Field methods for measurement of fluvial sediment: United States Geological Survey techniques of water-resources investigations, Book 3, Chapter C2, 59 p.

Guy, H.P., Simons, D.B., and Richardson, E.V., 1966, Summary of alluvial channel data from flume experiments, 1956-61: U.S. Geologic Survey Professional Paper 462-I, 96 p.

Hereford, R., 1983, Effect of climate and a geomorphic threshold on the historic geomorphology and alluvial stratigraphy of the Paria and Little Colorado Rivers, southwest Colorado Plateaus, *in* Wells, S.G., Love, D.W., and Gardner, T.W., eds., Chaco Canyon country: Albuquerque, New Mexico, American Geomorphological Field Group, Field Trip Guidebook, p. 247.

Hereford, R., 1986, Modern alluvial history of the Paria River drainage basin: Quaternary Research, v. 25, p. 293-311.

Hereford, R., 1987a, The short term: Fluvial processes since 1940, *in* Graf, W.L., Hereford, R., Laity, J., and Young, R.A., Colorado Plateau, *in* Graf, W.L., ed., Geomorphic systems of North America: Boulder, Colorado, Geological Society of America, Centennial Special Volume 2, p. 276-288.

Hereford, R., 1987b, Sediment storage since 1940 in channels of the Paria River basin, Utah - Implications for regional land management: Geological Society of America Abstracts with Programs, v.19, p. 701.

Hereford, R., 1989, Variation of warm-season rainfall frequency in the southern Colorado Plateau and its effect on runoff and alluvial-channel morphology: A preliminary analysis: U.S. Geological Survey Open-File Report 89-330, 16 p.

Hereford, R., 1993, Entrenchment and widening of the upper San Pedro River, Arizona: Boulder, Colorado, Geological Society of America Special Paper 282, 46 p.

Hereford, R., Jacoby, G.C., and McCord, V.A.S., 1996, Late Holocene alluvial geomorphology of the Virgin River in the Zion National Park area, southwest Utah: Boulder, Colorado, Geological Society of America Special Paper 310, 41 p.

Hey, R.D., and Thorne, C.R., 1986, Stable channels with mobile gravel beds: Journal of Hydraulic Engineering, v. 112, p. 671-689.

Hunt, J.N., 1969, On the turbulent transport of a heterogeneous sediment: The Quarterly Journal of Mechanics and Applied Mathematics, v. 22, p. 235-246.

Ikeda, S., 1981, Self-formed straight channels in sandy beds: Journal of the Hydraulics Division, American Society of Civil Engineers, v. 107, n. HY4, p. 389-406.

Ikeda, S., 1982, Incipient motion of sand particles on side slopes: Journal of the Hydraulics Division, Proceedings of the American Society of Civil Engineers, v. 108, n. HY1, p. 95-114.

Ikeda, S., and Izumi, N., 1990, Width and depth of self-formed straight gravel rivers with bank vegetation: Water Resources Research, v. 26, p. 2353-2364.

Ikeda, S., and Izumi, N., 1991, Stable channel cross-sections of straight sand rivers: Water Resources Research, v. 27, p. 2429-2438.

Ikeda, S., Parker, G., and Kimura, Y., 1988, Stable width and depth of straight gravel rivers with heterogeneous bed materials: Water Resources Research, v. 24, p. 713-722.

Interagency Advisory Committee on Water Data, 1981, Guidelines for determining flood flow frequency: Washington, D.C., Interagency Advisory Committee on Water Data, Hydrology Subcommittee, Bulletin 17B, 28 p.

Iorns, W.V., Hembree, C.H., Phoenix, D.A., and Oakland, G.L., 1964, Water resources of the upper Colorado River basin - Basic data: U.S. Geologic Survey Professional Paper 442, 1036 p.

Janda, R.J., and Meyer, D.F., 1986, Sediment concentration and channel morphology: Proceedings of the Fourth Federal Interagency Sedimentation Conference, Las Vegas, Nevada, p. 3-83 to 3-92.

Kennedy, J.F., 1961, Stationary waves and antidunes in alluvial channels, California Institute of Technology, Division of Engineering, W.M. Keck Laboratory of Hydraulics and Water Resources Report No. KH-R-2, 146 p.

Kennedy, J.F., 1963, The mechanics of dunes and antidunes in erodible-bed channels: Journal of Fluid Mechanics, v. 16, p. 521-544.

Laboratory of Tree-Ring Research, University of Arizona, 1990, Tree-Ring data, 293 SouthWest USA sites. World Data Center-A for Paleoclimatology Data Contribution Series #90-005. NOAA/NGDC Paleoclimatology Program, Boulder, CO, USA.

Leliavsky, S., 1955, An introduction to fluvial hydraulics: London, Constable and Company Ltd., 257 p.

Leopold, L.B., 1994, A view of the river: Cambridge, Massachusetts, Harvard University Press, 298 p.

Leopold, L.B., and Maddock, T., Jr., 1953, The hydraulic geometry of stream channels and some physiographic implications: U.S. Geologic Survey Professional Paper 252, 57 p.

Leopold, L.B., and Miller, J.P., Ephemeral streams - Hydraulic factors and their relation to the drainage net: U.S. Geologic Survey Professional Paper 282-A, 37 p.

Long, C.E., Wiberg, P.L., and Nowell, A.R.M., 1993, Evaluation of von Karman's constant from integral flow parameters: Journal of Hydraulic Engineering, v. 119, p. 1182-1190.

Mackin, J.H., 1948, Concept of the graded river: Geological Society of America Bulletin, v. 59, p. 463-512.

Mason, P.J., and Derbyshire, S.H., 1990, Large-eddy simulation of the stably-stratified atmospheric boundary layer: Boundary-Layer Meteorology, v. 53, p. 117-162.

McLean, S.R., 1991a, Depth-integrated suspended-load calculations: Journal of Hydraulic Engineering, v. 117, p. 1440-1458.

McLean, S.R., 1991b, Stratification effects due to suspended sediments: Proceedings of the International Symposium on the Transport of Suspended Sediment and its Mathematical Modeling, Florence, Italy, p. 145-164.

McLean, S.R., 1992, On the calculation of suspended load for noncohesive sediments: Journal of Geophysical Research, v. 97, p. 5759-5770.

Melis, T.S., Phillips, W.M., Webb, R.H., and Bills, D.J., 1996, When the blue-green waters turn red: Historical flooding in Havasu Creek, Arizona: U.S. Geologic Survey Open-File Report 96-4059, 136 p.

Meyer-Peter, E., and Müller, R., 1948, Formulas for bed-load transport: International Association of Hydraulics Research, 2nd Meeting, Stockholm, p. 39-64.

Michell, J.H., 1893, The highest waves in water: Philosophy Magazine, v.36, p. 430-437.

Middleton, G.V., and Southard, J.B., 1984, Mechanics of sediment movement: Tulsa, Oklahoma, SEPM Short Course Number 3, 401 p.

Mohrig, D.C., 1994, Spatial evolution of dunes in a sandy river: University of Washington, unpublished Ph.D. thesis, 119 p.

Monin, A.S., and Yaglom, A.M., 1965, Statisicheskaya gidromekhanika - Mekhanika Turbulentnosti: Moscow, Nauka Press (English translation, Statistical Fluid Mechanics: Mechanics of Turbulence, v. 1: Cambridge, Massachusetts, MIT Press, 1971, translated by Scripta Technica, Inc.)

National Park Service, 1975, Lee's Ferry, Glen Canyon National Recreation Area, Drawing Number 608/41,070: Denver, Colorado, Kucera and Associates, Scale 1:600, 14 sheets.

Nelson, J.N., and Smith, J.D., 1989, Evolution and stability of erodible channel beds, *n* Ikeda, I., and Parker, G., eds., River Meandering: Washington, D.C., American Geophysical Union Monograph 12, p. 321-377.

Nelson, J.M., Emmett, W.W., and Smith, J.D., 1991, Flow and sediment transport in rough channels: Proceedings of the Fifth Federal Interagency Sedimentation Conference, Las Vegas, Nevada, p. 4-55 to 4-62.

Nelson, J.M., McLean, S.R., and Wolfe, S.R., 1993, Mean flow and turbulence fields over 2-dimensional bed forms: Water Resources Research, v. 29, p. 3935-3953.

Nikuradse, J., 1933, Strömungsgesetze in rauhen Röhrne, VDI-Fohrshungsheft 361. (English translation, Laws of flows in rough pipes, NACA Technical Memorandum 1292: National Advisory Committee for Aeronautics, Washington, D.C., 1950, translated by A.A. Briclmaier.)

Nordin, C.F., Jr., 1963, A preliminary study of sediment transport parameters, Rio Puerco near Bernardo, New Mexico: U.S. Geologic Survey Professional Paper 462-C, 21 p.

Nordin, C.F., Jr., 1964, Study of channel erosion and sediment transport: Journal of the Hydraulics Division, American Society of Civil Engineers, v. 90, n. HY4, p. 173-192.

Nordin, C.F., Jr., and Dempster, G.R., Jr., 1963, Vertical distribution of velocity and suspended sediment, middle Rio Grande, New Mexico: U.S. Geologic Survey Professional Paper 462-B, 20 p.

O'Brian, M.P., 1933, Review of the theory of turbulent flow and its relation to sediment transportation: Transactions of the American Geophysical Union, v. 14, p. 487-491.

Paola, C., and Mohrig, D., 1996, Palaeohydraulics revisited: palaeoslope estimation in coarse-grained braided rivers: Basin Research, v. 8, p. 243-254.

Parker, G., 1978a, Self-formed straight rivers with equilibrium banks and mobile bed. Part 2. The gravel river: Journal of Fluid Mechanics, v. 89, p. 127-146.

Parker, G., 1978b, Self-formed straight rivers with equilibrium banks and mobile bed. Part 1. The sand-silt river: Journal of Fluid Mechanics, v. 89, p. 109-125.

Parker, G., 1979, Hydraulic geometry of active gravel rivers: Journal of the Hydraulics Division, American Society of Civil Engineers, v. 105, n. HY9, p. 1185-1201.

Parker, G., and Peterson, A.W., 1980, Bar resistance of gravel-bed streams: Journal of the Hydraulics Division, American Society of Civil Engineers, v. 106, n. HY10, p. 1559-1575.

Parker, G., Klingeman, P.C., and McLean, D.G., 1982, Bedload and size distribution in paved gravel-bed streams: Journal of the Hydraulics Division, American Society of Civil Engineers, v. 108, n. HY4, p. 544-571.

Pemberton, E.L., 1976, Channel changes in the Colorado River below Glen Canyon Dam: Proceedings of the Third Federal Interagency Sedimentation Conference, p. 5-61 to 5-73.

Pierson, T.C., and Costa, J.E., 1987, A rheological classification of subaerial sediment-water flows, *in* Costa, J.E., and Wieczorek, G.F., eds., Debris flows/avalanches: Process, recognition, and mitigation: Geological Society of America Reviews in Engineering Geology, v. 7, p. 1-12.

Pierson, T.C., and Scott, K.M., 1985, Downstream dilution of a lahar: Transition from debris flow to hyperconcentrated streamflow: Water Resources Research, v. 21, p. 1151-1524.

Pitlick, J, 1992, Flow resistance under conditions of intense gravel transport: Water Resources Research, v. 28, p. 891-903.

Randle, T.J., and Pemberton, E.L., 1987, Results and analysis of STARS modeling efforts of the Colorado River in Grand Canyon: Glen Canyon Environmental Studies Report, 41 p. plus 95 figures and 26 tables.

Rattray, M., Jr., and Mitsuda, E., 1974, Theoretical analysis of conditions in a salt wedge: Estuarine Coastal Marine Science, v. 2, p. 373-394.

Rohr, J.J., Itsweire, E.C., Helland, K.N., and van Atta, C.W., 1988, Growth and decay of turbulence in a stably stratified shear flow: Journal of Fluid Mechanics, v. 195, p. 77-111.

Rusho, W.L., and Crampton, C.G., 1992, Lee's Ferry: Desert river crossing: Salt Lake City, Utah, Cricket Publications, 168 p.

Schlichting, H., 1979, Boundary-layer theory: New York, McGraw-Hill Book Company, 817 p.

Smillie, G.M., Jackson, W.L., and Tucker, D., 1993, Colorado River sand budget: Lees Ferry to Little Colorado River: National Park Service Technical Report NPS/NRWRD/NRTR-92/12, 11 p.

Smith, J.D., 1977, Modeling of sediment transport on continental shelves, *in* Goldberg, E.D., ed., The Sea, v. 6: New York, John Wiley and Sons, p. 539-577.

Smith, J.D., and McLean, S.R., 1977a, Spatially averaged flow over a wavy surface: Journal of Geophysical Research (Oceans), v. 82, p. 1735-1746.

Smith, J.D., and McLean, S.R., 1977b, Boundary layer adjustments to bottom topography and suspended sediment, *in* Nihoul, J.C.J., ed., Proceedings of the 8th International Liege Colloquium on Ocean Hydrodynamics: Elsevier Publishing Company, p. 123-151.

Stein, R.A., 1965, Laboratory studies of total load and apparent bed load: Journal of Geophysical Research, v. 70, p. 1831.

Subcommittee on Sedimentation, Federal Inter-agency River Basin Committee, 1952, The study of methods used in measurement and analysis of sediment loads in streams, Report no. 6, The design of improved types of suspended-sediment samplers: Minneapolis, Minnesota, St. Anthony Falls Hydraulic Laboratory, 103 p.

Tennekes, H., and Lumley, J.L., 1972, A first course in turbulence: Cambridge, Massachusetts, MIT Press, 300 p.

Thoma, J.C., and Rathbone, T.C., 1917, Cadastral resurvey of township no. 41 south, range no. 1 west of the Salt Lake meridian, Utah: Denver, Colorado, U.S. Bureau of Land Management Archives.

Topping, D.J., and Smith, J.D., 1993, One hundred twenty three years of data on the Paria River: Implications for geomorphology and hydrology: EOS, Transactions, American Geophysical Union, v. 74, n. 43, p. 320.

Turner, R.M., and Karpiscak, M.M., 1980, Recent vegetation changes along the Colorado River between Glen Canyon Dam and Lake Mead, Arizona: U.S. Geologic Survey Professional Paper 1132, 125 p.

U.S. Geological Survey, 1951, Aerial photograph no. 10-6-51, 15-108, GS-QZ.

U.S. Geological Survey, 1952, Aerial photograph no. 10-8-52, 20-55, GS-WG.

U.S. Geological Survey, 1977, Aerial photograph no. Jun 15, 1977, 1-129, GS-VELE.

U.S. Geological Survey, 1980, Aerial photograph no. 6-13-80, 48-132, 361004, HAP, 80.

Vanoni, V.A., 1944, Transportation of suspended sediment by water: Transactions of the American Society of Civil Engineers, v. 109, p. 67-133.

Vanoni, V.A., and Brooks, N.H., 1957, Laboratory studies of the roughness and suspended load of alluvial streams: California Institute of Technology Report No. E-68.

Webb, R.H., 1985, Late Holocene flooding on the Escalante River, south-central Utah: University of Arizona, unpublished Ph.D. thesis, 204 p.

Webb, R.H., 1987, Occurrence and geomorphic effects of streamflow and debris flow floods in northern Arizona and southern Utah, *in* Mayer, L., and Nash, D., eds., Catastrophic flooding: Boston, Allen and Unwin, Inc., p. 247-265.

Webb, R.H., 1996, Grand Canyon, a century of environmental change: Rephotography of the 1889-1890 Stanton expedition: Tucson, Arizona, University of Arizona Press, 290 p.

Webb, R.H., Smith, S.S., and McCord, V.A.S., 1991, Historical channel change of Kanab Creek, southern Utah and northern Arizona: Grand Canyon Natural History Association Monograph Number 9, 91 p.

Webb, R.H., Melis, T.H., Wise, T.W., and Elliott, J.G., "The great cataract": Effects of late Holocene debris flows on Lava Falls Rapid, Grand Canyon National Park and Hualapai Indian Reservation, Arizona: U.S. Geologic Survey Open-File Report 96-460, 96 p.

Wiberg, P.L., and Rubin, D.M., 1989, Bed roughness produced by saltating sediment: Journal of Geophysical Research (Oceans), v. 90, p. 5011-5016.

Wiberg, P.L., and Smith, J.D., 1987a, Calculations of the critical shear stress for motion of uniform and heterogeneous sediments: Water Resources Research, v. 23, p. 1471-1480.

Wiberg, P.L., and Smith, J.D., 1987b, Initial motion of coarse sediment in streams of high-gradient, *in* Erosion and sedimentation in the Pacific rim: Proceedings of the International Association of Hydraulic Research, v. 165, p. 299-308.

Wiberg, P.L., and Smith, J.D., 1989, Model for calculating bed load transport of sediment: Journal of Hydraulic Engineering, v. 115, p. 101-123.

Wiberg, P.L., and Smith, J.D., 1991, Velocity distribution and bed roughness in high-gradient streams: Water Resources Research, v. 27, p. 825-838.

Wiele, S.M., and Smith, J.D., 1996, A reach-averaged model of diurnal discharge wave propagation down the Colorado River through the Grand Canyon: Water Resources Research, v. 32, p. 1375-1386.

Wieringa, J., 1980, A revaluation of Kansas mast influence on measurements of stress and cup anemometer overspeeding: Boundary Layer Meteorology, v. 18, p. 411-430.

Wilcock, P.R., and McArdell, B.W., 1993, Surface-based fractional transport rates: Mobilization thresholds and partial transport of a sand-gravel sediment: Water Resources Research, v. 29, p. 1297-1312.

Williams, G.P., 1978, Bankfull discharge of rivers: Water Resources Research, v. 14, p. 1141-1154.

Williams, G.P., and Wolman, M.G., 1984, Downstream effects of dams on alluvial rivers: U.S. Geologic Survey Professional Paper 1286, 83 p.

Wilson, K.C., 1966, Bed-load transport at high shear stress: Journal of the Hydraulics Division, Proceedings of the American Society of Civil Engineers, v. 92, p. 49-59.

Wolman, M.G., 1954, A method of sampling coarse river-bed materials: EOS, Transactions of the American Geophysical Union, v. 35, no. 6, p. 951-956.

Wolman, M.G., and Brush, L.M., Jr., 1961, Factors controlling the size and shape of stream channels in coarse noncohesive sands: U.S. Geologic Survey Professional Paper 282-G, 210 p.

Wolman, M.G., and Miller, J.P., 1960, Magnitude and frequency of forces in geomorphic processes: Journal of Geology, v. 68, p. 54-74.

Appendix 1: STATISTICAL ANALYSIS OF PARIA RIVER CROSS-SECTION GEOMETRY

INDIVIDUAL "TIME PERIOD" DATA BINS	n	R^2	SS_r	SS_d	DEG. OF FREEDOM ASSOC. w/ SS_d	F_1 from equation 2.4 (with associated level of significance, p)
11-22-23 through 8-14-72	2165	0.310	16000	35900	2163	964 (p < 1.0e-16)
8-15-72 through 9-30-92	280	0.458	1500	1780	278	234 (p < 1.0e-16)
9-9-80 through 9-30-92	178	0.229	237	796	176	52.4 (p = 1.4e-11)
11-22-23 through 12-31-39	731	0.219	3610	12900	729	204 (p < 1.0e-16)
1-1-40 through 8-14-72	1434	0.350	12400	23000	1432	772 (p < 1.0e-16)
11-22-23 through 12-31-49	1121	0.196	5610	23000	1119	273 (p < 1.0e-16)
1-1-50 through 8-14-72	1046	0.449	10500	12800	1044	856 (p < 1.0e-16)
11-22-23 through 12-31-59	1693	0.254	10100	29500	1691	579 (p < 1.0e-16)
1-1-60 through 8-14-72	472	0.489	5880	6150	470	449 (p < 1.0e-16)
COMBINED DATA BINS	j	R^2	SS_r	SS_d	DEG. OF FREEDOM ASSOC. w/ SS_d	F_1 from equation 2.4 (with associated level of significance, p)
11-22-23 through 9-30-92	2445	0.307	17200	38800	2443	1080 (p < 1.0e-16)
11-22-23 through 9-30-92 except 8-15-72 through 9-8-80	2267	0.317	17200	37000	2265	1050 (p < 1.0e-16)

TEST WHETHER THE FOLLOWING BINS CAN BE REPRESENTED BY A COMMON REGRESSION LINE	MS_{diff}	MS_{ind}	F_2 from equation 2.5	CRITICAL LEVEL OF SIGNIFICANCE (p)	REJECT NULL HYPOTHESIS OF A COMMON REGRESSION LINE AT p = 0.05
11-22-23 through 8-14-72, 8-15-72 through 9-30-92	1160	15.4	75.3	< 1.0e-16	**YES** (CHANNEL IS 30% NARROWER AFTER 8-15-72)
11-22-23 through 8-14-72, 9-9-80 through 9-30-92	308	16.2	19.0	1.4e-5	**YES** (CHANNEL IS 30-40% NARROWER AFTER 9-9-80)
11-22-23 through 12-31-39, 1-1-40 through 8-14-72	5.00	16.6	0.301	0.58	**NO**
11-22-23 through 12-31-49, 1-1-40 through 8-14-72	22.0	16.6	1.33	0.25	**NO**
11-22-23 through 12-31-59, 1-1-60 through 8-14-72	177	16.5	10.7	0.0011	**YES** (CHANNEL IS SLIGHTLY WIDER AFTER 1-1-60)

Appendix 2: STATISTICAL ANALYSIS OF THE GRAIN-SIZE ANALYZED PARIA RIVER SUSPENDED-SEDIMENT DATA

Notes for tables in this appendix:
* Indicates that the regression is not significant at the 0.0001 level of significance; in this case the variance about the mean of the log-transformed concentration and the degrees of freedom associated with the total sum of squares are shown in parentheses in the previous 2 columns. See text for further explanation.
† Indicates that the calculated level of significance is less than the level of significance associated with one of the regressions fit to the binned data.

Table 1: (TEST 1) At a given instantaneous fluid discharge, does the concentration of suspended sand depend on the year of the suspended-sediment measurement?

INDIVIDUAL "YEAR OF MEASUREMENT" DATA BINS	n	R^2	SS_r	SS_d	DEG. OF FREEDOM ASSOC. w/ SS_d	F_1 from equation 2.4 (with associated level of significance, p)
1954-1961	28	0.784	29.8	8.20	26	94.3 (p = 3.9e-10)
1962-1968	81	0.573	156	117	79	106 (p = 3.3e-16)
1969-1976	36	0.723	39.8	15.2	34	88.9 (p = 5.1e-11)
1983	81	0.544	25.2	21.1	79	94.3 (p = 4.0e-15)
COMBINED DATA BINS	j	R^2	SS_r	SS_d	DEG. OF FREEDOM ASSOC. w/ SS_d	F_1 from equation 2.4 (with associated level of significance, p)
1954-1983	226	0.532	241	212	224	255 (p < 1.0e-16)
1954-1976	145	0.635	254	146	143	249 (p < 1.0e-16)

TEST WHETHER THE FOLLOWING BINS CAN BE REPRESENTED BY A COMMON REGRESSION LINE	MS_{diff}	MS_{ind}	F_2 from equation 2.5	CRITICAL LEVEL OF SIGNIFICANCE (p)	REJECT NULL HYPOTHESIS OF A COMMON REGRESSION LINE AT p = 0.0001
1954-1961, 1962-1968, 1969-1976, 1983	16.8	0.741	22.7	†7.9e-13 (cannot be less than 3.9e-10)	**YES**
1954-1961, 1962-1968, 1969-1976	1.87	1.01	1.85	0.16	**NO**
1954-1976, 1983	44.9	0.753	59.6	3.9e-13	**YES**

Table 2: (TEST 2) At a given instantaneous fluid discharge, does the 1954-1976 concentration of suspended sand depend on season?

INDIVIDUAL "SEASON OF MEASUREMENT" DATA BINS	n	R^2	SS_r	SS_d	DEG. OF FREEDOM ASSOC. w/ SS_d	F_1 from equation 2.4 (with associated level of significance, p)
MONSOON SEASON (July 1 - October 31)	93	0.596	163	110	91	134 (p < 1.0e-16)
"NON-MONSOON" SEASON (Nov. 1 - June 30)	52	0.599	49.0	32.7	50	74.8 (p = 1.7e-11)
COMBINED DATA BINS	j	R^2	SS_r	SS_d	DEG. OF FREEDOM ASSOC. w/ SS_d	F_1 from equation 2.4 (with associated level of significance, p)
ENTIRE YEAR	145	0.635	254	146	143	249 (p < 1.0e-16)

TEST WHETHER THE FOLLOWING BINS CAN BE REPRESENTED BY A COMMON REGRESSION LINE	MS_{diff}	MS_{ind}	F_2 from equation 2.5	CRITICAL LEVEL OF SIGNIFICANCE (p)	REJECT NULL HYPOTHESIS OF A COMMON REGRESSION LINE AT p = 0.0001
MONSOON SEASON, "NON-MONSOON" SEASON	3.30	1.01	3.27	0.073	**NO**

Table 3: (TEST 2) At a given instantaneous fluid discharge, does the 1983 concentration of suspended sand depend on season?

INDIVIDUAL "SEASON OF MEASUREMENT" DATA BINS	n	R^2	SS_r	SS_d (SS_t in parentheses)	DEG. OF FREEDOM ASSOC. w/ SS_d	F_1 from equation 2.4 (with associated level of significance, p)
MONSOON SEASON (July 1 - October 31)	77	0.543	24.9	21.0	75	89.2 (p = 2.1e-14)
"NON-MONSOON" SEASON (Nov. 1 - June 30)	4	0.657	0.304	0.159 (0.463)	2 (3)	*3.83 (p = 0.19)
COMBINED DATA BINS	j	R^2	SS_r	SS_d	DEG. OF FREEDOM ASSOC. w/ SS_d	F_1 from equation 2.4 (with associated level of significance, p)
ENTIRE YEAR	81	0.544	25.2	21.1	79	94.3 (p = 4.0e-15)

TEST WHETHER THE FOLLOWING BINS CAN BE REPRESENTED BY A COMMON REGRESSION LINE	MS_{diff}	MS_{ind}	F_2 from equation 2.5	CRITICAL LEVEL OF SIGNIFICANCE (p)	REJECT NULL HYPOTHESIS OF A COMMON REGRESSION LINE AT p = 0.0001
MONSOON SEASON, "NON-MONSOON" SEASON	-0.363	0.275	-1.32	1.0	**NO**

Table 4: (TEST 3) At a given instantaneous fluid discharge, does the 1954-1976 concentration of suspended sand depend on the time since the last flood peak?

INDIVIDUAL "TIME SINCE FLOOD PEAK" DATA BINS	n	R^2	SS_r	SS_d	DEG. OF FREEDOM ASSOC. w/ SS_d	F_1 from equation 2.4 (with associated level of significance, p)
≤15 MINUTES AFTER PEAK	1	—	—	—	—	—
>15 MIN. & ≤10 HRS. AFTER PEAK	34	0.656	23.6	12.4	32	60.9 (p = 6.7e-9)
>10 & ≤100 HOURS AFTER PEAK	27	0.494	30.0	30.7	25	24.4 (p = 4.4e-5)
>100 & ≤1000 HRS. AFTER PEAK	31	0.585	76.3	54.0	29	41.0 (p = 5.3e-7)
>1000 HOURS AFTER PEAK	46	0.587	53.8	37.8	44	62.6 (p = 5.4e-10)
COMBINED DATA BINS	j	R^2	SS_r	SS_d	DEG. OF FREEDOM ASSOC. w/ SS_d	F_1 from equation 2.4 (with associated level of significance, p)
ALL MEASUREMENTS	139	0.643	254	141	137	247 (p < 1.0e-16)
≤10 HOURS AFTER PEAK	35	0.658	25.4	13.2	33	63.6 (p = 3.4e-9)
> 10 HOURS AFTER PEAK	104	0.568	165	125	102	134 (p < 1.0e-16)
≤100 HOURS AFTER PEAK	62	0.615	73.0	45.8	60	95.7 (p = 4.9e-14)
>100 HOURS AFTER PEAK	77	0.586	130	92.0	75	106 (p = 5.6e-16)
≤1000 HOURS AFTER PEAK	93	0.629	174	103	91	154 (p < 1.0e-16)

TEST WHETHER THE FOLLOWING BINS CAN BE REPRESENTED BY A COMMON REGRESSION LINE	MS_{diff}	MS_{ind}	F_2 from equation 2.5	CRITICAL LEVEL OF SIGNIFICANCE (p)	REJECT NULL HYPOTHESIS OF A COMMON REGRESSION LINE AT p = 0.0001
≤10 HOURS AFTER PEAK, >10 & ≤100 HOURS AFTER PEAK, >100 & ≤1000 HRS. AFTER PEAK, >1000 HOURS AFTER PEAK	1.04	1.77	0.588	0.62	**NO**
≤10 HOURS AFTER PEAK, >10 HOURS AFTER PEAK	2.80	1.01	2.77	0.098	**NO**
≤100 HOURS AFTER PEAK, >100 HOURS AFTER PEAK	3.20	1.02	3.14	0.079	**NO**
≤1000 HOURS AFTER PEAK, >1000 HOURS AFTER PEAK	0.200	1.04	0.192	0.66	**NO**

Table 5: (TEST 3) At a given instantaneous fluid discharge, does the 1983 concentration of suspended sand depend on the time since the last flood peak?

INDIVIDUAL "TIME SINCE FLOOD PEAK" DATA BINS	n	R^2	SS_r	SS_d (SS_t in parentheses)	DEG. OF FREEDOM ASSOC. w/ SS_d (& SS_t)	$F1$ from equation 2.4 (with associated level of significance, p)
≤15 MINUTES AFTER PEAK	0	----	----	----	----	----
>15 MIN. & ≤10 HRS. AFTER PEAK	6	0.0134	0.0244	1.80 (1.82)	4 (5)	*0.0543 (p = 0.83)
>10 & ≤100 HOURS AFTER PEAK	25	0.304	2.24	5.12 (7.36)	23 (24)	*10.1 (p = 0.0042)
>100 & ≤1000 HRS. AFTER PEAK	43	0.623	9.15	5.54	41	67.7 (p = 3.2e-10)
>1000 HOURS AFTER PEAK	7	0.324	2.76	5.77 (8.53)	5 (6)	*2.39 (p = 0.18)
COMBINED DATA BINS	j	R^2	SS_r	SS_d	DEG. OF FREEDOM ASSOC. w/ SS_d	$F1$ from equation 2.4 (with associated level of significance, p)
ALL MEASUREMENTS	81	0.544	25.2	21.1	79	94.3 (p = 4.0e-15)
≤100 HOURS AFTER PEAK	31	0.441	7.08	9.00	29	22.8 (p = 4.7e-5)
>100 HOURS AFTER PEAK	50	0.514	12.2	11.5	48	50.8 (p = 4.7e-9)

TEST WHETHER THE FOLLOWING BINS CAN BE REPRESENTED BY A COMMON REGRESSION LINE	MS_{diff}	MS_{ind}	F_2 from equation 2.5	CRITICAL LEVEL OF SIGNIFICANCE (p)	REJECT NULL HYPOTHESIS OF A COMMON REGRESSION LINE AT p = 0.0001
>15 MIN. & ≤10 HRS. AFTER PEAK, >10 & ≤100 HOURS AFTER PEAK, >100 & ≤1000 HRS. AFTER PEAK, >1000 HOURS AFTER PEAK	-0.717	0.306	-2.34	1.0	**NO**
≤100 HOURS AFTER PEAK, >100 HOURS AFTER PEAK	0.600	0.266	2.26	0.14	**NO**

Table 6: (TEST 4) At a given instantaneous fluid discharge, does the 1954-1976 concentration of suspended sand depend on the time between the last two flood peaks?

INDIVIDUAL "TIME BETWEEN FLOOD PEAKS" DATA BINS	n	R^2	SS_r	SS_d (SS_t in parentheses)	DEG. OF FREEDOM ASSOC. w/ SS_d (& SS_t)	F_1 from equation 2.4 (with associated level of significance, p)
≤50 HOURS	42	0.595	74.1	50.4	40	58.8 (p = 1.4e-8)
>50 & ≤100 HOURS	9	0.828	30.3	6.28 (36.5)	7 (8)	*33.8 (p = 6.5e-4)
>100 & ≤1000 HRS.	67	0.742	149	51.8	65	187 (p < 1.0e-16)
>1000 HOURS	21	0.552	12.8	10.4 (23.2)	19 (20)	*23.4 (p = 1.1e-4)

COMBINED DATA BINS	j	R^2	SS_r	SS_d	DEG. OF FREEDOM ASSOC. w/ SS_d	F_1 from equation 2.4 (with associated level of significance, p)
ALL MEASUREMENTS	139	0.643	254	141	137	247 (p < 1.0e-16)
>50 HOURS	97	0.674	179	86.7	95	197 (p < 1.0e-16)
≤100 HOURS	51	0.642	104	57.9	49	87.9 (p = 1.6e-12)
>100 HOURS	88	0.657	151	78.8	86	165 (p < 1.0e-16)
≤1000 HOURS	118	0.682	248	115	116	249 (p < 1.0e-16)

TEST WHETHER THE FOLLOWING BINS CAN BE REPRESENTED BY A COMMON REGRESSION LINE	MS_{diff}	MS_{ind}	F_2 from equation 2.5	CRITICAL LEVEL OF SIGNIFICANCE (p)	REJECT NULL HYPOTHESIS OF A COMMON REGRESSION LINE AT p = 0.0001
≤50 HOURS, >50 & ≤100 HOURS, >100 & ≤1000 HRS., >1000 HOURS	-6.97	1.21	-5.76	1.0	**NO**
≤50 HOURS, >50 HOURS	3.90	1.02	3.82	0.053	**NO**
≤100 HOURS, >100 HOURS	4.30	1.01	4.26	0.041	**NO**
≤1000 HOURS, >1000 HOURS	2.80	1.02	2.75	0.10	**NO**

Table 7: (TEST 4) At a given instantaneous fluid discharge, does the 1983 concentration of suspended sand depend on the time between the last two flood peaks?

INDIVIDUAL "TIME BETWEEN FLOOD PEAKS" DATA BINS	n	R^2	SS_r	SS_d (SS_t in parentheses)	DEG. OF FREEDOM ASSOC. w/ SS_d (& SS_t)	F_1 from equation 2.4 (with associated level of significance, p)
≤50 HOURS	8	0.658	0.593	0.308 (0.900)	6 (7)	*11.5 (p = 0.015)
>50 & ≤100 HOURS	26	0.333	3.76	7.53 (11.3)	24 (25)	*12.0 (p = 0.0020)
>100 & ≤1000 HRS.	43	0.810	16.0	3.76	41	174 (p = 2.2e-16)
>1000 HOURS	4	0.408	3.99	5.79 (9.78)	2 (3)	*1.38 (p = 0.36)
COMBINED DATA BINS	j	R^2	SS_r	SS_d (SS_t in parentheses)	DEG. OF FREEDOM ASSOC. w/ SS_d (& SS_t)	F_1 from equation 2.4 (with associated level of significance, p)
ALL MEASUREMENTS	81	0.544	25.2	21.1	79	94.3 (p = 4.0e-15)
>50 HOURS	73	0.552	25.1	20.4	71	87.6 (p = 5.1e-14)
≤100 HOURS	34	0.309	3.94	8.81 (12.8)	32 (33)	*14.3 (p = 6.4e-4)
>100 HOURS	47	0.638	19.1	10.9	45	79.1 (p = 1.8e-11)
≤1000 HOURS	77	0.592	21.0	14.5	75	109 (p = 3.3e-16)

TEST WHETHER THE FOLLOWING BINS CAN BE REPRESENTED BY A COMMON REGRESSION LINE	MS_{diff}	MS_{ind}	F_2 from equation 2.5	CRITICAL LEVEL OF SIGNIFICANCE (p)	REJECT NULL HYPOTHESIS OF A COMMON REGRESSION LINE AT p = 0.0001
≤50 HOURS, >50 & ≤100 HOURS, >100 & ≤1000 HRS., >1000 HOURS	-1.55	0.339	-4.57	1.0	**NO**
≤50 HOURS, >50 HOURS	-0.200	0.273	-0.733	1.0	**NO**
≤100 HOURS, >100 HOURS	-2.60	0.304	-8.55	1.0	**NO**
≤1000 HOURS, >1000 HOURS	-3.18	0.311	-10.2	1.0	**NO**

Table 8: (TEST 5) At a given instantaneous fluid discharge, does the 1954-1976 concentration of suspended sand depend on the size of the last flood peak?

INDIVIDUAL "DISCHARGE OF FLOOD PEAK" DATA BINS	n	R^2	SS_r	SS_d (SS_t in parentheses)	DEG. OF FREEDOM ASSOC. w/ SS_d (& SS_t)	F_1 from equation 2.4 (with associated level of significance, p)
>8.5 & ≤24.8 m^3/s	54	0.734	79.1	28.6	52	144 (p = 1.1e-16)
>24.8 & ≤41.1 m^3/s	29	0.664	73.2	37.1	27	53.3 (p = 7.5e-8)
>41.1 & ≤57.4 m^3/s	20	0.881	77.6	10.5	18	133 (p = 9.5e-10)
>57.4 & ≤73.7 m^3/s	10	0.920	5.66	0.490	8	92.4 (p = 1.1e-5)
>73.7 & ≤90.0 m^3/s	18	0.693	27.2	12.0	16	36.2 (p = 1.8e-5)
>90.0 m^3/s	8	0.290	4.51	11.0 (15.6)	6 (7)	*2.45 (p = 0.17)
COMBINED DATA BINS	j	R^2	SS_r	SS_d	DEG. OF FREEDOM ASSOC. w/ SS_d	F_1 from equation 2.4 (with associated level of significance, p)
ALL MEASUREMENTS	139	0.643	254	141	137	247 (p < 1.0e-16)
>8.5 & ≤41.1 m^3/s	83	0.667	154	76.9	81	162 (p < 1.0e-16)
>41.1 & ≤73.7 m^3/s	30	0.883	89.9	12.0	28	211 (p = 1.5e=14)
>73.7 m^3/s	26	0.532	30.0	26.3	24	27.3 (p = 2.4e-5)
>8.5 & ≤57.4 m^3/s	103	0.688	224	102	101	223 (p < 1.0e-16)
>57.4 m^3/s	36	0.595	40.5	27.6	34	50.0 (p = 3.6e-8)
>8.5 & ≤90.0 m^3/s	131	0.674	255	124	129	266 (p < 1.0e-16)
>24.8 m^3/s	85	0.662	178	91.0	83	162 (p < 1.0e-16)

TEST WHETHER THE FOLLOWING BINS CAN BE REPRESENTED BY A COMMON REGRESSION LINE	MS_{diff}	MS_{ind}	F_2 from equation 2.5	CRITICAL LEVEL OF SIGNIFICANCE (p)	REJECT NULL HYPOTHESIS OF A COMMON REGRESSION LINE AT p = 0.0001
>8.5 & ≤24.8 m^3/s, >24.8 & ≤41.1 m^3/s, >41.1 & ≤57.4 m^3/s, >57.4 & ≤73.7 m^3/s, >73.7 & ≤90.0 m^3/s, >90.0 m^3/s	7.34	0.815	9.01	2.3e-7	**YES**
>8.5 & ≤41.1 m^3/s, >41.1 & ≤73.7 m^3/s, >73.7 m^3/s	12.9	0.866	14.9	1.4e-6	**YES**
>8.5 & ≤57.4 m^3/s, >57.4 m^3/s	11.4	0.960	11.9	7.5e-4	**NO**
>8.5 & ≤90.0 m^3/s, >90.0 m^3/s	1.4	1.03	1.36	0.25	**NO**
>24.8 & ≤41.1 m^3/s, >41.1 & ≤57.4 m^3/s, >57.4 & ≤73.7 m^3/s, >73.7 & ≤90.0 m^3/s, >90.0 m^3/s	1.60	0.996	1.61	0.18	**NO**
>8.5 & ≤24.8 m^3/s, >24.8 m^3/s	21.4	0.886	24.2	8.6e-6	**YES**

Table 9: (TEST 5) At a given instantaneous fluid discharge, does the 1983 concentration of suspended sand depend on the size of the last flood peak?

INDIVIDUAL "DISCHARGE OF FLOOD PEAK" DATA BINS	n	R^2	SS_r	SS_d	DEG. OF FREEDOM ASSOC. w/ SS_d	F_1 from equation 2.4 (with associated level of significance, p)
>8.5 & ≤24.8 m^3/s	52	0.462	15.4	17.9	50	42.9 (p = 3.0e-8)
>24.8 & ≤41.1 m^3/s	28	0.821	9.73	2.13	26	119 (p = 3.4e-11)
>41.1 & ≤57.4 m^3/s	0	—	—	—	—	—
>57.4 & ≤73.7 m^3/s	0	—	—	—	—	—
>73.7 & ≤90.0 m^3/s	0	—	—	—	—	—
>90.0 m^3/s	1	—	—	—	—	—
COMBINED DATA BINS	j	R^2	SS_r	SS_d	DEG. OF FREEDOM ASSOC. w/ SS_d	F_1 from equation 2.4 (with associated level of significance, p)
ALL MEASUREMENTS	81	0.544	25.2	21.1	79	94.3 (p = 4.0e-15)

TEST WHETHER THE FOLLOWING BINS CAN BE REPRESENTED BY A COMMON REGRESSION LINE	MS_{diff}	MS_{ind}	F_2 from equation 2.5	CRITICAL LEVEL OF SIGNIFICANCE (p)	REJECT NULL HYPOTHESIS OF A COMMON REGRESSION LINE AT p = 0.0001
8.5 - 24.8 m^3/s, 24.8 - 41.1 m^3/s	1.07	0.264	4.05	0.048	**NO**

Table 10: (TEST 6) At a given instantaneous fluid discharge, does the measured 1954-1976 concentration of suspended sand depend on the number of measurement verticals?

INDIVIDUAL "NUMBER OF VERTICALS" DATA BINS	n	R^2	SS_r	SS_d (SS_t in parentheses)	DEG. OF FREEDOM ASSOC. w/ SS_d (& SS_t)	F_1 from equation 2.4 (with associated level of significance, p)
1 vertical	32	0.621	18.6	11.4	30	49.2 (p = 8.5e-8)
2 verticals	84	0.550	126	103	82	100 (p = 7.8e-16)
3 verticals	24	0.698	53.5	23.1	22	50.8 (p = 3.8e-7)
≥4 verticals	5	0.756	9.88	3.19 (13.1)	3 (4)	*9.30 (p = 0.055)
COMBINED DATA BINS	j	R^2	SS_r	SS_d	DEG. OF FREEDOM ASSOC. w/ SS_d	F_1 from equation 2.4 (with associated level of significance, p)
ALL MEASUREMENTS	145	0.635	254	146	143	249 (p < 1.0e-16)
≥3 verticals	29	0.736	75.1	26.9	27	75.5 (p = 2.6e-9)

TEST WHETHER THE FOLLOWING BINS CAN BE REPRESENTED BY A COMMON REGRESSION LINE	MS_{diff}	MS_{ind}	F_2 from equation 2.5	CRITICAL LEVEL OF SIGNIFICANCE (p)	REJECT NULL HYPOTHESIS OF A COMMON REGRESSION LINE AT p = 0.0001
1 vertical, 2 verticals, 3 verticals, ≥4 verticals	-1.53	1.09	-1.40	1.0	**NO**
1 vertical, 2 verticals, ≥3 verticals	2.75	1.02	2.70	0.071	**NO**

Table 11: (TEST 1) At a given instantaneous fluid discharge, does the concentration of suspended silt and clay depend on the year of the suspended-sediment measurement?

INDIVIDUAL "YEAR OF MEASUREMENT" DATA BINS	n	R^2	SS_r	SS_d (SS_t in parentheses)	DEG. OF FREEDOM ASSOC. w/ SS_d (& SS_t)	F_1 from equation 2.4 (with associated level of significance, p)
1954-1961	28	0.339	5.54	10.8 (16.4)	26 (27)	*13.3 (p = 0.0012)
1962-1968	81	0.468	24.2	27.4	79	69.6 (p = 1.9e-12)
1969-1976	36	0.362	8.23	14.5 (22.7)	34 (35)	*19.3 (p = 1.0e-4)
1983	81	0.387	21.5	33.9	79	49.9 (p = 5.6e-10)
COMBINED DATA BINS	j	R^2	SS_r	SS_d	DEG. OF FREEDOM ASSOC. w/ SS_d	F_1 from equation 2.4 (with associated level of significance, p)
1954-1983	226	0.457	77.3	91.7	224	189 (p < 1.0e-16)
1954-1976	145	0.465	47.7	54.8	143	124 (p < 1.0e-16)

TEST WHETHER THE FOLLOWING BINS CAN BE REPRESENTED BY A COMMON REGRESSION LINE	MS_{diff}	MS_{ind}	F_2 from equation 2.5	CRITICAL LEVEL OF SIGNIFICANCE (p)	REJECT NULL HYPOTHESIS OF A COMMON REGRESSION LINE AT p = 0.0001
1954-1961, 1962-1968, 1969-1976, 1983	-2.90	0.456	-6.36	1.0	**NO**
1954-1976, 1983	3.00	0.400	7.50	6.7e-3	**NO**

Table 12: (TEST 2) At a given instantaneous fluid discharge, does the 1954-1976 concentration of suspended silt and clay depend on season?

INDIVIDUAL "SEASON OF MEASUREMENT" DATA BINS	n	R^2	SS_r	SS_d	DEG. OF FREEDOM ASSOC. w/ SS_d	F_1 from equation 2.4 (with associated level of significance, p)
MONSOON SEASON (July 1 - October 31)	170	0.444	50.4	63.0	168	134 (p < 1.0e-16)
"NON-MONSOON" SEASON (Nov. 1 - June 1)	56	0.459	16.0	18.8	54	45.9 (p = 9.6e-9)
COMBINED DATA BINS	j	R^2	SS_r	SS_d	DEG. OF FREEDOM ASSOC. w/ SS_d	F_1 from equation 2.4 (with associated level of significance, p)
ENTIRE YEAR	226	0.457	77.3	91.7	224	189 (p < 1.0e-16)

TEST WHETHER THE FOLLOWING BINS CAN BE REPRESENTED BY A COMMON REGRESSION LINE	MS_{diff}	MS_{ind}	F_2 from equation 2.5	CRITICAL LEVEL OF SIGNIFICANCE (p)	REJECT NULL HYPOTHESIS OF A COMMON REGRESSION LINE AT p = 0.0001
MONSOON SEASON, "NON-MONSOON" SEASON	9.9	0.368	26.9	4.8e-7	**YES**

Table 13: (TEST 3) At a given instantaneous fluid discharge, does the monsoon season concentration of suspended silt and clay depend on the time since the last flood peak?

INDIVIDUAL "TIME SINCE FLOOD PEAK" DATA BINS	n	R^2	SS_r	SS_d (SS_t in parentheses)	DEG. OF FREEDOM ASSOC. w/ SS_d (& SS_t)	F_1 from equation 2.4 (with associated level of significance, p)
≤15 MINUTES AFTER PEAK	1	—	—	—	—	—
>15 MIN. & ≤10 HRS. AFTER PEAK	35	0.124	0.827	5.84 (6.67)	33 (34)	*4.67 (p = 0.038)
>10 & ≤100 HOURS AFTER PEAK	49	0.445	5.04	6.29	47	37.6 (p = 1.7e-7)
>100 & ≤1000 HRS. AFTER PEAK	65	0.328	16.9	34.6	63	30.7 (p = 6.3e-7)
>1000 HOURS AFTER PEAK	17	0.601	10.5	6.96 (17.4)	15 (16)	*22.6 (p = 2.6e-4)
COMBINED DATA BINS	j	R^2	SS_r	SS_d (SS_t in parentheses)	DEG. OF FREEDOM ASSOC. w/ SS_d (& SS_t)	F_1 from equation 2.4 (with associated level of significance, p)
ALL MEASUREMENTS	167	0.442	49.7	62.6	165	130.9 (p = 3.5e-13)
≤10 HOURS AFTER PEAK	36	0.130	0.879	5.86 (6.74)	34 (35)	*5.10 (p = 0.030)
> 10 HOURS AFTER PEAK	131	0.422	39.4	53.8	129	94.3 (p < 1.0e-16)
≤100 HOURS AFTER PEAK	85	0.377	7.57	12.5	83	50.2 (p = 4.2e-10)
>100 HOURS AFTER PEAK	82	0.419	30.3	42.1	80	57.6 (p = 5.1e-11)
≤1000 HOURS AFTER PEAK	150	0.418	39.6	55.2	148	106 (p < 1.0e-16)

Table 13 (continued):

TEST WHETHER THE FOLLOWING BINS CAN BE REPRESENTED BY A COMMON REGRESSION LINE	MS_{diff}	MS_{ind}	F_2 from equation 2.5	CRITICAL LEVEL OF SIGNIFICANCE (p)	REJECT NULL HYPOTHESIS OF A COMMON REGRESSION LINE AT $p = 0.0001$
≤10 HOURS AFTER PEAK, >10 & ≤100 HOURS AFTER PEAK, >100 & ≤1000 HRS. AFTER PEAK, >1000 HOURS AFTER PEAK	-0.787	0.406	-1.94	1.0	**NO**
≤10 HOURS AFTER PEAK, >10 HOURS AFTER PEAK	2.06	0.386	5.34	0.022	**NO**
≤100 HOURS AFTER PEAK, >100 HOURS AFTER PEAK	8.00	0.335	23.9	2.4e-6	**YES**
≤1000 HOURS AFTER PEAK, >1000 HOURS AFTER PEAK	-10.0	0.443	-22.6	1.0	**NO**
≤10 HOURS AFTER PEAK, >10 & ≤100 HOURS AFTER PEAK	-0.530	0.159	-3.33	1.0	**NO**
>100 & ≤1000 HRS. AFTER PEAK, >1000 HOURS AFTER PEAK	-9.90	0.658	-15.0	1.0	**NO**

Table 14: (TEST 3) At a given instantaneous fluid discharge, does the "non-monsoon" season concentration of suspended silt and clay depend on the time since the last flood peak?

INDIVIDUAL "TIME SINCE FLOOD PEAK" DATA BINS	n	R^2	SS_r	SS_d (SS_t in parentheses)	DEG. OF FREEDOM ASSOC. w/ SS_d (& SS_t)	F_1 from equation 2.4 (with associated level of significance, p)
≤15 MINUTES AFTER PEAK	0	—	—	—	—	—
>15 MIN. & ≤10 HRS. AFTER PEAK	5	0.814	2.34	0.534 (2.87)	3 (4)	*13.1 (p = 0.036)
>10 & ≤100 HOURS AFTER PEAK	3	0.999	1.78	0.00140 (1.78)	1 (2)	*1270 (p = 0.018)
>100 & ≤1000 HRS. AFTER PEAK	9	0.418	1.10	1.53 (2.63)	7 (8)	*5.03 (p = 0.060)
>1000 HOURS AFTER PEAK	36	0.563	12.1	9.37	34	43.9 (p = 1.3e-7)
COMBINED DATA BINS	j	R^2	SS_r	SS_d (SS_t in parentheses)	DEG. OF FREEDOM ASSOC. w/ SS_d (& SS_t)	F_1 from equation 2.4 (with associated level of significance, p)
ALL MEASUREMENTS	53	0.526	17.7	15.9	51	56.6 (p = 8.1e-10)
>10 HOURS AFTER PEAK	48	0.504	15.1	14.8	46	46.7 (p = 1.6e-8)
≤100 HOURS AFTER PEAK	8	0.802	3.74	0.920 (4.66)	6 (7)	*24.4 (p = 2.6e-3)
>100 HOURS AFTER PEAK	45	0.473	13.0	14.5	43	38.6 (p = 1.8e-7)
≤1000 HOURS AFTER PEAK	17	0.450	3.30	4.03 (7.33)	15 (16)	*12.3 (p = 3.2e-3)

TEST WHETHER THE FOLLOWING BINS CAN BE REPRESENTED BY A COMMON REGRESSION LINE	MS_{diff}	MS_{ind}	F_2 from equation 2.5	CRITICAL LEVEL OF SIGNIFICANCE (p)	REJECT NULL HYPOTHESIS OF A COMMON REGRESSION LINE AT p = 0.0001
>15 MIN. & ≤10 HRS. AFTER PEAK, >10 & ≤100 HOURS AFTER PEAK, >100 & ≤1000 HRS. AFTER PEAK, >1000 HOURS AFTER PEAK	-0.250	0.347	-0.720	1.0	**NO**
>15 MIN. & ≤10 HRS. AFTER PEAK, >10 HOURS AFTER PEAK	-1.77	0.353	-5.01	1.0	**NO**
≤100 HOURS AFTER PEAK, >100 HOURS AFTER PEAK	-3.26	0.383	-8.51	1.0	**NO**
≤1000 HOURS AFTER PEAK, >1000 HOURS AFTER PEAK	-0.800	0.334	-2.40	1.0	**NO**

Table 15: (TEST 4) At a given instantaneous fluid discharge, does the monsoon season concentration of suspended silt and clay ≤100 hours after a flood peak depend on the time between the last two flood peaks?

INDIVIDUAL "TIME BETWEEN FLOOD PEAKS" DATA BINS	n	R^2	SS_r	SS_d (SS_t in parentheses)	DEG. OF FREEDOM ASSOC. w/ SS_d (& SS_t)	F_1 from equation 2.4 (with associated level of significance, p)
≤50 HOURS	17	0.232	0.643	2.12 (2.76)	15 (16)	*4.54 (p = 0.050)
>50 & ≤100 HOURS	16	0.615	3.02	1.89 (4.91)	14 (15)	*22.4 (p = 3.2e-4)
>100 & ≤1000 HRS.	40	0.673	5.78	2.81	38	78.2 (p = 9.3e-11)
>1000 HOURS	12	0.0309	0.0999	3.13 (3.23)	10 (11)	*0.319 (p = 0.58)

COMBINED DATA BINS	j	R^2	SS_r	SS_d	DEG. OF FREEDOM ASSOC. w/ SS_d	F_1 from equation 2.4 (with associated level of significance, p)
ALL MEASUREMENTS	85	0.377	7.57	12.5	83	50.2 (p = 4.2e-10)
> 50 HOURS	68	0.428	7.21	9.64	66	49.4 (p = 1.4e-9)
≤100 HOURS	33	0.410	3.33	4.79	31	21.5 (p = 6.1e-5)
>100 HOURS	52	0.386	4.59	7.30	50	31.4 (p = 9.0e-7)
≤1000 HOURS	73	0.523	8.80	8.02	71	78.0 (p = 4.8e-13)

TEST WHETHER THE FOLLOWING BINS CAN BE REPRESENTED BY A COMMON REGRESSION LINE	MS_{diff}	MS_{ind}	F_2 from equation 2.5	CRITICAL LEVEL OF SIGNIFICANCE (p)	REJECT NULL HYPOTHESIS OF A COMMON REGRESSION LINE AT p = 0.0001
≤50 HOURS, >50 & ≤100 HOURS, >100 & ≤1000 HRS., >1000 HOURS	-0.403	0.171	-2.36	1.0	**NO**
≤50 HOURS, >50 HOURS	0.100	0.151	0.662	0.42	**NO**
≤100 HOURS, >100 HOURS	0.410	0.149	2.75	0.10	**NO**
≤1000 HOURS, >1000 HOURS	1.25	0.137	9.12	3.4e-3	**NO**

Table 16: (TEST 4) At a given instantaneous fluid discharge, does the monsoon season concentration of suspended silt and clay >100 hours after a flood peak depend on the time between the last two flood peaks?

INDIVIDUAL "TIME BETWEEN FLOOD PEAKS" DATA BINS	n	R^2	SS_r	SS_d (SS_t in parentheses)	DEG. OF FREEDOM ASSOC. w/ SS_d (& SS_t)	F_1 from equation 2.4 (with associated level of significance, p)
≤50 HOURS	16	0.467	4.40	5.01 (9.40)	14 (15)	*12.3 (p = 3.5e-3)
>50 & ≤100 HOURS	16	0.142	0.102	0.617 (0.719)	14 (15)	*2.33 (p = 0.15)
>100 & ≤1000 HRS.	44	0.460	20.9	24.5	42	35.8 (p = 4.2e-7)
>1000 HOURS	6	0.652	6.03	3.22 (9.25)	4 (5)	*7.48 (p = 0.052)
COMBINED DATA BINS	j	R^2	SS_r	SS_d (SS_t in parentheses)	DEG. OF FREEDOM ASSOC. w/ SS_d (& SS_t)	F_1 from equation 2.4 (with associated level of significance, p)
ALL MEASUREMENTS	82	0.419	30.3	42.1	80	57.6 (p = 5.1e-11)
>50 HOURS	66	0.416	26.0	36.6	64	45.5 (p = 5.2e-9)
≤100 HOURS	32	0.362	4.19	7.40 (11.6)	30 (31)	*17.0 (p = 2.7e-4)
>100 HOURS	50	0.476	26.0	28.6	48	43.6 (p = 3.0e-8)
≤1000 HOURS	76	0.386	24.2	38.5	74	46.5 (p = 2.1e-9)

TEST WHETHER THE FOLLOWING BINS CAN BE REPRESENTED BY A COMMON REGRESSION LINE	MS_{diff}	MS_{ind}	F_2 from equation 2.5	CRITICAL LEVEL OF SIGNIFICANCE (p)	REJECT NULL HYPOTHESIS OF A COMMON REGRESSION LINE AT p = 0.0001
≤50 HOURS, >50 & ≤100 HOURS, >100 & ≤1000 HRS., >1000 HOURS	-0.590	0.570	-1.04	1.0	**NO**
≤50 HOURS, >50 HOURS	-3.90	0.582	-6.70	1.0	**NO**
≤100 HOURS, >100 HOURS	1.90	0.509	3.73	0.057	**NO**
≤1000 HOURS, >1000 HOURS	-5.65	0.604	-9.35	1.0	**NO**

Table 17: (TEST 4) At a given instantaneous fluid discharge, does the "non-monsoon" season concentration of suspended silt and clay depend on the time between the last two flood peaks?

INDIVIDUAL "TIME BETWEEN FLOOD PEAKS" DATA BINS	n	R^2	SS_r	SS_d (SS_t in parentheses)	DEG. OF FREEDOM ASSOC. w/ SS_d (& SS_t)	F_1 from equation 2.4 (with associated level of significance, p)
≤50 HOURS	17	0.377	2.21	3.65 (5.86)	15 (16)	*9.07 (p = 8.8e-3)
>50 & ≤100 HOURS	3	0.922	3.50	0.295 (3.79)	1 (2)	*11.8 (p = 0.18)
>100 & ≤1000 HRS.	26	0.516	8.47	7.94	24	25.6 (p = 3.6e-5)
>1000 HOURS	7	0.517	1.82	1.71 (3.53)	5 (6)	*5.34 (p = 0.069)
COMBINED DATA BINS	j	R^2	SS_r	SS_d (SS_t in parentheses)	DEG. OF FREEDOM ASSOC. w/ SS_d (& SS_t)	F_1 from equation 2.4 (with associated level of significance, p)
ALL MEASUREMENTS	53	0.526	17.7	16.0	51	56.6 (p = 8.1e-10)
>50 HOURS	36	0.559	15.5	12.2	34	43.2 (p = 1.6e-7)
≤100 HOURS	20	0.556	6.68	5.33 (12.0)	18 (19)	*22.6 (p = 1.6e-4)
>100 HOURS	33	0.511	10.3	9.90	31	32.3 (p = 3.0e-6)
≤1000 HOURS	46	0.531	16.0	14.1	44	49.8 (p = 9.4e-9)

TEST WHETHER THE FOLLOWING BINS CAN BE REPRESENTED BY A COMMON REGRESSION LINE	MS_{diff}	MS_{ind}	F_2 from equation 2.5	CRITICAL LEVEL OF SIGNIFICANCE (p)	REJECT NULL HYPOTHESIS OF A COMMON REGRESSION LINE AT p = 0.0001
≤50 HOURS, >50 & ≤100 HOURS, >100 & ≤1000 HRS., >1000 HOURS	-1.71	0.440	-3.89	1.0	**NO**
≤50 HOURS, >50 HOURS	-2.06	0.361	-5.71	1.0	**NO**
≤100 HOURS, >100 HOURS	-5.90	0.438	-13.5	1.0	**NO**
≤1000 HOURS, >1000 HOURS	-1.63	0.353	-4.62	1.0	**NO**

Table 18: (TEST 5) At a given instantaneous fluid discharge, does the monsoon season concentration of suspended silt and clay ≤100 hours after the last flood peak depend on the size of the last flood peak?

INDIVIDUAL "DISCHARGE OF FLOOD PEAK" DATA BINS	n	R^2	SS_r	SS_d (SS_t in parentheses)	DEG. OF FREEDOM ASSOC. w/ SS_d (& SS_t)	F_1 from equation 2.4 (with associated level of significance, p)
>8.5 & ≤24.8 m^3/s	36	0.420	1.92	2.66	34	24.6 (p = 1.9e-5)
>24.8 & ≤41.1 m^3/s	23	0.424	3.67	5.00 (8.67)	21 (22)	*15.4 (p = 7.8e-4)
>41.1 & ≤57.4 m^3/s	10	0.555	1.56	1.25 (2.82)	8 (9)	*9.98 (p = 0.013)
>57.4 & ≤73.7 m^3/s	5	0.545	0.0686	0.0574 (0.126)	3 (4)	*3.59 (p = 0.15)
>73.7 & ≤90.0 m^3/s	7	0.944	0.167	0.00966 (0.177)	5 (6)	*83.9 (p = 2.6e-4)
>90.0 m^3/s	4	0.930	0.0996	0.00749 (0.107)	2 (3)	*26.6 (p = 0.036)
COMBINED DATA BINS	j	R^2	SS_r	SS_d (SS_t in parentheses)	DEG. OF FREEDOM ASSOC. w/ SS_d (& SS_t)	F_1 from equation 2.4 (with associated level of significance, p)
ALL MEASUREMENTS	85	0.377	7.57	12.5	83	50.2 (p = 4.2e-10)
>8.5 & ≤41.1 m^3/s	59	0.356	5.58	10.1	57	31.6 (p = 5.9e-7)
>41.1 & ≤73.7 m^3/s	15	0.548	1.68	1.38 (3.06)	13 (14)	*15.8 (p = 1.6e-3)
>73.7 m^3/s	11	0.840	0.273	0.0522	9	47.1 (p = 7.4e-5)
>8.5 & ≤57.4 m^3/s	69	0.386	7.18	11.4	67	42.0 (p = 1.3e-8)
>57.4 m^3/s	16	0.713	0.324	0.131	14	34.7 (p = 3.9e-5)
>8.5 & ≤90.0 m^3/s	81	0.402	8.01	11.9	79	53.2 (p = 2.0e-10)

TEST WHETHER THE FOLLOWING BINS CAN BE REPRESENTED BY A COMMON REGRESSION LINE	MS_{diff}	MS_{ind}	F_2 from equation 2.5	CRITICAL LEVEL OF SIGNIFICANCE (p)	REJECT NULL HYPOTHESIS OF A COMMON REGRESSION LINE AT p = 0.0001
>8.5 & ≤24.8 m^3/s, >24.8 & ≤41.1 m^3/s, >41.1 & ≤57.4 m^3/s, >57.4 & ≤73.7 m^3/s, >73.7 & ≤90.0 m^3/s, >90.0 m^3/s	-0.412	0.187	-2.20	1.0	**NO**
>8.5 & ≤41.1 m^3/s, >41.1 & ≤73.7 m^3/s, >73.7 m^3/s	-0.356	0.172	-2.07	1.0	**NO**
>8.5 & ≤57.4 m^3/s, >57.4 m^3/s	0.969	0.142	6.82	0.011	**NO**
>8.5 & ≤90.0 m^3/s, >90.0 m^3/s	0.493	0.146	3.38	0.070	**NO**

Table 19: (TEST 5) At a given instantaneous fluid discharge, does the monsoon season concentration of suspended silt and clay >100 hours after the last flood peak depend on the size of the last flood peak?

INDIVIDUAL "DISCHARGE OF FLOOD PEAK" DATA BINS	n	R^2	SS_r	SS_d (SS_t in parentheses)	DEG. OF FREEDOM ASSOC. w/ SS_d (& SS_t)	F_1 from equation 2.4 (with associated level of significance, p)
>8.5 & ≤24.8 m^3/s	53	0.386	21.7	34.5	51	32.1 (p = 6.8e-7
>24.8 & ≤41.1 m^3/s	17	0.692	3.70	1.64	15	33.8 (p = 3.4e-5)
>41.1 & ≤57.4 m^3/s	4	0.877	3.43	0.480 (3.91)	2 (3)	*14.3 (p = 0.063)
>57.4 & ≤73.7 m^3/s	0	—	—	—	—	—
>73.7 & ≤90.0 m^3/s	6	0.251	0.783	2.34 (3.12)	4 (5)	*1.34 (p = 0.31)
>90.0 m^3/s	2	1.00	0.488	0.00 (0.488)	0 (1)	*—
COMBINED DATA BINS	j	R^2	SS_r	SS_d (SS_t in parentheses)	DEG. OF FREEDOM ASSOC. w/ SS_d (& SS_t)	F_1 from equation 2.4 (with associated level of significance, p)
ALL MEASUREMENTS	82	0.419	30.3	42.1	80	57.6 (p = 5.1e-11)
>8.5 & ≤41.1 m^3/s	70	0.424	27.1	36.8	68	50.1 (p = 1.0e-9)
>41.1 & ≤73.7 m^3/s	4	0.877	3.43	0.480 (3.91)	2 (3)	*14.3 (p = 0.063)
>73.7 m^3/s	8	0.355	1.39	2.52 (3.91)	6 (7)	*3.31 (p = 0.12)
>8.5 & ≤57.4 m^3/s	74	0.437	29.7	38.2	72	55.8 (p = 1.5e-10)
>57.4 m^3/s	8	0.355	1.39	2.52 (3.91)	6 (7)	*3.31 (p = 0.12)
>8.5 & ≤90.0 m^3/s	80	0.410	29.2	42.0	78	54.3 (p = 7.5e-9)

TEST WHETHER THE FOLLOWING BINS CAN BE REPRESENTED BY A COMMON REGRESSION LINE	MS_{diff}	MS_{ind}	F_2 from equation 2.5	CRITICAL LEVEL OF SIGNIFICANCE (p)	REJECT NULL HYPOTHESIS OF A COMMON REGRESSION LINE AT p = 0.0001
>8.5 & ≤24.8 m^3/s, >24.8 & ≤41.1 m^3/s, >41.1 & ≤57.4 m^3/s, >73.7 & ≤90.0 m^3/s, >90.0 m^3/s	-0.390	0.582	-0.670	1.0	**NO**
>8.5 & ≤41.1 m^3/s, >41.1 & ≤73.7 m^3/s, >73.7 m^3/s	-1.26	0.572	-2.20	1.0	**NO**
>8.5 & ≤57.4 m^3/s, >57.4 m^3/s	-0.0100	0.533	-0.0188	1.0	**NO**
>8.5 & ≤90.0 m^3/s, >90.0 m^3/s	-0.388	0.538	-0.721	1.0	**NO**

Table 20: (TEST 5) At a given instantaneous fluid discharge, does the "non-monsoon" season concentration of suspended silt and clay depend on the size of the last flood peak?

INDIVIDUAL "DISCHARGE OF FLOOD PEAK" DATA BINS	n	R^2	SS_r	SS_d (SS_t in parentheses)	DEG. OF FREEDOM ASSOC. w/ SS_d (& SS_t)	F_1 from equation 2.4 (with associated level of significance, p)
>8.5 & ≤24.8 m^3/s	17	0.542	7.04	5.95 (13.0)	15 (14)	*17.8 (p = 7.4e-4)
>24.8 & ≤41.1 m^3/s	17	0.589	3.82	2.67 (6.49)	15 (16)	*21.5 (p = 3.2e-4)
>41.1 & ≤57.4 m^3/s	6	0.542	1.40	1.18 (2.58)	4 (5)	*4.74 (p = 0.095)
>57.4 & ≤73.7 m^3/s	5	0.941	0.157	0.00987 (0.167)	3 (4)	*47.7 (p = 6.2e-3)
>73.7 & ≤90.0 m^3/s	5	0.645	0.597	0.328 (0.925)	3 (4)	*5.46 (p = 0.10)
>90.0 m^3/s	3	0.989	0.646	0.00697 (0.653)	1 (2)	*92.8 (p = 0.066)
COMBINED DATA BINS	j	R^2	SS_r	SS_d (SS_t in parentheses)	DEG. OF FREEDOM ASSOC. w/ SS_d (& SS_t)	F_1 from equation 2.4 (with associated level of significance, p)
ALL MEASUREMENTS	53	0.526	17.7	16.0	51	56.6 (p = 8.1e-10)
>8.5 & ≤41.1 m^3/s	34	0.509	10.9	10.5	32	33.2 (p = 2.2e-6)
>41.1 & ≤73.7 m^3/s	11	0.586	1.78	1.26 (3.03)	9 (10)	*12.8 (p = 6.0e-3)
>73.7 m^3/s	11	0.133	0.504	3.28 (3.78)	9 (10)	*1.38 (p = 0.27)
>8.5 & ≤57.4 m^3/s	40	0.454	12.2	14.7	38	31.6 (p = 1.9e-6)
>57.4 m^3/s	16	0.449	2.83	3.47 (6.30)	14 (15)	*11.4 (p = 4.5e-3)
>8.5 & ≤90.0 m^3/s	50	0.516	16.5	15.5	48	51.2 (p = 4.2e-9)

TEST WHETHER THE FOLLOWING BINS CAN BE REPRESENTED BY A COMMON REGRESSION LINE	MS_{diff}	MS_{ind}	F_2 from equation 2.5	CRITICAL LEVEL OF SIGNIFICANCE (p)	REJECT NULL HYPOTHESIS OF A COMMON REGRESSION LINE AT p = 0.0001
>8.5 & ≤24.8 m^3/s, >24.8 & ≤41.1 m^3/s, >41.1 & ≤57.4 m^3/s, >57.4 & ≤73.7 m^3/s, >73.7 & ≤90.0 m^3/s, >90.0 m^3/s	-1.56	0.529	-2.95	1.0	**NO**
>8.5 & ≤41.1 m^3/s, >41.1 & ≤73.7 m^3/s, >73.7 m^3/s	-0.655	0.333	-1.97	1.0	**NO**
>8.5 & ≤57.4 m^3/s, >57.4 m^3/s	-5.00	0.396	-12.6	1.0	**NO**
>8.5 & ≤90.0 m^3/s, >90.0 m^3/s	-0.153	0.323	-0.474	1.0	**NO**

Table 21: (TEST 6) At a given instantaneous fluid discharge, does the measured 1954-1976 concentration of suspended silt and clay depend on the number of measurement verticals?

INDIVIDUAL "NUMBER OF VERTICALS" DATA BINS	n	R^2	SS_r	SS_d (SS_t in parentheses)	DEG. OF FREEDOM ASSOC. w/ SS_d (& SS_t)	F_1 from equation 2.4 (with associated level of significance, p)
1 vertical	32	0.0728	0.194	2.47 (2.67)	30 (31)	*2.36 (p = 0.13)
2 verticals	84	0.374	21.3	35.7	82	48.9 (p = 6.6e-10)
3 verticals	24	0.669	8.57	4.24	22	44.5 (p = 1.0e-6)
≥4 verticals	5	0.857	7.02	1.17 (8.19)	3 (4)	*18.0 (p = 0.024)
COMBINED DATA BINS	j	R^2	SS_r	SS_d	DEG. OF FREEDOM ASSOC. w/ SS_d	F_1 from equation 2.4 (with associated level of significance, p)
ALL MEASUREMENTS	145	0.465	47.7	54.8	143	124 (p < 1.0e-16)

TEST WHETHER THE FOLLOWING BINS CAN BE REPRESENTED BY A COMMON REGRESSION LINE	MS_{diff}	MS_{ind}	F_2 from equation 2.5	CRITICAL LEVEL OF SIGNIFICANCE (p)	REJECT NULL HYPOTHESIS OF A COMMON REGRESSION LINE AT p = 0.0001
1 vertical, 2 verticals, 3 verticals, ≥4 verticals	1.33	0.365	3.64	0.014	**NO**

Appendix 3: VELOCITY PROFILES OVER UPPER-PLANE BEDS AND ANTIDUNES

Regressions of quasi-logarithmic velocity profiles through the spatial average of the velocity profiles measured by Guy and others (1966) over upper-plane beds and antidunes. The order of presentation of the runs in this appendix is the same as reported by Guy and others (1966) and the same as in Table 3.2.

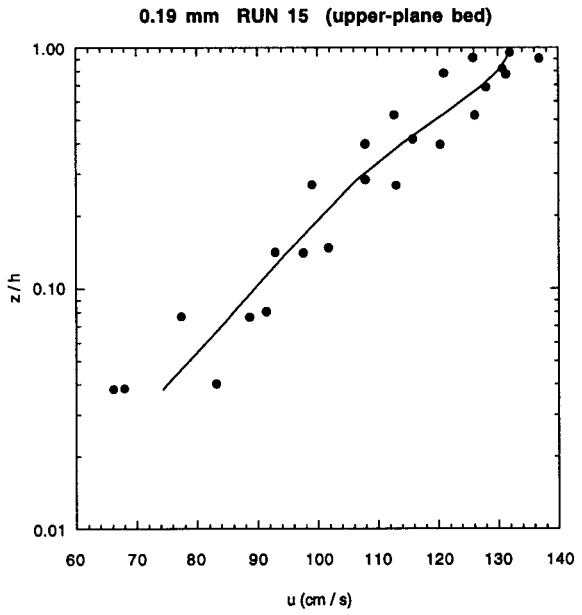

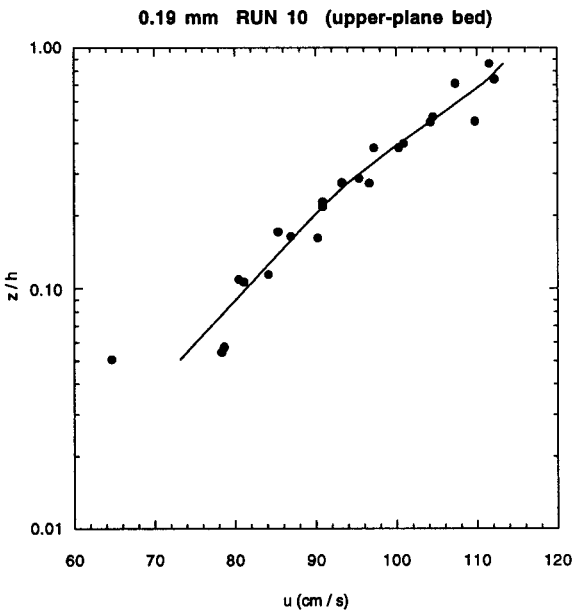

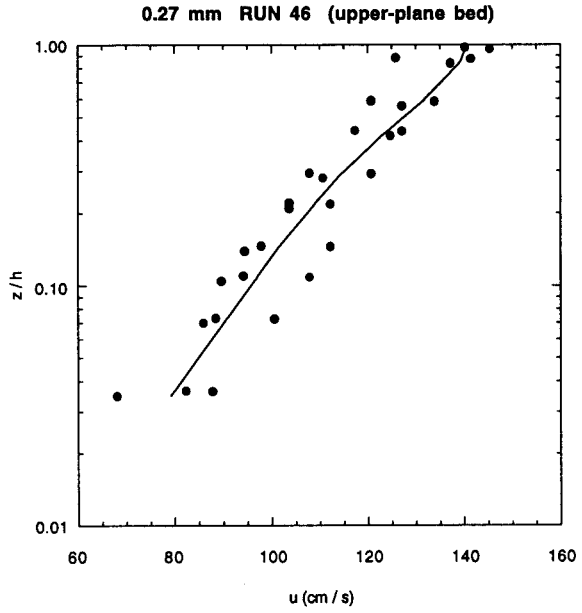

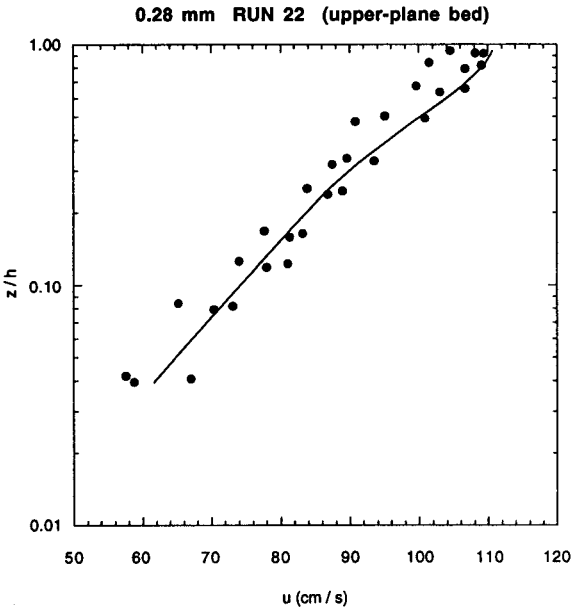

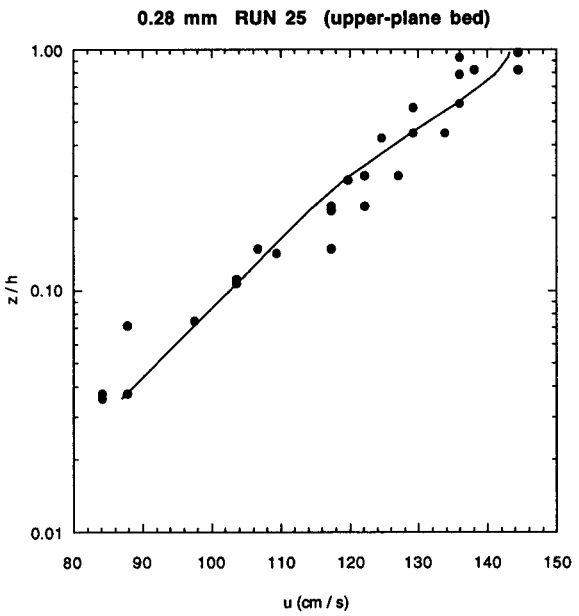
0.28 mm RUN 25 (upper-plane bed)
1.00
0.10
0.01
z / h
80 90 100 110 120 130 140 150
u (cm / s)

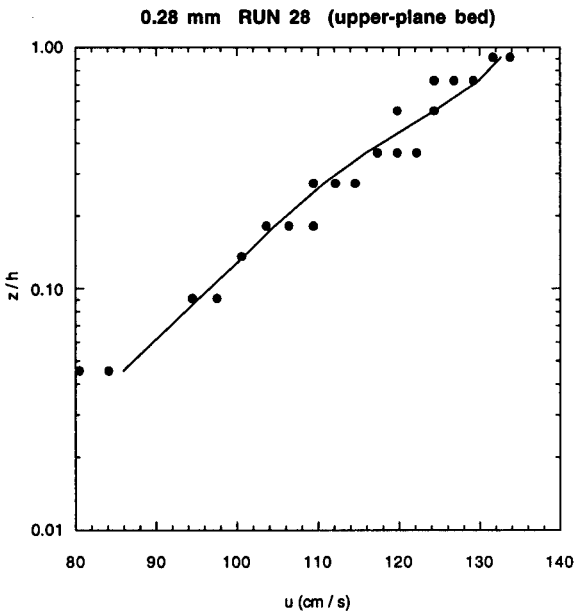
0.28 mm RUN 28 (upper-plane bed)
1.00
0.10
0.01
z / h
80 90 100 110 120 130 140
u (cm / s)

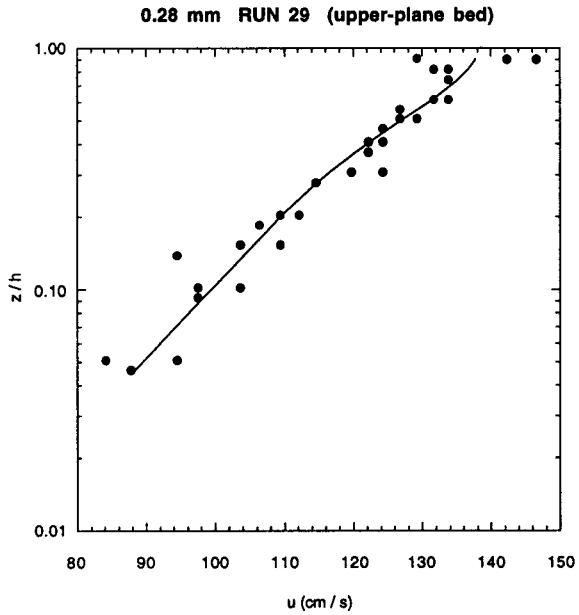
0.28 mm RUN 29 (upper-plane bed)
1.00
0.10
0.01
z / h
80 90 100 110 120 130 140 150
u (cm / s)

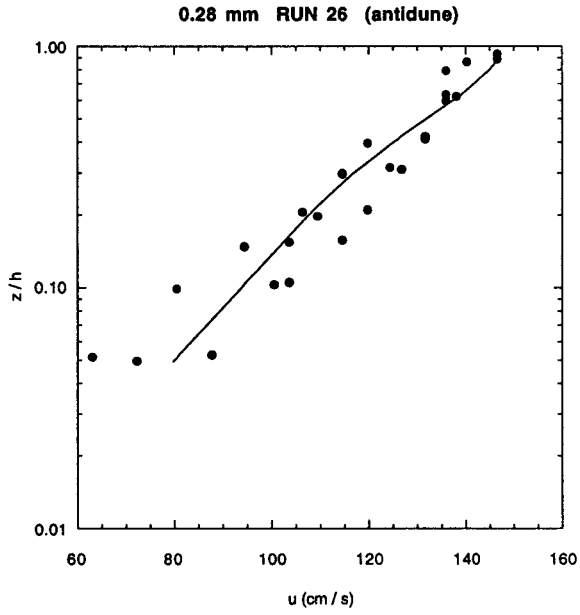
0.28 mm RUN 26 (antidune)
1.00
0.10
0.01
z / h
60 80 100 120 140 160
u (cm / s)

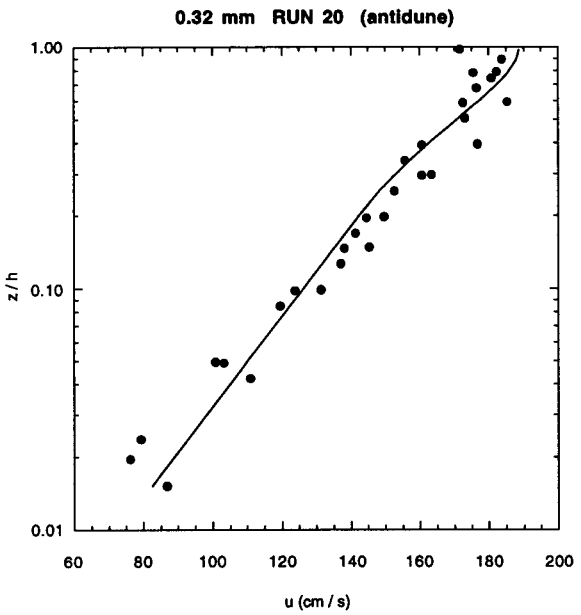
0.32 mm RUN 20 (antidune)
1.00
0.10
0.01
z / h
60
80
100
120
140
160
180
200
u (cm / s)

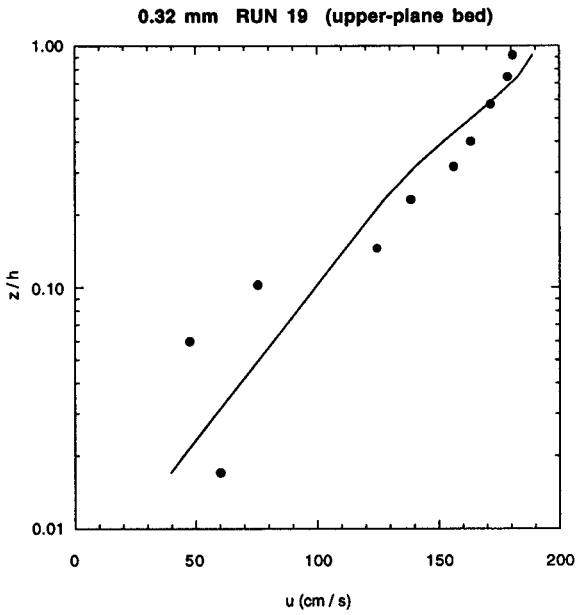
0.32 mm RUN 19 (upper-plane bed)
1.00
0.10
0.01
z / h
0
50
100
150
200
u (cm / s)

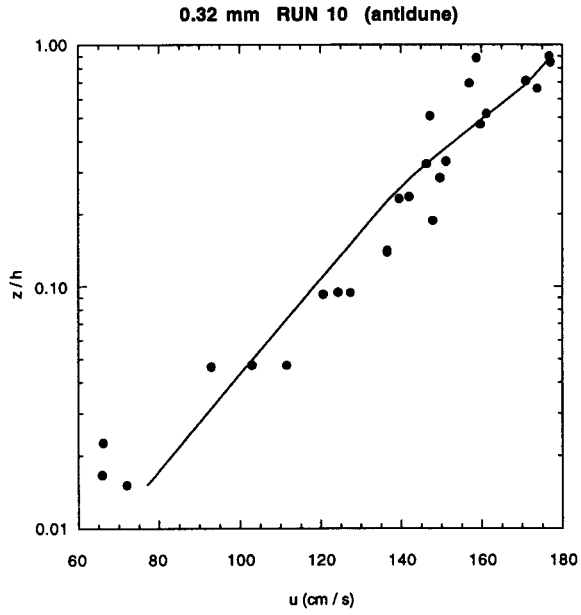
0.32 mm RUN 10 (antidune)
1.00
0.10
0.01
z / h
60
80
100
120
140
160
180
u (cm / s)

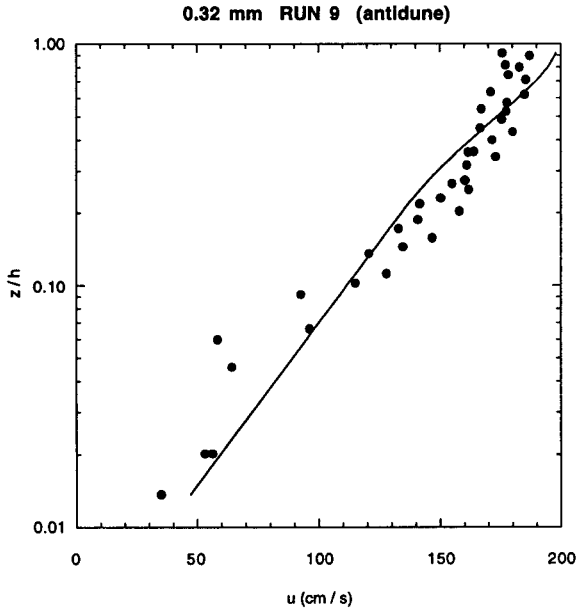
0.32 mm RUN 9 (antidune)
1.00
0.10
0.01
z / h
0
50
100
150
200
u (cm / s)

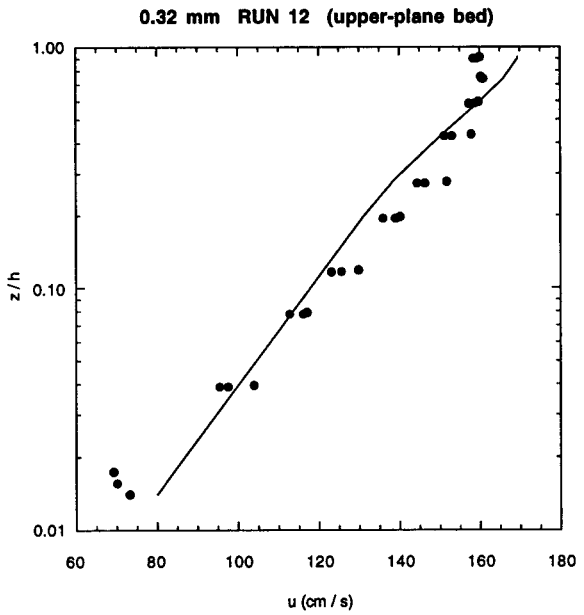
0.32 mm RUN 12 (upper-plane bed)
1.00
0.10
0.01
z / h
60
80
100
120
140
160
180
u (cm / s)

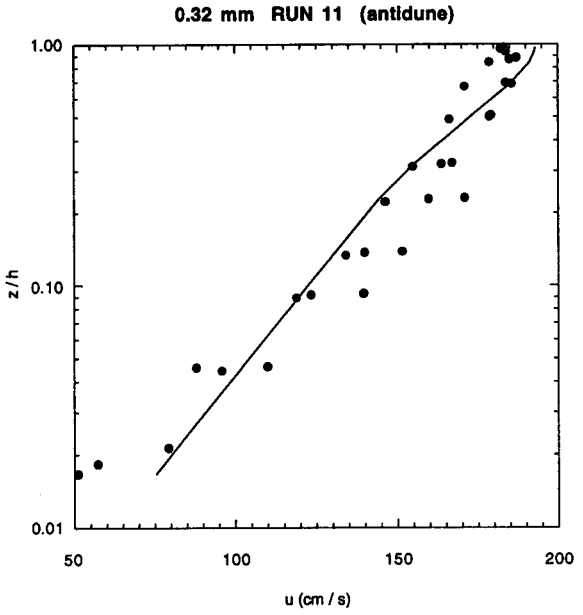
0.32 mm RUN 11 (antidune)
1.00
0.10
0.01
z / h
50
100
150
200
u (cm / s)

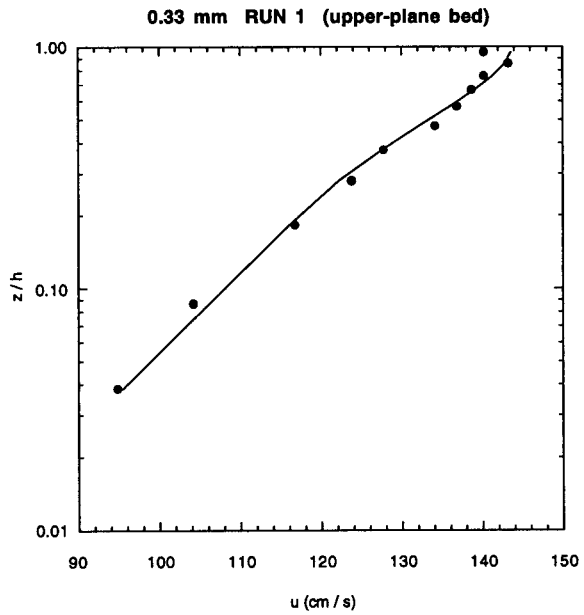
0.33 mm RUN 1 (upper-plane bed)
1.00
0.10
0.01
z / h
90
100
110
120
130
140
150
u (cm / s)

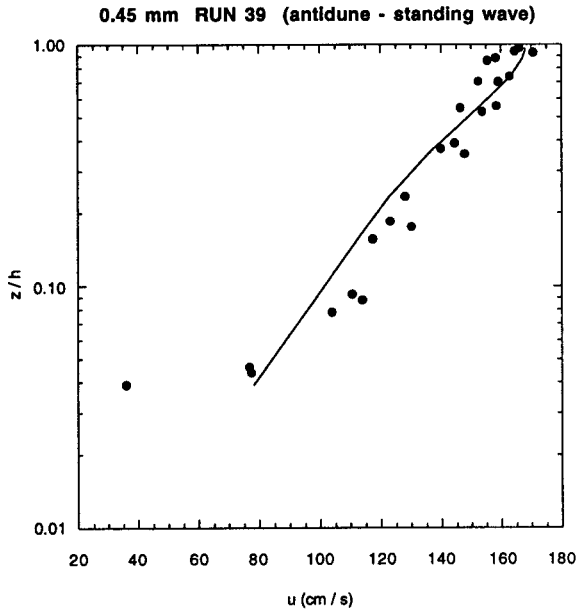
0.45 mm RUN 39 (antidune - standing wave)
1.00
0.10
0.01
z / h
20
40
60
80
100
120
140
160
180
u (cm / s)

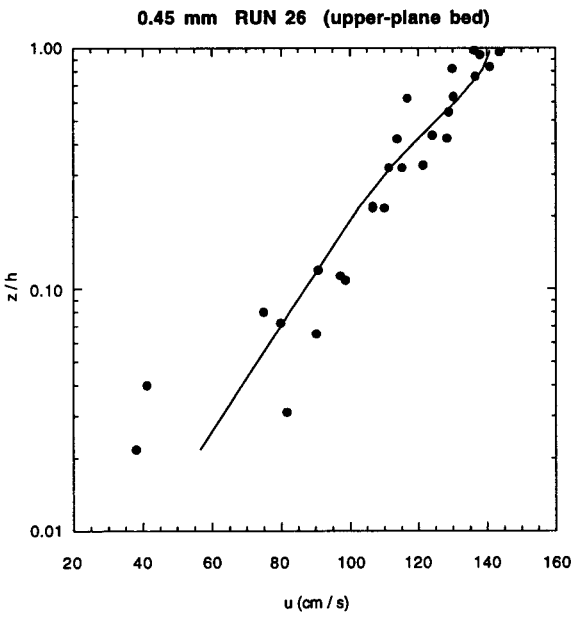
0.45 mm RUN 26 (upper-plane bed)
1.00
0.10
0.01
z / h
20
40
60
80
100
120
140
160
u (cm / s)

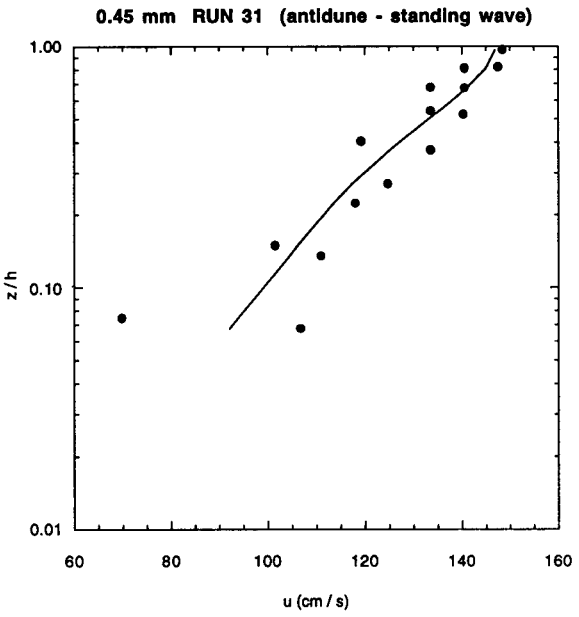
0.45 mm RUN 31 (antidune - standing wave)
1.00
0.10
0.01
z / h
60
80
100
120
140
160
u (cm / s)

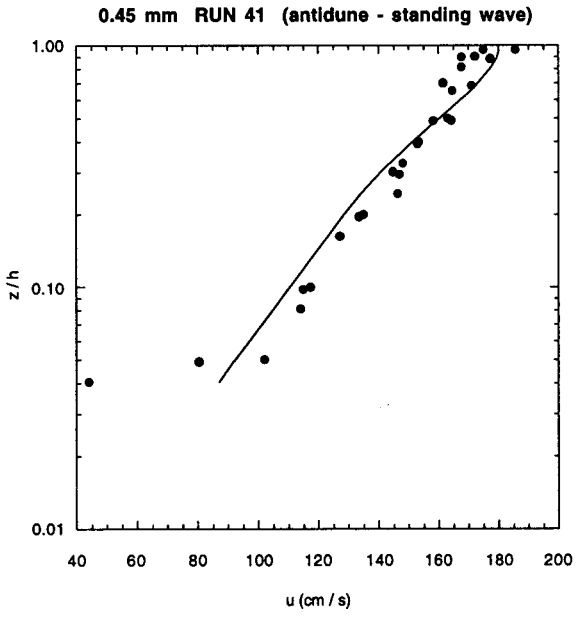
0.45 mm RUN 41 (antidune - standing wave)
1.00
0.10
0.01
z / h
40
60
80
100
120
140
160
180
200
u (cm / s)

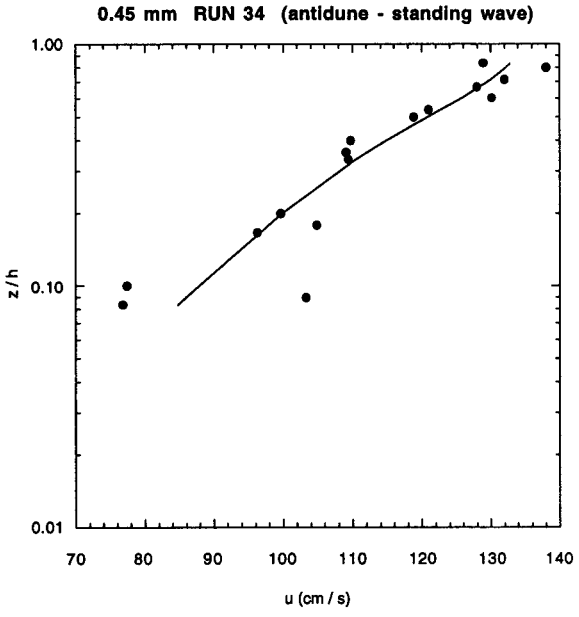
0.45 mm RUN 34 (antidune - standing wave)
1.00
0.10
0.01
z / h
70
80
90
100
110
120
130
140
u (cm / s)

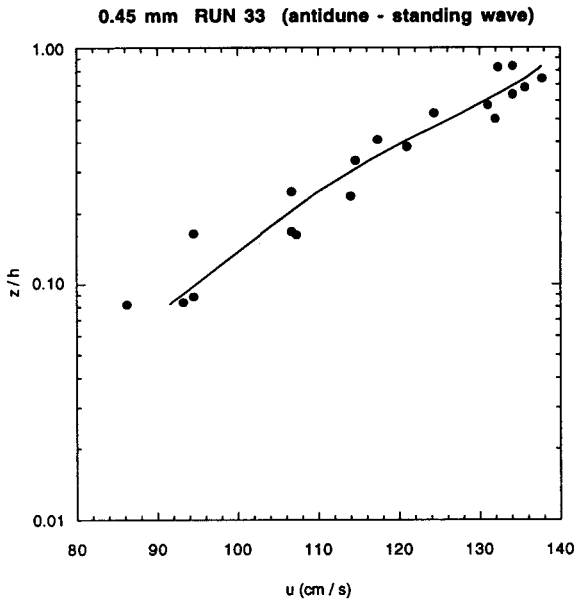
0.45 mm RUN 33 (antidune - standing wave)
1.00
0.10
0.01
z / h
80
90
100
110
120
130
140
u (cm / s)

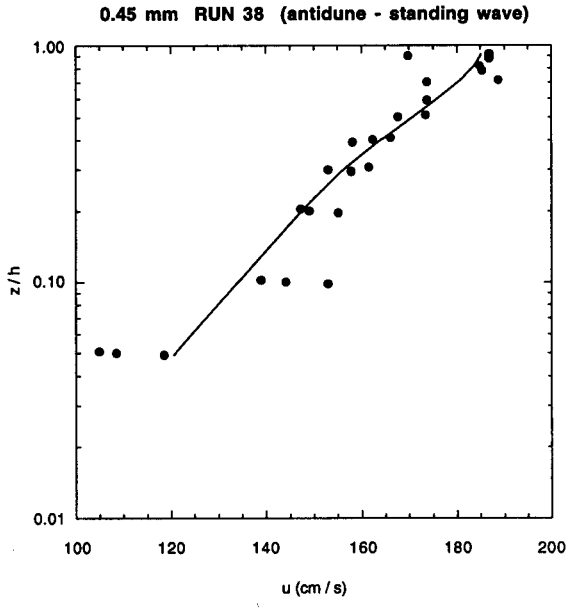
0.45 mm RUN 38 (antidune - standing wave)
1.00
0.10
0.01
z / h
100
120
140
160
180
200
u (cm / s)

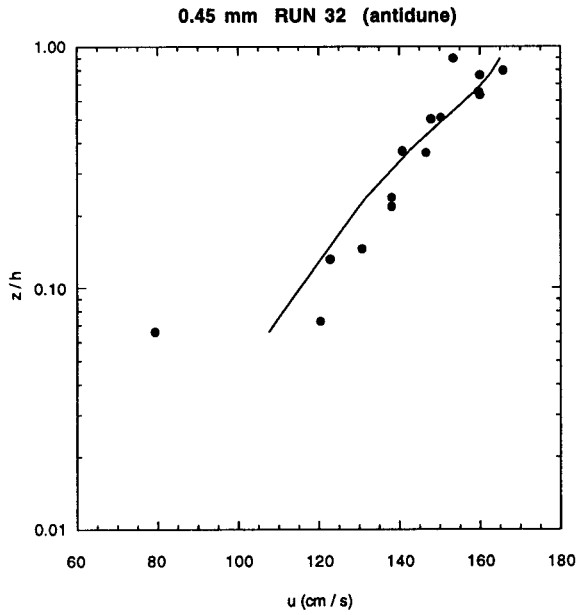
0.45 mm RUN 32 (antidune)
1.00
0.10
0.01
z / h
60
80
100
120
140
160
180
u (cm / s)

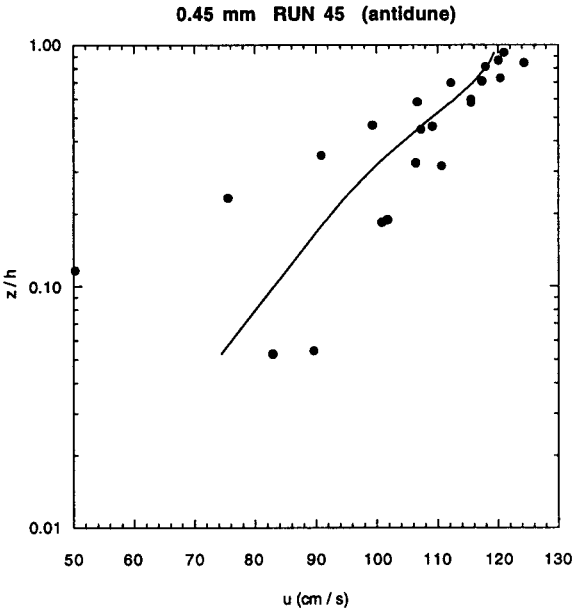
0.45 mm RUN 45 (antidune)
1.00
0.10
0.01
z / h
50
60
70
80
90
100
110
120
130
u (cm / s)

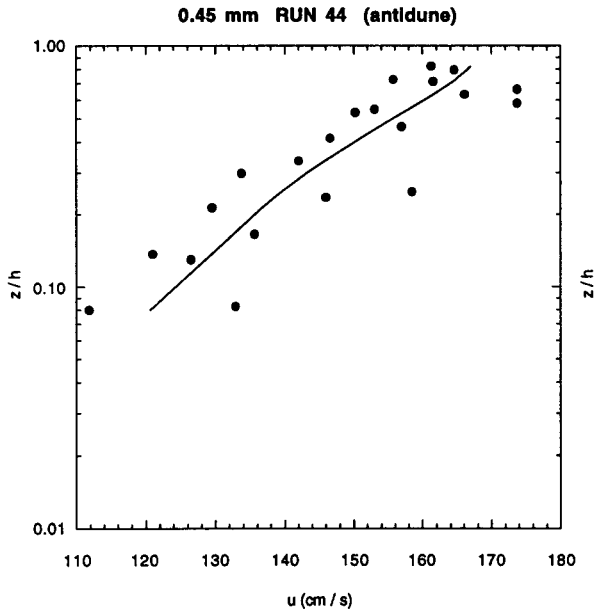
0.45 mm RUN 44 (antidune)
1.00
0.10
0.01
z / h
110 120 130 140 150 160 170 180
u (cm / s)

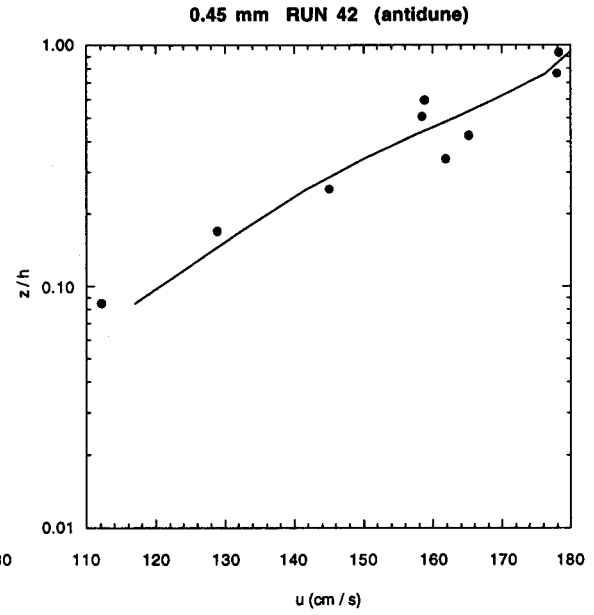
0.45 mm RUN 42 (antidune)
1.00
0.10
0.01
z / h
110 120 130 140 150 160 170 180
u (cm / s)

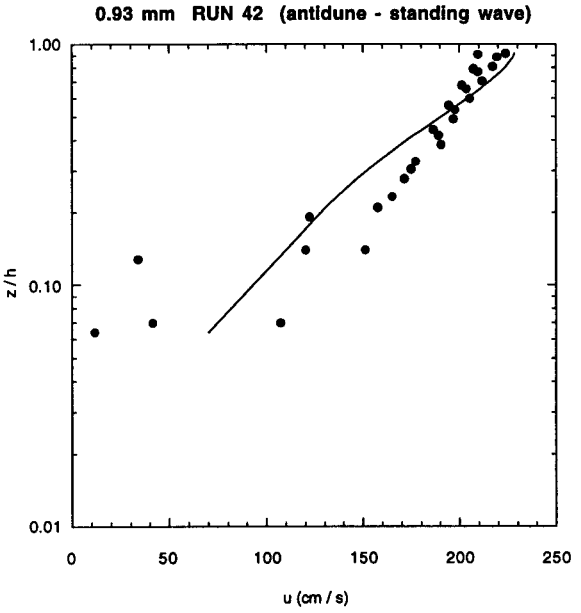
0.93 mm RUN 42 (antidune - standing wave)
1.00
0.10
0.01
z / h
0 50 100 150 200 250
u (cm / s)

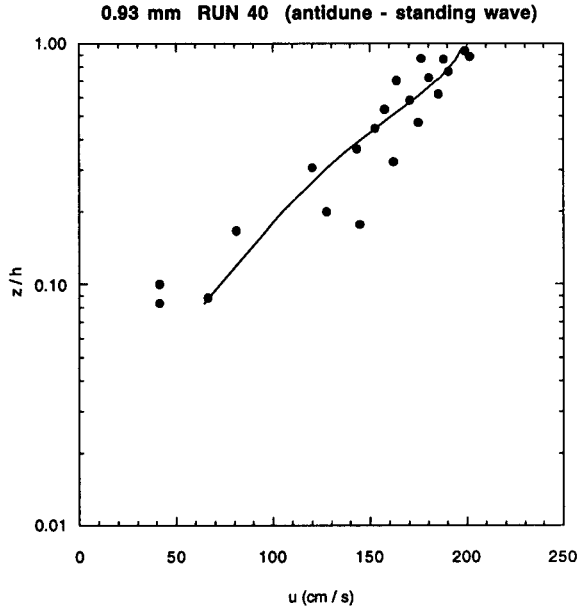
0.93 mm RUN 40 (antidune - standing wave)
1.00
0.10
0.01
z / h
0 50 100 150 200 250
u (cm / s)

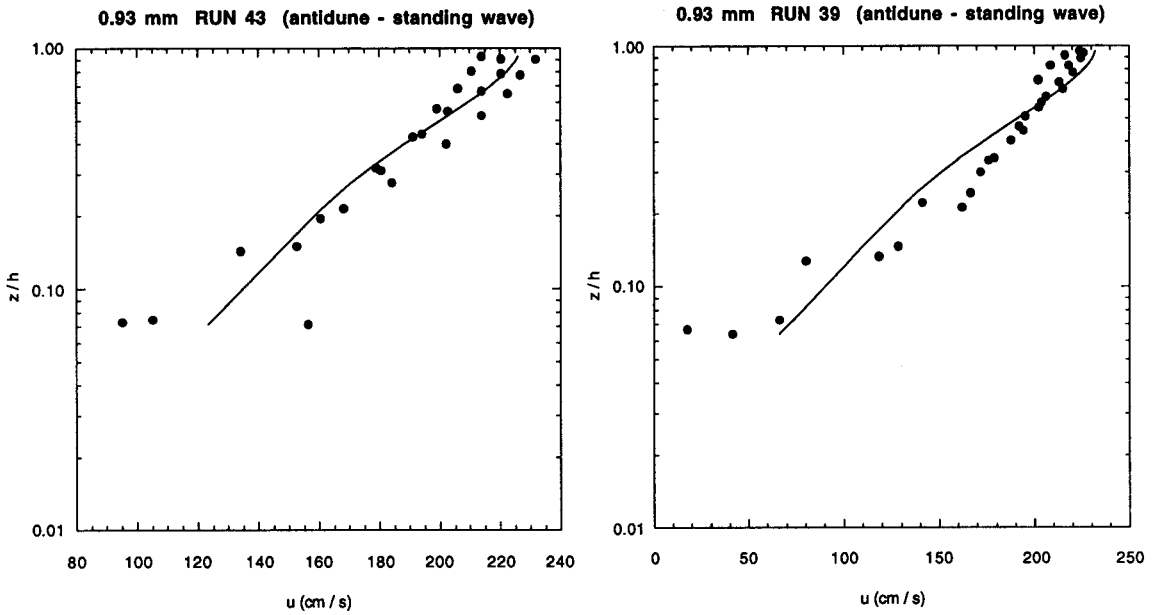
0.93 mm RUN 43 (antidune - standing wave)
1.00
0.10
0.01
z / h
80
100
120
140
160
180
200
220
240
u (cm / s)
0.93 mm RUN 39 (antidune - standing wave)
1.00
0.10
0.01
z / h
0
50
100
150
200
250
u (cm / s)

VITA

Name: David Joseph Topping

Born: October 6, 1966
Warwick, Rhode Island

Education: North Kingstown Senior High School, 1984
North Kingstown, Rhode Island

B.S., Earth, Atmospheric, and Planetary Sciences, 1988
Massachusetts Institute of Technology
Cambridge, Massachusetts

M.S., Geological Sciences, 1991
Ph.D., Geological Sciences, 1997
University of Washington
Seattle, Washington